Tidal Turbine Array Modelling

Justine Schluntz

St. John's College

University of Oxford

A thesis submitted for the degree of

Doctor of Philosophy

Trinity Term 2014

Abstract

Computational fluid dynamics (CFD) is used in this thesis to model wind and tidal stream turbines and to investigate tidal turbine fence performance. There are two primary objectives of this work. The first is to develop and validate an actuator line method for the simulation of wind and tidal turbines which applies the blade forces to the flow field without the need for a regularisation kernel. The second is to examine tidal fences using, in part, the newly developed actuator line method.

A potential flow equivalence method for determining the relative velocity to the blade chord and flow angle at the rotor blades in the actuator line method is proposed and validated. Results for simulations using this method compare favourably with those from both experiments and alternative computational methods, although the present model's results deviate from experimental results in the vicinity of the blade tips.

A CFD-embedded blade element-momentum tool is used to design rotors for operation in infinitely wide tidal fences spanning a tidal channel. Rotors are designed for fences with several different blockage ratios, with those designed for high blockage flows having greater solidity than those designed for operation in fences with lower blockage. It is found that designing rotors for operational blockage conditions can significantly improve the power output achieved by a tidal fence. Improved power output for higher blockage conditions is achieved by the application of greater thrust to the flow.

Actuator line simulations of short (up to 8 turbines) fences with varying intra-rotor spacing and number of rotors confirm that hydrodynamic performance of the rotors improves as the spacing is reduced and as rotors are added to a fence. The position of a rotor within the fence impacts its performance; rotors at the ends of a fence extract reduced power compared to those at the centre of the fence, particularly for tip speed ratios greater than the design tip speed ratio.

Acknowledgments

I would like to thank my colleagues in the Oxford Tidal Energy Research Group and in Jenkin Room 11 for your support and feedback. In particular, thanks to Clarissa, Conor, Simon, Chris, and my supervisor, Richard, for your generous assistance and guidance. Also, thanks to my college advisor, Ian Sobey, for your feedback and advice when I needed it most.

I am very grateful to the Rhodes Trust, which has funded this work, as well as St. Johns College, which provided grants enabling me to present my findings at two international conferences.

Advanced Research Computing (ARC) at the University of Oxford provided resources on which the larger simulations in this thesis were performed. I would like to express my gratitude to the ARC staff for the support they provided with this resource.

Finally, and most importantly, thank you to all of my friends, in England and elsewhere, who provided invaluable support and friendship throughout this endeavor.

Contents

Nomenclature

Scalars

a	axial induction factor
A	rotor area
B	blockage ratio
C_d	drag coefficient
C_l	lift coefficient
$C_{\dot{m}}$	coefficient of mass flow rate
C_n	normal force coefficient
C_p	power coefficient
$C_{pressure}$	pressure coefficient
C_t	thrust coefficient; alternatively, tangential force coefficient
c	blade chord
c_x	local thrust coefficient
c_θ	local tangential force coefficient
d	rotor diameter
e	length of mesh element
f	tip correction factor
f_{cutoff}	cutoff frequency
h	channel height
k	turbulent kinetic energy
$\mathbf{M}_\theta$	angular momentum
m	number of spanwise blade segments
$\dot{m}$	mass flow rate
N	number of blades per rotor
n	number of devices in a tidal array
P	power
p	pressure
Q	torque
q	velocity perturbation

R	rotor radius
r	radius of blade element
r_s	radius from collocation point
Re	Reynolds number
s	wing span; alternatively, lateral intra-rotor spacing
t	time
U	flow speed
u	flow speed in x-direction
u_x	streamwise flow speed
u_θ	swirl velocity
V	volume
v	flow speed in y-direction
w	flow speed in z-direction
$w_{channel}$	channel width
α	blade angle of attack
α_e	effective angle of attack
β	blade pitch/twist
Γ	circulation
γ	azimuth angle
δr	spanwise width of blade element
ϵ	turbulent kinetic energy dissipation rate; alternatively, regularisation parameter
η_ϵ	regularisation kernel
λ	tip speed ratio $[R\Omega/U_{ref}]$
μ	dynamic viscosity
μ_t	turbulent viscosity
ν	kinematic viscosity
ρ	fluid density
σ	solidity
Ω	angular velocity
ω	vorticity magnitude; alternatively, specific turbulent kinetic energy dissipation rate

Vectors

$\mathbf{D}$	drag
$\mathbf{F}$	force
$\mathbf{f}$	force per unit volume
$\mathbf{L}$	lift
$\mathbf{S}$	source
$\mathbf{T}$	thrust
$\mathbf{U}$	velocity
$\mathbf{U}_\infty$	upstream velocity
$\mathbf{U}_{rel}$	blade relative velocity
$\boldsymbol{\omega}$	vorticity
$\boldsymbol{\omega}_b$	bound vorticity

Acronyms

1D / 2D / 3D	one- / two- / three-dimensional
AMG	algebraic multigrid
BEM	blade element-momentum
CFD	computational fluid dynamics
CFL condition	Courant-Friedrichs-Lewy condition
DNS	direct numerical simulation
EMEC	European Marine Energy Centre
LES	large eddy simulation
MEXICO	Measurements and EXperiments In COntrolled conditions
NACA	National Advisory Committee for Aeronautics (United States)
NASA	National Aeronautics and Space Administration (United States)
NREL	National Renewable Energy Laboratory (United States)
OpenFOAM	Open Field Operation and Manipulation
RANS	Reynolds-averaged Navier-Stokes
SOWFA	Simulator for Offshore Wind Farm Application
SIMPLE	semi-implicit method for pressure linked equations
SST	shear stress transport
TGU	Turbine Generator Unit
THAWT	Transversal Horizontal Axis Water Turbine
VTM	Vorticity Transport Model

Chapter 1

Introduction and Background

The potential for tidal energy in the United Kingdom energy system is introduced in this chapter. An overview of various tidal energy devices and completed and planned prototype testing is also provided. An outline of this thesis is included in the final section of this chapter.

1.1 Introduction

Concerns regarding the effect of fossil fuels on climate change, the desire for greater energy security, and the acknowledgment of limited fossil fuel resources have served as the main motivations to reduce fossil fuel consumption and increase renewable energy production [1]. The United Kingdom has committed to a goal of increasing renewable energy usage from about 2% of the country's overall energy demand in 2008 to 15% by 2020 (The UK Renewable Energy Strategy [2]). A variety of sectors, including onshore and offshore wind, solar, wave, and tidal, are expected to continue to experience growth as the country attempts to make this transition (Renewable Advisory Board [3]).

Tidal mills in the UK dating to the middle ages provide evidence that the potential energy resource of the tides has been utilised on a small scale for centuries [4]. However, modern

approaches to capturing the energy potential between ebb and flood tides have yet to be implemented on a large scale in the UK. Recent proposals have included a 10-mile tidal barrage across the Severn Estuary with a minimum lifespan of 120 years, but this plan was abandoned due to high cost as well as environmental concerns [5]. Due to this setback and other difficulties in the conversion of potential and kinetic energy of tides to electrical energy, most current tidal energy projects are instead focused on capturing tidal stream kinetic energy using arrays consisting of a number of individual, free-standing tidal stream turbines, rather than tidal barrages.

Serious investigations into tidal stream turbines began in the 1980s when Davis, Swan, and Kenneth performed experimental turbine tests in a flume [6]. A number of advances in tidal energy technology have been made in the last three decades, but tidal energy devices have yet to reach costs of energy comparable to those reached by the more developed offshore wind industry (the levelised cost of offshore wind energy in the UK is estimated to be in the range of £95 to £185 per MWh in 2025 [7]). Thus, there is scope and need for improvement.

Nevertheless, tidal stream energy has the potential to play an important role in the transition toward low-carbon energy because of the particularly large resource in the UK's waters, which contain about half of Europe's extractable tidal and ocean current energy source. Black & Veach estimated in 2005 that the UK's technically extractable marine current resource (that which could be extracted within expected environmental and cost limitations) is 18 TWh/year [8], the majority of which is in sites with mean current velocity greater than 2.5 m/s and depth greater than 30 m. In 2011, the Carbon Trust reported a revised technical resource estimate of 29 TWh/year, of which 20.6 TWh/year is the practical resource (the technical resource that can be extracted after grid, spatial, and other external constraints are accounted for) [9, 10].

1.2 Tidal Energy Devices and Prototype Testing

The primary tidal energy device classifications will be discussed in this section. In addition, a brief overview of tidal turbine prototype testing and tidal turbine array developments is presented.

1.2.1 Tidal Energy Device Categorisation

Free-standing tidal energy devices typically fall into one of three categories: axial-flow turbines, cross-flow turbines, and oscillating hydrofoils. Axial-flow tidal turbines, shown in Figure 1.1 (a), rotate about a horizontal axis that is aligned with the flow direction and look similar to the prominent three-bladed wind turbine designs, although the number of blades can vary. The incoming flow must be parallel or nearly parallel to the axis of rotation for axial-flow turbines to be efficient. There are a number of axial-flow tidal turbine designs, including OpenHydro's Open-Centre Turbine [11] and Marine Current Turbines' SeaGen turbines [12].

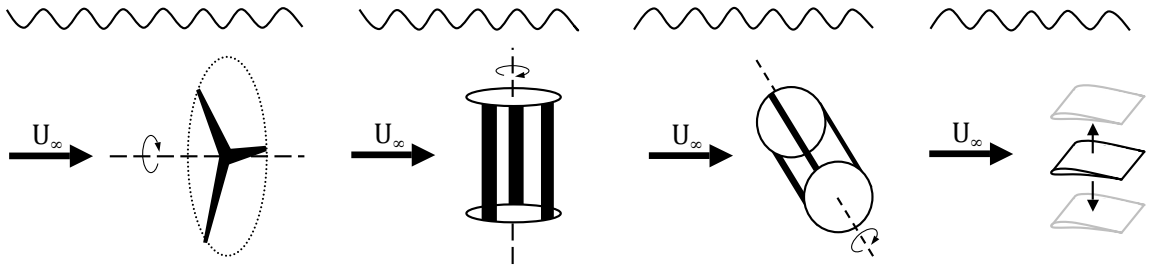

Figure 1.1: (a) Axial-flow turbine, (b) Vertical-axis cross-flow turbine, (c) Horizontal-axis cross-flow turbine, and (d) Oscillating hydrofoil.

Cross-flow tidal turbines may have either a vertical or horizontal axis of rotation. These are depicted in parts (b) and (c) of Figure 1.1, respectively. The incoming flow is perpendicular to the axis of rotation of these devices. Vertical-axis cross-flow turbines offer the advantage that, unlike axial-flow turbines, they do not need to be oriented toward the direction of the

flow to extract energy. Because of this, these devices are attractive for deployment in an environment where the flow direction is changing. An example of a vertical-axis cross-flow turbine is the turbine developed by Blue Energy [13].

The main advantage of horizontal-axis cross-flow turbines is that they are well-suited for shallow water deployment. THAWT, a horizontal-axis cross-flow turbine developed at the University of Oxford, was designed so that it can be stretched across a channel or basin [14]. Another horizontal-axis cross-flow device is Ocean Renewable Power Company's Turbine Generator Unit, or TGU [15].

One of the primary shortcomings of cross-flow turbines (both horizontal- and vertical-axis) is that the blades traverse the wake of the other turbine blades for a large part of each cycle. The blades experience reduced hydrodynamic efficiency when this occurs. In addition, this causes the blades to face a high variation in loading as they sweep through a rotation, reducing the turbines' fatigue life.

Oscillating hydrofoil devices, shown in Figure 1.1 (d), extract energy from a flow by way of a hydrofoil connected to a moving arm. The arm's oscillating motion, caused by the tidal current, drives a hydraulic or mechanical system to generate power. Several developers are pursuing oscillating hydrofoil devices. Examples of this type of device include BioPower Systems' bioSTREAM [16] and Pulse Tidal's Pulse-Stream 100 [17].

Oscillating hydrofoils have a number of shortcomings. They provide a cyclical power output due to the oscillating motion of the arm and also have low hydrodynamic efficiency because the hydrofoil is not always at the optimum angle of attack. The loading and unloading of the hydrofoil also result in fatigue problems for these devices. Finally, oscillating hydrofoil designs have typically required a substantial support structure, which can significantly increase their cost.

1.2.2 Tidal Turbine Development and Testing

Despite the abundance of tidal turbine concepts, the vast majority of designs at the full-scale prototype development stage are axial-flow designs. The field is still relatively immature, and the physical nature of the flow through these devices is not fully understood. For instance, the effects that waves, sheared inflow, turbulent inflow, and support structure geometry, among other things, have on tidal turbine performance are only partially known. The flow characteristics for tidal turbine arrays, including blockage and wake effects, are even less understood.

Experimental tests (both laboratory scale and prototype scale), analytical methods, and computational fluid dynamics (CFD) methods are used by researchers and developers to continue filling this void in understanding. Experimental tests generally rely on fewer assumptions than numerical methods, but it is impossible to match non-dimensional groups such as the Reynolds number and Froude number in scaled experimental tests. Also, prototype-scale experimental tests can be very costly. Analytical studies and CFD simulations are often employed to study tidal energy devices due to their ability to predict many details about the characteristics of the flow at a reasonable cost. Further, all non-dimensional groups can be properly matched in CFD simulations. However, analytical and CFD methods have several shortcomings. For instance, some CFD modelling techniques (such as 3D blade-resolved models) can have high computational cost. In addition, it is difficult to correctly model a number of physical flow features that can impact rotor performance, for instance free-stream turbulence and blade separation, in analytical and CFD methods.

Analytical and CFD methods, as well as their limitations, will be discussed in detail in Chapter 2. The remainder of this section will discuss some of the significant developments in prototype and array experimental tests.

In addition to numerous flume experiments, a growing number of tidal energy device concepts have been tested in the sea and/or rivers. Among the first tidal turbine prototypes to be tested in the field were Verdant Power's Free Flow, first deployed in the East River in New York in 2006 [18], Marine Current Turbines' SeaGen, installed in Strangford Lough in 2008 [19], and OpenHydro's Open-Centre Turbine at the European Marine Energy Centre (EMEC) in Scotland (2006) as well as in Canada's Bay of Fundy (2009) [20]. An increasing number of field prototype tests have been undertaken in the time since these initial tests.

Upcoming field testing is expected to shift from single-device testing to turbine array testing. In 2011, OpenHydro announced a 4-turbine, 8 MW demonstration farm to be installed off the coast of France [21]. In 2013, the UK government awarded £20 million to two tidal turbine site owners as part of the Marine Energy Array Demonstrator scheme [22]. One of the recipients of this funding, MeyGen, is currently planning field tests of a 6-rotor array in the Inner Sound (Scotland) [23]. The other funding recipient, SeaGeneration Wales, is planning to deploy an array of up to 9 turbines off the coast of Anglesey [24]. Among additional tidal turbine arrays in development is a 10 MW array being planned by Scottish Power [25].

A number of laboratory-scale tidal array experimental investigations have been carried out in recent years. Scale tests in flumes can provide valuable information in a more controlled environment and at lower expense than field tests. The results from these investigations (as well as those from analytical and CFD studies) can be used to inform the design of demonstration arrays. Daly et al. analysed the effects that side wall proximity had on the flow field around a single-row tidal array [26]. In this investigation, the tidal array consisted of an actuator fence rather than individual rotors. This actuator fence was a rectangular porous plate (varying porosities were used) which applied a thrust on the flow to simulate the presence of tidal rotors in the flow field. Myers et al. used actuator discs, which are

porous plates that simulate the effects of individual rotors on the flow field, to examine the effects of varying the lateral spacing between rotors in a tidal array [27]. Experiments with rotors, rather than actuator discs, have also been carried out. For example, Stallard et al. examined wake recovery rates for single-row arrays of varying numbers of rotors using 3-bladed rotors [28].

1.3 Outline

This project focuses on CFD modelling of tidal turbines and arrays. First, a robust actuator line model is implemented and validated. Actuator line models are unsteady CFD-embedded rotor models in which the effect of each rotor blade on the flow field is simulated by a line of point sources (an actuator line). These sources may be either vorticity or momentum sources, depending on the formulation of the governing equations. Because the blades are not explicitly included in the computational mesh, the blade boundary layers do not need to be discretised. Thus, actuator line models are capable of simulating unsteady flow through wind and tidal turbines in an efficient manner. The standard actuator line model for wind and tidal turbine simulation is modified in the current work; the current model utilises a novel blade-flow field coupling which allows for the flow speed and direction at the blade to be determined without the use of the artificial smearing techniques employed in other actuator line model implementations.

Next, the modified actuator line model and a blade element-momentum (BEM) model are employed in the study of tidal fences, i.e. turbine arrays in which the rotors are arranged in a single lateral row, with no rotors operating in the wake of others. Two classes of tidal fences are considered in this thesis; infinitely long fences spanning the entire width of a channel and finite-length fences partially spanning a wide channel.

The material covered in this thesis includes:

- Analysis Techniques:

  In this chapter, a range of methods used to analyse wind and tidal turbines are introduced. An overview of the literature covering studies completed with each method is also included. The methods discussed are actuator disc models, blade element-momentum models, vortex methods, 3D blade-resolved Navier-Stokes simulations, and actuator line models. In addition, a discussion of the governing equations and associated computational fluid dynamics numerical methods used in this thesis is included.

- Actuator Line Model Modifications, Verification, and Implementation:

  A new method of determining the flow characteristics at the actuator line blade segments is introduced and verified in this chapter. The routine requires velocities at known locations to be sampled and utilised to determine the velocity at the the blade for each corresponding blade segment. The method used to adapt the actuator line model to an unstructured mesh is also described. Finally, an overview of the 3D unsteady actuator line model implementation in ANSYS Fluent is presented.

- Model Validation:

  The actuator line model, including the flow analysis routine and unstructured mesh adaptation introduced in the previous chapter, has been validated using experimental data from the NREL/NASA Ames Phase VI wind tunnel tests. This chapter includes details of the experimental tests, a brief review of NREL Phase VI CFD validation studies selected for comparison, and a discussion of the actuator line computational results.

- Rotor Performance in Infinite-Length Tidal Fences:

  It is of particular interest to investigate the effects of lateral spacing on rotor performance in tidal turbine fences. However, there is a dearth of rotors designed for the ranges of local blockage that a tidal turbine would experience when located within a closely packed fence. A CFD-embedded BEM tool is employed in this chapter to design rotors for operation in 4 infinite fence configurations, each with a different rotor spacing. Next, a series of array simulations is completed in which each rotor design is tested in its design lateral spacing conditions as well as in several off-design spacings.

- Rotor Performance in Finite-Length Tidal Fences:

  Although the infinite fence assumption proves useful for CFD modelling, a more realistic assumption is that tidal turbines will be deployed in finite arrays which do not span the entire width of a channel. In this chapter, the effects of variations in lateral rotor spacing on hydrodynamic rotor performance in tidal fences consisting of 2, 4, and 8 turbines in a wide channel are presented. In addition, the effects encountered at the ends of the finite-width arrays, both time-averaged and unsteady, are discussed.

- Conclusions:

  The main findings of the completed work are presented in this chapter. Limitations to the approaches used are also discussed and recommendations are given for future research.

Chapter 2

Analysis Techniques

In this chapter, a range of methods used to analyse wind and tidal turbines are introduced and literature covering studies completed with each model is discussed. The advantages and drawbacks of each method are also examined. The methods covered include actuator disc models, blade element-momentum models, vortex methods, 3D blade-resolved Navier-Stokes simulations, and actuator line models (Sections 2.1 - 2.5). In addition, a discussion of the governing equations and associated computational fluid dynamics numerical methods used in this thesis is included in Section 2.6.

2.1 Actuator Disc Method

Actuator disc theory, also known as momentum theory, was first developed by Rankine [29] as a tool to analyse propellers. It was later extended upon by Froude [30], among others. It is now frequently applied in the analysis of propellers as well as horizontal-axis axial wind and water turbines. The actuator disc method relies on the assumptions that the flow is incompressible, steady, inviscid, and irrotational. It is also assumed that the fluid passing through the rotor is contained in a streamtube and does not mix with the fluid passing around the rotor, that the pressure in the wake recovers to the upstream pressure,

and that the mass flux through the streamtube is constant and not affected by the thrust imparted by the rotor on the flow.

In actuator disc models, the horizontal-axis turbine rotor is modelled as an infinitesimally thin actuator disc that presents a resistance to the flow, resulting in decreased velocity downstream of the rotor. Continuity requires that the mass flow rate must be the same at every cross-section of the streamtube, as shown in Eq. 2.1:

$$\rho A_{\infty} U_{\infty} = \rho A_{disc} U_{disc} = \rho A_{wake} U_{wake}. \tag{2.1}$$

In the above equation, ρ is the fluid density and A and U are the cross-sectional area and flow speed far upstream of the turbine (∞), at the rotor plane ($disc$), and far downstream of the turbine ($wake$).

It is clear from Eq. 2.1 that the reduced velocity in the wake must correspond with an increased cross-sectional area of the streamtube. An actuator disc representation of a turbine and the corresponding expanding streamtube are shown in Figure 2.1.

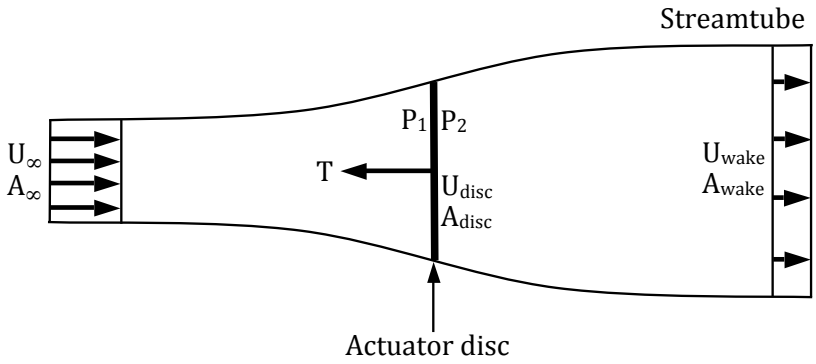

Figure 2.1: Actuator disc representation of a turbine and the corresponding streamtube.

In linear momentum actuator disc theory, continuity, conservation of momentum, and Bernoulli's equation are applied to determine the force acting on the fluid, also known

as the thrust, **T**. The magnitude of the thrust can be shown to be:

$$\|\mathbf{T}\| = 2\rho A_{disc} U_{\infty}^2 a\,(1-a)\,, \tag{2.2}$$

where a is the axial flow induction factor. a is a measure of the reduction in flow velocity at the rotor plane and is defined as

$$a = \frac{U_{\infty} - U_{disc}}{U_{\infty}} = 1 - \frac{U_{disc}}{U_{\infty}}. \tag{2.3}$$

The power, P, extracted from the fluid by the turbine is the rate of work done by the thrust and is given by

$$P = \|\mathbf{T}\| U_{disc} = 2\rho A_{disc} U_{\infty}^3 a\,(1-a)^2 \tag{2.4}$$

for an actuator disc representation of a turbine.

Actuator disc models are particularly useful as an idealised steady state method to predict power and thrust for given flow speeds and cross-sectional areas. Two useful non-dimensional parameters for the evaluation and analysis of wind and tidal turbines are the thrust and power coefficients, C_t and C_p, respectively. The magnitude of the thrust is non-dimensionalised in order to determine C_t:

$$C_t = \frac{\|\mathbf{T}\|}{\frac{1}{2}\rho U_{\infty}^2 A_{disc}}. \tag{2.5}$$

C_p is the ratio of the power the rotor extracts from the fluid to the kinetic power available in the upstream flow through an area equal to the actuator disc area. It is defined as

$$C_p = \frac{P}{\frac{1}{2}\rho U_{\infty}^3 A_{disc}}. \tag{2.6}$$

Combining Eqs. 2.2 and 2.5 results in a simplified equation for C_t for an actuator disc:

$$C_t = 4a\left(1-a\right). \tag{2.7}$$

Similarly, combining Eqs. 2.4 and 2.6 yields

$$C_p = 4a\left(1-a\right)^2. \tag{2.8}$$

The theoretical maximum power coefficient for a wind or tidal turbine in a channel of infinite cross-sectional area therefore occurs when

$$\frac{dC_p}{da} = 0. \tag{2.9}$$

It is thus found that an induction factor $a = 1/3$ corresponds to the theoretical $C_{p,max}$, and that $C_{p,max} = 16/27 = 0.593$. This theoretical maximum power coefficient is generally known as the Lanchester-Betz limit.

Actuator disc models are often embedded in computational fluid dynamics (CFD) simulations to evaluate the effects of channel boundaries and bodies such as nacelles, towers, and ducts on rotor performance. One of the main advantages of the actuator disc method is that it allows for useful information relating to the performance of turbines, such as the thrust and power coefficients, to be determined without requiring detailed knowledge of a specific rotor design. Another advantage of CFD-embedded actuator disc methods is that the rotor geometry and the blade boundary layers are not resolved in the computational mesh. This allows for convergence with a relatively low number of cells in the computational domain, resulting in low computational costs.

A number of studies have utilised actuator disc representations in CFD models of horizontal-axis marine turbines. In these studies, the presence of the turbine in the flow is simulated

in a Reynolds-averaged Navier-Stokes (RANS) solver by the inclusion of sources in the momentum equations (RANS solution methods will be discussed in detail in Section 2.6.2). These sources resist the flow in the axial direction. Sun et al. [31], Gaden and Bibeau [32] and Harrison et al. [33] simulated tidal turbines using CFD methods by applying these sources to a cylindrical region enclosing the rotor. Sun et al. [31] used this method to investigate free surface and wake effects, Gaden and Bibeau [32] studied the effectiveness of diffusers and used the model to optimise a diffuser at the outlet of a shrouded turbine, and Harrison et al. [33] compared numerical results with experimental porous disc results. The numerical and experimental results of normalised velocity and turbulence intensity showed good agreement in the far wake, although there were some discrepancies for the turbulence intensity in the near wake, which led to variation in wake recovery rates.

Rather than apply the sources in the CFD simulation over a cylindrical region with nonzero length, some studies employ a slightly different method in which the sources are applied as a porous jump with no thickness. This method has been implemented by Gant and Stallard [34], who showed that a rotor operating downstream of large turbulent structures has shorter wake length than a rotor operating in steady flow with the same mean velocity. It was also used by Belloni and Willden [35] in a study of the effects of ducts on tidal turbine performance.

Results from these simulations provide useful information relating to the flow through idealised horizontal-axis turbines. A drawback to actuator disc methods is that they cannot easily be applied to other turbine types, such as cross-flow turbines. Their main shortcomings, however, are that they can only provide an upper limit for energy extraction and a more detailed rotor model is often required for more in-depth design and study. Also, actuator disc methods do not simulate the radial variation of momentum extraction typical of a tidal stream rotor or the swirl induced by a rotating turbine. Actuator disc models are

also insufficient if analysis of the loads on the rotor due to aerodynamic (or hydrodynamic) forces is desired.

2.1.1 Actuator Disc Methods for Rotors in Channels

In 2007, Garrett and Cummins developed a theoretical model which extends linear momentum actuator disc theory to incorporate the effects of bounded flow into the analysis [36]. This model can be applied to a single turbine in a tidal channel as well as to a uniformly spaced fence of rotors spanning the width of a tidal channel, which are treated equivalently in the numerical analysis. As in linear momentum actuator disc theory, continuity, conservation of momentum, and Bernoulli's equation are applied. However, because the flow expansion in the wake is bounded in this analysis, the pressure far downstream is not assumed to have recovered to the far upstream pressure (unlike in classic linear momentum actuator disc theory). The Garrett and Cummins theoretical model considers both the core flow through the actuator disc and the flow outside of the core wake, unlike the unbounded actuator disc model which only considers flow in the streamtube passing through the actuator disc. The model assumes a rigid channel lid and constant mass flux through the channel.

Garrett and Cummins showed in this analysis that the theoretical maximum power coefficient for a rotor in a tidal channel is

$$C_{p,max} = \frac{16}{27}(1-B)^{-2}, \tag{2.10}$$

where B is the blockage ratio, the ratio of rotor swept area to channel cross-sectional area. Note that the limit for $C_{p,max}$ returns to the Lanchester-Betz limit of 16/27 for the unblocked case, $B = 0$. The power coefficient increases from this unblocked limit as the blockage ratio is increased.

Various extensions to the Garrett and Cummins model have been introduced in subsequent

work. Whelan et al. extended Garrett and Cummins' model to account for free surface effects, rather than assume a rigid lid for the channel [37]. Vennell [38] combined the 2007 Garrett and Cummins model with Garrett and Cummins' 2005 channel dynamics model [39] to investigate the balance between optimal power extraction and channel flow. In this work, Vennell removes the assumption in the Garrett and Cummins model that the mass flux through the channel is constant. Vennell later extended his previous work to account for variations in the cross-sectional area along the length of a channel in [40]. Nishino and Willden extended the Garrett and Cummins model to examine a long tidal turbine fence which only partially spans a wide channel [41], and later amended this model to make it more applicable to short fences with a finite number of tidal turbines [42].

Actuator Disc Method for Turbine Arrays

The model introduced in Nishino and Willden [41] allows for the optimal hydrodynamic efficiency of a tidal turbine fence partially spanning a wide channel to be assessed. The model maintains the rigid lid and constant mass flux assumptions of Garrett and Cummins. It is also assumed in this analysis that there is complete separation between array-scale and device-scale events, and that device-scale wake mixing occurs much closer to the array than array-scale wake mixing. With this assumption, the problem may be considered to be a coupling of two problems on different scales, and continuity, conservation of momentum, and Bernoulli's equation are applied to each problem separately. The array-scale and device-scale flow expansion are depicted in Figure 2.2 (from [41]). In this figure, U_C is the upstream channel flow speed, U_A is the flow speed through the array, and U_D is the flow speed through the devices. n is the number of devices in the tidal fence, and each device has diameter d and is a distance $s + d$ from its neighbour. Thus, s is the lateral spacing between neighbouring disc edges.

Nishino and Willden differentiate between local, global, and array values of flow characteristics. Local blockage, B_l, array blockage, B_a, and global blockage, B_g, are assigned

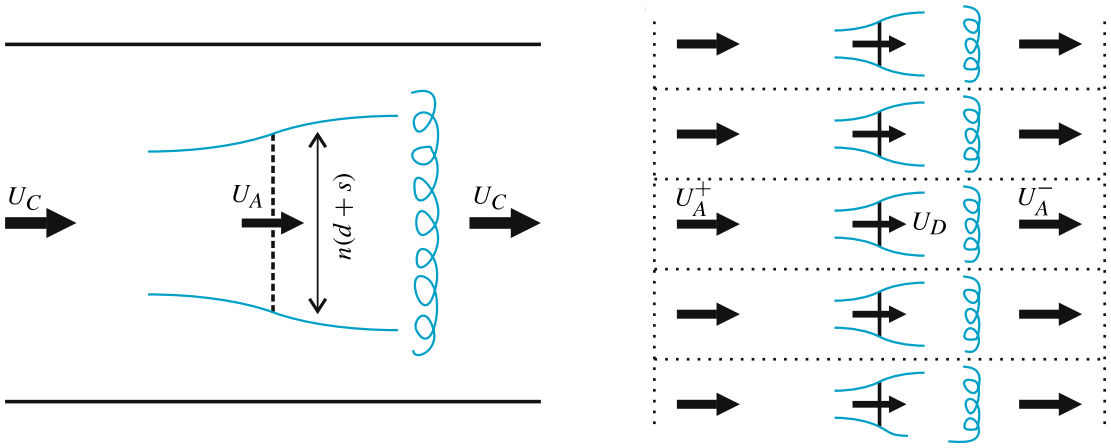

Figure 2.2: Left: array-scale streamtube and wake mixing; right: device-scale streamtubes and wake mixing. From [41].

the following definitions:

$$B_l = \frac{\text{single device area}}{\text{local passage cross-sectional area}} = \frac{\frac{\pi d^2}{4}}{h\,(d+s)} \tag{2.11}$$

$$B_a = \frac{\text{(representative) array area}}{\text{channel cross-sectional area}} = \frac{hn\,(d+s)}{hw} \tag{2.12}$$

$$B_g = \frac{\text{total device area}}{\text{channel cross-sectional area}} = \frac{n\frac{\pi d^2}{4}}{hw}, \tag{2.13}$$

where h and w are the height and width of the channel, respectively. Similarly, the local, array, and global power coefficient definitions are

$$C_{pl} = \frac{P_D}{\frac{1}{2}\rho U_A^3 \frac{\pi d^2}{4}} \tag{2.14}$$

$$C_{pa} = (1-a_A)^3\, B_l C_{pl} \tag{2.15}$$

$$C_{pg} = (1-a_A)^3\, C_{pl}, \tag{2.16}$$

where U_A is related to the upstream flow speed U_C by array axial induction factor $a_A = 1 - U_A/U_C$ and P_D is the power extracted by a single device.

Nishino and Willden showed in this analysis that B_l can be optimised to deliver a maximum

C_{pg} for any given B_g. In the case where $B_g \to 0$ (for instance if the channel is infinitely wide), there is a theoretical maximum global power coefficient $C_{pg,max} = 0.798$ for a tidal fence partially spanning the channel. This limit occurs at $B_l \approx 0.4$.

In subsequent work, Nishino and Willden compared results from the analytical tidal fence model, adjusted to better model short fences, to results from a set of RANS-embedded actuator disc simulations [42]. In the simulations, the number of discs ranged from 2 to 40 and the disc spacing varied from $s = 0.1d$ to $s = 1d$, resulting in local blockages $0.357 \geq B_l \geq 0.196$. The channel height for all simulations was $h = 2d$ and a constant global blockage $B_g = 0.039$ was maintained by adjusting the channel width as necessary. Although the analytical results were in good agreement with the RANS simulations, some discrepancies, likely due to the effects of far-wake mixing in the RANS simulations, were noted.

2.2 Blade Element-Momentum (BEM) Method

The blade element-momentum (BEM) method combines blade element theory with momentum theory. The theory is largely based on ideas from the 'Vortex Theory of Airscrews', which was introduced in the 1920's [43, 44, 45]. This section will include a brief introduction to blade element theory prior to the discussion of BEM.

2.2.1 Blade Element Theory

Blade element theory was developed first by Froude (1878) and later Drzewiecki (1892) to analyse propellers. The theory is based on the assumption that individual spanwise sections of a rotor blade, δr, can be treated as locally two-dimensional aerofoils. This assumption allows the aerodynamic forces per spanwise width to be calculated for each blade section.

Figure 2.3 depicts a 2D blade element at radius r rotating with angular velocity Ω. β is the blade pitch angle and α is the angle of attack.

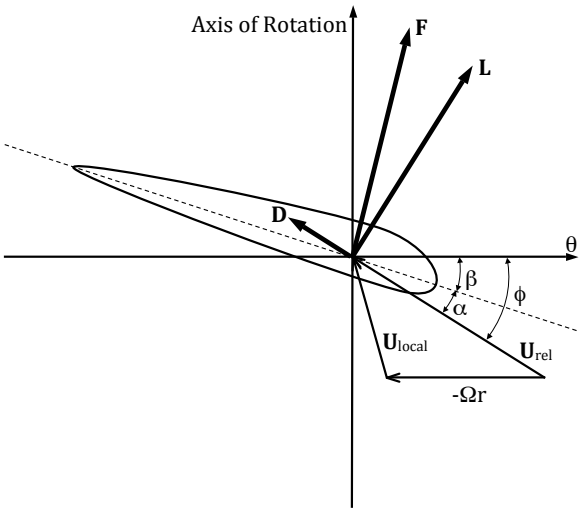

Figure 2.3: Aerodynamic forces on an element of a rotor blade rotating about the axis of rotation (axial flow rotor). The element corresponds to the shaded element in Figure 2.4, as viewed from above.

The drag force, **D**, on the blade element is in the direction of the relative velocity of flow to the blade element, $\mathbf{U}_{rel}$. The lift force, **L**, is perpendicular to **D**. In blade element theory, it is assumed that there are no forces acting in the spanwise direction of the blade. Therefore, the total force on the blade element is simply the sum of the lift and drag vectors.

The magnitude of the lift force of the blade per spanwise width is

$$\frac{\|\mathbf{L}\|}{\delta r} = \frac{1}{2}\rho\|\mathbf{U}_{rel}\|^2 cC_l \tag{2.17}$$

where c is the local chord and C_l is the sectional lift coefficient. Similarly, the magnitude of drag of the blade per spanwise width is

$$\frac{\|\mathbf{D}\|}{\delta r} = \frac{1}{2}\rho\|\mathbf{U}_{rel}\|^2 cC_d \tag{2.18}$$

where C_d is the sectional drag coefficient.

The coefficients C_l and C_d are both dependent on the Reynolds number, Re, of the flow and the angle of attack, α, of the blade element. The Reynolds number is the ratio of inertial to viscous forces and is defined as

$$Re = \frac{\rho U l}{\mu}, \tag{2.19}$$

where U is the characteristic flow speed, l is a characteristic length scale, and μ is the dynamic viscosity of the fluid.

Due to their dependence on Re and α, experimental aerofoil C_l and C_d data tabulated as a function of Re and α are often used in blade element theory.

2.2.2 Blade Element-Momentum Theory

In the blade element-momentum method, each rotor blade is divided into m spanwise sections. The forces on each blade section are calculated using blade element theory. The forces are then integrated along the blade and time-averaged over a revolution of the rotor in order to determine the overall performance of the rotor (Leishman [46]).

The control volumes considered in traditional BEM models are concentric stream tubes. Each corresponds to an annulus, of radial width δr, that is swept out by a blade element at a specific radius (see Figure 2.4). It is assumed that each of these stream tubes can be treated as independent of the others and therefore that radial flow along the blade span may be neglected.

For a given annulus, the incremental thrust, δT, at a radial position r is equal to the rate of change of axial momentum for the fluid flowing through the annulus. Similarly, the incremental torque for a given annulus, δQ, is equal to the rate of change of angular momentum for the fluid flowing through that annulus. In analytical BEM, the axial momentum/force balance and the angular momentum/torque balance are solved iteratively in order to find

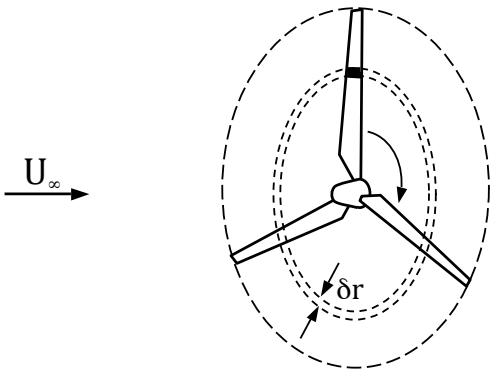

Figure 2.4: Annulus representing the cross-section of a streamtube at the rotor plane.

the flow velocities and forces at each annulus. This iterative solving technique is continued until a converged solution is achieved.

Some of the most commonly used software utilising analytical BEM methods include DNV GL's Bladed [47] and Tidal Bladed [48], as well as the open source AeroDyn module [49], provided by the National Renewable Energy Laboratory (NREL).

BEM methods are more representative of turbine rotors than actuator disc models because they allow the loads to vary in the radial direction rather than assume uniform loading on the rotor blades. BEM models are also useful for rotor design as they include considerations for the geometric and aerodynamic properties of the blade, unlike idealised actuator disc models.

While BEM models provide a significant advantage over actuator disc models, they nevertheless include some inherent drawbacks. The influence of the blade geometry is included in BEM models, but the finite effects of the blades cannot be directly included because the solution is time-averaged over a turbine revolution (although a tip correction, which will be discussed later in this section, is typically applied to account for this). The major drawback of BEM models is that transient flow features in the wake cannot be resolved due to the steady state nature of the solution. Still, such approaches can be used to model time-varying loading due to time-varying onset flow (e.g. a shear flow).

BEM models may be embedded within CFD solvers by coupling BEM theory with the RANS equations (these equations will be discussed in Section 2.6.2). This method is known as RANS-embedded BEM, or RANS-BEM, and is one of the most common CFD methods for simulating wind and tidal turbines. In many RANS-BEM simulations, the time-averaged forces on the blades are calculated using blade element theory and input as sources in the simulated momentum equations. This process is repeated during each solver iteration until a converged solution is achieved.

CFD simulations utilising RANS-BEM models are relatively fast because, much like in RANS-embedded actuator disc models, it is not necessary to resolve the blade boundary layers. Another similarity between the BEM and actuator disc models is that both generally result in steady state solutions, which lowers the computational costs.

CFD-BEM coupling is commonly employed to model wind turbines. For example, Hallanger and Sand utilised a RANS-BEM model to study wind turbine wake effects [50]. In addition, it is often employed for tidal turbine modelling. Harrison et al. [51] used BEM methods in conjunction with CFD to study turbine wake modelling and array performance prediction. Malki et al. have implemented a BEM model into a CFD solver for use in modelling tidal stream turbines [52]. Also, a University of Oxford in-house RANS-BEM code and rotor design tool embedded in ANSYS Fluent was verified and employed to evaluate the performance of ducted horizontal-axis tidal turbines (McIntosh et al. [53], Fleming et al. [54]). It has subsequently been utilised by Belloni [55] to investigate axial and yawed flow in bare, ducted, and open-centre tidal turbines.

The Oxford in-house RANS-BEM code includes an optional design optimisation loop which requires the aerofoil section(s) and general rotor geometry, including the nacelle diameter and rotor radius, to be defined via a series of input files. The tool allows for a tidal rotor to be designed for optimal performance in specified operating blockage conditions. The method iteratively adjusts the sectional chord and twist of the blade for each annulus in

order to achieve the maximum rotor power coefficient, C_p, for an assigned tip speed ratio, λ, and target local thrust coefficient, c_x:

$$c_x = \frac{\delta T}{\frac{1}{2}\rho \delta A_{disc} u_x^2}, \tag{2.20}$$

where $T = F_x$ is the magnitude of the streamwise force on a corresponding disc element of area δA_{disc}. The optimum twist for each blade section is the twist required to maintain the angle of attack that maximises the lift to drag ratio for the given blade section.

The rotor design returned by the optimisation tool is different for every combination of λ and c_x. A global $C_{p,max}$ is found by comparing the values for $C_{p,max}$ for varying input combinations of λ and c_x, and the rotor design corresponding to this global $C_{p,max}$ is considered to be the optimal design.

Although the design tool allows the user to define the aerofoil section or sections used in the rotor blades, the tool does not directly adjust or optimise blade thickness or aerofoil section in the rotor design process.

In McIntosh et al.'s model, the effects of the forces applied by the rotor on the flow are replicated in the RANS simulations by the implementation of a static pressure jump, δp, across the cells that occupy the disc and the specification of a swirl velocity on the downstream side of each rotor disc cell. The pressure drop for an annulus at radius r is equal to the axial force, or thrust, applied by the rotor on the flow per unit area for the given annulus. The area of each annulus is approximated as $\delta A = 2\pi r \delta r$.

$$\delta p = \frac{\delta T}{\delta A} = \frac{\frac{1}{2} c_x \rho U_{rel}^2 c N \delta r}{2\pi r \delta r}. \tag{2.21}$$

Here, c is the local blade chord, N is the number of blades, and c_x is the local axial force

coefficient (also called the local thrust coefficient) and is defined as

$$c_x = C_l cos\phi + C_d sin\phi, \tag{2.22}$$

where ϕ is the angle between the rotor plane and the relative velocity vector, $\mathbf{U}_{rel}$, at the blade segment. The solidity, σ, for an annular element is

$$\sigma = \frac{Nc}{2\pi r}. \tag{2.23}$$

Therefore, the expression for change in pressure across an annulus is simplified to:

$$\delta p = \frac{1}{2}\rho U_{rel}^2 \sigma c_x. \tag{2.24}$$

For a rotor operating with no yaw, the magnitude of the relative velocity for a blade element is

$$U_{rel} = \left(u_x^2 + (\Omega r - u_\theta)^2\right)^{1/2}. \tag{2.25}$$

The swirl velocity is found through conservation of angular momentum. Specifically, the torque on a disc element is equal to the rate of change of angular momentum for the corresponding disc area, $\delta\dot{\mathrm{M}}_\theta$:

$$\begin{aligned} \delta Q &= \delta\dot{\mathrm{M}}_\theta \\ \delta F_\theta N r &= \delta\dot{m}\Delta u_\theta r \\ \frac{1}{2}\rho U_{rel}^2 c_\theta \delta r c N &= \delta A u_x \rho \Delta u_{\theta,ud}, \end{aligned} \tag{2.26}$$

where u_x is the local velocity in the streamwise direction, $\dot{m}$ is the mass flow rate, and δF_θ is the tangential force for the specified disc element. $\Delta u_{\theta,ud}$ is the change in tangential/swirl velocity between the upstream and downstream sides of the rotor. c_θ is the local

tangential force coefficient and is defined as

$$c_\theta = C_l sin\phi - C_d cos\phi. \tag{2.27}$$

Again, we approximate the area of the annulus as $2\pi r\delta r$. Hence, Eq. 2.26, when simplified and rearranged, gives the following difference between the swirl velocity downstream and upstream of the rotor:

$$\Delta u_{\theta,ud} = u_{\theta,upstream} - u_{\theta,downstream} = \frac{U_{rel}^2 \sigma c_\theta}{2u_x}. \tag{2.28}$$

Bernoulli's equation, continuity, and conservation of momentum may be used to show that in unconstrained flow, the axial velocity at the rotor plane is half of the difference between the axial velocities upstream and downstream of the rotor. Similarly, we assume that the tangential velocity in the rotor plane may be expressed as

$$u_\theta = \frac{\Delta u_{\theta,ud}}{2}. \tag{2.29}$$

This relationship cannot be derived analytically, and is one of the main assumptions used in this implementation of RANS-BEM.

The magnitude of the relative velocity at each blade section is therefore

$$U_{rel} = \left[\left(\Omega r - \frac{\Delta u_{\theta,ud}}{2} \right)^2 + u_x^2 \right]^{1/2}, \tag{2.30}$$

where Ω is the angular velocity of the rotor and is determined from the tip speed ratio (which is an input of the model).

McIntosh et al.'s model applies the rotor forces independently to each cell in the rotor plane rather than to annuli. Thus, rather than utilising concentric streamtubes for the

momentum balances, the McIntosh et al. RANS-BEM implementation employs a number of thin streamtubes, each with cross-sectional area equal to the cross-sectional area of the corresponding cell in the rotor disc plane. In this manner, azimuthal variations in the rotor plane may be modelled.

In Eqs. 2.21 and 2.26, the incremental thrust and torque, respectively, were calculated using a blade area of $\delta A_{blade,annulus} = cN\delta r$ for each annulus. To adjust the equations for implementation in a model in which the momentum balances are computed for individual rotor disc cells rather than annuli, this area term must be adjusted. The blade area in a given rotor disc cell may be written as

$$\delta A_{blade,cell} = cN\delta r \frac{\delta A_{cell}}{\delta A_{annulus}}, \tag{2.31}$$

thus introducing the ratio $\frac{\delta A_{cell}}{\delta A_{annulus}}$ to each $cN\delta r$ term in Eqs. 2.21 and 2.26. Also, the δA terms in Eqs. 2.21 and 2.26, which represented the area of an annulus, or $\delta A_{annulus}$, must now represent the area of a cell, δA_{cell}. It is thus a simple matter to show that, when adjusting the momentum balance equations for use on flow through individual rotor disc cells rather than flow through an annulus, the terms adjusting for the area of cell and the area of the blade within a cell in fact cancel out. Eqs. 2.21 and 2.26, therefore, are valid for flow through an individual rotor disc cell as well as flow through an annulus.

Corrections to BEM Models

The BEM method is quite simple and its application requires a number of assumptions, some of which can cause significant error. There exist a number of corrections, both analytic and empirical, which have been employed to improve BEM results for certain flow and rotor operating conditions. These include tip and root corrections [56, 45], corrections to the thrust coefficient in cases with turbulent wake effects which occur for high axial induction [57], corrections for the effects of skewed wake for rotors operating in yaw [58],

and corrections to the 2D aerodynamic data to account for rotational effects, particularly in cases in which stall delay is relevant [59, 60].

The most commonly employed BEM correction, and the most relevant for the current work, is the Prandtl tip correction. Prandtl's tip correction model [56, 45] is included in many BEM solutions, including McIntosh et al.'s RANS-BEM implementation, to account for the influence of the unsteady wake structures. The 3D tip vortices that form as a result of the presence of discrete blades can not be directly modelled in BEM methods, which are unable to explicitly simulate the influence of discrete blades on the flow.

Prandtl approximated the 3D helicoidal vortex sheets that form in the wake of a wind or tidal turbine as a series of vertical material sheets. The material sheets are considered to be impermeable and are transported downstream in the near wake of the rotor at velocity

$$U_{disc} = u_x = U_\infty(1-a), \tag{2.32}$$

where a is the axial induction factor. Eq. 2.32 is found by rearranging the equation for the definition of the axial induction factor (Eq. 2.3). The bypass flow, which travels at a speed U_∞ when $B = 0$, mixes with the wake flow between the discs, as shown in Figure 2.5 (from Burton et al. [61]). This mixing between the higher velocity bypass flow and the lower velocity wake flow increases the velocity of the flow in the wake. This increased velocity causes greater flow to be entrained through the rotor plane, particularly in the tip region of the blade, where the majority of the mixing occurs. This, in turn, results in a higher streamwise velocity at the blade elements in the blade tip region than that which would be calculated in a computation neglecting the effect.

The axial induction factor, a, is a measure of the reduction in flow velocity relative to the upstream flow velocity as the flow approaches the rotor plane from far upstream. Hence, the application of a correction factor to increase the axial flow velocity at the disc, u_x,

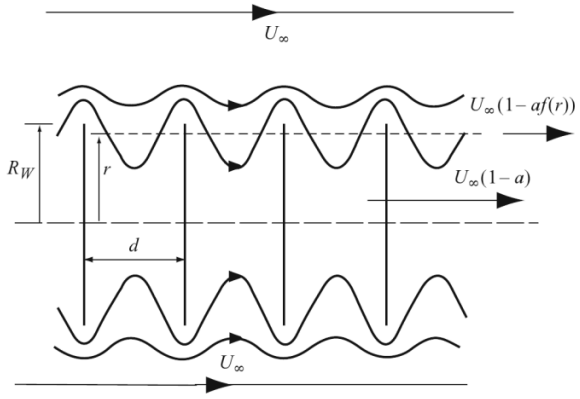

Figure 2.5: Schematic of Prandtl's vortex sheet approximation (from [61]). R_W is the rotor radius and $f(r)$ is the tip correction factor.

should also reduce the value of a. The Prandtl tip correction factor, f, is therefore applied to the axial induction factor, a, in Eq. 2.32.

The Prandtl tip correction is defined as

$$f(r) = \frac{2}{\pi} cos^{-1}\left[exp\frac{N\left(1-\frac{R}{r}\right)}{2sin\phi}\right], \tag{2.33}$$

where R is the outer radius of the rotor. $f(r)$ is always less than unity; hence, the application of the Prandtl tip correction always reduces the axial induction factor for the blade elements in the blade tip region, thereby increasing the streamwise flow speed for the respective blade elements.

The angle of attack, α, for a rotor operating with no yaw is

$$\alpha = tan^{-1}\left(\frac{u_x}{\Omega r - u_\theta}\right) - \beta, \tag{2.34}$$

where β is the blade pitch. Also, recall from Eqs. 2.25, 2.28, and 2.29 that u_θ is dependent on both U_{rel} and u_x. Thus, the relationship between u_x and the relative velocity and angle of attack is nonlinear and depends, in addition to other parameters, on how C_l and C_d vary with α for the specific aerofoil under consideration. An increase in axial velocity at the disc

due to modelling the effect of vortical wake structures may result in an increase or decrease of U_{rel} and similarly an increase or decrease in α. Hence, the inclusion of the Prandtl tip correction may result in an increase or decrease in the total force on the blade element, **F**, as compared with the results of a simulation where the effects of unsteady wake structures are not considered.

It is vital that the reasoning behind the Prandtl tip correction as well as the physical implications of this correction are understood. A number of works have assumed that the implementation of the Prandtl tip correction necessarily reduces the computed rotor power output, and have incorrectly applied the loss factor $f(r)$ to the local streamwise or relative velocity, the local axial and/or angular momentum, or the force on each blade element, rather than to the axial induction factor, rendering the results inaccurate.

2.3 Vortex Methods

Vortex methods utilise distributions of either discrete vortices [62] or vortex line or sheet elements [63, 64] to determine the induced velocity field of a blade. The vortex line element methods are based on Prandtl's lifting line theory, which states that a wing's lift can be approximated by horseshoe vortices at spanwise stations of a wing [65]. Each horseshoe vortex consists of a bound vortex on the quarter-chord of the wing and two semi-infinite trailing vortices.

At each time step, the vorticity is shed from the trailing edge of the lifting surface into the flow. This results in the wake being modelled as a vortex lattice. Figure 2.6 depicts a lifting line and the corresponding shed vortex lattice. Vortices with circulation Γ are shed at the indicated time step.

Free wake vortex models are capable of providing much more detailed and accurate rotor wake simulations than RANS-embedded actuator disc and RANS-BEM models. This improvement in accuracy is largely due to the ability of vortex methods to include the

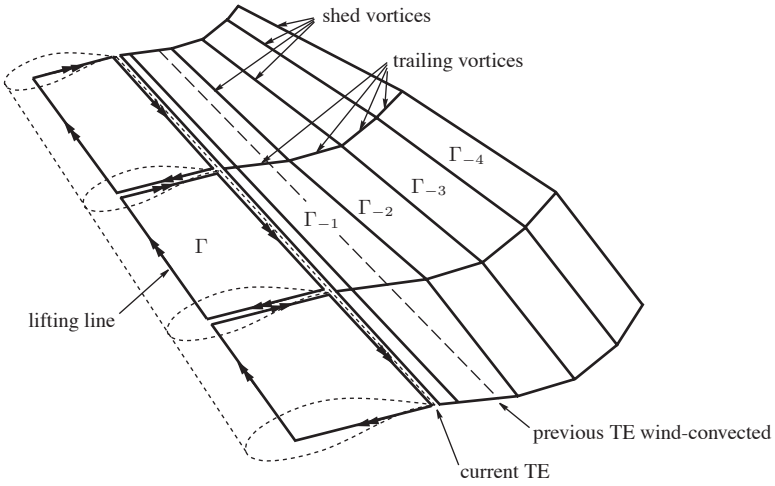

Figure 2.6: Vortex line element method [64]. TE is the trailing edge.

time-dependent influence of the rotor blades, whereas actuator disc and BEM models rely on the average influence of the rotor blades over a revolution.

Another advantage of vortex methods is that they are capable of simulating a wide range of turbine geometries. Li and Çalişal [66] demonstrated this by employing a vortex line element model to simulate a three-bladed vertical-axis tidal turbine. These simulations were validated with experimental results of a turbine in a towing tank as well as with other numerical solutions.

Despite the advantages, there are some drawbacks to modelling flow using vortex methods. Free wake models produce more useful results than prescribed wake models but require large computational resources [63] and are also susceptible to divergence [67].

2.4 Three-Dimensional Blade-Resolved Models

RANS actuator disc and RANS-BEM tidal turbine models both use approximations to simulate the influence of a rotor or rotors on a flow using CFD. However, it is also possible to model tidal turbines using blade-resolved CFD simulations, in which the blade geometry is explicitly meshed and no rotor approximation is required. This method of modelling tur-

bines can provide solutions of higher accuracy in the vicinity of the blades as corresponding boundary layers can be fully discretised. For instance, blade surface pressure distributions are commonly computed using blade-resolved modelling.

However, the capability of 3D blade-resolved models to accurately simulate flow is limited to attached flows. Turbulent transition and separation prediction is often inaccurate, which renders the simulations less reliable if separation occurs.

This limitation is notable, but the foremost drawback of this modelling technique is that it significantly increases the computational cost of the simulation. The cost increase occurs because a very high mesh resolution is required in the near vicinity of the blades in order to discretise the blade boundary layers (discretisation will be discussed in more detail in Section 2.6). In addition, many 3D blade-resolved rotor simulations use an inner cylindrical domain containing the mesh around the rotor blades. A computationally expensive sliding mesh is then used at the interface of this domain and the outer domain to simulate the rotation of the rotor. The potential gain in accuracy of blade-resolved turbine models must be weighed against the increased simulation cost.

Fleming et al. studied the difference in computational cost between 3D blade-resolved turbine simulations and RANS-BEM simulations of the same turbine [54]. In this study, 3D blade-resolved tidal turbine simulations were performed with a mesh comprised of 4.4 million cells as part of a ducted rotor analysis. The results of the RANS-BEM simulations of the ducted tidal turbine compared favourably to the blade-resolved simulations while requiring only 1/6 of the number of cells for a converged solution.

Limited computational resources combined with the high computational demand of 3D blade-resolved models make it prohibitive to simulate multiple turbines in a single flow field with this method. Therefore, it is often computationally necessary that any simulations of interactions between turbines in an array be performed using a more efficient approximation, such as RANS-BEM.

2.5 Actuator Line Model

In actuator line models, each turbine blade is represented in a CFD simulation by an actuator line - a series of sources distributed along the blade's quarter-chord. These sources may be either vorticity or momentum sources, depending on the formulation of the Navier-Stokes equations. The series of points at which the sources are calculated are called collocation points (also called 'actuator points' in other works). The blades themselves are not resolved in the mesh in this method. The actuator lines move through the computational domain in a prescribed manner, thereby simulating the effect of the rotor blades on the flow. During each time step, the appropriate source to be applied at a given collocation point is determined from the flow returned by the solver at the corresponding blade element. The sources are input into the flow field and the momentum equations are solved. The positions of the lines are updated at the beginning of each time step and the process is repeated.

The actuator line method is similar to vortex methods in that it allows for the time-dependent influence of the individual blades to be modelled in an unsteady solution. This provides an advantage over RANS-embedded actuator disc and RANS-BEM methods, which are limited to providing steady state, time-averaged results because the representation of individual blades allows for more accurate modelling of the turbine wake. Actuator line models also hold an advantage over vortex methods as they are less likely to diverge as the wake grows and the computational resource requirement does not significantly increase as the wake develops.

Actuator line CFD models are similar to RANS-embedded actuator disc and RANS-BEM models in that the boundary layers are not discretised. This results in relatively fast computations and reduces the computational cost when compared to blade-resolved turbine models. Because of the method's efficiency, actuator lines can be used to model multiple turbines in a single domain.

Actuator line methods have been used in numerous rotorcraft and horizontal-axis wind turbine studies, as well as in a growing number of horizontal-axis tidal turbine studies. The details of the methods used for the rotorcraft, wind turbine, and tidal turbine models will be discussed in more detail below.

2.5.1 Rotorcraft Wake Models

Brown [68] developed the vorticity transport model (VTM) as a method of modelling rotorcraft wakes. This model uses the same principles as described above for an actuator line method; however, Brown does not refer to this method as an actuator line method. This term only came into use when the method was utilised in wind turbine simulations.

The VTM utilises the unsteady vorticity transport equations and applies sources of strength $\mathbf{S}_\omega$ to the flow. These sources account for the effect of the vorticity generated as a result of the aerodynamic forces on the rotor blades. The unsteady vorticity transport equations are written in vorticity-velocity variables and, with the assumption that the flow is incompressible, can be written in vector form as

$$\frac{\partial \boldsymbol{\omega}}{\partial t} + \mathbf{U} \cdot \nabla \boldsymbol{\omega} - \boldsymbol{\omega} \cdot \nabla \mathbf{U} = \nu \nabla^2 \boldsymbol{\omega} + \mathbf{S}_\omega, \tag{2.35}$$

where $\boldsymbol{\omega} = \nabla \times \mathbf{U}$ is the vorticity, $\mathbf{U}$ is the flow velocity, and ν is the kinematic viscosity of the fluid ($\nu = \mu/\rho$, where μ is the dynamic viscosity of the fluid). At high-Reynolds number flows, the diffusion becomes negligible and the $\nu \nabla^2 \boldsymbol{\omega}$ term can be neglected.

The velocity of the flow at a specific point can be related to the vorticity distribution at that point by the Poisson relationship:

$$\nabla^2 \mathbf{U} = -\nabla \times \boldsymbol{\omega}, \tag{2.36}$$

Equations 2.35 and 2.36 are evolved and solved to generate a time-dependent simulation of the flow.

The aerodynamic forces on the blade and the velocity of the bound vorticity, $\mathbf{U}_b$, are determined from the flow field. The aerodynamic forces are then used to calculate the bound vorticity of the rotor blades. Finally, the vorticity sources are determined using:

$$\mathbf{S}_\omega = \left(\frac{\partial \boldsymbol{\omega}_b}{\partial t} + \mathbf{U}_b \cdot \nabla \boldsymbol{\omega}_b \right) \hat{b}, \tag{2.37}$$

where $\hat{b}$ is a unit vector in the direction of the bound vorticity. It is assumed that the bound vorticity is concentrated on the quarter-chord point of each blade element. The quarter-chord point may be shown to be the aerodynamic centre of a blade element for symmetric foils. Although the quarter-chord is not necessarily the aerodynamic center for cambered aerofoils, it is approximated as such for simplicity in this and other actuator line implementations. The rotor blades are divided into a finite number of spanwise segments, each of which is represented by a single collocation point. Each source $\mathbf{S}_{wm}$, corresponding to the m^{th} segment of the blade, is then calculated and applied at the appropriate collocation point.

The VTM has been validated against experimental data for a hovering 2-bladed rotor through comparison of blade loading and wake geometry [69]. It was also validated against experimental data for simulations of a 4-bladed rotor in forward flight.

2.5.2 Actuator Line Simulations of Wind and Tidal Turbines

Navier-Stokes Vorticity Transport Model

Sørensen and Shen [67] were the first to develop an actuator line model for use in horizontal-axis wind turbine simulations. Much like the VTM, this model uses the vorticity transport

equation and vorticity-velocity variables. Sørensen and Shen formulated this model in cylindrical coordinates.

In Sørensen and Shen's model, the source term in the vorticity transport equation, Eq. 2.35, is $\frac{1}{\rho}\nabla \times \mathbf{f}$ where the vector $\mathbf{f}$ is the applied force per unit volume.

In this model, the forces at each collocation point on the actuator line must be calculated in order to determine the appropriate source terms. These calculations are performed using blade element theory, which was introduced in Section 2.2. The 2D representation of a blade section in blade element theory assumes that only the velocity components in the blade-plane result in blade loads and allows for the lift and drag forces per unit width to be calculated for each spanwise blade section. It is assumed that these forces can be concentrated at the quarter-chord of the blade element.

To avoid singular behaviour at the collocation points, however, the blade forces are distributed in a Gaussian manner over multiple elements rather than applied only to elements containing the collocation points. In order to calculate the desired distribution, the convolution of the local load and a regularisation kernel, η_ϵ, is taken, resulting in the regularised load, $\mathbf{f}_\epsilon$.

$$\mathbf{f}_\epsilon = \frac{1}{V}\left(\mathbf{F} \otimes \eta_\epsilon\right). \tag{2.38}$$

In Eq. 2.38, V is the volume of the cell that the force is to be applied to.

The 3D regularisation kernel is defined as

$$\eta_\epsilon^{3D}(d) = \frac{1}{\epsilon^3 \pi^{3/2}} e^{-\left(\frac{d}{\epsilon}\right)^2}, \tag{2.39}$$

where d is the distance between cell centroids and points on the actuator line. The parameter ϵ allows the concentration of the regularised load to be adjusted.

The Navier-Stokes vorticity transport actuator line model that was developed for simula-

tions of horizontal-axis wind turbines was validated through comparison with experimental measurements of the Nordtank wind turbine [67]. In the validation, the simulated power yield was compared with experimental measurements of the power yield for constant tip velocity and a range of wind speeds. The numerical model agreed very well with the experiments, with the greatest error occurring at higher wind speeds. The model over-predicted the power by about 5% at the highest wind speeds presented, although results for wind speeds in which the rotor was in stall were not included.

Navier-Stokes Equation Models - Primitive Variable Formulation

Mikkelsen reformulated the Navier-Stokes vorticity transport actuator line method developed by Sørensen and Shen into a Navier-Stokes method in primitive (pressure-velocity) variables. The reformulation was completed in order to couple the actuator line method with an in-house RANS solver, EllipSys3D [70, 71]. The primitive variable actuator line model retained the cylindrical coordinates used in Sørensen and Shen's model and required the use of a structured polar grid for turbine models.

In the primitive variable actuator line model, the flow speed and angle of attack at each collocation point are determined from the flow field during each iteration. The lift and drag on each element are calculated using Eqs. 2.17 and 2.18. The total force for a given collocation point is divided by the volume of the cells on which it is to be applied and implemented as a momentum source term in the discretised Navier-Stokes equations. For each time step, this process is repeated until the solution has converged. The position of the lines is then updated at the beginning of the next time step and the process is repeated. An actuator line representation of a blade is shown in Figure 2.7.

Mikkelsen implemented a 2D Gaussian distribution of the sources rather than the 3D source distribution used by Sørensen and Shen [70]. This distribution was chosen because the 3D distribution caused sources to be applied beyond the blade tips, resulting in inaccuracies.

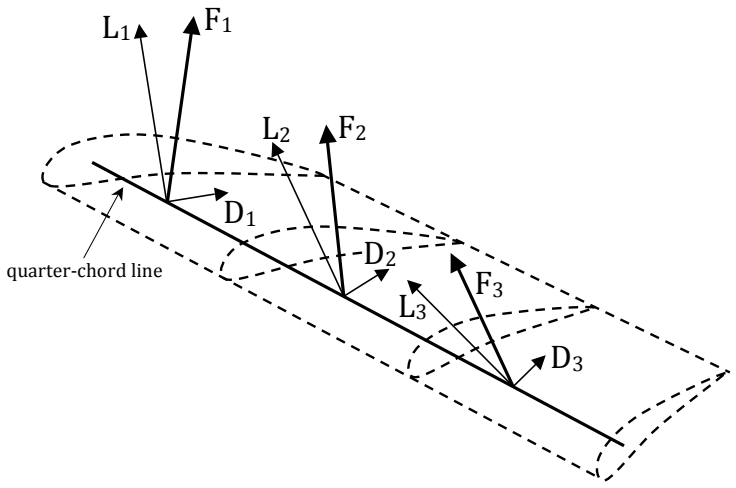

Figure 2.7: Application of an actuator line model for a blade with taper and twist.

The 2D regularisation kernel is defined by Mikkelsen as

$$\eta_{\epsilon}^{2D}(d) = \frac{1}{\epsilon^2 \pi} e^{-\left(\frac{d}{\epsilon}\right)^2}. \tag{2.40}$$

The Gaussian distribution of forces is utilised in order to avoid singularities at the collocation points, the points on the actuator line at which the blade segment forces are computed. This has a smoothing effect and results in more accurate velocities at the collocation points than would exist if the force applied for each collocation point was simply a point force. ϵ, the parameter used to define the concentration of the distributed load for each collocation point, is a numerical constant. Mikkelsen used values ranging from 1.5 to 3 for a model of an elliptic wing. The actuator line in this case consisted of a series of equidistant collocation points [70]. The results of this exercise showed that the value chosen for ϵ has an effect on the accuracy of the results. It was also noted that, regardless of the value of ϵ, the solution for the downwash failed near the tips.

Initial validation of Mikkelsen's actuator line technique was completed by Ivanell et al. [72] in a study which compared computed values of C_p with experimental values of C_p for a Tjaereborg horizontal-axis wind turbine. In addition, Shen et al. completed further

validation by comparing radial loads computed using an actuator line model with experimental results for the MEXICO rotor [73]. This work also compared simulated results for near-wake velocities with the experimental measurements. Shen et al. concluded that the 2D aerofoil data resulted in inaccuracies in the loading at the blade tips and introduced a correction to the data, which improved the results. Jha et al. employed a similar method, implemented in OpenFOAM, to compare actuator line simulations results with NREL Phase VI experimental results [74]. This analysis also included comparisons to the radial variation of blade loads, and, although the results at the mid-span were accurate, there was also error at the blade tip and root.

The primitive variable actuator line model has been employed in various horizontal-axis wind turbine studies. Many of these studies couple the actuator line model with large eddy simulation (LES), which will be discussed in Section 2.6.2. Troldborg et al. utilised large eddy simulation techniques to analyse wind turbine wake in uniform and turbulent inflow [75, 76]. A study of the wake interactions for a row of wind turbines in wind shear employed this method as well (Mikkelsen et al. [77]). Churchfield et al. completed actuator line simulations of a wind farm consisting of 48 turbines [78]. The Churchfield et al. wind farm simulations included an atmospheric boundary layer and turbulent inflow, but due to the size of the computation (315 million cells in the domain and one million processor-hours required for completion) the researchers were unable to make the domain large enough for farm-scale wake structures to be properly simulated.

The actuator line model has also been employed to simulate tidal turbines. Churchfield et al. utilised an actuator line method very similar to Mikkelsen's primitive variable actuator line model in a study of marine turbine arrays [79, 80]. In this work, large-eddy simulations of tidal turbine arrays in sheared, turbulent inflow were completed using the OpenFOAM CFD solver. Ten different configurations, with varying intra-rotor cross-stream and downstream spacings were used. Periodic boundary conditions were employed for the side walls of the

computational domain, and thus the simulations were effectively of an infinitely wide array spanning an entire channel. It was concluded that variations in turbulence in the upstream flow can have a significant effect on the power produced and on the wake structure.

Several studies have examined variations in the method in which the Gaussian spreading width, ϵ, in Eqs. 2.39 and/or 2.40 is computed. For example, Shives and Crawford compared actuator line results for both constant circulation and elliptically loaded wings for simulations with constant ϵ over the span of the blade as well as for simulations with ϵ proportional to the blade chord, c [81]. It was determined in this study that using ϵ proportional to c improves the results for downwash at the wing tips as compared to the constant ϵ cases. Further, Shives and Crawford suggest that the ratio ϵ/c should be between $1/8$ to $1/4$, based on the expected radius of the tip vortex core. Also, Jha et al. compared actuator line results for simulations of several different blade planforms with analytical and experimental results for two ϵ definitions: with constant ϵ across the blade span and with ϵ varying over the blade span according to an elliptic distribution [74]. The simulations employing the latter method provided improved results when compared to the simulations using constant ϵ, however, some inaccuracies at the blade root and tip were still present in the results for radial blade loads even with this improvement.

2.6 Numerical Implementation

The studies in this thesis were completed using computational fluid dynamics (CFD). CFD simulations solve discretised versions of the governing equations of fluid flow. The governing equations, as well as two methods of including turbulence in CFD simulations (Reynolds-averaged Navier-Stokes and large eddy simulation) are discussed in this section.

2.6.1 Governing Equations

Fluid flow is governed by a set of nonlinear partial differential equations. These equations are the mass conservation (or continuity) equation, the momentum conservation equation (based on the principles of Newton's second law, $\mathbf{F} = m\mathbf{a}$), and the energy conservation equation. The momentum conservation equation is a vector equation with three components (in Cartesian coordinates, these are the x-, y-, and z-components). Historically, the momentum equation has become known as the Navier-Stokes equations.

All of the flows in the work presented in this thesis are considered incompressible. In addition, heat transfer is considered to be negligible. Under these conditions, the energy conservation equation may be neglected. Therefore, it will not be discussed further.

The mass conservation equation for an inertial (non-accelerating) reference frame is

$$\frac{\partial \rho}{\partial t} + \nabla \cdot (\rho \mathbf{U}) = S_m, \tag{2.41}$$

where ρ is fluid density, $\mathbf{U}$ is the velocity vector, and S_m is the mass source. In the current study the mass source is always 0 and, as the flow is considered incompressible, the density is always constant. Thus, the mass conservation equation is simplified to

$$\nabla \cdot \mathbf{U} = 0 \tag{2.42}$$

for the current work.

The momentum conservation equation for flow in an inertial reference frame is given by

$$\frac{\partial}{\partial t}(\rho \mathbf{U}) + \mathbf{U} \cdot \nabla (\rho \mathbf{U}) = -\nabla p + \nabla \cdot (\overline{\overline{\tau}}) + \rho \mathbf{g} + \mathbf{F} + \mathbf{S}, \tag{2.43}$$

where p is static pressure, $\rho \mathbf{g}$ is the gravitational body force, $\mathbf{F}$ contains the external body forces, and $\mathbf{S}$ is a source term with units of force per unit volume. $\overline{\overline{\tau}}$ is the stress tensor. For

a Newtonian, incompressible fluid,

$$\nabla \cdot (\overline{\overline{\tau}}) = \mu \nabla^2 \mathbf{U}, \tag{2.44}$$

where μ is the molecular viscosity of the fluid. If the flow is inviscid (i.e. the friction is considered to be negligible), the stress term may be excluded from the momentum conservation equation. Also, for flows that are steady and independent of time, the first term in the momentum equation is equal to zero.

The complete derivation of the continuity and momentum conservation equations is provided in a number of texts, among them those of Batchelor [82], Anderson [83], and Panton [84].

2.6.2 Turbulence Closure Schemes

Fluid flow is typically categorised into one of three flow regimes: laminar, transition, and turbulent flow. Laminar flow is dominated by viscous forces and therefore occurs at low Reynolds numbers. The fluid viscosity in laminar flow is sufficient to dampen any perturbations.

Conversely, turbulent flow is dominated by inertial forces and appears at high Reynolds numbers. Because the viscous forces are of low influence, perturbations in the flow are not damped and eddies form in the flow. The presence of eddies in turbulent flow causes substantial mixing, which results in irregular spatial and temporal pressure and velocity fluctuations.

Flow is considered transitional when there is a mixture of laminar and turbulent flow. Transition flow is present, for instance, between the laminar and turbulent flow in turbulent boundary layers.

Fluctuations in turbulent flow can be modelled by direct numerical simulation (DNS), but

these fluctuations occur frequently and at very small scales, rendering them computationally expensive to simulate. Rather than simulate turbulent flow directly, therefore, modified governing equations which remove the requirement to resolve small scale turbulence are commonly employed. Additional variables are introduced when the governing equations are modified, and turbulence models are used to close the problem and to compute these variables.

Two separate sets of modified governing equations are considered in the current work: the Reynolds-averaged Navier-Stokes equations and a set of filtered Navier-Stokes equations (associated with large eddy simulation). These are discussed in detail below. A thorough overview of turbulence modelling and simulation may be found in Pope [85] and Wilcox [86].

Reynolds-Averaged Navier-Stokes

The Reynolds-averaged Navier-Stokes (RANS) equations are derived from the Navier-Stokes equations using the assumption that the solution variables each consist of a mean (time-averaged) component and a fluctuating (time-variant) component. With this assumption, the velocity u_i ($i = 1, 2, 3$) can be expressed as a Reynolds decomposition:

$$u_i(\mathbf{x}, t) = \overline{u}_i(\mathbf{x}) + u'_i(\mathbf{x}, t), \tag{2.45}$$

where $\overline{u}_i$ is the mean velocity and u'_i represents the turbulent fluctuations. Similarly, the other solution variables may also be written as the sum of a mean and a fluctuating quantity. The RANS equations are derived by substituting these decomposed expressions into the continuity and momentum equations and time-averaging the result. In Cartesian tensor notation, the RANS formulations of the incompressible continuity and momentum

equations, neglecting external body forces, are

$$\nabla \cdot \overline{u}_i = 0 \tag{2.46}$$

$$\frac{\partial}{\partial t}\left(\rho \overline{u}_i\right) + \frac{\partial}{\partial x_j}\left(\rho \overline{u}_i \overline{u}_j\right) = \frac{\partial}{\partial x_j}\left[-\overline{p}\delta_{ij} + \mu\left(\frac{\partial \overline{u}_i}{\partial x_j} + \frac{\partial \overline{u}_j}{\partial x_i}\right) - \rho\overline{u_i^{'} u_j^{'}}\right] + S_i \tag{2.47}$$

All solution variables in Eqs. 2.46 and 2.47 are time-averaged (mean) values. S_i is a momentum source in the i^{th} direction and δ_{ij} is the Kronecker delta. $\delta_{ij} = 1$ when $i = j$ and 0 when $i \neq j$.

The $-\rho\overline{u_i^{'} u_j^{'}}$ term in Eq. 2.47 represents the Reynolds stresses and appears as a result of turbulent fluctuations. This term introduces six additional unknowns, and hence additional equations are required; this is the turbulence closure problem. Turbulence models are therefore used to model the Reynolds stresses and close the RANS equations.

Turbulence models for the RANS equations usually fall into one of two general classifications: Reynolds stress transport models and models employing the Boussinesq approach. In Reynolds stress transport models, transport equations are used to model each of the six unknown stresses [87, 88]. While these hold the advantage of computing stresses directly, and thus the ability to capture anisotropic turbulence, the complexity which arises from the high number of equations is not desirable, and Reynolds stress transport models are not commonly used.

Models employing the Boussinesq approach, also called eddy viscosity models, typically require zero to two additional transport equations. Thus, these models are attractive as compared to Reynolds stress transport models when computational expense is considered. The Boussinesq hypothesis for incompressible flow is

$$-\rho\overline{u_i^{'} u_j^{'}} = \mu_t\left(\frac{\partial \overline{u}_i}{\partial x_j} + \frac{\partial \overline{u}_j}{\partial x_i}\right) - \frac{2}{3}\rho k \delta_{ij}. \tag{2.48}$$

Two new variables are introduced in Eq. 2.48: the turbulent viscosity, μ_t, and the turbulent kinetic energy, k. It is assumed in the Boussinesq approach that μ_t is isotropic and that its value is independent of the direction; this is one of the primary differences between eddy viscosity models and Reynolds stress transport models.

Linear eddy viscosity models fall into one of three primary categories: algebraic (zero-equation) models, one-equation models, and two-equation models. In algebraic models, no transport equations are used and a simple algebraic relationship closes the problem. History effects, such as convection and dissipation of turbulent energy, are not correctly predicted by algebraic models as they use only local relations.

One-equation models solve one additional transport equation, for either turbulent viscosity (i.e. in the Spalart-Allmaras approach [89]) or the turbulent kinetic energy. In these models, the turbulent length scale is typically related to a flow dimension algebraically, rather than modelled. The length scale can be affected by turbulent convection and dissipation, however, and it is not ideal to employ a length scale that cannot be adapted for this.

Finally, two-equation models solve two additional transport equations. These are considered to be more satisfactory models because the turbulent velocity and turbulent length scales may be found independently and without prior knowledge of the flow structure. The most developed RANS turbulence closures fall into the two-equation model category. Three two-equation turbulence closures, the standard $k-\epsilon$ model, the standard $k-\omega$ model, and the $k-\omega$ shear stress transport (SST) model, are discussed below.

- *Standard $k-\epsilon$ model*

  In the standard $k-\epsilon$ model, first proposed by Launder and Spalding [90], the two additional transport equations that are solved are those for the turbulent kinetic energy (k) and turbulent kinetic energy dissipation rate (ϵ). This is a semi-empirical model, with k determined using the exact transport equation but ϵ determined using a transport equation obtained using physical insights. In this model, it is assumed

that the flow is fully turbulent. Hence, while it is valid for far-field modelling of fully turbulent flows, it cannot be used to model boundary layer transition.

- *Standard $k-\omega$ model*

  In the standard $k-\omega$ model, the two additional transport equations that are solved are those for the turbulent kinetic energy (k) and specific turbulent kinetic energy dissipation rate (ω). The model, introduced by Wilcox [86], forms the basis for the model employed by ANSYS Fluent. Unlike the standard $k-\epsilon$ turbulence closure, the standard $k-\omega$ turbulence closure is more capable of modelling the transition and separation that occurs in adverse pressure gradients (although the modelling of transition and separation is certainly far from perfect [91]).

- *$k-\omega$ shear stress transport (SST) model*

  The $k-\omega$ SST turbulence closure for the RANS equations, introduced by Menter [92], employs the $k-\omega$ turbulence closure near no-slip boundaries and a $k-\epsilon$ method (adapted to a $k-\omega$ formulation) in the remainder of the domain (i.e. the far field). A blending function is employed between the edges of the two models. The $k-\omega$ SST turbulence closure model transport equations are

$$\frac{\partial}{\partial t}(\rho k)+\frac{\partial}{\partial x_i}(\rho k\overline{u}_i)=\frac{\partial}{\partial x_j}\left(\Gamma_k\frac{\partial k}{\partial x_j}\right)+\tilde{G}_k-Y_k+S_k \tag{2.49}$$

  and

$$\frac{\partial}{\partial t}(\rho\omega)+\frac{\partial}{\partial x_i}(\rho\omega\overline{u}_i)=\frac{\partial}{\partial x_j}\left(\Gamma_\omega\frac{\partial \omega}{\partial x_j}\right)+G_\omega-Y_\omega+S_\omega+D_\omega. \tag{2.50}$$

  $\tilde{G}_k$ and G_ω are the generation of k and ω; Y_k and Y_ω are the respective dissipations; Γ_k and Γ_ω are the effective diffusivities; and S_k and S_ω are user-input source terms (which are always zero in the current work). D_ω is a cross-diffusion term which

arises as the result of the transformation from the $k-\epsilon$ model to the $k-\omega$ framework. The generation, dissipation, diffusivity, and cross-diffusion are defined by a set of equations that, with the use of a number of empirical coefficients, close the system. k and ω are related to the measured parameters turbulence intensity (I) and turbulent length scale (l) by

$$k = \frac{3}{2}\left(\overline{u}I\right)^2, \tag{2.51}$$

where $\overline{u}$ is the mean velocity, and

$$\omega = \frac{k^{\frac{1}{2}}}{C_{\mu}^{\frac{1}{4}} l}, \tag{2.52}$$

where $C_{\mu} \approx 0.9$ is an empirical constant. The turbulent viscosity is determined using the solutions for k and ω:

$$\mu_t = \frac{\rho k}{\omega} \frac{1}{\max\left[\frac{1}{\alpha^*}, \frac{SF_2}{a_1 \omega}\right]}, \tag{2.53}$$

where S is the strain rate, F_2 is a blending function, and α^* and a_1 are empirically determined model constants.

The two-equation $k-\omega$ SST turbulence closure has been employed in a number of tidal and wind turbine studies, including Sørensen et al. [93], Mahu and Popescu [94], Fleming et al. [54], and McNaughton et al. [95]. The method is also used in the majority of the current work due to its ability to model flow near surfaces (i.e. the blades, nacelle, and tower), and it's ability to model large vortex structures in the far-field.

The model coefficients used throughout this thesis for the $k-\omega$ SST method are as specified in [96].

Large Eddy Simulation

While the RANS formulation of the governing equations employs time-averaging to remove the need to compute small scale fluctuations, large eddy simulation (LES) uses a local spatial filtering approach. This yields the filtered Navier-Stokes equations used in LES.

It is assumed that mass and momentum are transported primarily by large scale flow structures, and also that these large turbulent structures are more heavily dependent on the geometry of the problem than small scale turbulent structures. Hence, a universal model for small scale structures should lead to more accurate simulation results than a universal model for large scale structures. In LES, therefore, the large scale turbulence is directly resolved, while a subgrid scale model is used to account for the effects of small scale turbulent structures.

In the derivation of the RANS equations, a Reynolds decomposition, in which solution variables are written as the sum of the mean and fluctuating components, was used. In the derivation of the filtered Navier-Stokes equations for LES, the solution variables are instead decomposed into large (resolved) scale and small (subgrid) scale parts. This LES decomposition may be expressed as:

$$u_i(\mathbf{x},t) = \tilde{u}_i(\mathbf{x},t) + u_i'(\mathbf{x},t), \tag{2.54}$$

where $\tilde{u}_i$ represents the large scale part and u_i' the small scale part. Although the notation of u_i' is the same as in the Reynolds decomposition in Eq. 2.45, it is important to note that this variable in the LES decomposition represents a different quantity than in the Reynolds decomposition. Also, both components of the LES decomposition are functions of both space and time, unlike in the Reynolds decomposition, in which the mean velocity

is independent of time, or at least is varying sufficiently slowly to allow a separation of scales argument to apply.

A filter which removes eddies with length scales smaller than the grid scale is applied to the incompressible continuity and momentum conservation equations, yielding

$$\nabla \cdot \tilde{u}_i = 0 \tag{2.55}$$

and

$$\frac{\partial}{\partial t}\left(\rho \tilde{u}_i\right) + \frac{\partial}{\partial x_j}\left(\rho \tilde{u}_i \tilde{u}_j\right) = \frac{\partial}{\partial x_j}\left[-\tilde{p}\delta_{ij} + \mu\left(\frac{\partial \tilde{u}_i}{\partial x_j} + \frac{\partial \tilde{u}_j}{\partial x_i}\right) - \tau_{ij}\right] + S_i, \tag{2.56}$$

respectively, where τ_{ij} is the subgrid scale stress and is

$$\tau_{ij} = \rho\widetilde{u_i u_j} - \rho \tilde{u}_i \tilde{u}_j. \tag{2.57}$$

This subgrid scale stress must be modelled. A model based on the Boussinesq hypothesis may be applied to relate τ_{ij} with the subgrid scale turbulent viscosity, μ_t and the rate of strain tensor, $\tilde{S}_{ij}$ (see [97]):

$$-\tau_{ij} = 2\mu_t \tilde{S}_{ij}. \tag{2.58}$$

The rate of strain tensor is defined as

$$\tilde{S}_{ij} = \frac{1}{2}\left(\frac{\partial \tilde{u}_i}{\partial x_j} + \frac{\partial \tilde{u}_j}{\partial x_i}\right). \tag{2.59}$$

A model is required for the subgrid scale turbulent viscosity, μ_t. A number of models have been proposed, however, only the Smagorinsky-Lilly model, proposed in [98] and one of the simplest closures for the filtered Navier-Stokes equations, will be discussed at present.

In this model, the turbulent viscosity is given by

$$\mu_t = \rho L_s^2 \sqrt{2\tilde{S}_{ij}\tilde{S}_{ij}}. \tag{2.60}$$

L_s is the subgrid scale mixing length and is determined in the current work from

$$L_s = \min\left(\kappa d, C_s V^{1/3}\right), \tag{2.61}$$

where κ is the Von Kármán constant, d is the distance to the nearest domain wall, V is the volume of the given computational cell, and C_s is the Smagorinsky constant (in this work, $C_s = 0.1$). The κd term is a damping term which causes L_s to approach 0 in the vicinity of the domain walls.

LES offers reduced numerical dissipation as compared to RANS methods, and is hence typically employed in wake-related turbine studies. A number of authors, including Troldborg et al. [75] and Afgan et al. [99], have employed LES methods in the study of wind and tidal turbines. LES has also been used in conjunction with actuator line methods in the simulation of wind farms (Porté-Agel et al. [100]; Churchfield et al. [78]) and tidal current turbine arrays (Churchfield et al. [80]). Porté-Agel et al. employ a dynamic model, in which model coefficients (including C_s) are locally optimised. Conversely, Churchfield et al. [78] set the coefficient C_s to be a constant ($C_s = 0.135$) and Churchfield et al. [80] set $C_s = 0.125$.

In the current work, large eddy simulations of a wind rotor are completed only for comparison to RANS $k-\omega$ SST simulation results (this comparison is found in Section 4.5).

2.6.3 CFD Solution Methods

The CFD solver employed for this work is ANSYS Fluent [96] [101]. This is a commercial CFD package and is capable of solving both the RANS and filtered Navier-Stokes (LES)

equations, among others. In the current work, a pressure-based projection method using a segregated algorithm is employed. The ANSYS Fluent solver uses a finite volume approach for the spatial discretisation in all CFD solutions. The pressure-based solver, finite volume method, time discretisation scheme, and additional solution details are summarised in this section.

Pressure-Based Solver

Pressure-based solvers employ the projection method, in which conservation of mass is maintained via the use of a pressure correction equation. The segregated pressure-based algorithm solves the continuity and conservation of momentum equations consecutively. These equations, however, are coupled and nonlinear, so iterative solution techniques are used until a specified convergence tolerance is reached. Additional details of the implementation of the pressure-based solver in ANSYS Fluent may be found in [96].

Spatial Discretisation: Finite Volume Method

While the continuity and conservation of momentum equations can be solved analytically for simple flows, the vast majority of fluid dynamics problems require numerical solution methods. In order to solve the equations numerically, the relevant equations are discretised, i.e. converted to discrete algebraic equations. A set of these discretised equations may then be constructed and solved for a discretised (meshed) domain.

As previously stated, ANSYS Fluent employs a finite-volume approach for this spatial discretisation. The finite volume method is a common choice for fluid dynamics simulations. One of the advantages of the finite volume approach is that it may be straightforwardly applied to unstructured geometry. The finite volume method is discussed in depth in a number of sources, including the work of Versteeg and Malalasekera [102]. A brief overview is included below.

The finite volume method utilises integral formulations of equations. For example, the integral form of the unsteady conservation equation for a general scalar, χ, is

$$\int_V \frac{\partial \rho\chi}{\partial t} + \oint \rho\chi\mathbf{u}\cdot d\mathbf{A} = \oint \Gamma_\chi \nabla\chi \cdot d\mathbf{A} + \int_V S_\chi dV, \tag{2.62}$$

where $\mathbf{A}$ is an outward surface area vector on the control volume V, Γ_χ is a diffusion coefficient for χ, $\nabla\chi$ is the gradient of χ, and S_χ is a source term. The discretised form of Eq. 2.62 is

$$\frac{\partial \rho\chi}{\partial t}V + \sum_{f=1}^{N_{faces}} \rho_f \mathbf{u}_f \chi_f \cdot \mathbf{A}_f = \sum_{f=1}^{N_{faces}} \Gamma_\chi \nabla\chi_f \cdot \mathbf{A}_f + S_\chi V, \tag{2.63}$$

where N_{faces} is the number of faces of a cell (4 for a tetrahedron) and the subscript f denotes that the property is evaluated at the specified face. Also, V is the volume of the cell and $\rho_f \mathbf{u}_f \cdot \mathbf{A}_f$ is the mass flux through face f.

In ANSYS Fluent, the discretised equations follow the formulation of Eq. 2.63 and are applied to all cells in the simulation domain. All of the meshed domains used in the current work were created with ANSYS ICEM CFD [103].

The ANSYS Fluent solver is a cell-centred solver; the variable values are evaluated and stored at the centre of the respective cell. However, it is clear from the formulation of Eq. 2.63 that values at the cell faces are also required.

A number of interpolation methods for determining values at cell faces are available in ANSYS Fluent, including first and second order upwind schemes, a power law scheme, and a central differencing scheme. A second-order upwind scheme is employed for the convective terms in all RANS simulations in the current work. In this scheme, a Taylor series expansion is used to approximate a given face value using the cell centroid value as well as cell-centre values from upstream cells. A second-order central differencing scheme, which improves LES accuracy, is used for the convective terms in all LES simulations. In the central differencing scheme, both upstream and downstream cell centroid values are

used in the interpolation. Generally, this scheme results in lower numerical diffusion but is less stable than upwind schemes. The diffusion terms are found using second-order accurate central differencing for all simulations.

Temporal Discretisation: Implicit Time Integration

Unsteady simulations require the use of temporal discretisation in addition to spatial discretisation. Temporal discretisation is relatively simple; all terms in the differential equations are integrated over a user-defined time step, Δt. If we call $F(\chi)$ the variation of a representative variable χ with respect to time, we may write

$$F(\chi) = \frac{\partial \chi}{\partial t}. \tag{2.64}$$

Here, F includes the spatial discretisation. In ANSYS Fluent, backwards differences are used to discretise Eq. 2.64. Although a simpler first order discretisation may be used, second order discretisation is used exclusively throughout the current study because of its improved accuracy. The second order temporal discretisation is:

$$F(\chi^{n+1}) = \frac{3\chi^{n+1} - 4\chi^{n} + \chi^{n-1}}{2\Delta t}, \tag{2.65}$$

where n is the current time level, $n-1$ is the previous time level, and $n+1$ is the next time level.

All unsteady simulations in the current work employ an implicit time integration, in which Eq. 2.65 is solved iteratively for $F(\chi^{n+1})$ during each time step of the solution.

Implicit time marching is less sensitive to stability issues than explicit time marching. Because implicit time integration is used in the current work, the stability and convergence of the solution is not reliant on the Courant-Friedrichs-Lewy (CFL) condition [104]. Still, in order to ensure a solution converges to an accurate result, a range of time steps must

be implemented for a given unsteady flow problem. Generally, the time step is reduced in sequential test simulations until the solution values are unchanged, at which point the appropriate time resolution is deemed to have been determined.

Additional Solution Details

The SIMPLE algorithm for pressure-velocity coupling is used in all simulations in the current work. Also, an algebraic multigrid (AMG) algorithm is used to accelerate the solution convergence by reducing low-frequency (global) errors through the use of progressively coarser meshes within solution iterations. A Gauss-Seidel equation solver is employed to solve the set of linearised discretised equations. Further details of the implementation of the SIMPLE algorithm, Gauss-Seidel method, and AMG algorithm in ANSYS Fluent are given in [96].

2.7 Summary

The main methods for modelling turbines have been summarised in this chapter. In addition, a brief overview of the numerical implementation used for the CFD studies in this thesis has been presented.

There is a significant range in the computational resource required for the various rotor modelling techniques discussed in Sections 2.1 - 2.5. Approximate requirements for modelling a single rotor using each of the main methods on a high-performance computing cluster are given in Table 2.1.

Table 2.1: Approximate computational requirements for simulations of a single tidal turbine using various rotor modelling methods and a high-performance computing cluster.

Method	Approximate computational requirement
RANS actuator disc	$10^{-1} - 10^{0}$ CPU hours
RANS-BEM	$10^{0} - 10^{1}$ CPU hours
RANS actuator line	$10^{1} - 10^{2}$ CPU hours
RANS 3D blade-resolved	$10^{2} - 10^{4}$ CPU hours [93] [105]

It is important to note that the computational requirements outlined in Table 2.1 are only approximations. A number of factors affect the computational requirement, including the clock rate and the number of cores per CPU. Also, simulation parameters such as the spatial and temporal resolution, the size of the simulated domain, and the inclusion or lack thereof of additional turbine components (i.e. nacelle, tower, and/or duct) will affect the computational requirement. In addition, the inclusion of more complex flow features, such as bed shear or a waves, can significantly increase the computational requirement of a simulation.

Although some methods require significantly more computational resources than others, there is often a trade-off between the computational requirement and the detail and accuracy of the results.

RANS-embedded actuator disc methods model idealised energy extractors; although they are fast, they do not allow for specific rotor geometries to be simulated, do not model radial variations in rotor loading, and, due to their steady-state nature, cannot simulate transient flow features such as blade tip vortices.

RANS-BEM methods, which require greater computational resource than actuator disc methods, also cannot accurately simulate transient flow features in the wake, but do allow for radial variations in the blade loads. In addition, RANS-BEM methods employ blade element theory and are thus capable of simulating user-input rotor geometries.

Actuator line methods, which may be considered to be unsteady implementations of RANS-BEM, also employ blade element theory. This enables actuator line methods to simulate the unsteady effects of a specified rotor on a flow field (and vice versa). However, the unsteady implementation requires an increase in computational requirements as compared to steady-state RANS-BEM methods. Actuator line methods do not explicitly include the rotor blades in the computational domain; hence, these methods are not able to compute quantities on the blade surface, such as blade surface pressure distributions.

In 3D blade-resolved methods, the rotor blades are resolved in the computational mesh and blade surface pressure distributions may be obtained. In addition, unsteady 3D blade resolved methods are capable of providing all of the results that actuator line simulations provide. However, it is difficult to accurately model the transition from laminar to turbulent flow in 3D blade-resolved models, and the computational requirement required in order to resolve the blade boundary layers is high.

Chapter 3

Actuator Line Model Modifications, Verification, and Implementation

The actuator line method provides more accurate simulations than RANS-embedded actuator disc and RANS-BEM models because time-dependent physical phenomena, including transient flow features such as tip vortices, are directly simulated. In addition, it is much more efficient than 3D blade-resolved models and vortex methods while also providing more information about the flow field than vortex methods. The actuator line method, therefore, allows for an effective compromise between accuracy and efficiency. For these reasons, a main component of the current work is to implement an actuator line method suitable for the simulation of tidal turbines and tidal turbine arrays. It is important for the actuator line implementation to retain a general nature and be as universally applicable as possible. Therefore, care is taken to ensure that the capabilities of the model are not limited by the numerical methods employed.

In the actuator line method, each rotor blade is represented in the flow field by a series of point sources distributed along the blade's quarter-chord line. This method, as opposed to 3D blade-resolved methods, avoids the need to discretise the blade boundary layers while

still computing the effect of the blade's presence on the flow. However, the imposition of momentum sources at discrete points in space can result in substantial local flow field distortion, which can cause inaccuracies in the magnitude and direction of the simulated flow speeds at the collocation points (the series of points at which the sources are calculated) and result in unreliable values for the local velocity being returned by the CFD solver for these points. In some cases, this can also lead to numerical instabilities. Nevertheless, it can be seen from Eqs. 2.17 and 2.18 that the magnitude of the relative velocity at the blade must be known in order to calculate the force on the blade section and thus the appropriate momentum source. In addition, the angle of attack, α, must be known for C_l and C_d to be determined. Therefore, a method of determining the accurate relative velocity and the corresponding angle of attack at each blade segment is required.

In an effort to prevent unstable behaviour, previous actuator line model implementations have applied the momentum sources to the flow field using a Gaussian distribution over several cells rather than apply the sources at discrete locations [70, 106, 72]. Distributing each momentum source over a number of cells reduces the flow field distortion and the numerical instabilities that follow. The velocity can then be returned directly from the solver at each collocation point. However, this method requires the use of a numerical constant which adjusts the weighting of the Gaussian distribution. The value chosen for this constant can affect the magnitude and direction of the velocity returned from the solver, and hence the overall flow solution.

It is desirable to implement a method to obtain the relative velocity at the collocation points while minimising the introduction of non-physical weighting. A new method of determining the flow characteristics at the blade segments is introduced and verified in the present chapter. The method used to adapt the modified model to an unstructured mesh is also described. Finally, an overview of the 3D unsteady actuator line model implementation employed in this thesis is presented.

3.1 Velocity Analysis Routine

A new velocity analysis routine is introduced and discussed in the first section of this chapter. The inaccuracies due to the blade approximation extend over a certain region, outside of which the flow field is independent of the mesh for sufficiently high mesh resolution. In the proposed method of obtaining the relative velocity at a collocation point, the flow magnitude and direction are sampled at specified locations in the vicinity of the collocation point, but outside of this region of flow field distortion. The local flow speed and incidence at the corresponding blade segment are then determined from the sampled local flow field data.

This section includes the results of a 2D velocity field study. These results are used to determine flow velocity sampling locations for use in the velocity analysis routine, which is introduced at the end of this section.

3.1.1 2D Aerofoil Velocity Field Study

Prior to implementing the velocity analysis routine, it is first necessary to determine how the flow field depends on grid size, mesh topology, angle of attack, upstream flow velocity, and blade chord. The results of the 2D aerofoil velocity field study discussed in this section reveal the appropriate locations for velocity sampling in the velocity analysis routine. In addition, the results of this study give useful insight into the mesh resolution required for an embedded actuator line model to yield a converged solution.

Computational Model

A stationary 2D thin aerofoil is used in the velocity field study. All distances and lengths in this study are normalised on the aerofoil chord, c. Therefore, the grid size and the locations of velocity measurements are discussed in terms of chord length rather than

absolute distance. This ensures that the results of this study will be independent of the chord.

The domain used in the velocity field study extends $10c$ upstream and downstream of the aerofoil quarter-chord and also $10c$ above and below the quarter-chord point. The inlet of the domain is taken to be a velocity inlet with uniform free stream flow speed U_∞ and the outlet is a pressure outlet with constant gauge pressure of 0 Pa. The top and bottom of the domain are walls with zero shear. A schematic of the domain is shown in Figure 3.1.

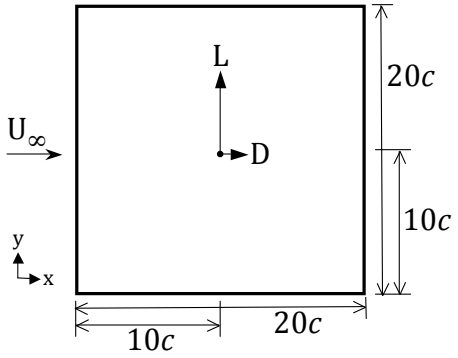

Figure 3.1: Schematic of the 2D thin aerofoil velocity field study domain.

From thin aerofoil theory [65], the lift coefficient, $C_{l_{sym}}$, of a thin symmetric 2D aerofoil depends only on the angle of attack:

$$C_{l_{sym}} = 2\pi\alpha. \tag{3.1}$$

Therefore, variation in the simulated aerofoil attack angle is achieved through adjustment of $C_{l_{sym}}$.

Although thin aerofoil theory utilises an assumption of inviscid flow, giving $C_d = 0$, it is desirable to include viscous drag effects in the CFD simulations. Hence, the drag coefficient in this study is taken to be $C_d = 0.01$.

Uniform flow with speed U_∞ enters the domain in the positive x-direction (see Figure 3.1). In this study, the aerofoil is stationary and therefore $||\mathbf{U}_{rel}|| = U_\infty$. The aerofoil drag is

therefore of magnitude $\frac{1}{2}\rho U_\infty^2 c C_d$ and acts in the positive x-direction, while the aerofoil lift is of magnitude $\frac{1}{2}\rho U_\infty^2 c C_{l_{sym}}$ and acts in the positive y-direction. The point at which the lift and drag are applied to the flow field (via a momentum source) is considered to be the quarter-chord point of the 2D aerofoil.

A RANS model with a $k-\epsilon$ turbulence closure and 2nd order solution methods is utilised for this study. This was selected over $k-\omega$ SST methods for the current study because of the absence of no-slip walls and associated boundary layers in the problem. In the absence of no-slip walls in the model, the $k-\epsilon$ closure is deemed sufficient.

Required Mesh Element Size

In order to determine the appropriate grid element length, simulations are completed using four meshes of different resolutions for a symmetric aerofoil at varying angles of attack. The four meshes consist of square elements of edge length $e = c/8$, $c/4$, $c/2$, and c, respectively. Each possible combination of $\alpha = 3^\circ$, 6°, 9°, and 12° and $U_\infty = 4$, 8, 12, and 16 m/s is simulated for each mesh resolution.

For each simulation, data for the velocity components (u in the x-direction and v in the y-direction) on four concentric circles centred on the quarter-chord (the location of the collocation point) are normalised by U_∞ and plotted. The radii of the concentric circles are: $c/4$, $c/2$, $3c/4$, and c. The results confirm that the normalised flow fields are independent of the upstream flow speed.

The results for $\alpha = 12^\circ$ are shown in Figure 3.2. Each pair of plots depicts u/U_∞ and v/U_∞ for the specified radius and for each mesh resolution as a function of the azimuth angle, γ. The convention used for γ is as follows: γ increases in the anticlockwise direction with $\gamma = 0$ on the chord line downstream of the aerofoil. Therefore, $\gamma = \pi/2$ is on the suction side of the aerofoil, $\gamma = \pi$ is upstream of the aerofoil on the chord line, and $\gamma = 3\pi/2$ is on the pressure side of the aerofoil.

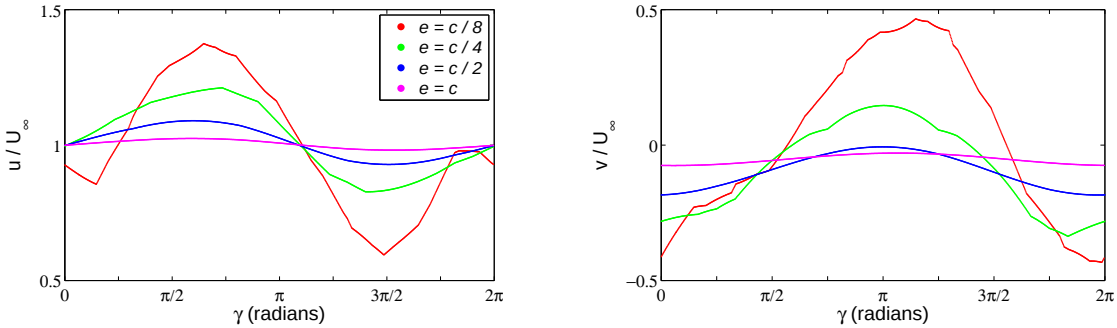

(a) $\frac{u}{U_\infty}$ vs. γ at radius $\frac{c}{4}$ **(b)** $\frac{v}{U_\infty}$ vs. γ at radius $\frac{c}{4}$

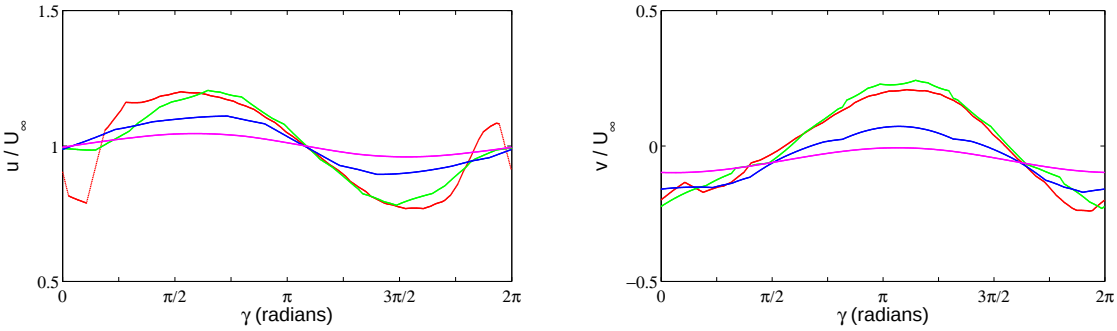

(c) $\frac{u}{U_\infty}$ vs. γ at radius $\frac{c}{2}$ **(d)** $\frac{v}{U_\infty}$ vs. γ at radius $\frac{c}{2}$

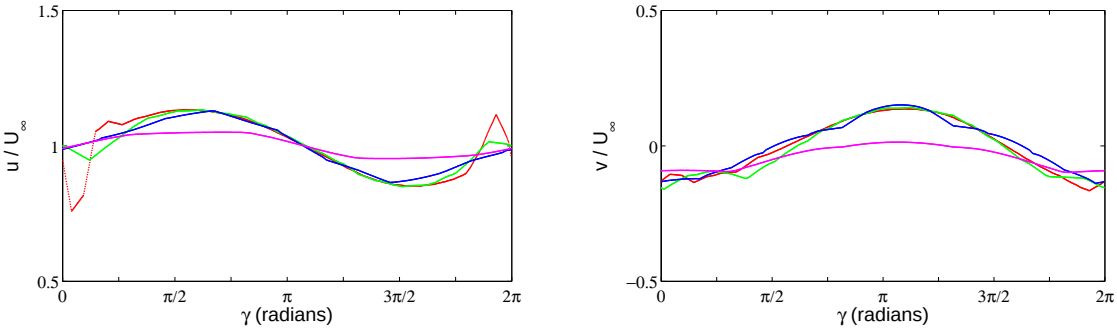

(e) $\frac{u}{U_\infty}$ vs. γ at radius $\frac{3c}{4}$ **(f)** $\frac{v}{U_\infty}$ vs. γ at radius $\frac{3c}{4}$

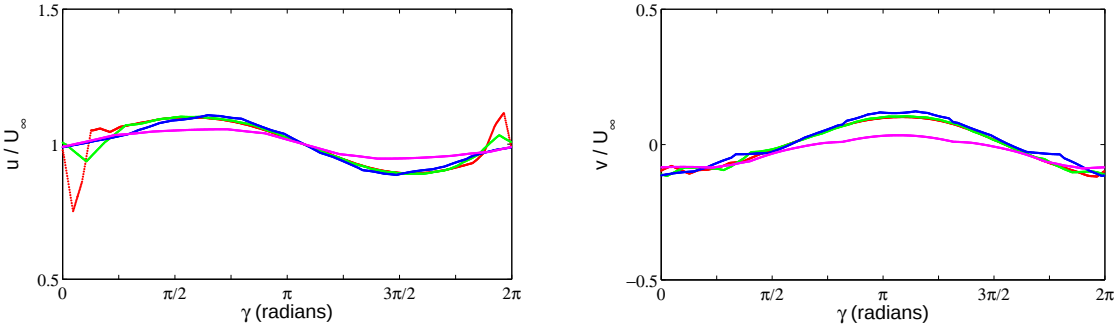

(g) $\frac{u}{U_\infty}$ vs. γ at radius c **(h)** $\frac{v}{U_\infty}$ vs. γ at radius c

Figure 3.2: Normalised u (left) and v (right) versus azimuthal position γ with $\alpha = 12°$ for varying mesh element length, e.

The results plotted in Figure 3.2 converge with increasing distance from the collocation point and decreasing values of e. A distance of c from the collocation point is sufficient for the velocity field upstream of the aerofoil (over the range $\pi/2 < \gamma < 3\pi/2$) to be converged for the the two finest meshes employed (those with element length $c/8$ and $c/4$). Similar conclusions are made from the results for the simulations for $\alpha = 3°$, $6°$, and $9°$. The results from simulations using a polar grid rather than a rectangular structured grid also support these conclusions. Therefore, the convergence behaviour is independent of the mesh topology, so long as the elements are of similar sizes.

From the results of the 2D velocity study, it is determined that a mesh element length, e, of $c/4$ is appropriate resolution near a CFD-embedded actuator line. The results of this study also indicate that, although there is some unsteadiness and a high dependency on mesh resolution in the immediate wake of the aerofoil (near $\gamma = 0$), the velocity field is converged at a distance of one chord length from the quarter-chord over the range $\pi/2 < \gamma < 3\pi/2$. Therefore, c is selected as the minimum distance from which the flow velocities used in the velocity analysis routine will be sampled. Also, the velocity samples used in the velocity analysis routine may only be taken at points that fall in the appropriate range for γ, between $\pi/2 < \gamma < 3\pi/2$.

3.1.2 Overview of Velocity Analysis Routine

A method to determine the local flow speed and angle of attack for a given blade element is introduced in this section. This method, the velocity analysis routine, utilises velocities sampled at three locations with respect to the aerofoil chord for each blade section. The velocity sampling locations have been selected based on the results of the 2D aerofoil velocity field study. The sampled velocities are first transformed from the inertial reference frame to the blade reference frame (Figure 3.3). It is then assumed that the application of a lifting force on the aerofoil induces a circulation, $\Gamma(r)$, around the blade quarter-chord point for each blade segment. This circulation causes a velocity perturbation, $q(r)$, for all

points in the plane of the blade element at a given radius, r_s, from the collocation point (see Figure 3.4). The blade reference frame velocities at the three sampling points are used to write three equations which are solved to determine q, U_{rel}, and α. The steps of the routine are discussed in greater detail below.

Velocity Lookup

The velocities presented in Figure 3.2 converged upstream of the aerofoil, over the range $\pi/2 < \gamma < 3\pi/2$, at a radius of c from the collocation point. In this routine, the velocity will be sampled at three points, each of which lies within this range. The points must be at a constant distance of at least c form the collocation point in the plane of the blade section. These points are taken to be: Point 1 ($\gamma = \pi/2$; above the aerofoil), Point 2 ($\gamma = \pi$; upstream of the aerofoil), and Point 3 ($\gamma = 3\pi/2$; below the aerofoil). A subscript of either 1, 2, or 3 will hereafter denote which of these points is being referenced.

The velocities in the inertial frame, denoted by the subscript I, are properties of the flow field and are easily passed from the CFD solver to the actuator line component of the model in each solver iteration. In the inertial frame, u_I, v_I, and w_I are in the x-, y-, and z-directions, respectively.

Transformation to Blade Plane

The sampled velocities are transformed to the inertial rotated frame, denoted by the subscript Ir. In the inertial rotated frame, also called the blade plane, u_{Ir} is parallel to the blade chord, $w_{Ir} = w_I$ is in the spanwise direction of the blade, and v_{Ir} is in the direction perpendicular to both u_{Ir} and w_{Ir}. Figure 3.3 is a 2D representation of the transformation to the blade plane.

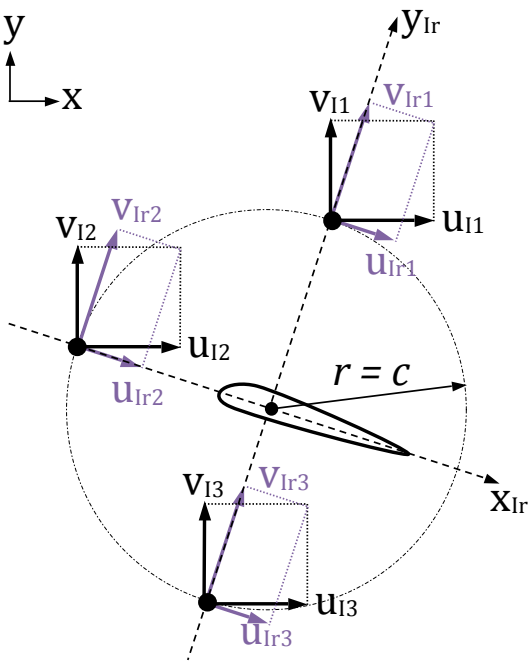

Figure 3.3: Velocities at Points 1, 2, and 3 transformed to the inertial rotated frame. The z-direction is out of the page.

Transformation to Blade Frame

In order to calculate the magnitude of $\mathbf{U}_{rel}$, the velocities must be transformed from the blade plane into the rotating blade frame of reference. This frame, denoted by the subscript B, moves with the blade through the computational domain. To transform to this frame, the blade's velocity is simply subtracted from the blade plane incident velocity $(u_{Ir}, v_{Ir}, w_{Ir})^T$.

The transformation into the blade frame allows for the perturbation of the velocity field due to the induced circulation around the collocation point to be determined. The perturbation, q, will be purely in the x_B-direction for Points 1 and 3 and purely in the y_B-direction for Point 2; see Figure 3.4.

Calculation of U_{rel} and α

As previously discussed, it is assumed that the implementation of a momentum source at the m^{th} point on an actuator line induces a circulation about that point. This is considered to be equivalent to introducing a vortex with constant circulation, Γ^m. The magnitude of Γ^m depends on α^m, $\mathbf{U}^m_{rel}$, c^m, and the camber of the aerofoil. We define q^m as the perturbation of the velocity due to the circulation induced by the momentum source at the m^{th} collocation point (also called an actuator point). The velocity perturbation q^m due to the circulation $\Gamma^m = 2\pi r q^m$ is shown in the blade frame in Figure 3.4 for the m^{th} blade element.

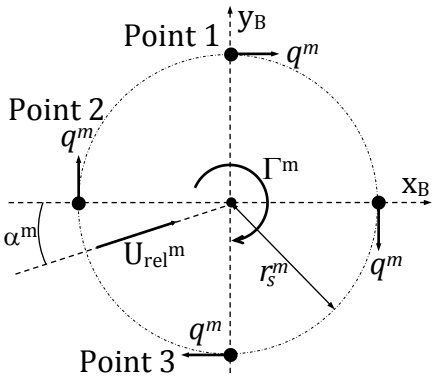

Figure 3.4: Induced velocity for the m^{th} blade segment.

A system of three equations with three unknowns may be written for the m^{th} collocation point by mapping the simulated flow field to that produced by the superposition of a point vortex with a free stream flow of magnitude U^m_{rel} and direction given by α^m.

$$\begin{cases} u^m_{B1} = U^m_{rel} cos\left(\alpha^m\right) + q^m & \text{(3.2a)} \\ u^m_{B3} = U^m_{rel} cos\left(\alpha^m\right) - q^m & \text{(3.2b)} \\ v^m_{B2} = U^m_{rel} sin\left(\alpha^m\right) + q^m & \text{(3.2c)} \end{cases}$$

The velocities u^m_{B1}, u^m_{B3}, and v^m_{B2} are known following the transformation of the velocities to the moving blade reference frame.

Equation 3.2b is subtracted from Eq. 3.2a to solve for q^m:

$$q^m = \frac{1}{2}\left(u^m_{B1} - u^m_{B3}\right). \tag{3.3}$$

Manipulation of Eqs. 3.2a, 3.2b, and 3.2c yields

$$U^m_{rel} = \left(\left(v^m_{B2} - q^m\right)^2 + \left[\frac{1}{2}\left(u^m_{B1} + u^m_{B3}\right)\right]^2\right)^{\frac{1}{2}}. \tag{3.4}$$

Finally, combining Eqs. 3.2c and 3.4 gives α^m:

$$\alpha^m = sin^{-1}\left(\frac{v^m_{B2} - q^m}{U^m_{rel}}\right) = sin^{-1}\left(\frac{v^m_{B2} - q^m}{\left(\left(v^m_{B2} - q^m\right)^2 + \left[\frac{1}{2}\left(u^m_{B1} + u^m_{B3}\right)\right]^2\right)^{\frac{1}{2}}}\right). \tag{3.5}$$

Aerofoils with camber will naturally induce higher velocity perturbation. The velocity analysis routine automatically takes any effects caused by camber into account because q^m is treated as a variable rather than as an imposed constant.

3.2 Velocity Analysis Routine Verification

To verify the velocity analysis routine introduced in Section 3.1.2, the routine is applied in simulations of 2D stationary aerofoils and a simulation of a 2D aerofoil moving at constant velocity. The results of these verification cases are presented in this section. In addition, results from stationary 3D elliptic wing simulations, which verify the actuator line method of approximating a lifting surface, are discussed. Water with $\rho = 998$ kg/m^3 and $\mu =$ 1 x 10^{-3} kg/(m·s) is the simulated fluid for all of the verification simulations presented in this section. In addition, some configurations are also simulated with air ($\rho = 1.225$ kg/m^3; $\mu = 1.79$ x 10^{-5} kg/(m·s)) as the working fluid. These cases are noted in the corresponding

text. All of the simulations are completed using structured grids constructed such that the collocation points and velocity sampling points coincide with cell centroids.

3.2.1 Stationary 2D Aerofoils

2D simulations are a useful first step in verifying the velocity analysis routine because, in addition to the reduced computational requirement due to fewer cells in the domain, the aerofoil may be represented by a momentum source at a single collocation point, greatly simplifying the problem. In addition, 2D tests allow the underlying assumption of the velocity analysis routine, that the imposition of the momentum source induces a circulation around an aerofoil, to be tested while decoupled from the actuator line assumption that blades can be represented by a series of segments, each of which sees locally 2D flow.

A domain in which the aerofoil is already in the inertial rotated frame is employed for the 2D stationary aerofoil verification study. Three sides of the domain are considered to be velocity inlets with uniform flow at a specified angle, α, and the aerofoil chord is in the x-direction. Aside from this velocity inlet boundary condition, the domain specifications used in the 2D stationary aerofoil verification cases are the same as for the domain employed in the velocity field study in Section 3.1.1. The solution methods applied follow those described in Section 3.1.1. The domain for the 2D stationary aerofoil verification cases is shown in Figure 3.5.

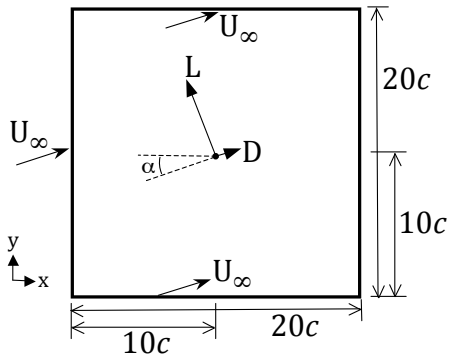

Figure 3.5: Domain for the 2D thin aerofoil velocity analysis routine verification cases.

In simulations of stationary aerofoils, the inertial rotated frame is the same as the blade frame of reference and there is thus no need to translate the velocities into another frame of reference. In addition, the magnitude of the relative velocity is simply U_∞ for the stationary aerofoil.

Two distinct sets of 2D stationary aerofoil simulations are completed in the velocity analysis routine verification. In the first, a constant source term is applied to the flow at the collocation point until flow field convergence is reached. In the second, the applied source is iteratively updated using the flow field data returned by the solver. Each of these is discussed in greater detail below.

Constant Source

The goal of the first set of 2D aerofoil simulations is to determine whether the velocity analysis routine returns accurate values for U_{rel} and α with the correct sources being applied to the flow during each iteration. In the following verification cases, a constant momentum source is applied to the flow at the collocation point and the values of U_{rel} and α returned by the flow analysis routine are compared with the known input values. The magnitudes and directions of **L** and **D** are determined by inputting the applied inlet values of U_∞, α, C_l, and C_d into Eqs. 2.17 and 2.18. There is no feedback in the computation; the applied forces do not depend on the local flow field. In these simulations, the upstream flow speed is $U_\infty = 4$ m/s and the mesh element length is $e = c/4$. The velocity samples are taken at a distance of c from the collocation point (the chord is unit length).

Simulations are completed for four different aerofoils and for varying α. The four aerofoils are: symmetric thin aerofoil, cambered thin aerofoil, NACA 0012, and NACA 4415. NACA 0012 is a symmetric aerofoil and NACA 4415 is a slightly thicker cambered aerofoil. These aerofoils are included to ensure that the method returns accurate results for real aerofoils in addition to thin aerofoil approximations. The lift coefficient used for the

cambered thin aerofoil is

$$C_{l_{camber}} = C_{l_o} + C_{l_{sym}} = 0.4 + 2\pi\alpha, \tag{3.6}$$

where C_{l_o} is the lift coefficient when the aerofoil angle of attack is zero. A value of 0.4 is used for C_{l_o} in the current study. α must be in radians in Eq. 3.6.

Tabulated data for C_l and C_d as functions of α are utilised for the NACA aerofoils [107, 108]. Profiles of the NACA aerofoils used in the study are shown in Figure 3.6.

Figure 3.6: NACA 0012 aerofoil (left) and NACA 4415 aerofoil (right).

The results for the 2D velocity analysis routine verification cases with constant sources are shown in Tables 3.1 and 3.2. These tables summarise the values of α and U_{rel} calculated by the velocity analysis routine for each aerofoil at varying angles of attack.

Table 3.1: Values returned for α (in degrees) for the 2D stationary aerofoil (constant source) verification cases.

Input α (degrees)	-12	-9	-6	-3	0	3	6	9	12	15	18
Symmetric thin aerofoil	—	—	—	—	—	3.015	6.031	9.010	11.990	—	—
Cambered thin aerofoil	-12.048	-9.042	-6.013	-2.996	0.018	3.022	5.980	8.932	11.883	—	—
NACA 0012 aerofoil	—	—	—	—	—	3.010	6.031	9.010	12.000	15.055	18.224
NACA 4415 aerofoil	—	—	-6.011	-2.996	0.018	3.023	5.988	8.967	—	—	—

Table 3.2: Values returned for U_{rel} (in m/s) for the 2D stationary aerofoil (constant source) verification cases. The input velocity magnitude is $U_{rel} = U_\infty = 4$ m/s.

Input α (degrees)	-12	-9	-6	-3	0	3	6	9	12	15	18
Symmetric thin aerofoil	—	—	—	—	—	4.000	3.998	3.992	3.983	—	—
Cambered thin aerofoil	3.993	3.998	4.000	4.001	3.999	3.997	3.991	3.982	3.968	—	—
NACA 0012 aerofoil	—	—	—	—	—	4.000	3.998	3.992	3.985	3.983	3.998
NACA 4415 aerofoil	—	—	4.000	4.000	3.999	3.997	3.992	3.986	—	—	—

It is clear from the results listed in Tables 3.1 and 3.2 that the velocity analysis routine is very accurate when the applied sources are constant for both the thin aerofoils and the NACA-series aerofoils. The largest error for α is 1.24% for the NACA 0012 aerofoil with input $\alpha = 18°$. The largest error for the relative velocity magnitude is 0.80% for the cambered thin aerofoil at $\alpha = 12°$. Notably, the NACA 0012 aerofoil is operating past the stall point for $\alpha = 15°$ and $18°$. The results for these angles indicate that the routine is capable of correctly calculating α and U_{rel} for aerofoils in stall.

Iterative Source

In the actuator line method, the sources input into the momentum equations are not constant. Rather, U_{rel} and α must be iteratively calculated from the flow field data at the velocity sampling points and these values used to calculate the appropriate momentum sources to be applied for each iteration of the simulation. The second set of 2D verification cases, therefore, utilises the values of U_{rel} and α returned by the velocity analysis routine for a given iteration to calculate the magnitude and direction of the source applied to the flow. The updated source value results in new U_{rel} and α values in the subsequent iteration. The iterative process is repeated until convergence is achieved for both the flow field as well as the values returned by the velocity analysis routine. The foremost aim of the 2D iterative source verification cases is to confirm that the iterative process in the velocity analysis routine is stable.

In the iterative source verification cases, the inlet velocity is again $U_\infty = 4$ m/s. Simulations are completed using each of the four aerofoils employed in the 2D constant source simulations (symmetric and cambered thin aerofoils, NACA 0012, and NACA 4415). The NACA aerofoils at $\alpha = 15°$ and $18°$ operate in post stall conditions. Tables 3.3 and 3.4 present the values of α and U_{rel}, respectively, returned by the routine at each simulated attack angle.

Table 3.3: Values returned for α (in degrees) for the 2D stationary aerofoil (iterative source) verification cases.

Input α (degrees)	-12	-9	-6	-3	0	3	6	9	12	15	18
Symmetric thin aerofoil	—	—	—	—	—	3.045	6.059	9.038	11.978	—	—
Cambered thin aerofoil	-12.058	-9.054	-6.031	-2.989	0.062	3.070	6.032	8.951	11.835	—	—
NACA 0012 aerofoil	—	—	—	—	—	3.045	6.086	9.038	11.998	14.953	18.029
NACA 4415 aerofoil	-12.044	-9.058	-6.054	-3.023	0.021	3.052	6.058	9.046	12.049	15.031	18.039

Table 3.4: Values returned for U_{rel} (in m/s) for the 2D stationary aerofoil (iterative source) verification cases. The input velocity magnitude is $U_{rel} = U_\infty = 4$ m/s.

Input α (degrees)	-12	-9	-6	-3	0	3	6	9	12	15	18
Symmetric thin aerofoil	—	—	—	—	—	4.001	4.005	4.006	4.001	—	—
Cambered thin aerofoil	4.016	4.009	4.003	4.000	3.998	3.998	3.997	3.992	3.986	—	—
NACA 0012 aerofoil	—	—	—	—	—	4.002	3.977	4.006	4.004	4.016	4.024
NACA 4415 aerofoil	4.014	4.010	4.005	4.002	4.000	4.002	4.005	4.008	4.014	4.013	4.016

For the 2D iterative source verification cases, the largest error for α returned by the velocity analysis routine is 2.33%, occurring for the cambered thin aerofoil at $\alpha = 3^\circ$. The largest error for the returned relative velocity magnitude is 0.35%, found for the cambered aerofoil at $\alpha = 12^\circ$.

Overall, the results for the 2D stationary aerofoil simulations (both the constant source cases and the iterative source cases) are very promising. The trend is toward slightly larger errors for higher values of α, consistent with an error associated with the magnitude of C_l or Γ.

3.2.2 2D Aerofoil Moving at Constant Velocity

The ability of the velocity analysis routine to return accurate values of α and U_{rel} when $U_{rel} = U_\infty$ is verified in the 2D stationary aerofoil verification cases discussed above. In the stationary aerofoil simulations, the inertial reference frame was the same as the blade frame of reference. It is of interest to test the approach of transforming the sampling point velocity (which is returned by the CFD solver) from the inertial reference frame to the blade

frame of reference. For this verification test, the case of a 2D aerofoil moving through water with constant velocity is simulated.

The free stream velocity for this unsteady simulation is 8 m/s in the horizontal direction. A 2D symmetric thin aerofoil pitched at 6° above the horizontal is represented by a single collocation point which moves through the domain at a constant speed of 2 m/s in the direction of the chord line into the flow. It can be shown through vector mathematics that the resultant magnitude of the relative velocity for the present case is 9.991 m/s and $\alpha = 4.8°$.

The position of the collocation point is updated on the first iteration of each time step. In each iteration of the simulation, U_{rel} and α are calculated using the velocity analysis routine and the magnitude and direction of the force applied by the virtual aerofoil on the flow field are updated. Figure 3.7 shows the convergence of U_{rel} and α for the 2D aerofoil with constant velocity for grids with $e = c/4$ and $e = c/8$. The time steps used are 0.0625 s for the smaller grid and 0.1250 s for the larger grid. The values for U_{rel} and α after 12 seconds have errors of 0.03% and 1.06%, respectively, for the finer grid and 0.03% and 1.88%, respectively, for the larger grid.

A starting vortex is expected to develop when an aerofoil begins moving. The starting vortex must be present to satisfy conservation of angular momentum; its circulation counters that around the aerofoil. The starting vortex will be convected downstream at approximately the free stream flow speed (in this case, approximately 8 m/s). This starting vortex can be seen in Figure 3.8, which shows the vorticity field for the 2D aerofoil at time t = 1, 2, and 3 seconds for the $e = c/8$ mesh. The initial position of the aerofoil quarter-chord is (50, 20). In each second of the simulation, the aerofoil moves 2 m to the left at an angle of 6° to the horizontal and the starting vortex moves about 8 m downstream.

Values of U_{rel} and α returned by the velocity analysis routine for the 2D moving aerofoil are within 2% of the actual values, confirming that the velocity analysis routine accurately

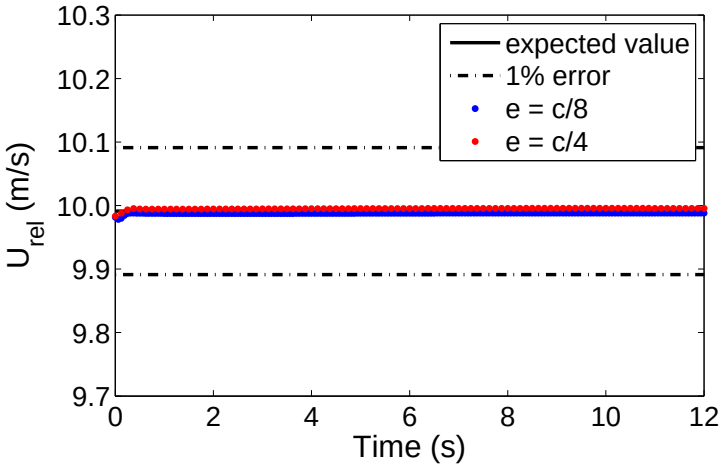

(a)

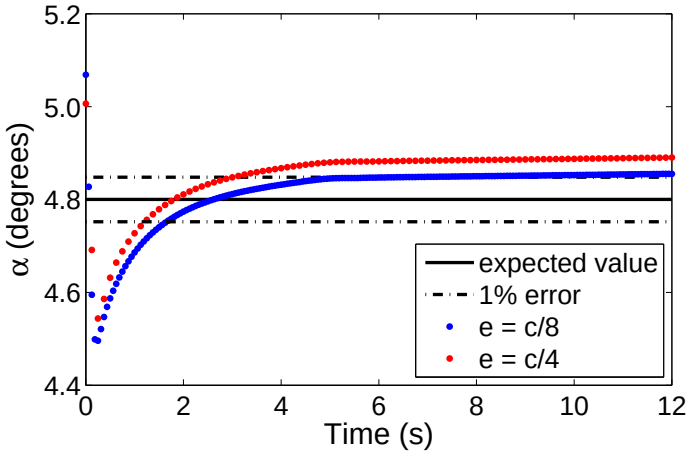

(b)

Figure 3.7: Convergence of U_{rel} and α for a 2D aerofoil with constant velocity.

determines the angle of attack and relative speed of a 2D aerofoil moving with constant velocity. Additionally, physical phenomena such as the starting vortex can be seen in the CFD results. Therefore, the concept of transforming the velocity to the blade frame prior to the use of Eqs. (3.3)-(3.5) has been verified.

3.2.3 3D Stationary Elliptic Wing

3D wings induce downwash, which changes the direction of $\mathbf{U}_{rel}$ and results in a reduced angle of attack, called the effective angle of attack, α_e. The goal of the final set of

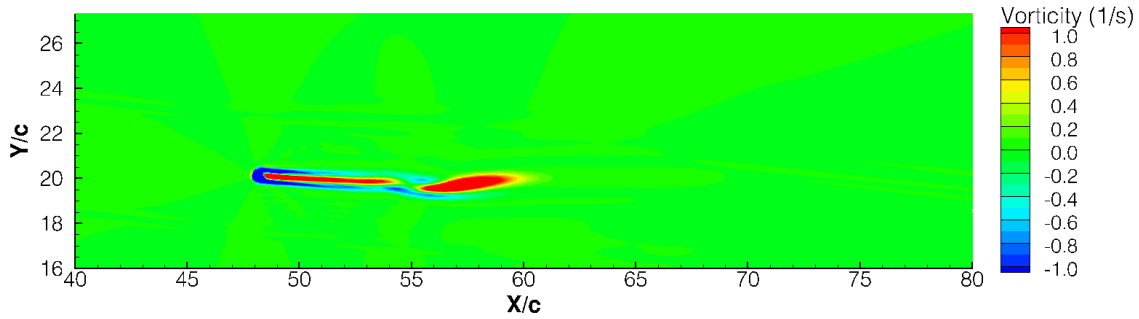

(a) t = 1s

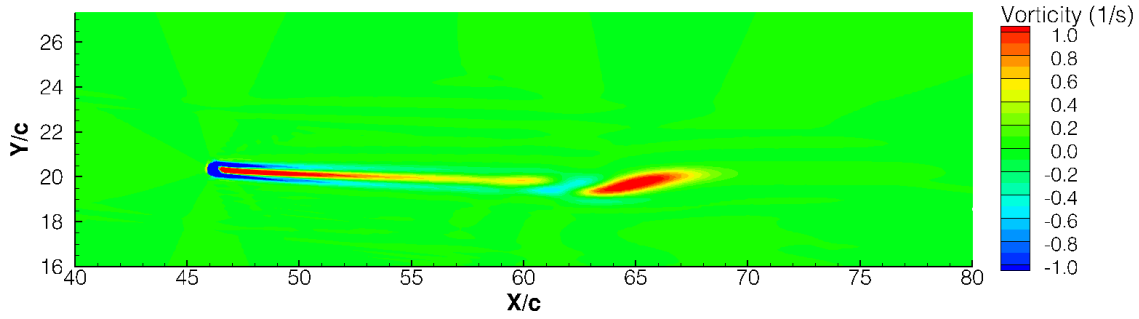

(b) t = 2s

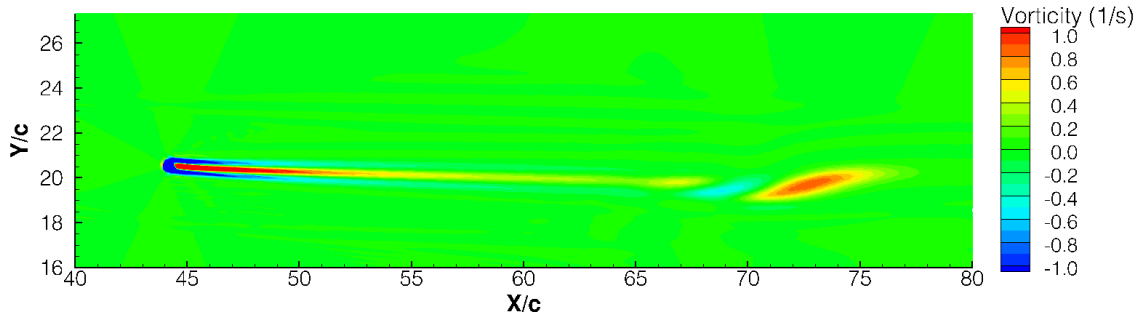

(c) t = 3s

Figure 3.8: Vorticity field for a 2D moving aerofoil at t = 1, 2, and 3s. The aerofoil is moving to the left and the starting vortex is convected to the right. The initial position of the aerofoil is (50, 20).

the velocity analysis routine verification simulations is to determine whether an actuator line simulation using the velocity analysis routine can accurately represent the the effects of downwash. An elliptic planform is used in this verification process because there is an analytical solution for the circulation distribution for an elliptic wing with specified geometry [65].

The dimensions of the simulated 3D wing are specified as $c_{root} = 1$ m for the root chord

and $s = 10 \cdot c_{root}$, or 10 m for the span. The surface area, S, of an elliptic wing is $\pi c_{root} s/4$ and the aspect ratio, AR, is s^2/S. Therefore, for the given wing, $S = 7.85$ m^2 and $AR = 12.73$. The wing is simulated using an actuator line consisting of 40 collocation points uniformly distributed along the wingspan, resulting in a spacing of $c_{root}/4$ between neighbouring collocation points. The described elliptic planform, with collocation points and corresponding blade segments indicated, is shown in Figure 3.9.

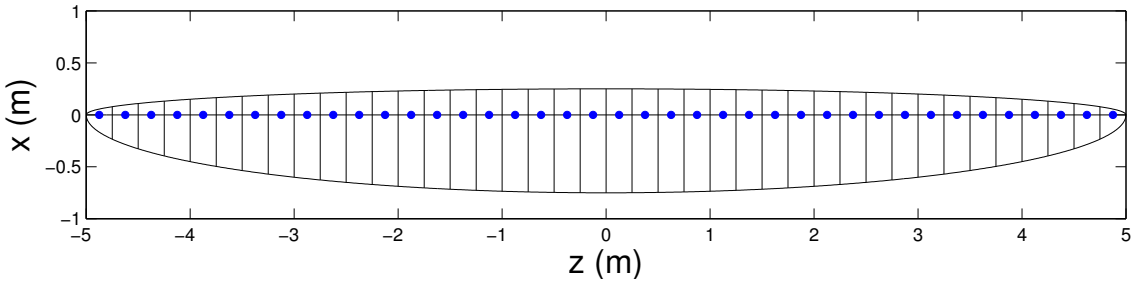

Figure 3.9: Elliptic wing planform used in the structured mesh elliptic wing simulations. The collocation points and corresponding blade segments are indicated.

The wing is held stationary in a domain extending $5s$ above and below the aerofoil, $5s$ in the positive and negative spanwise directions, $2s$ upstream, and $8s$ downstream of the wing. The computational domain used for the elliptic wing simulations is shown in Figure 3.10. A structured grid with a mesh element length $e = c_{root}/4$ near the wing is employed in this study. The wing span is orientated in the z-direction, while the wing chord is orientated in the x-direction; the inlet flow angle is thus equivalent to the wing attack angle. As in the 2D verification cases, the $k - \epsilon$ turbulence closure is employed.

The simulated wings are taken to be thin wings with sectional lift coefficient

$$C_l = C_{l_o} + 2\pi\alpha_e. \tag{3.7}$$

Both symmetric and cambered elliptic wings are simulated in the current study, with $C_{l_o} = 0.0$ for the symmetric wings and $C_{l_o} = 0.4$ for the cambered wings. The velocity sampling points are located at a distance of $r = c_{root} = 1$ m from the collocation points and α_e and

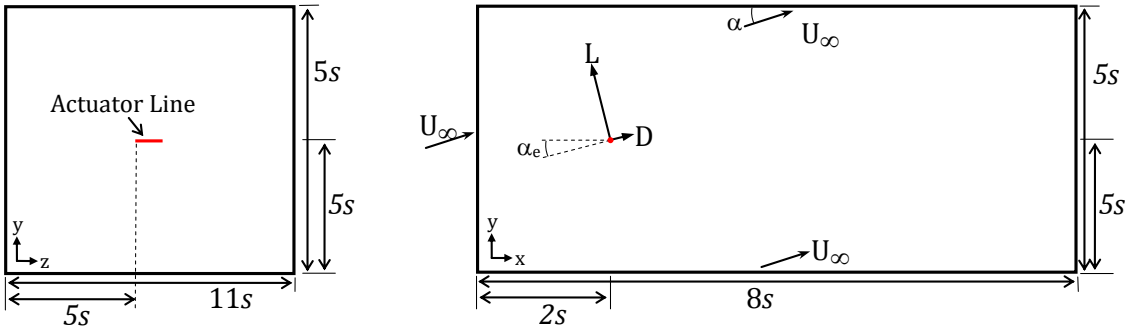

Figure 3.10: Domain for the velocity analysis routine verification simulations of an elliptic wing. The position of the actuator line is shown in red. Left: cross-section looking through the domain inlet; right: side-view.

U_{rel} for the 3D wing are returned by the velocity analysis routine during each iteration through solution of Eqs. 3.2a-3.2c on page 74. These values are used to calculate the lift of the blade section and hence the appropriate source to be applied at each collocation point. The steady-state solution is iterated until convergence is obtained with the wing's lift distribution in balance with the flow field, and the magnitude and direction of the applied sources are updated in each iteration.

The velocity analysis routine also returns the induced velocity perturbation, q, at a known radius, r, from each collocation point. The simulated circulation around each collocation point (in the plane of the blade element) is related to q by

$$\Gamma = 2\pi q r. \tag{3.8}$$

The analytical circulation distribution stems from Prandtl's lifting line theory [65]. From this theory, the circulation distribution for an elliptic wing spanning $-s/2 < z < s/2$ is given by

$$\Gamma(z) = \Gamma_{max}\left[1 - \left(\frac{z}{s/2}\right)^2\right]^{1/2}, \tag{3.9}$$

where Γ_{max} is the maximum circulation, occurring at $z = 0$. From lifting line theory, Γ_{max}

for an elliptic wing may be shown to be

$$\Gamma_{max} = \frac{2sU_\infty(\alpha - \alpha_{l_o})}{1 + AR/2}, \tag{3.10}$$

where α_{l_o} is the angle of zero lift for an aerofoil with camber and is a known property of the aerofoil.

Both air and water are used as working fluids, and uniform flow speed is employed as the boundary condition at the inlet, lid, and floor or the domain. Simulations are completed over a range of inlet flow speeds ($4 \leq U_\infty \leq 16$ m/s) and inlet flow angles ($3^\circ \leq \alpha \leq 12^\circ$, with respect to the x-axis). The side walls of the domain are slip walls, while, as in previous simulations, constant gauge pressure of 0 Pa is stipulated at the outlet.

The analytical circulation distribution, normalised by U_∞, is compared with the normalised circulation distribution from the actuator line results in Figure 3.11 for the elliptic wings at $\alpha = 3^\circ, 6^\circ, 9^\circ$, and 12°. Figure 3.11a shows the distribution for the symmetric aerofoil wing while Figure 3.11b shows the distribution for the cambered aerofoil wing. Because the solution for circulation does not depend on density or viscosity, the circulation distribution is the same for both air and water. Also, due to the linear relationship between $\Gamma(z)$ and U_∞, the results for Γ/U_∞ are independent of the upstream velocity. Therefore, the results for a given attack angle, when normalised by U_∞, should collapse onto a single curve, regardless of the inlet flow speed and simulated fluid. As expected, only one set of simulation results is visible for each attack angle in Figures 3.11a and 3.11b.

The error for the circulation at the wing mid-span ranges from 0.40% for the symmetric wing at $\alpha = 3^\circ$ to 3.96% for the cambered wing at $\alpha = 12^\circ$. Overall, the circulation distributions for the simulations compare very well to the analytical solutions.

Streamlines originating at the quarter-chord line of a 3D elliptic wing represented by an actuator line in water are shown in Figure 3.12. The wing presented here experiences

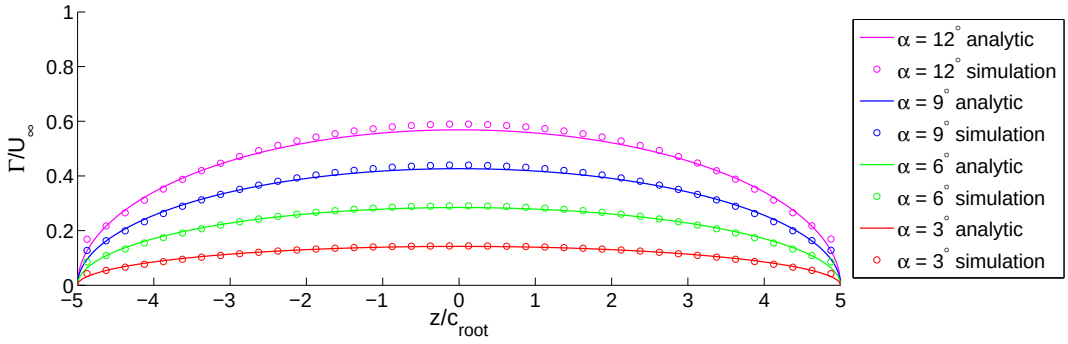

(a) Symmetric elliptic wing.

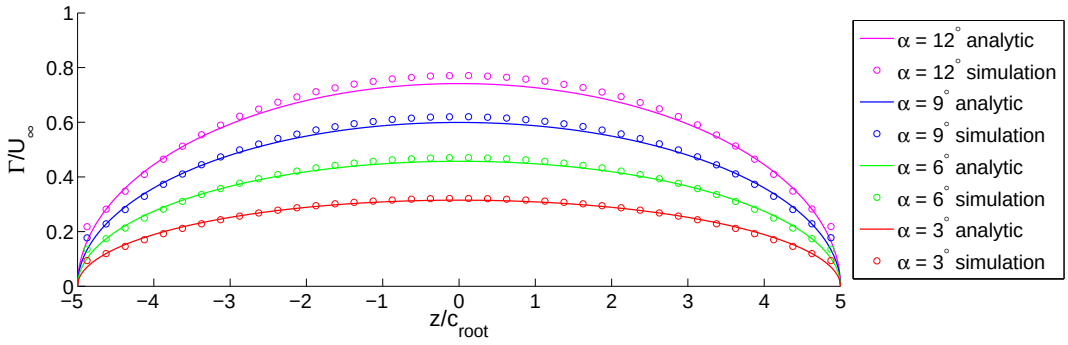

(b) Cambered elliptic wing with $C_{l_o} = 0.4$.

Figure 3.11: Circulation distribution for (a) symmetric and (b) cambered elliptic wing at $\alpha = 3°, 6°, 9°$, and $12°$. The simulations were computed using a structured mesh.

incoming flow at $\alpha = 12°$ and had $C_{l_0} = 0.4$ (this wing induces the greatest circulation of the wings considered in this study). The streamlines originate at the blade quarter-chord line, which is on the left of the figure. The streamlines are coloured according to streamwise vorticity (vorticity in the x-direction). The colouring shows that the wing-tip vortices are oriented in the appropriate directions, with the vortex trailing from the left side of the wing circulating in the clockwise direction (red) and the vortex trailing from the right side of the wing circulating in the anti-clockwise direction (blue).

The elliptic wing verification cases, performed on a structured grid, demonstrate that the actuator line method, coupled with the new velocity analysis routine, is capable of properly simulating the effects of a lifting surface on a flow. Specifically, they verify that the actuator line method is capable of correctly accounting for the influence of the induced downwash of 3D wings and of inducing the appropriate circulation in the flow.

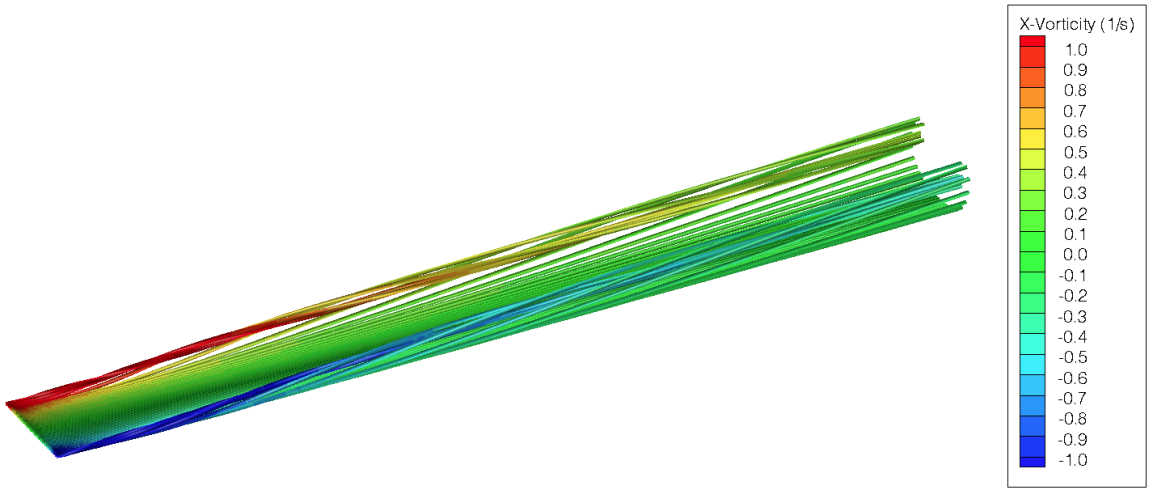

Figure 3.12: Streamlines for cambered 3D elliptic wing at $\alpha = 12°$.

3.3 Unstructured Mesh Implementation

It is desirable for the actuator line model to be adaptable to various mesh geometries, including unstructured tetrahedral meshes, which allow for turbine components such as the nacelle and tower to be directly represented using a body-fitted mesh.

ANSYS Fluent is a cell-centred solver and hence calculates the flow values at the cell centroids. On an unstructured mesh, the velocity sampling points and collocation points do not necessarily coincide with the cell centroids. Therefore, the magnitude and direction of the velocity at the velocity sampling points must be interpolated from surrounding cell centroids and similarly, the force at the collocation points must be distributed to the centroids surrounding each collocation point. Simply using the velocity at the centroid closest to the respective collocation point is insufficient as this provides a low order solution in which skew may occur. An improved approach is to apply a first-order approximation for velocity at a collocation point using both the velocity and velocity gradient at the nearest cell. This approach is used in the SOWFA (Simulator for Offshore Wind Farm Application) actuator line implementation in OpenFOAM [109], but the approach still does not prevent skew. To preserve accuracy it is important that the velocity is interpolated from and the

force is distributed to centroids on all sides of the velocity sampling point or collocation point (subsequently referred to as points of interest).

A simple but efficient method of selecting four centroids surrounding each point of interest is presented here. In a pre-processing step, the cell centroid coordinates from the existing mesh are extracted and used to create a secondary mesh through Delaunay triangulation using an external library, Qhull [110]. The triangulation results in a secondary mesh in which the cell centroids of the original mesh are the vertices of the newly triangulated mesh. This process is illustrated in 2D in Figure 3.13.

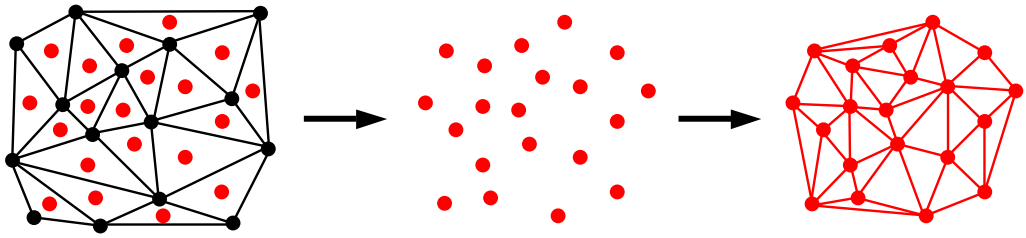

Figure 3.13: Creation of the secondary mesh using centroids of the original mesh (shown in 2D). The original mesh is black and the secondary mesh is red.

A jump and walk search algorithm [111] in the Qhull library is used to efficiently locate the cells of the secondary mesh that contain either a velocity sampling point or a collocation point. As the nodes of the secondary mesh are cell centroids in the true mesh, this search method quickly returns four cell centroids to be used for interpolation or force distribution.

The velocity at the velocity sampling points is interpolated from the four surrounding centroids using Shepard's inverse distance weighting method (IDW) [112]. In this method, the value of a property $G(x, y, z)$ is determined using the property values $g(x_i, y_i, z_i)$ at l scatter point locations. In the current work, $l = 4$ because the velocity is interpolated from the four nodes of a tetrahedra in the secondary mesh. Thus

$$G\left(x, y, z\right) = \sum_{i=1}^{l} w_i g_i \left(x_i, y_i, z_i\right), \tag{3.11}$$

where w_i describes the weight assigned to each value g_i and is defined as

$$w_i = \frac{{h_i}^{-p}}{\sum_{j=1}^{l} {h_j}^{-p}}. \tag{3.12}$$

h_i is the distance from the sampling point to the i^{th} scatter point. p is the power parameter and is taken to be 2 in the present work, as recommended by Shepard [112]. A larger value of p results in a higher influence on G from the closer scatter points.

The sum of the forces applied to the flow at the cell centroids, $\mathbf{f}_i(x_i, y_i, z_i)$, must be equal to the total force calculated for the corresponding actuator line collocation point, $\mathbf{F}(x, y, z)$:

$$\sum_{i=1}^{l} \mathbf{f}_i(x_i, y_i, z_i) = \mathbf{F}(x, y, z). \tag{3.13}$$

The total force for the blade element is the sum of the lift and drag forces and is found using Eqs. 2.17 and 2.18.

The force at each of the i surrounding centroids is determined using

$$\mathbf{f}_i(x_i, y_i, z_i) = \mathbf{F}(x, y, z) \frac{1}{h_i} \left(\sum_{j=1}^{l} \frac{1}{h_j} \right)^{-1}, \tag{3.14}$$

where h_i is the distance from the collocation point to the i^{th} centroid. Hence, the force applied is inversely proportional to the distance from the collocation point.

In the case where multiple sources are associated with the same cell, the sources are simply summed together prior to being applied to the governing equations.

3.3.1 Elliptic Wing Simulation On An Unstructured Mesh

The stationary elliptic wing verification case is repeated, this time using an unstructured tetrahedral mesh and the adaptation for unstructured meshes described above. The wing is of the same dimensions as the wing in Section 3.2.3 and the distribution of the 40

collocation points along the span is shown in Figure 3.14. This distribution varies from that used for the structured grid verification cases (shown in Figure 3.9); although the number of collocation points remains the same, a cosine distribution of the points is employed rather than a uniform distribution. The cosine distribution results in a higher concentration of collocation points at the tips of the wing and a lower concentration in the vicinity of the mid-span. This distribution is used in an effort to improve the results for the circulation distribution at the wing tips for the structured grid elliptic wing verification case (Figure 3.11); it is expected that the higher resolution of the actuator line at the blade tips will enable this improvement. Additional simulations were completed using 20, 30, 50, and 60 collocation points, with the results for circulation converging for wings simulated with 40 or more collocation points.

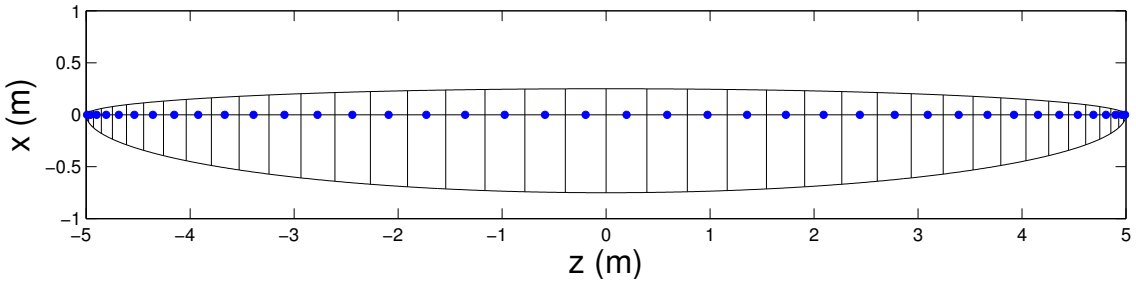

Figure 3.14: Elliptic wing planform used in the 3D unstructured mesh elliptic wing simulation. The collocation points and corresponding blade sections are indicated. A cosine distribution of the collocation points is implemented.

A cross-section of the unstructured mesh employed for the elliptic wing simulation is shown in Figure 3.15. The cross-section is in the wing plane and the position of the actuator line is indicated by the grey line. As the cross-section is cropped, it does not accurately represent the width or length of the computational domain. The fluid flows with uniform velocity from left to right, at angle α with respect to the horizontal axis. A mesh element length of approximately $c_{local}/4$ is used in the vicinity of the actuator line, in accordance with the findings of the 2D velocity field convergence analysis discussed in Section 3.1.1. The cells expand with a growth rate of 1.1 in the wake, and the resulting mesh consists of

roughly 1.7 x 10^6 elements. The velocity sampling points are located a distance of c_{local} from their respective collocation point.

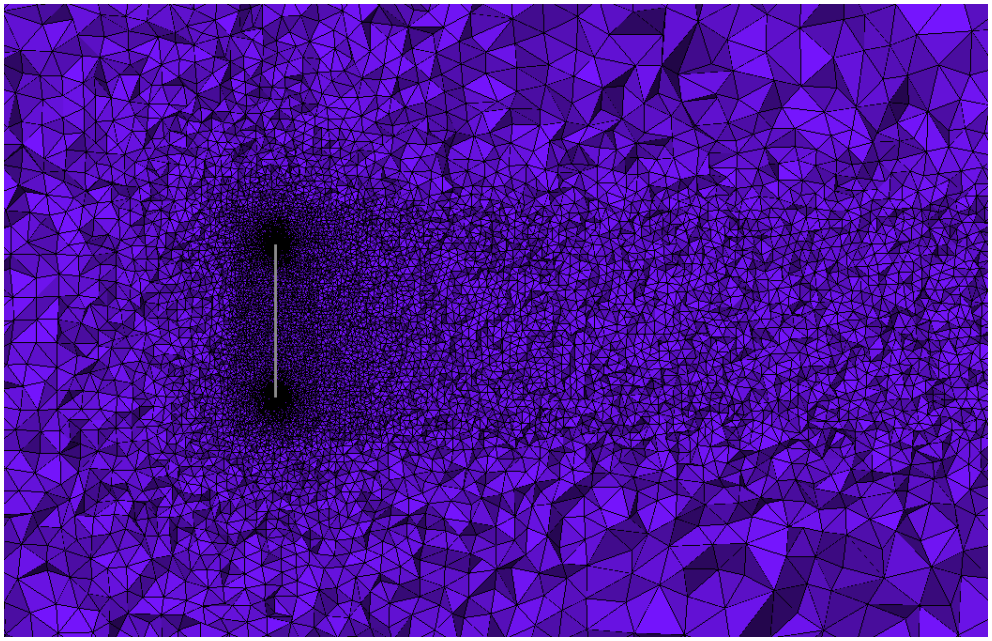

Figure 3.15: Cross-section at the wing plane of the unstructured mesh used for the elliptic wing verification case. The flow is from left to right and the position of the actuator line is indicated by the grey line.

Simulations of an elliptic wing using the unstructured mesh are presented for the highest circulation case from Section 3.2.3 (cambered wing with $\alpha = 12^\circ$) as this was the case with the highest error in the structured grid verification cases. The lift coefficient applied for the unstructured mesh simulation is the same as for the cambered wing in the structured grid simulations, $C_l = 0.4 + 2\pi\alpha$ (here, α is in radians). The spanwise circulation distribution, normalised by U_∞, for the elliptic wing simulated using the unstructured mesh at $\alpha = 12^\circ$ is shown in Figure 3.16. Both the analytical distribution as well as the actuator line simulation results are shown.

The percentage error over most of the wing span varies from less than 1% to 5.6%, with the error at the root 3.3%. Greater percentage error is seen at the wing tips, most likely due to the assumption in the analytical solution that the circulation at a spanwise blade station is planar, while in the simulation there is flow along the span of the blade as well.

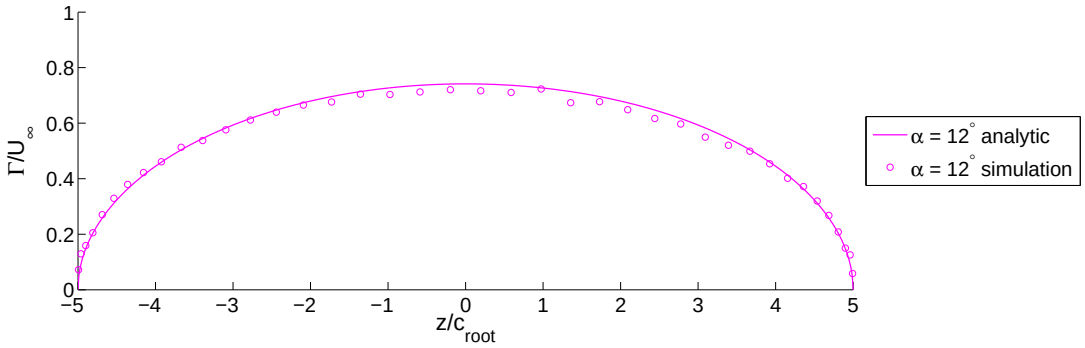

Figure 3.16: Circulation distribution for cambered elliptic wing at $\alpha = 12°$. An unstructured mesh is utilised in the simulation.

Still, the absolute error at the tips is small due to the very low values of circulation in these regions. It is also noted that the circulation distribution in the vicinity of the blade tips is much improved over the results from the structured grid simulation, which used a uniform collocation point distribution. This is due to the higher concentration of the actuator line collocation points in the blade tip regions when the cosine distribution is employed.

The results of the current cambered elliptic wing simulation confirm that the actuator line method and accompanying velocity analysis routine have been successfully adapted for unstructured grids.

The results in Section 3.1.1 provide useful information regarding the required mesh resolution for actuator line simulations; it has been determined that a grid element length of $c/4$ is appropriate. However, while this addresses the required resolution in the plane of the blade elements, it does not address the required mesh element length in the radial direction, along the actuator line. In the unstructured mesh simulation of an elliptic wing, a spatial resolution of roughly $e = c/4$ is used in the radial direction of the blade and 40 collocation points are employed to resolve the actuator line. However, the appropriate mesh resolution in the radial direction, as well as the appropriate resolution of the actuator line (these two resolutions are interdependent), may be affected by the specific geometry of the simulated blade. Therefore, the mesh resolution in the radial direction and number of

collocation points in the actuator lines should be determined separately for different blade geometries.

3.4 3D Unsteady Actuator Line Model Overview and Implementation

A 3D unsteady actuator line model, with the velocity analysis routine and unstructured mesh adaptation included, is embedded within the CFD solver ANSYS Fluent. A flowchart of the embedded 3D unsteady actuator line model with the velocity analysis routine is presented in this section. The individual steps of the model are also discussed.

3.4.1 Actuator Line Model Implementation

The 3D unsteady actuator line model implemented in this work is capable of simulating multiple horizontal-axis axial turbines of specified blade geometry. The orientation of each rotor (i.e. axis of rotation and direction of rotation) and the number of blades per rotor are set by the user. The unstructured mesh adaptation allows turbine components, such as nacelles and towers, to be explicitly included in the computational domain.

A flowchart outlining the actuator line model procedure is included in Figure 3.17. The blue boxes are the main steps of the actuator line model and the red ellipses are inputs and outputs. The steps contained within the green dashed box are performed during a single iteration, while the purple dashed box contains the steps that are repeated for each time step. The steps of the actuator line model, as outlined in Figure 3.17, are discussed in further detail in the remainder of this section.

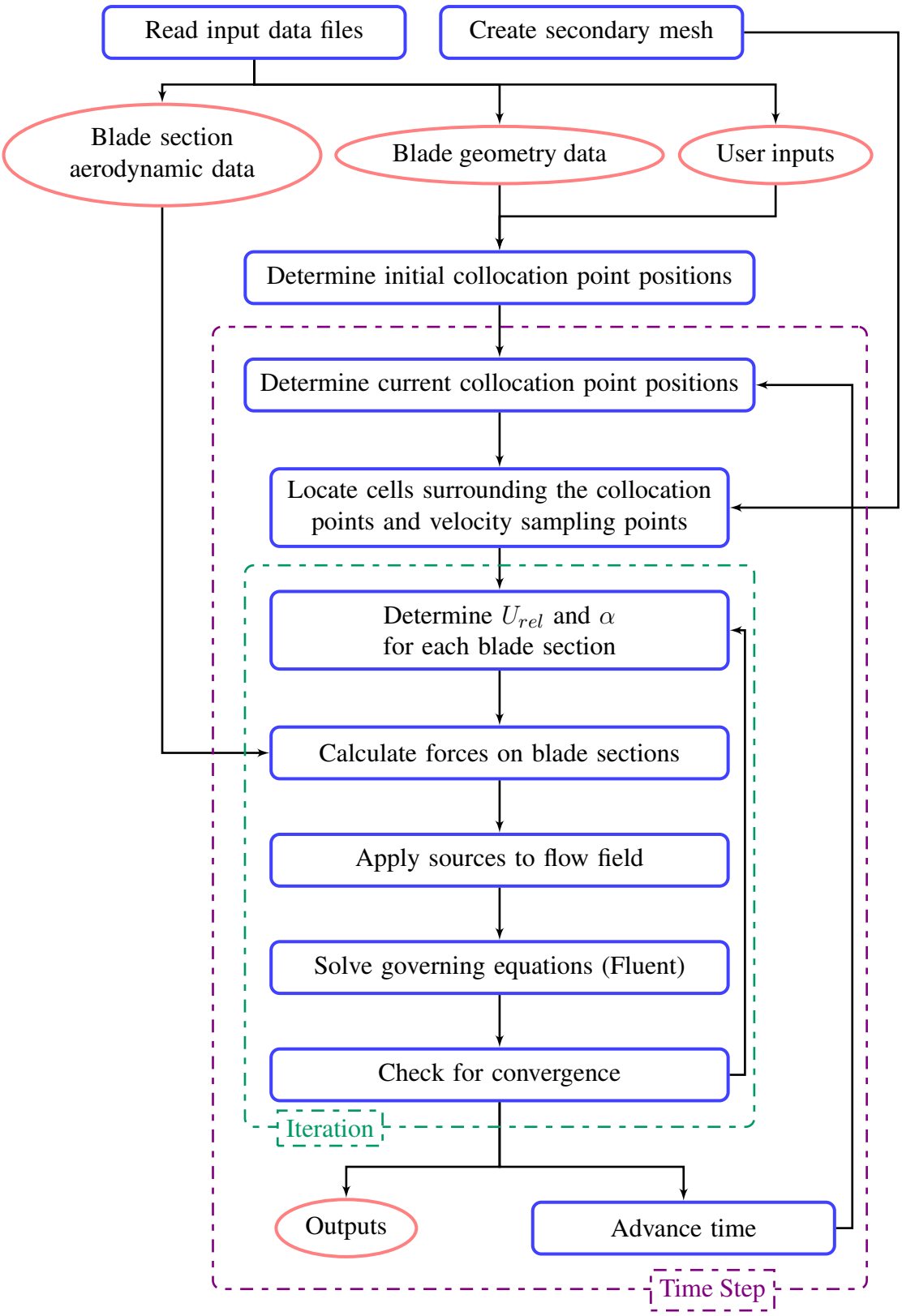

Figure 3.17: Actuator line model schematic.

Create Secondary Mesh

A secondary mesh is created using Delaunay triangulation, as discussed in Section 3.3.1. The centroids of the original mesh are the nodes of this secondary mesh. This step is completed only once during each simulation, as a pre-processing step.

Read Input Data Files

The actuator line model employed in the current study requires three input files for each rotor to be simulated. These are detailed below.

- **User inputs:** This file contains user-defined information including parameters required to determine the initial position of the rotor along with various numerical parameters including discretisation specifications. This information includes the number of rotor blades, the number of collocation points per blade, the initial locations of the endpoints of a single blade, the location of the rotor hub, the direction of rotation, and the axis of rotation. This file also includes the reference flow speed and the desired tip speed ratio, which are used to calculate the appropriate angular velocity of the blades.
- **Blade geometry data:** This file is used to define the geometry of the blades. Chord and pitch values are tabulated in this file as a function of the blade radius.
- **Blade section aerodynamic data:** This file includes tabulated data for the lift and drag coefficients of the selected aerofoil as a function of the angle of attack, α. If sufficient data is available, this data is listed for a range of Reynolds numbers.

Determine Initial Collocation Point Positions

The initial positions of the collocation points for each blade are determined in a pre-processing step at the beginning of each simulation. First, the blade span and desired number of collocation points (defined in the user input file) are utilised to determine the

location of each collocation point on a single blade for each rotor. These collocation points define the quarter-chord line of the first blade. The data from the blade geometry input file is then interpolated to find the chord, c, and pitch, β, of the blade at each of the collocation points. The vectors defining the position of the first blade of each rotor are then rotated about the respective rotor's rotation axis to determine the initial positions of the collocation points for the remaining blades.

Determine Current Collocation Point Positions

The current positions of the collocation points for each rotor are calculated in the first iteration of each time step. In order to determine the collocation point position at a given time, the angle of rotation, θ, must first be calculated. For a non-accelerating rotor, θ is

$$\theta = \Omega t, \tag{3.15}$$

where t is time. Ω is the angular velocity, defined as

$$\Omega = \frac{\lambda U_{ref}}{R}, \tag{3.16}$$

where λ is the tip speed ratio, U_{ref} is the reference flow speed, and R is the turbine radius (all defined in the user inputs file). The vectors defining the initial position of the collocation points for each rotor blade are rotated about the respective rotor's axis of rotation by the appropriate angle θ for the current time step.

Locate Cells Surrounding the Collocation Points and Velocity Sampling Points

The indices of the cells surrounding the collocation points and velocity sampling points are found for the current position of each rotor using the unstructured mesh adaptation discussed in Section 3.3. This step is performed only in the first iteration of each time step.

Determine U_{rel} and α for Each Blade Section

The magnitude of the relative velocity and the corresponding angle of attack are determined using the velocity analysis routine introduced in Section 3.1.2, coupled with the unstructured mesh adaptation presented in Section 3.3.

Calculate Forces on Blade Sections

The magnitudes of the lift and drag forces on each blade segment are calculated using Eqs. 2.17 and 2.18. Of the variables in these equations, the fluid density, ρ, the magnitude of the relative velocity, U_{rel}, the chord, c, and the spanwise width, δr, of each blade section are known at this point of the iteration. C_l and C_d for a given blade section are determined by interpolating aerodynamic data, which is tabulated as a function of α and Re.

The directions of **L** and **D** for a blade section are shown in Figure 3.18. The direction of **D** (which is the same as that of $\mathbf{U}_{rel}$) is found using α and the known chord vector. The direction of **L** is a result of the cross-product of **D** and the blade quarter-chord line. The sum of **L** and **D** gives the vector that represents the total force on the blade section, **F**.

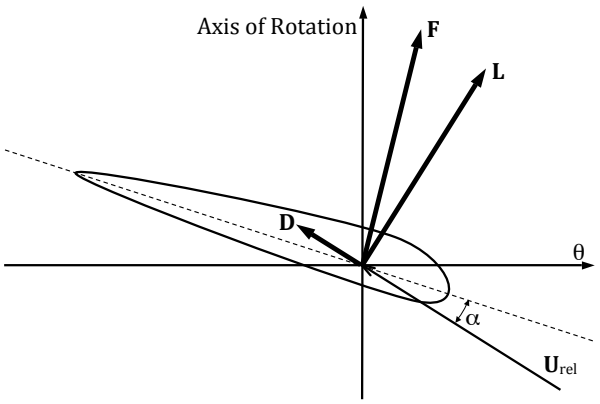

Figure 3.18: Directions of the aerodynamic forces on a rotor blade element. The blade quarter-chord line is perpendicular to the page.

Apply Momentum Sources

The force the blade applies to the fluid is equal and opposite to the force the fluid applies to the blade. The influence of the blades on the flow is included in the simulation by the introduction of source terms in the discretised conservation of momentum equations. The x-, y-, and z-forces for each blade segment are distributed and applied at 4 cell centroids, as described in Section 3.3. ANSYS Fluent requires momentum equation sources to have units N/m^3; thus, the sources passed to the flow solver are computed by dividing the force applied to each cell by the volume of the respective cell.

Check for Convergence

In this step, solver residuals (i.e. the continuity, momentum, and turbulence closure residuals) and the flow characteristic residuals (i.e. the relative velocity and angle of attack residuals), are evaluated. If each of the solver and flow characteristic residuals are lower than the user-set criteria, the solution advances to the next time step. If the convergence criteria are not met, a further iteration at the current time step is computed.

Advance Time

The simulation time is advanced by Fluent when the solution for the current time step is sufficiently converged. The size of the time step is user-defined.

Outputs

The outputs of the model are selected based on the goals of a given simulation. The outputs may include (but are not limited to) integrated blade loads, such as torque and thrust, and radially distributed loads, such as local force coefficients. Desired outputs are written to a series of .txt files at the end of each time step.

3.5 Conclusions

A method for determining the relative flow speed and direction at the blade segments in actuator line model simulations has been introduced and verified in this chapter. The method is based on potential flow equivalence and, unlike the methods used in previous actuator line implementations, does not require the use of a regularisation kernel.

The potential flow equivalence method has been verified for both 2D and 3D aerofoils. It has been demonstrated to be capable of returning accurate values for relative velocity and angle of attack for 2D aerofoils. In addition, it has been shown that the actuator line implementation with the new flow analysis routine is able to correctly account for the influence of induced downwash and accurately compute the circulation for a 3D elliptic wing.

Finally, the actuator line method, with the velocity analysis routine and as well as an unstructured grid adaptation, has been implemented in a 3D unsteady flow solver, ANSYS Fluent.

Chapter 4

Model Validation

The actuator line model, including the flow analysis routine introduced in Section 3.1.2 and adapted for use with unstructured grids as discussed in Section 3.3, has been validated using experimental data from the NREL/NASA Ames Phase VI wind tunnel tests. The following chapter includes details of the experimental tests, a brief review of NREL Phase VI CFD validation studies selected for comparison, an outline of the computational domain and resolution parameters used in the current model validation, and a discussion of the actuator line computational results.

4.1 NREL Phase VI Wind Tunnel Experiments

The NREL Phase VI series of experimental wind turbine tests was carried out by researchers from the United States National Renewable Energy Laboratory (NREL) at the NASA Ames Research Center in California, USA in 2000 [113]. The Phase VI experimental results are commonly used in the wind energy industry for computational model validation. The NREL Phase VI experimental results were selected for the current validation because at the time the study was undertaken, there was not sufficient publicly available experimental data to complete a validation study using a tidal turbine.

The Phase VI experiments were performed using a two-bladed, 10.058 m diameter horizontal-axis rotor [114, 113]. The NREL S809 aerofoil section is used from $0.25R$ to the blade tip (R is the rotor radius). An S809 aerofoil section is shown in Figure 4.1. The blades had nonlinear twist and the chord tapered linearly from 0.737 m at the root to 0.355 m at the tip. Further details of the rotor geometry can be found in reference [114].

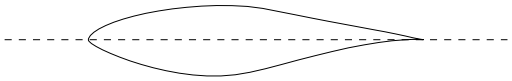

Figure 4.1: S809 aerofoil section.

The NASA Ames wind tunnel test section was 24.4 m tall by 36.6 m wide. The hub of the turbine was 12.2 m above the floor of the test section. The tower diameter was 0.61 m at the base and 0.41 m at the top. The wind turbine used in the experiments is shown in Figure 4.2.

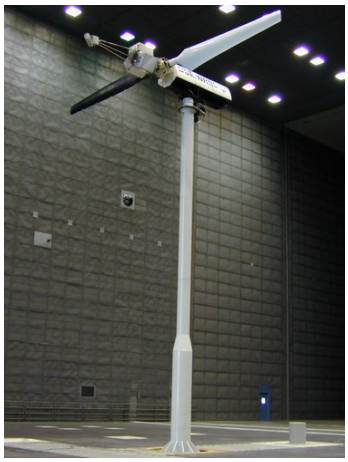

Figure 4.2: Wind turbine used in the NREL Phase VI wind tunnel experiments. [115].

The rotor was equipped with pressure taps at 5 radial blade stations, $0.300R$, $0.466R$, $0.633R$, $0.800R$, and $0.950R$. This instrumentation allowed for the tangential force coefficient, C_t (in the direction of the blade chord), and the normal force coefficient, C_n (perpendicular to the blade chord in the plane of the 2D blade element) to be determined at each of the stations.

A number of CFD validation studies have compared computed results with results from the S sequence of the NREL Phase VI experiments. In the S sequence configuration, the rotor was in an upwind position and the blade tip pitch was 3° towards feather. The rotor cone angle was set at 0° and, for the experiments selected for comparison, the yaw angle was 0°. Experiments were performed at wind speeds ranging from 5 m/s to 25 m/s. The turbine operated at a constant 72 rotations per minute (RPM), resulting in a range of tip speed ratios.

4.2 NREL Phase VI Validation Studies Selected for Comparison

Sørensen et al. [93], Mahu and Popescu [94], and Gómez-Iradi et al. [116], among others, have published studies comparing results from 3D blade-resolved turbine simulations with the NREL S Sequence experimental data. Sørensen et al. applied a 3D RANS solver to model the NREL/NASA Ames wind tunnel tests for flow speeds ranging from 7 to 25 m/s [93]. Two sets of simulations were performed. The first set employed a free rotor configuration, in which blockage effects due to the wind tunnel walls were not included, and was used in the NREL blind comparison for the Phase VI experiments. The second series of simulations was performed following the release of the blind comparison results. In this series, a cylindrical approximation of the rectangular wind tunnel section was used in an effort to include the tunnel blockage effects. The Sørensen et al. results shown in plots in Section 4.4 are results from the tunnel configuration. These simulations used a semi-cylindrical domain with periodic boundary conditions to reduce computation time. Although the rotor blades were explicitly modelled in the computations performed by Sørensen et al., the turbine tower was not included. An inner cylindrical face, extending from the domain inlet to outlet, was included to account for the presence of the nacelle. The $k-\omega$ shear stress transport (SST) turbulence model was used in this work.

Mahu and Popescu modelled the NREL Phase VI rotor in wind speeds ranging from 7 to 15 m/s [94]. A half-cylinder domain with periodic boundary conditions was used in these investigations. The configuration was similar to the half-cylinder configuration used by Sørensen et al.; the turbine tower was not included in the model and the centre of the tunnel was hollow to account for the nacelle's presence. Unlike the simulations by Sørensen et al., however, no attempt was made to mimic the effect of blockage in the wind tunnel. The $k-\omega$ SST turbulence model was employed in Mahu and Popescu's study.

Gómez-Iradi et al. utilised a cylindrical domain to validate 3D blade-resolved CFD calculations for wind speeds 7, 10, and 20 m/s [116, 117]. The nacelle and tower were not included in this domain. Subsequent computations were performed with the nacelle and tower included in the domain but these were limited to the pre-stall $U_\infty = 7$ m/s case.

The resulting values for shaft torque in the 3D blade-resolved simulations discussed above compared favourably to the NREL Phase VI experimental results for attached flow and low-stall cases, but the error increased for the deep-stall simulations. This is most likely related to the limitations of RANS models with regard to modelling flow separation.

In addition to the 3D blade-resolved validation studies, BEM and vortex method validation studies utilising the NREL Phase VI results have also been performed. Tangler [118], for example, compared results using BEM and vortex panel methods for wind speeds 7, 10, and 13 m/s. Cosine distributions of the radial blade segments were used for both of these methods. This distribution allowed for greater accuracy in the root and tip regions than a uniform distribution would provide. Still, Tangler's results over-predicted the normal force coefficients at the blade tips. In addition, although the normal force coefficient for the attached flow case ($U_\infty = 7$ m/s) was in agreement with the experimental results at the blade root, notable under-prediction of the normal force coefficients was observed at the blade roots for the stall onset and low-stall cases ($U_\infty = 7$ and 10 m/s, respectively).

Tangler postulated that the inclusion of a stall delay model would have improved these results.

Jha et al. compared actuator line simulation results to Phase VI experimental wind tunnel results, but simulations of a moving rotor were limited to the $U_\infty = 7$ m/s case [74]. These actuator line results were similar to the BEM results of Tangler et al., also experiencing over-prediction of the normal force coefficient at the blade tips. The error was reduced when a Prandtl correction (with Glauert's formulation [45]) was employed, however, as noted by the authors, this correction, which accounts for discrete blade effects, should not be necessary in 3D unsteady CFD simulations, suggesting that more work in this area is required.

4.3 Computational Domain and Simulation Conditions

Sequence S of the Phase VI wind tunnel testing was selected for the actuator line model validation because this configuration allowed for comparisons with both experimental results as well as the computational results from the studies discussed above. Both experimental and computational results were available for several integrated quantities. These include shaft torque (Q) and root flap and root edge bending moments (denoted by RFM and REM). In addition to the integrated quantities, experimental results for the spanwise distributions of the normal and tangential force coefficients (C_n and C_t) at five radial locations were utilised for comparison.

Six different steady wind speeds are used in the actuator line model validation: $U_\infty = 7$, 10, 13, 15, 20, and 25 m/s. These wind speeds are consistent with the speeds simulated in the 3D blade-resolved validation studies discussed in Section 4.2, allowing for a direct comparison of results. The test conditions for each of the selected experimental runs are outlined in Table 4.1.

The computational domain extends $3R$ (15.1 m) upstream and $6R$ (30.2 m) downstream

Table 4.1: Test conditions for selected validation cases.

NREL Run	Wind Speed (m/s)	RPM	ρ (kg/m^3)	μ (kg/(m·s))	Tip speed ratio, λ
S070000	7.0	71.9	1.246	1.769 x 10^{-5}	5.41
S100000	10.0	72.1	1.246	1.769 x 10^{-5}	3.80
S130000	13.0	72.1	1.227	1.781 x 10^{-5}	2.92
S150000	15.1	72.1	1.224	1.784 x 10^{-5}	2.51
S200000	20.1	72.0	1.221	1.786 x 10^{-5}	1.89
S250000	25.1	72.1	1.220	1.785 x 10^{-5}	1.51

of the rotor plane. The cross section is 24.4 m high and 36.6 m wide, in accordance with the wind tunnel dimensions. The turbine tower and a simplified nacelle are included via a body-fitted mesh with the nacelle at the tunnel centreline, 12.2 m above the wind tunnel floor. The computational domain is shown in Figure 4.3. The inlet boundary condition is uniform velocity, U_∞. The wind tunnel test section turbulence intensity is less than 0.5% [119]; no onset turbulence is modelled in the current wind tunnel simulations (both RANS and LES). The outlet is a pressure outlet with constant gauge pressure set to 0 Pa. Slip conditions are applied at the side walls, floor, and lid of the domain, while no-slip walls are utilised on the surfaces of the turbine tower and nacelle.

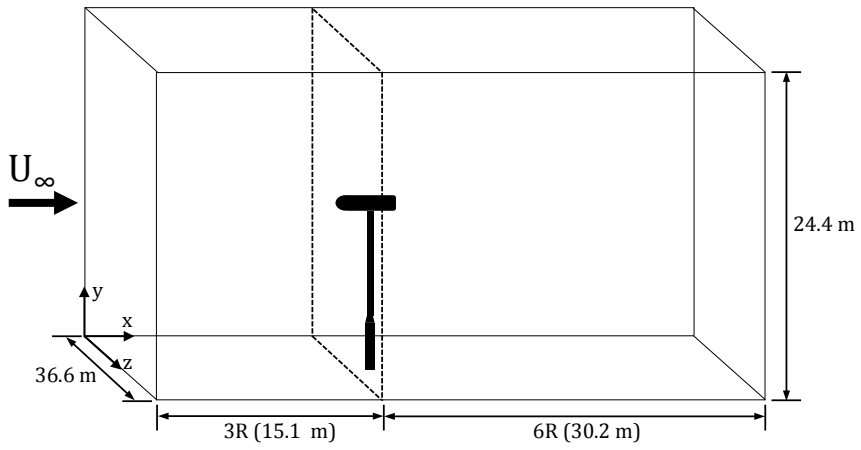

Figure 4.3: Simulation domain. The flow travels from left to right. The turbine tower and a simplified nacelle are resolved in the domain. The domain extends $3R$ upstream of the rotor plane, which is indicated in the figure by the dashed lines.

The mesh for the validation simulations consists of 1.35 x 10^6 tetrahedral cells. This mesh was selected following a mesh resolution study (discussed in Section 4.4.1). For

comparison, the 3D blade-resolved simulations of the NREL Phase VI rotor, discussed in Section 4.2, utilise meshes with cell counts ranging from 3.4 x 10^6 to 11.3 x 10^6.

The SIMPLE algorithm was used for pressure-velocity coupling, with a second-order upwind discretisation scheme used to discretise the convective terms of the momentum equations. The diffusion terms were discretised using a second-order accurate central differencing scheme. A $k-\omega$ SST turbulence closure was used, though a comparison of RANS $k-\omega$ SST results with results using a large eddy simulation (LES) model is presented following the validation results.

4.3.1 Aerodynamic Data

The actuator line method is reliant on accurate and complete aerodynamic data for the relevant aerofoil. The required data includes lift and drag coefficients as a function of the angle of attack and Reynold's number. The Reynolds numbers for the current validation simulations are calculated for each blade segment during every iteration. Values for Re for the selected cases fall in the range of 6.0 x 10^5 to 1.4 x 10^6.

Experimental wind tunnel results for the aerodynamic coefficients of the S809 aerofoil as a function of α are available for $Re =$ 3.0 x 10^5, 5.0 x 10^5, 6.5 x 10^5, 7.5 x 10^5, and 1.0 x 10^6 [114]. C_l and C_d data for the three lowest Reynolds numbers are available from Colorado State University (CSU) experiments for $\alpha = 0^\circ$ to $\alpha = 90^\circ$. Wind tunnel experiments at Ohio State University (OSU) provide data from $-20^\circ < \alpha < 26^\circ$ for Reynolds numbers 7.5 x 10^5 and 1.0 x 10^6. Additional wind tunnel data was obtained at Delft University of Technology (DUT) for $Re =$ 1.0 x 10^6 over the range $-1^\circ < \alpha < 20^\circ$. The DUT wind tunnel data was the data used for $Re =$ 1.0 x 10^6 in the present study.

In the NREL Phase VI actuator line validation simulations C_l and C_d for a given α and Reynolds number are linearly interpolated from the values for the available Reynolds numbers. In cases where $Re >$ 1.0 x 10^6, coefficients for $Re =$ 1.0 x 10^6 are used. For the

validation cases with $U_\infty \geq 10$ m/s, α exceeds the maximum experimental α for $Re = 1.0$ x 10^6, 20°, at some or all of the collocation points. Therefore, the available angle of attack range given by the experimental aerodynamic data is insufficient.

It is assumed that the aerodynamic coefficients for the range of Reynolds numbers converge onto the same curve in the post-stall region. This assumption is based on Ostowari and Naik's findings that the aerodynamic coefficients of NACA 44-series aerofoils were insensitive to Reynolds number effects in the post-stall region [120]. The CSU (lower Reynolds number) data was therefore averaged over the range $45^\circ < \alpha < 90^\circ$ and the averaged values of C_l and C_d over this range were used for all Reynolds numbers. Following this approximation, gaps remained in the aerodynamic data from $26^\circ < \alpha < 45^\circ$ for $Re = 7.5$ x 10^5 and from $20^\circ < \alpha < 45^\circ$ for $Re = 1.0$ x 10^6. Polynomial fits were used to fill these gaps for both the C_l and C_d data.

The experimental and modified lift and drag coefficients are presented in Figure 4.4. The coloured symbols represent experimental data. The solid black line depicts the average of the three CSU data sets for $45^\circ < \alpha < 90^\circ$. The dashed coloured lines represent the interpolated data from $26^\circ < \alpha < 45^\circ$ for $Re = 7.5$ x 10^5 and from $20^\circ < \alpha < 45^\circ$ for $Re = 1.0$ x 10^6.

Correction for 3D Tip Flow Effects

2D data are used for the aerodynamic coefficients because blade element theory (Section 2.2.1) assumes that the forces on each blade segment are 2D in the plane of the element and result from the component of relative flow velocity in that plane. This assumption is considered acceptable over most of the blade span but is inaccurate and can lead to errors at the blade tips, where there is significant flow in the spanwise direction as well as greater rotational effects. A tip correction that accounts for the 3D rotational effects was introduced by Shen et al. and is applied to the 2D aerodynamic data in the present validation study

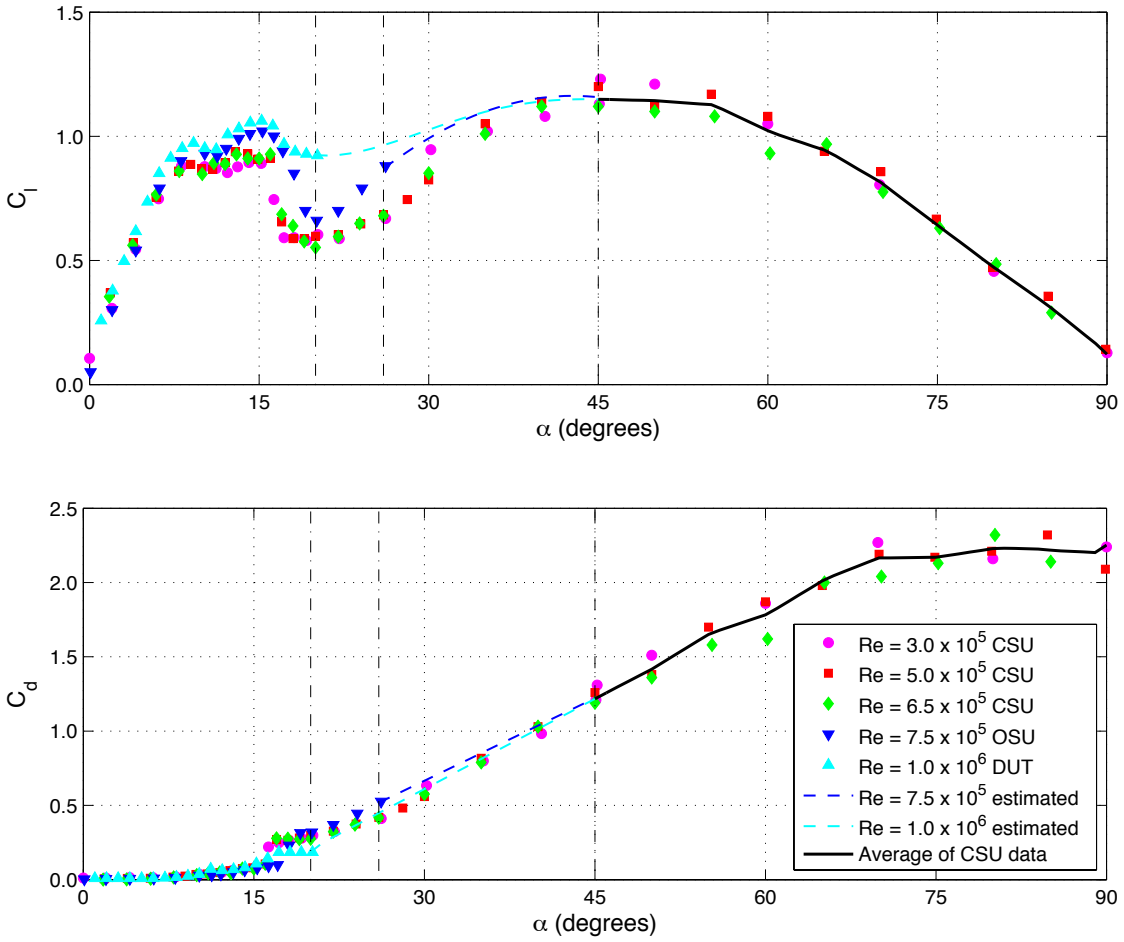

Figure 4.4: S809 aerofoil C_l (top) and C_d (bottom) data. The coloured symbols represent experimental data. The solid black lines depict data averaged over the three lowest Reynolds numbers for $45° < \alpha < 90°$. The dashed coloured lines depict the polynomial fits used to estimate data from $26° < \alpha < 45°$ for $Re = 7.5$ x 10^5 and from $20° < \alpha < 45°$ for $Re = 1.0$ x 10^6.

[121]. This correction has also been used in previous BEM and actuator line model studies of wind turbines [73]. The correction factor, f_1, is a function of the blade segment radius, r:

$$f_1(r) = \frac{2}{\pi} cos^{-1}\left[exp\left(-g_1 \frac{N(R-r)}{2rsin\phi}\right)\right], \tag{4.1}$$

where N is the number of rotor blades, R is the rotor radius, and ϕ is the angle between the local relative velocity vector, $\mathbf{U}_{rel}$, and the rotor plane. g_1 is defined as

$$g_1 = exp[-c_1(b\lambda - c_2)] + 0.1, \tag{4.2}$$

where λ is the tip speed ratio. From experimental wind turbine data at two different tip speed ratios ($\lambda = 3.79$ and $\lambda = 14$), Shen et al. determined that $c_1 = 0.125$ and $c_2 = 21$. Due to the use of experimental constants, the tip correction used is case specific and not a general correction. For this reason, it is expected that it will not be capable of fully correcting for tip effects in the current validation study.

4.4 Actuator Line Model Results

The results of the actuator line model simulations of the NREL Phase VI wind tunnel experiments will be presented in this section. First, a detailed description of the mesh resolution study will be given. Time resolution and convergence to the steady operational state will also be discussed. Next, the results for the integrated loads will be presented. Finally, the spanwise force distribution results will be reviewed.

4.4.1 Resolution Studies

Resolution studies were undertaken to determine the appropriate mesh size and time resolution as well as the number of rotor revolutions required for convergence to the steady operational state. Steady operational state in the current work occurs when revolution to revolution convergence has been reached. The 3D tip correction presented in Section 4.3.1 was not included in the actuator line model for the resolution studies, thus resulting in different values than those presented in Sections 4.4.2 and 4.4.3. However, it is the relative change in loads, not the magnitude of the loads, that is most relevant in the following resolution studies.

Spatial Resolution

A spatial resolution study was carried out to determine the appropriate mesh element size at the rotor plane as well as in the wake. The rotor torque and root flap bending moment were compared for simulations using four different meshes. In addition, centreline wake velocity deficit profiles were plotted at distances of $1R$, $2R$, $3R$, $4R$, and $5R$ downstream of the rotor for each of the meshes. All of the profiles include time-averaged results from revolutions after the solution has reached revolution to revolution convergence.

Four meshes were developed using two different values of the rotor plane element size as a function of chord and different element dimensions in the wake region. The first rotor plane element size, used in Meshes 1 and 3, required cells to be of element edge length $e \approx c_{local}/4$ at the rotor (c_{local} is the local aerofoil chord). This is in accordance with the findings of the 2D flow field analysis discussed in Section 3.1.1, which indicated that a mesh element edge length of $c/4$ is appropriate for the actuator line method. Therefore, as the radius increases and the chord decreases, the cell size decreases. This method resulted in cells of element edge length $e \approx 0.18$ m at the blade roots and $e \approx 0.09$ m at the tips where the chord is smaller. A cross-section at the rotor plane of a mesh created following these criteria is shown in Figure 4.5. In the second rotor plane mesh (Figure 4.6), used in Meshes 2 and 4, all cells in the vicinity of the rotor were ascribed element edge length $e = 0.25$ m. This criteria resulted in $e_{tip} \approx 0.7c_{tip}$ and $e_{root} \approx 0.34c_{root}$.

In addition, two criteria were used to develop the mesh in the rotor wake. The first constrains the elements to increase in size at a growth rate of 1.1 from the rotor plane to a maximum element edge length $e = 1.00$ m (Meshes 1 and 2). For the second, cells in the rotor wake have a maximum size of $e = 0.25$ m (Meshes 3 and 4).

The spatial resolution study was undertaken for the $U_\infty = 7$ m/s case. 300 time steps were

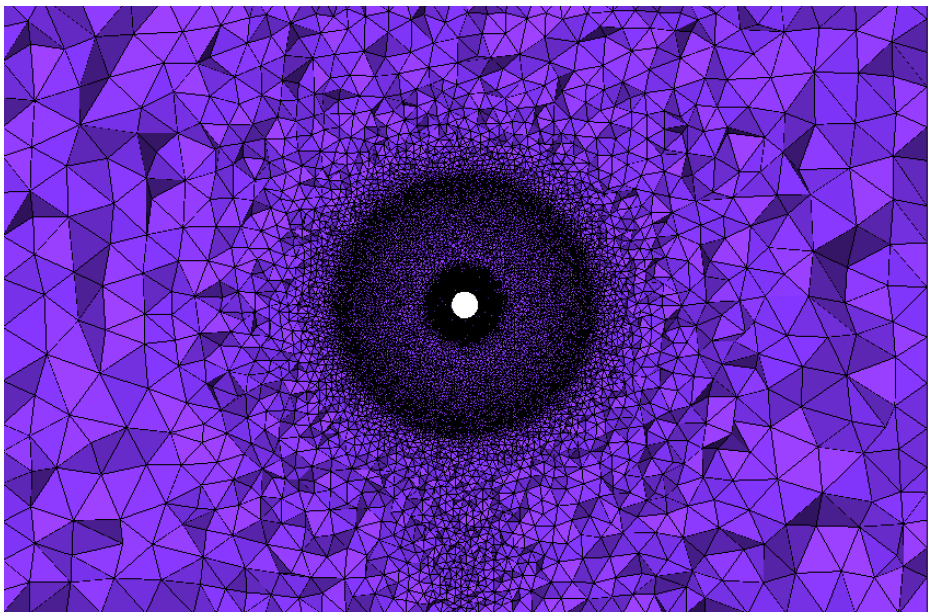

Figure 4.5: Cross-section of the mesh at the rotor plane with $e = c_{local}/4$ at the rotor. This element size was used for Meshes 1 and 3.

simulated per rotor revolution and each blade was approximated by a cosine distribution of 60 collocation points.

The mesh parameters for each of the four meshes are listed in Table 4.2. Broadly, Meshes 1 and 3 have the better rotor resolution, while 3 and 4 have the better wake resolution. Hence, 2 and 3 present the lowest and highest resolutions considered, respectively. Also listed in Table 4.2 are the results for shaft torque and single-blade root flap bending moment for simulations using each of the four meshes and no tip correction, and the percent difference between the Mesh 1 results and those for the other meshes. Torque and root flap bending moment will be discussed in further detail in Section 4.4.2.

Table 4.2: Torque and root flap bending moment results for the RANS $k-\omega$ SST spatial resolution study. Percentage differences are relative to Mesh 1.

Mesh	e (Rotor Plane)	e (Wake)	Total Cells	Torque (Nm)	% Difference	RFM (Nm)	% Difference
1	$c_{local}/4$	1.00 m	1.35 x 10^6	997.56	–	2,111.44	–
2	0.25 m	1.00 m	1.17 x 10^6	1,004.40	0.69	2,112.49	0.05
3	$c_{local}/4$	0.25 m	4.87 x 10^6	996.76	0.08	2,110.20	0.06
4	0.25 m	0.25 m	4.64 x 10^6	1,005.36	0.73	2,112.92	0.07

The resulting values of time-averaged spanwise integrated torque and single-blade root flap

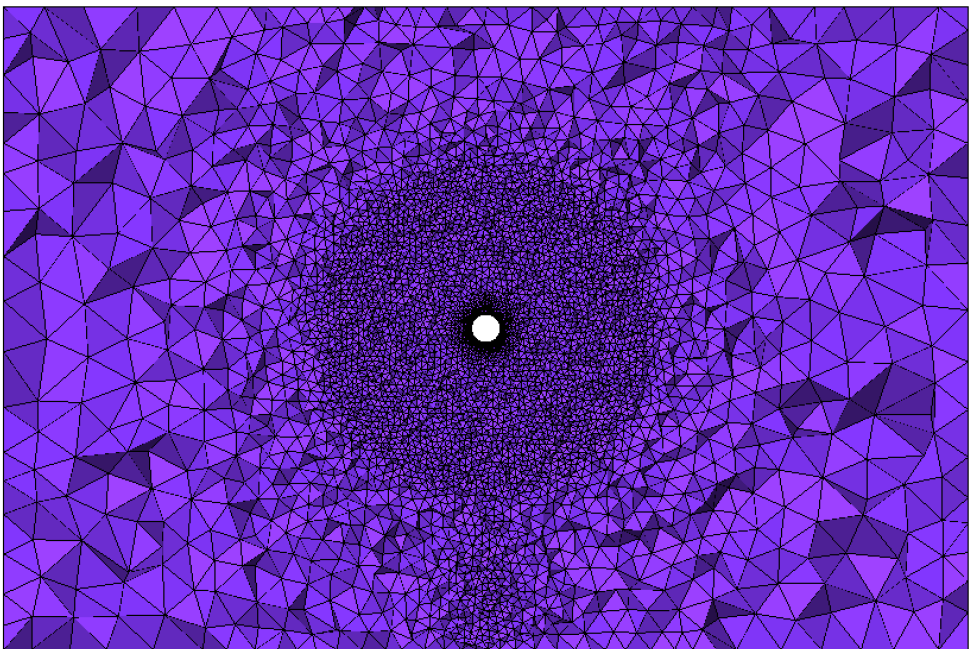

Figure 4.6: Cross-section of the mesh at the rotor plane with $e = 0.25$ m at the rotor. This element size was used for Meshes 2 and 4.

bending moment for simulations using each of the four meshes varied by less than 1%. This indicates that the mesh resolution had little effect on the values of the rotor loads. However, the mesh resolution did affect the rotor wake, as seen in the wake centreline velocity deficit profiles in Figure 4.7. The profiles depict the x-velocity normalised by U_∞ along vertical lines at 5 locations directly downstream of the turbine. The results in Figure 4.7 have been time-averaged over one revolution of the rotor.

It is observed that there is little difference between the centreline velocity deficit profiles for all wakes in the immediate wake of the rotor, $x/R = 1$.The fluctuations observed on the lower half of domain at the at the $x/R = 1$ position are due to the close proximity of the tower upstream. Further downstream ($x/R \geq 2$), the velocity profiles are influenced by the mesh resolution in the wake region, with the results from Meshes 1 and 2 (low wake resolution) in substantial agreement, and those of Meshes 3 and 4 (high wake resolution) also in agreement with each other. The results from Meshes 3 and 4 exhibit more rapid centreline velocity recovery behind the rotor hub than in the lower wake resolution simulations.

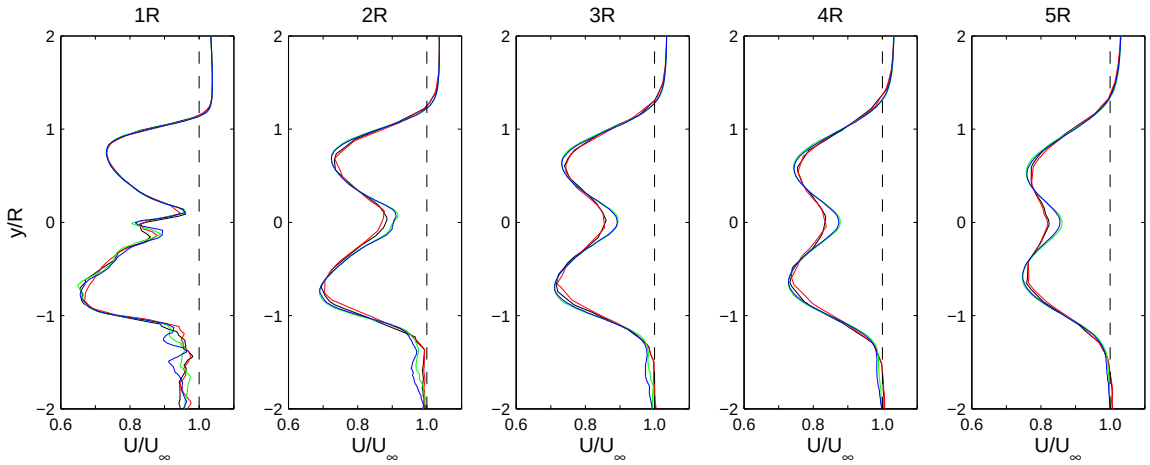

Figure 4.7: $U_\infty = 7$ m/s centreline wake velocity deficit profiles $1R$, $2R$, $3R$, $4R$, and $5R$ downstream of the rotor plane. The profile depicts x-velocity normalised by U_∞. The turbine hub is centred at $y/R = 0$. Mesh 1: black; Mesh 2: red; Mesh 3: green; Mesh 4: blue.

Dependency on the mesh resolution in the wake can also be seen in the vorticity contours downstream of the rotor. Vorticity contours on an x-z cross-section at height $y/R = 0$ are shown in Figure 4.8 for the four meshes. Higher resolution in the wake (Figures 4.8c and 4.8d) results in improved definition and preservation of the tip and root vortices. The rotor plane resolution does not appear to have a large influence on the vorticity contours in the rotor wake, which is consistent with the low dependency of rotor loads, and hence shed vorticity, on rotor plane resolution.

The tip vortices in the rotor wake are visible in the vorticity isosurface shown in Figure 4.9. This isosurface is for the $U_\infty = 7$ m/s case using Mesh 3. The isosurface is at a vorticity magnitude of $\omega = 1$ s^{-1}. The positions of the nacelle and tower are visible and the helical structure of the tip vortices is clearly visible.

The wake downstream of the tower in Figure 4.9 is not an accurate representation of flow past a cylinder. This is because a relatively coarse mesh was used for the nacelle and tower in the interest of computational efficiency. However, this is not believed to have a large impact on the computed rotor loads, as the mesh is of sufficient resolution to capture the momentum deficit caused by the presence of the tower.

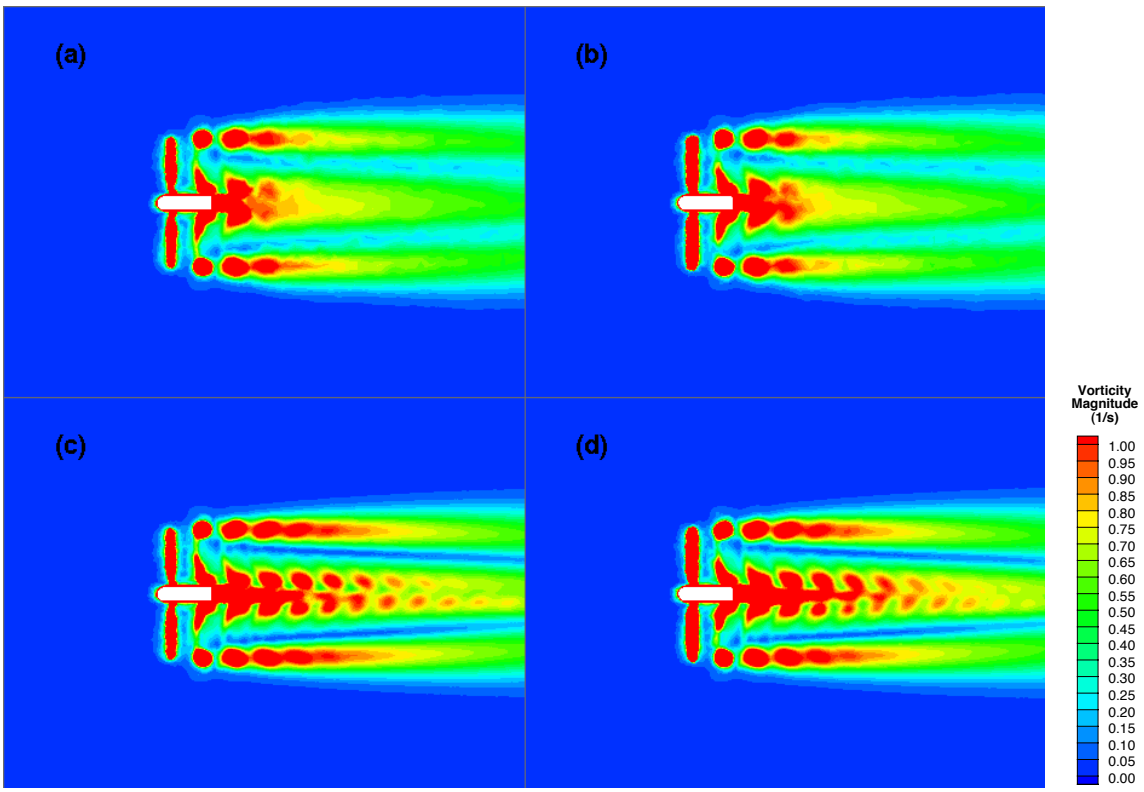

Figure 4.8: Vorticity magnitude contours of the NREL Phase VI simulations for $U_\infty = 7$ m/s using (a) Mesh 1; (b) Mesh 2; (c) Mesh 3; and (d) Mesh 4. The flow is from left to right.

The results of the spatial resolution study indicate that although the resolution of the mesh downstream of the turbine has an effect on the vorticity contours in the rotor wake and on the centreline wake velocity deficit profiles, it has little effect on the rotor loads. Due to the increase in the number of cells, simulations using meshes with highly resolved wakes require far greater computational resources than those using coarser resolution in the wake. The validation study presented has focused on rotor load comparisons and no comparison has been drawn between simulated and experimental wake velocity measurements. Therefore, the coarse rotor wake resolution used in Meshes 1 and 2 was employed.

The difference in calculated torque due to the different rotor plane resolutions (0.7%) was slightly higher than the difference due to wake resolution (0.1%). Further, Mesh 1, with the higher rotor plane resolution, contains only 13% more cells than Mesh 2. The increase

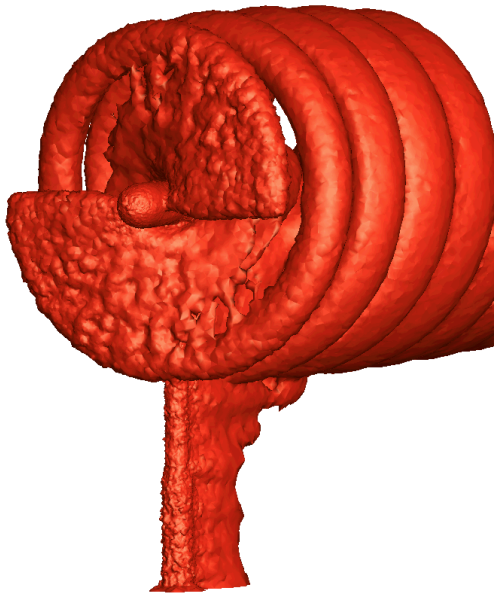

Figure 4.9: Vorticity isosurface at $\omega = 1$ s^{-1} for the $U_\infty = 7$ m/s case (using Mesh 3). The flow is from left to right.

in computation time due to the additional cells was considered acceptable, and Mesh 1 was chosen for the NREL Phase VI validation study.

To ensure the selected spatial resolution was acceptable for all flow upstream flow speeds considered in the present validation study, simulations were completed using each of the four meshes for the highest flow speed, $U_\infty = 25$ m/s. The results were similar to those of the lower flow speed ($U_\infty = 7$ m/s) case, with a 1% difference in computed torque due to the different rotor plane resolutions and less than 0.1% difference in torque due to wake resolution. These results confirm that the choice of Mesh 1 for the validation study is acceptable for all flow speeds considered.

Time Resolution

The effect of time resolution on the simulation results was studied using Mesh 1 from the mesh resolution study. The $U_\infty = 7$ m/s case was run with 100, 200, 300, 400, and 500 time steps per rotor revolution (ts/rev) for 8 revolutions. Cosine distributions of 60 collocation points were again used to discretise each rotor blade. It is possible for the time resolution

to result in collocation points 'jumping' over mesh cells in consecutive time steps due to large collocation point displacement, particularly for the coarse time resolutions. Although this affects solution accuracy, it does not affect the ability of the model to converge to a solution.

The average torque and single-blade RFM over the 8^{th} revolution are shown in Table 4.3 for each time resolution. Revolution to revolution convergence had been attained prior to the 8^{th} revolution for each simulation. Table 4.3 also includes the percent change of torque and single-blade RFM from the previous (less refined) time resolution. As in the mesh resolution study, the 3D tip correction was not utilised in the time resolution study.

Table 4.3: Torque and root flap bending moment results for the five time resolutions ($U_\infty = 7$ m/s). Percent change is relative to the previous time resolution.

ts/rev	Torque (Nm)	% Change	RFM (Nm)	% Change
100	1,058.44	–	2,194.27	–
200	1,009.79	4.60	2,128.12	3.01
300	997.56	1.21	2,111.44	0.78
400	991.63	0.59	2,104.04	0.35
500	988.91	0.27	2,100.74	0.16

As indicated in Table 4.3, the time-averaged torque changed just 1.21% when the number of time steps per revolution was increased from 200 to 300. The same refinement in time resolution resulted in 0.78% change in the single-blade root flap bending moment. From these results, it was determined that 200 time steps per revolution was an adequate time resolution for the Phase VI validation study.

Convergence to Steady Operational State

The Mesh 1 results from the mesh resolution study were used to determine how many rotor revolutions must be simulated for the time-averaged rotor loads to converge to the same value from one revolution to the next. The torque and single-blade RFM averaged over each of 8 revolutions are shown in Table 4.4. The percent change from the loads for the previous revolution is also included.

Table 4.4: Torque and root flap bending moment results for eight rotor revolutions ($U_\infty = 7$ m/s). Percent change is relative to the previous revolution.

Revolution	Torque (Nm)	% Change	RFM (Nm)	% Change
1	1,077.72	–	2,191.39	–
2	1,016.48	5.68	2,132.39	2.69
3	1,002.70	1.36	2,117.21	0.71
4	999.63	0.31	2,113.73	0.16
5	998.47	0.12	2,112.45	0.06
6	997.94	0.05	2,111.87	0.03
7	997.70	0.02	2,111.60	0.01
8	997.56	0.01	2,111.44	0.01

The values of torque and single-blade RFM both change less than 1% between the 3rd and 4th revolutions. The results for the actuator line model simulations completed as part of the validation study are therefore averaged results for the 3rd rotor revolution.

Iterative Convergence Within a Time Step

Table 4.5 lists convergence statistics for relative velocity at the root and tip of a single blade within a time step. The tabulated results are for the $U_\infty = 7$ m/s simulation using Mesh 1 and are for the 600^{th} time step. The tip correction has been included in the simulation. Convergence of the continuity residual for the same simulation, also for the 600^{th} time step, is presented in Table 4.6.

Table 4.5: Iterative convergence of U_{rel} at the blade tip and root within a selected time step for the $U_\infty = 7$ m/s simulation.

Iteration	U_{rel} root (m/s)	% difference from converged value	U_{rel} tip (m/s)	% difference from converged value
1	11.6261	0.0211	38.4573	-0.1086
5	11.6235	-0.0009	38.4878	-0.0292
15	11.6236	0.0	38.4987	-0.0011
25	11.6236	0.0	38.4990	-0.0002
46	11.6236	–	38.4991	–

Table 4.6: Iterative convergence of the continuity residual within a selected time step for the $U_\infty = 7$ m/s simulation.

Iteration	continuity residual
1	1.902 x 10^{-2}
5	8.474 x 10^{-3}
15	6.183 x 10^{-4}
25	5.927 x 10^{-5}
46	8.471 x 10^{-7}

This is simply a representative case. The number of iterations required for convergence is dependent on factors including the upstream flow speed and the number of time steps previously solved.

4.4.2 Integrated Loads

Integrated loads including shaft torque, root flap bending moment, and root edge bending moment are determined by calculating the appropriate moment on each actuator line segment and integrating over the span of the blade, giving the total moment on each blade. Results for these integrated quantities are presented in this section and compared with published results from 3D blade-resolved simulations. In addition, the power coefficient as a function of tip speed ratio is discussed. In the current section, the data presented is time-averaged. The actuator line simulations presented in this section include the 3D tip correction discussed in Section 4.3.1.

Shaft Torque

The torque, Q, on a rotor blade is determined for a given time step using

$$Q = \sum_{i=1}^{m} \mathrm{F}_{\theta i} r_i \tag{4.3}$$

where $\mathrm{F}_{\theta i}$ is the magnitude of the force on the i^{th} blade segment in the direction of rotation and r_i is the radius at the midpoint of the i^{th} blade segment. m is the total number of collocation points. The shaft torque is the sum of the individual blade torques (in this study there are 2 rotor blades).

Figure 4.10 is a comparison of results for the shaft torque versus the upstream flow speed, U_∞. The figure includes experimental results, the present actuator line model results, and results from the 3D blade-resolved CFD models used by Sørensen et al. (tunnel

configuration), Gómez-Iradi et al., and Mahu and Popescu. The torque reported in these results is time-averaged.

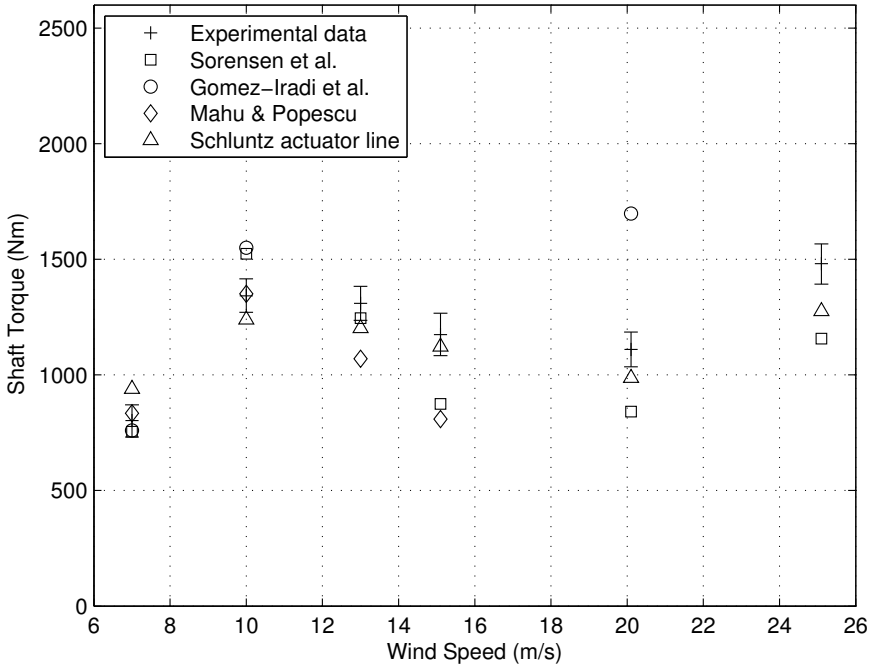

Figure 4.10: Comparison of experimental and computed values of shaft torque for a range of upstream flow speeds. All computations are 3D blade-resolved except the present actuator line results.

The actuator line model results are generally in good agreement with the experimental data. In addition, the accuracy of the actuator line results is comparable with the accuracy of the 3D blade-resolved results shown. Further, for the three highest flow speeds, the shaft torque calculated using the actuator line model lies closer to the experimental measurement than that of the 3D blade-resolved models.

The torque for the $U_\infty = 7$ m/s case is over-predicted by the actuator line model by about 17%. This case falls in the pre-stall regime, in which attack angles are low. The 2D aerodynamic data at the attack angles for the $U_\infty = 7$ m/s case was directly available from experiments. Therefore the over-prediction is not due to the use of interpolated/estimated aerodynamic data. However, it is possible that the tip effects are not completely accounted

for by the Shen et al. tip correction discussed in Section 4.3.1. The over-prediction of torque for the $U_\infty = 7$ m/s case is discussed further in Section 4.4.3, in which the spanwise distributions of the blade forces are presented.

Root Flap Bending Moment

The root flap bending moment (RFM) of a rotor blade is defined for this study as

$$RFM = \sum_{i=1}^{m} \mathrm{F}_{RFMi} \left(r_i - 0.432\right) \tag{4.4}$$

where F_{RFMi} is the magnitude of the force on the i^{th} blade segment in the root flap direction. This direction is offset from the axis of rotation by the blade tip pitch angle (3° toward feather in the current cases). The moment arm is $(r_i - 0.432)$ because the strain gauges used to measure the root flap and edge loads in the Phase VI experiment were located at 8.6% span ($r = 0.432$ m).

A comparison of single-blade RFM values averaged over a revolution is shown in Figure 4.11. This figure includes experimental results, actuator line results, and computational results for two 3D blade-resolved models, Sørensen et al. (tunnel configuration) and Mahu and Popescu.

The actuator line model results are generally in good agreement with the experimental results. There is notable over-prediction of the single-blade RFM at wind speeds of 7 and 25 m/s (34% and 18% error, respectively). The over-prediction for $U_\infty = 7$ m/s is similar to the results from the 3D blade resolved simulation of Mahu and Popescu. The $U_\infty = 25$ m/s case is operating in highly stalled conditions with high attack angles. These attack angles fall in the range in which the aerodynamic data was interpolated/estimated, and it is thus possible that this is the source of error at this very low tip speed ratio.

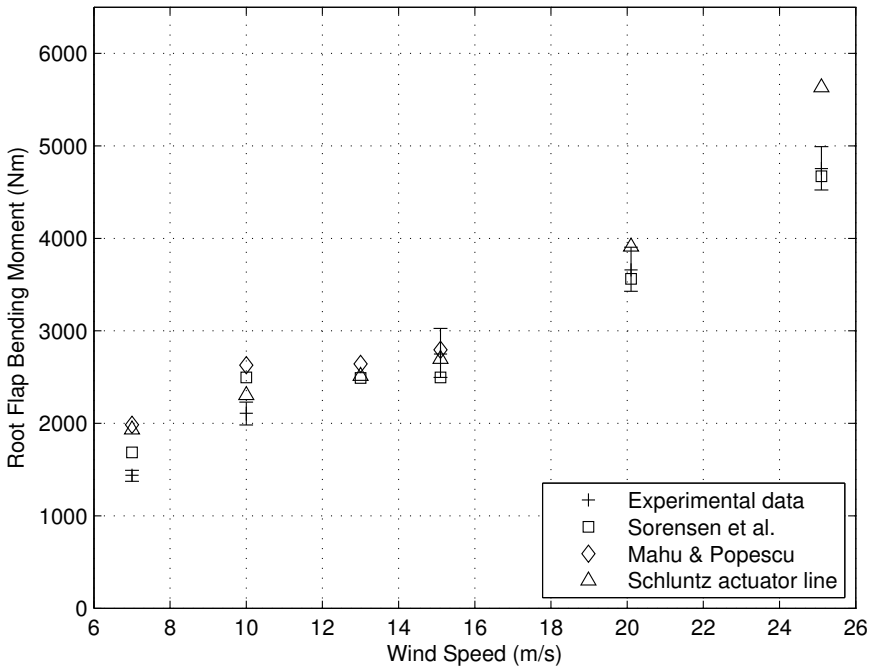

Figure 4.11: Comparison of experimental and computed values of the root flap bending moment for a range of upstream flow speeds.

Root Edge Bending Moment

The root edge bending moment (REM) on a rotor blade is, in this study, given by

$$REM = \sum_{i=1}^{m} \mathrm{F}_{REMi} \, (r_i - 0.432) \tag{4.5}$$

where F_{REMi} is the magnitude of the force on the i^{th} blade segment in the root edge direction. This direction is offset from the direction of rotation by the blade pitch angle (3° toward feather in the current cases). As in Eq. 4.4, the moment arm is adjusted due to the location of the strain gauges in the wind tunnel experiments.

Experimental and computational single-blade REM results, averaged over a rotor revolution, are shown in Figure 4.12.

At some wind speeds, the experimental results for REM are under-predicted by the actuator

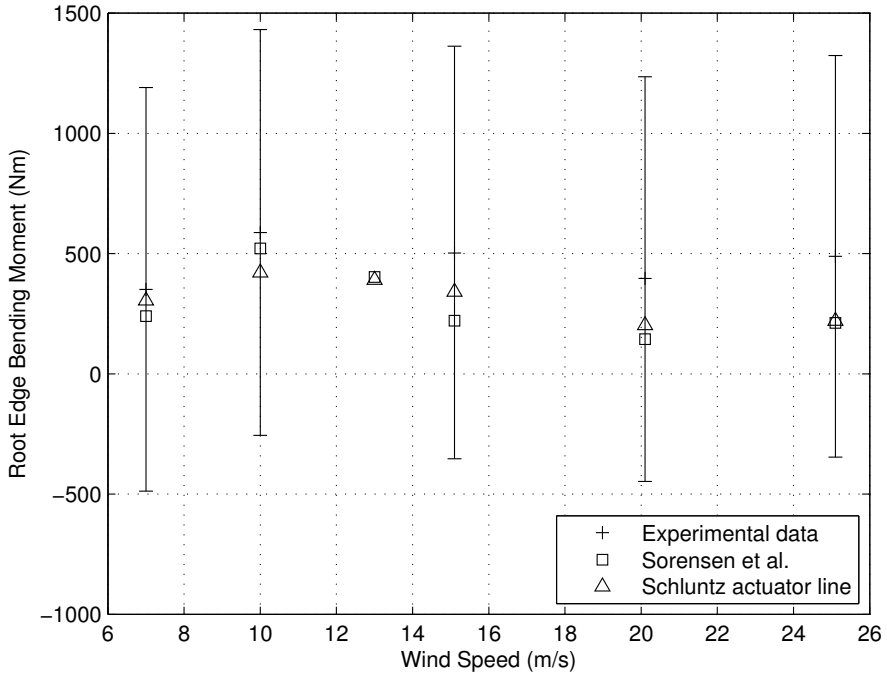

Figure 4.12: Comparison of experimental and computed values of the root edge bending moment for a range of upstream flow speeds.

line model and the 3D blade-resolved model of Sørensen et al. by over 50%. However, given the large standard deviation for the REM measurements, the results are considered to be acceptable.

Power Coefficient

The turbine power coefficient, C_p, is defined as

$$C_p = \frac{Q_{shaft}\Omega}{\frac{1}{2}\rho U_\infty^3 A_{rotor}} \tag{4.6}$$

where A_{rotor} is the cross-sectional area of the rotor and Ω is the angular velocity of the rotor. The power coefficient is presented as a function of the tip speed ratio (λ) in Figure 4.13. Because the experimental rotor operated at a constant RPM, the lowest wind speed (7

m/s) corresponds to the highest λ and the highest wind speed (25 m/s) corresponds to the lowest λ.

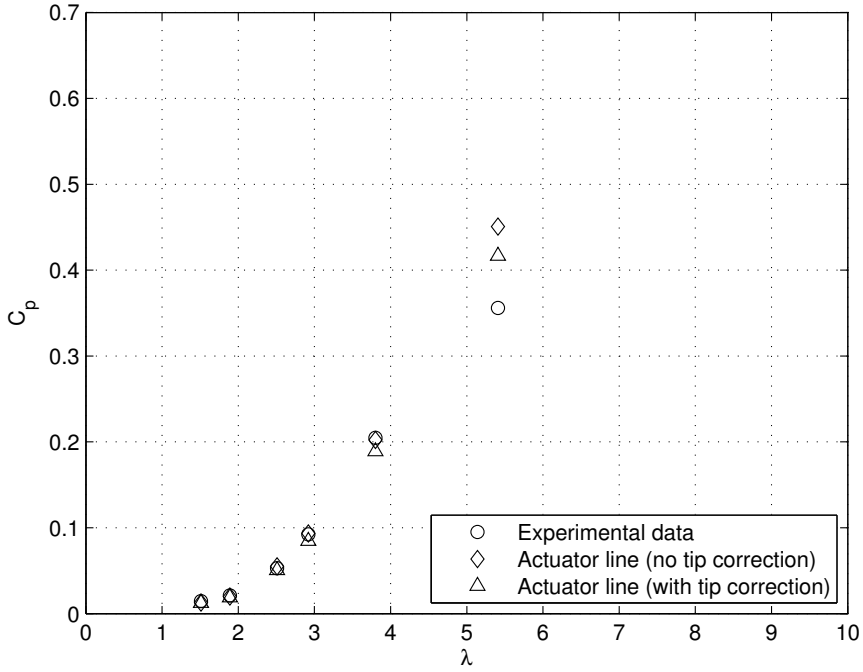

Figure 4.13: Power coefficient versus tip speed ratio.

Figure 4.13 includes results for the actuator line method with and without the 3D tip correction. The correction improves the results for the highest tip speed ratio but has little effect on the other cases. Even with the tip correction, the calculated value of C_p for $\lambda = 5.41$ is over-predicted by about 18%. It is possible that the tip correction is not completely accounting for the 3D flow effects at the blade tips.

Figure 4.13 highlights the relevance of the $U_\infty = 7$ m/s case ($\lambda = 5.41$). The power coefficients for the other cases are very low and it is unlikely wind turbines would be operating at the lower tip speed ratios.

4.4.3 Spanwise Force Distribution

The turbine used in the NREL Phase VI wind tunnel testing was equipped with pressure taps at 5 radial blade stations, $0.300R$, $0.466R$, $0.633R$, $0.800R$, and $0.950R$. Experimental results for the normal and tangential force coefficients were available at these radial locations for each of the cases listed in Table 4.1.

The tangential force, $\mathbf{F}_T$, is defined as the component of the force on the blade element in the direction of the aerofoil chord. The direction of the normal force component, $\mathbf{F}_N$, is perpendicular to the chord in the plane of the 2D blade element. Figure 4.14 shows the directions of $\mathbf{F}_T$ and $\mathbf{F}_N$ relative to a 2D blade element for a horizontal-axis turbine.

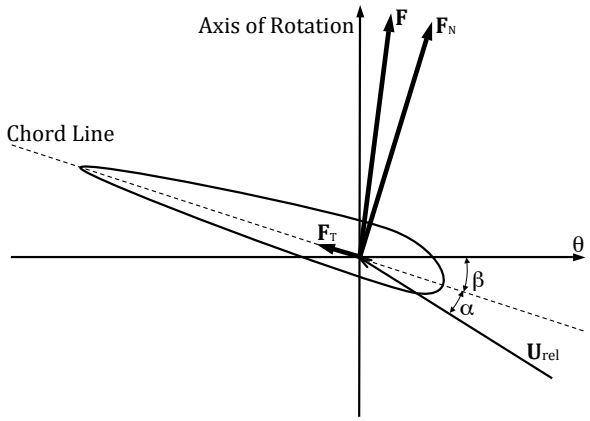

Figure 4.14: Tangential ($\mathbf{F}_T$) and normal ($\mathbf{F}_N$) forces on a blade element for a horizontal-axis turbine.

The tangential force coefficient, C_t, on a blade segment is

$$C_t = \frac{\|\mathbf{F}_T\|}{\frac{1}{2}\rho\left(\|\mathbf{U}_\infty\|^2 + (\Omega r)^2\right) c\delta r} \tag{4.7}$$

where ρ is the fluid density, Ω is the angular velocity, r is the radius of the midpoint of the blade segment, c is the chord of the blade element, and δr is the spanwise width of the blade element.

Similarly, the normal force coefficient, C_n, on a blade segment is

$$C_n = \frac{\|\mathbf{F}_N\|}{\frac{1}{2}\rho\left(\|\mathbf{U}_\infty\|^2 + (\Omega r)^2\right) c\delta r} \tag{4.8}$$

In the current work, the simulated values of C_t and C_n at the appropriate radial positions were determined by linearly interpolating from the values at the neighbouring collocation points.

Results for the spanwise distributions of C_n and C_t are shown in Figure 4.15 for each of the six flow speeds simulated. The wind tunnel results, as well as results for the present actuator line study with and without the 3D tip correction, are included.

The most significant case is the $U_\infty = 7$ m/s case. This case is pre-stall and operates at a tip speed ratio that is within the normal range for wind turbine power generation. For this case, the tip speed ratio, λ, is 5.41, while $\lambda < 4$ for all of the other cases. Stall onset occurs at $U_\infty = 10$ m/s and all other cases are in stall.

For $U_\infty = 7$ m/s, very good agreement is seen for C_n and C_t at the three radial stations nearest the blade root. The force coefficients at the 95% span location, however, are over-predicted by the actuator line method. The over-prediction is reduced by about 50% with the introduction of the Shen et al. tip correction (discussed in Section 4.3.1). However, the tip correction does not entirely eliminate the error at the blade tip. The remaining over-prediction of the forces at the blade tips is the origin of the over-prediction of the torque, single-blade root flap bending moment, and power coefficient seen in Section 4.4.2. It is possible that the tip correction used does not completely account for the tip effects. A greater modification to the underlying 2D aerofoil data to account for 3D tip flow effects may therefore be required.

For the $U_\infty \geq 10$ m/s cases, there is notable disagreement with experimental results at the inboard blade stations. Under-prediction of the force coefficients at the 30% span location

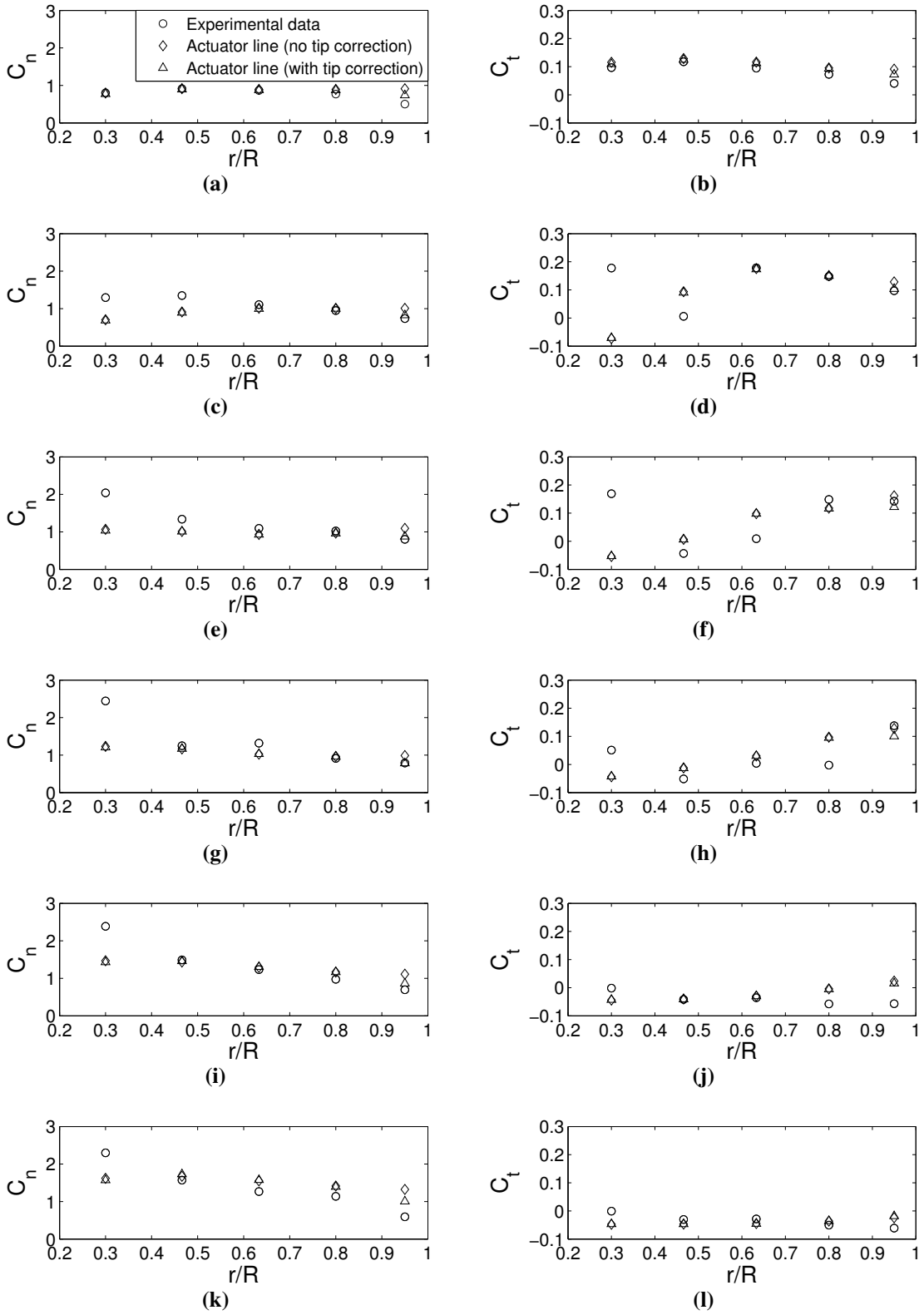

Figure 4.15: Spanwise distribution of C_n (left column) and C_t (right column) for $U_\infty = 7$ m/s (a & b), 10 m/s (c & d), 13 m/s (e & f), 15 m/s (g & h), 20 m/s (i & j), and 25 m/s (k & l).

is observed for all flow speeds other than 7 m/s. This effect was also observed by Tangler in BEM predictions for the NREL Phase VI rotor [118]. The discrepancy at the blade root is expected because a stall delay model has not been included in the actuator line model for this study. Such a model may be able to account for the 3D rotational effects at the root of a blade in stall by adjusting the 2D aerodynamic data [59, 122]. An accurate stall delay model would likely improve the inboard results for blades in stall, as discussed by Breton et al. in a study of the effects of various stall delay models on NREL Phase VI rotor simulation results [123].

The under-prediction of forces at the blade root, however, has little effect on the integrated blade moments, including torque and single-blade root flap bending moment, because the moment arm is small. In addition, the tip speed ratios for the cases in stall in the Phase VI validation are not realistic for horizontal-axis turbines in operation.

4.5 Large Eddy Simulation Model

The $U_\infty = 7$ m/s ($\lambda = 5.41$) case used in the mesh resolution study was repeated using a large eddy simulation (LES) model with a Smagorinsky closure (Smagorinsky constant $C_s = 0.1$) rather than a RANS $k-\omega$ SST model. A comparison between the LES and RANS results provides an assessment of the robustness of the actuator line method and gives insight into the influence of the turbulence closure model on the rotor loading and wake. In the large eddy simulations, second-order-accurate bounded central-differencing scheme was used for the momentum equations and the boundary conditions remained the same as for the RANS $k-\omega$ SST simulations. The tip correction was not included in this simulation, because consistency with the RANS $k-\omega$ SST mesh resolution study was desired.

Spatial Resolution

The spatial resolution study (Section 4.4.1) was repeated for each of the 4 meshes using LES rather than RANS $k-\omega$ SST. First, a time resolution study was completed using Mesh 3 (the mesh with the highest resolution). The time-averaged shaft torque changed by 1.3% and 0.4%, respectively, when the number of time steps per revolution was increased from 200 to 300 and from 300 to 400. Given these results, 300 time steps were simulated per rotor revolution in the LES spatial resolution study. The LES results for shaft torque and single-blade RFM for the 4 meshes are listed in Table 4.7. Also listed is the percent difference for each value with respect to the Mesh 1 results.

Table 4.7: Torque and root flap bending moment results for the LES spatial resolution study. Percentage differences are relative to Mesh 1.

Mesh	e (Rotor Plane)	e (Wake)	Torque (Nm)	% Difference	RFM (Nm)	% Difference
1	$c_{local}/4$	1.00 m	993.94	–	2,106.76	–
2	0.25 m	1.00 m	998.78	0.49	2,106.18	0.03
3	$c_{local}/4$	0.25 m	992.04	0.19	2,104.81	0.09
4	0.25 m	0.25 m	999.35	0.54	2,106.15	0.03

The results of the LES spatial resolution study indicate, as for RANS $k-\omega$ SST simulations, that the mesh resolution at the rotor plane and in the rotor wake had little effect on the rotor loads.

Vorticity magnitude contours on a horizontal plane through the rotor hub are shown in Figure 4.16 for each of the four meshes. The contours show that the wake resolution has a large effect on the vorticity dissipation in the wake. While the rotor plane resolution does influence the vorticity magnitude in the wake, this effect is far less pronounced than that of the wake resolution. It is evident that, although the spatial resolution for all meshes is sufficient for analysing the rotor loads, the higher wake resolution may be desirable if wake effects are of primary interest. However, without comparison to physical measurement of wake flows, it cannot be said with certainty that the results computed using the higher wake resolution are more accurate.

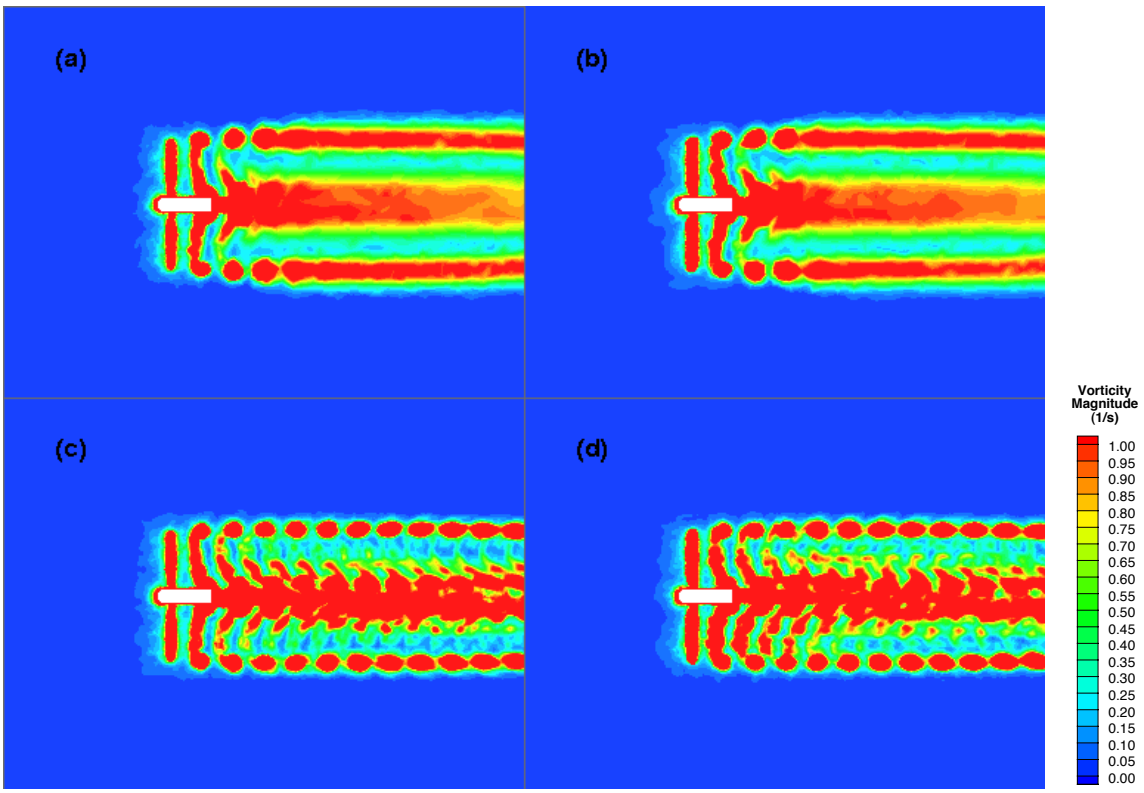

Figure 4.16: Vorticity magnitude contours of the NREL Phase VI LES simulations for $U_\infty = 7$ m/s using (a) Mesh 1; (b) Mesh 2; (c) Mesh 3; and (d) Mesh 4. The flow is from left to right.

Comparison with RANS $k-\omega$ SST Results

A detailed comparison of the LES and RANS $k-\omega$ SST results is now presented for the $U_\infty = 7$ m/s cases using the mesh with the finest spatial resolution in both the wake and the rotor plane (Mesh 3).

The torque and single-blade RFM averaged over the 8^{th} revolution of the $k-\omega$ SST and LES simulations using Mesh 3 of the mesh resolution study are compared in Table 4.8. In the LES simulation, the torque was reduced by 0.47% while the root flap moment was reduced by 0.26% relative to the $k-\omega$ SST results. Hence, the turbulence model is observed to have little effect on the integrated loads.

The centreline wake velocity deficit profiles for the $k-\omega$ SST and LES simulations are

Table 4.8: Torque and root flap bending moment results for the $k-\omega$ SST and LES turbulence models.

Turbulence Model	Torque (Nm)	% Difference	RFM (Nm)	% Difference
$k-\omega$ SST	996.76	–	2,110.20	–
LES	992.04	0.47	2,104.81	0.26

shown in Figure 4.17. The LES simulation is seen to have a large effect on the wake velocity. The velocity deficit profiles for the LES simulations are richer in small scale detail (particularly for $y/R \leq 0$ behind the rotor tower) and the wake dissipates more slowly than in the $k-\omega$ SST simulation.

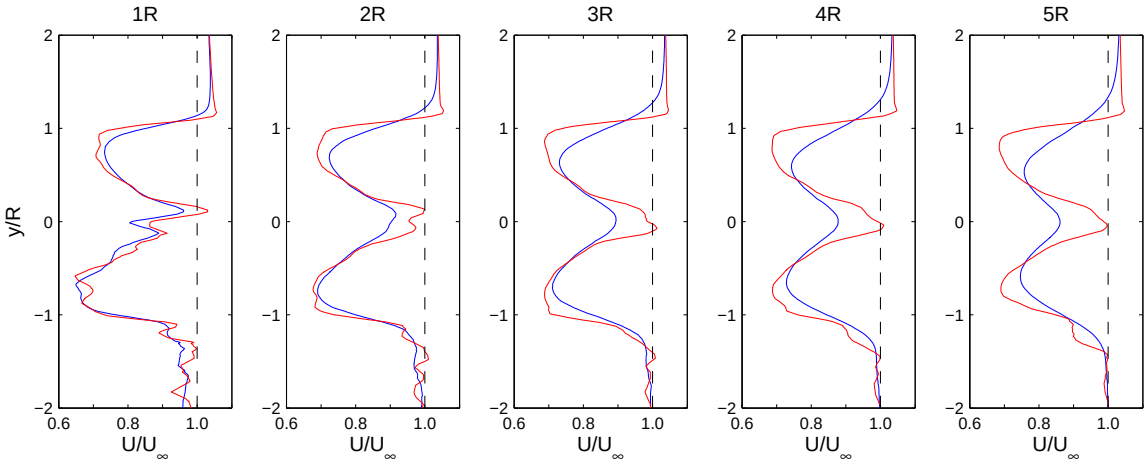

Figure 4.17: $U_\infty = 7$ m/s centreline wake velocity deficit profiles $1R$, $2R$, $3R$, $4R$, and $5R$ downstream of the rotor plane. The profile depicts x-velocity normalised by U_∞. The turbine hub is centred at height $y/R = 0$. $k-\omega$ SST: blue; LES: red.

Figure 4.18 presents vorticity contours on a horizontal plane at $y/R = 0$ (the nacelle height). The simulation using the LES turbulence model has much clearer definition of the tip and root vortices in the far wake, indicating that the vorticity dissipation is reduced. Both the wake velocity deficit profiles and the vorticity plots clearly show the reduced rate of wake expansion for the LES case.

The tip vortices of the two simulations are seen in the vorticity isosurfaces shown in Figure 4.19. The isosurfaces are at vorticity magnitude $\omega = 3$ s^{-1}. The nacelle and shaft are visible and the helical structure of the tip vortices is clearly visible. It is clear from the

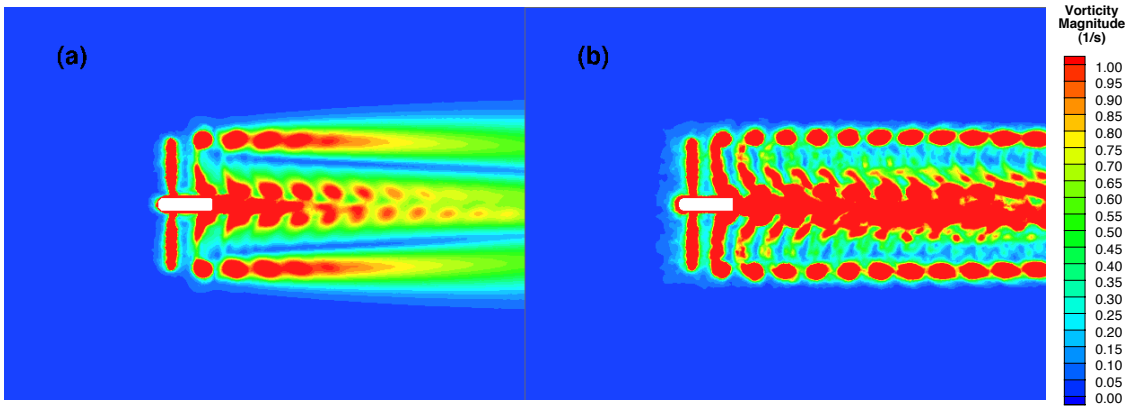

Figure 4.18: Vorticity magnitude contours of the NREL Phase VI simulations for $U_\infty = 7$ m/s using Mesh 3 with (a) $k-\omega$ SST model and (b) LES turbulence model. The flow is from left to right.

vorticity isosurfaces, as it was for the velocity deficit profiles and vorticity contours, that the tip and root vortices dissipate at a lower rate in the LES simulation than in the $k-\omega$ SST simulation.

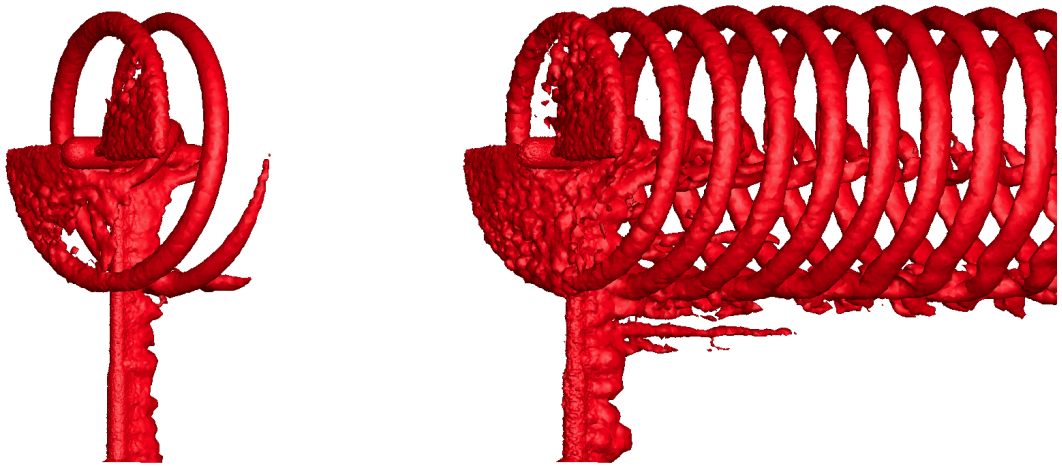

Figure 4.19: Vorticity isosurfaces at $\omega = 3$ s^{-1} for the $U_\infty = 7$ m/s case (using Mesh 3) with RANS $k-\omega$ SST (left) and LES (right). The flow is from left to right.

4.6 Conclusions

An actuator line model for simulation of wind and tidal turbines has been validated using results from the NREL/NASA Ames Phase VI wind tunnel experiments. The model in-

cludes the new potential flow equivalence method of obtaining the relative flow velocity at blade collocation points through velocity field sampling (introduced in Section 3.1.2). This method enables computed blade loads to be projected onto the flow field without the requirement for regularisation kernels, which are often employed to prevent flow field distortion and resulting instabilities. Additionally, the velocity analysis routine is coupled with the method of projecting the momentum sources onto the flow field on an unstructured mesh (Section 3.3.1). The compatibility of the potential flow equivalence method with unstructured meshes enables turbine components, such as the nacelle and tower, to be explicitly resolved in the simulations.

Although spatial resolution was found to have large effects on the velocity field in the rotor wake, rotor loads were found to be relatively insensitive to rotor wake resolution in both the RANS $k-\omega$ SST and the LES simulations. This result indicates that relatively coarse resolution in the wake may be acceptable if the rotor loads are the main focus of a study. The computed rotor loads for the RANS $k-\omega$ SST and LES simulations were consistent, although the tip and root vortices in the far wake of the turbine have much clearer definition for the LES simulations, due to less vorticity dissipation.

The validation results show good general agreement with the NREL Phase VI wind tunnel results and indicate that the present actuator line model is comparable to 3D blade-resolved models in terms of accuracy of integrated rotor loads. Further, the simulations were completed using far fewer mesh cells than the 3D blade-resolved studies selected for comparison. The results for spanwise force coefficients suggest that the model could be improved with the addition of a stall-delay model for simulations of rotors operating in stall. In addition, the correction employed for 3D effects at the blade tips improves the result, but discrepancies with the experimental results are still observed. Although artificial corrections to 2D aerodynamic data can be useful, more in-depth research is required in order to improve the prediction of tip loads.

Chapter 5

Rotor Performance in Infinite-Length Tidal Fences

It is of particular interest to investigate rotor performance in tidal turbine fences with varying local blockage. However, few rotor geometries have been published and none have yet been designed specifically for operation in the high blockage conditions that turbines may experience when deployed in long fences. Therefore, the RANS-BEM tool discussed in Section 2.2.2 is employed in this chapter to design rotors for operation in 4 infinite fence configurations, each with a different rotor spacing. Section 5.2 details the computational setup used in the present study, including the details of the varying domain sizes and resultant blockage ratios considered. The hydrodynamically optimised rotor geometries are presented in Section 5.3.1. Next, a matrix of array simulations is completed with each rotor design tested for its design blockage conditions as well as several off-design blockage conditions. The results, including power curves and streamwise velocity contours, are included in Section 5.3.2. The discussion in Section 5.3.3 provides insight into the mechanisms that affect rotor performance in blocked flow and an examination of the radial variation in local thrust coefficients presented in Section 5.3.4 resolves some of

the apparent discrepancies in the power coefficient curves. Finally, a comparison between the RANS-BEM results and actuator line simulation results for a selected case is included in Section 5.4.

5.1 Effects of Blockage on Rotor Performance

Unlike most wind turbines, tidal turbines will operate in partially blocked conditions, for instance in a tidal channel and/or a closely packed array. A group of closely packed tidal turbines partially blocking a channel may operate under low global blockage conditions yet still experience large local blockage effects. Actuator disc theory predicts the maximum power coefficient for a rotor operating in unbounded flow, also known as the Lanchester-Betz limit, to be $C_{p_{max}} = 0.593$, as discussed in Section 2.1 [124, 125]. It is widely understood that the Betz limit may be exceeded by operating a rotor in blocked conditions [36]. In addition, Nishino and Willden have shown that high local blockage, in other words a high ratio of swept rotor area to local flow passage area, can significantly increase array hydrodynamic efficiency (i.e. the global power coefficient of the tidal fence) [41]. As discussed in Section 2.1.1, Nishino and Willden's theoretical model of turbines partially blocking an infinitely wide tidal channel leads to a limiting value for the global power coefficient, $C_{pg,max} = 0.798$, which occurs at local blockage $B_l \approx 0.40$. Despite the prospective performance improvements, however, the effects of blockage on optimal rotor design are not well understood. Blockage corrections for use in analytical BEM models have been introduced [37] but rotors are not generally designed with regard to the blockage conditions the rotor is expected to face in operation.

RANS-BEM methods are particularly well-suited for designing rotors for operation in specified blockage conditions, as well as for the investigation of performance comparisons of specific rotor designs. First, the steady-state solution allows for a relatively fast design iteration and gives BEM methods a computational advantage over unsteady methods of rotor

analysis such as actuator line and 3D blade-resolved methods. Second, unlike actuator disc methods, which model the rotor as an idealised disc, BEM methods include the influence of the blade geometry by calculating the force on radial blade segments and applying the time-averaged forces to corresponding concentric annuli. Finally, the advantage of this method over simple analytic BEM methods is that the flow constraints (such as blockage and boundary conditions) and the presence of supporting structures can be accounted for through the CFD model, hence enabling the limiting assumption of unblocked flow, and thus full upstream to downstream pressure recovery, in traditional BEM to be relaxed. The RANS solver passes the local velocity at the rotor blade elements to the coupled BEM code, which then computes the relative velocity and blade attack angle, and hence the force vector, for each blade element, thereby allowing for the influence of the array effects on the flow to be included in the simulations. An iteration proceeds in which the blade forces, as calculated in the BEM code, and resultant flow field are alternately updated until a converged solution is obtained.

In this computational study, a RANS-BEM method [53] is employed to evaluate the effects of local blockage on rotor design and to investigate the enhancement in rotor performance when tidal turbines are closely spaced in tidal turbine fences. First, the RANS-BEM rotor optimisation tool is utilised to determine hydrodynamically optimal rotor designs for infinitely long tidal fences with lateral intra-rotor spacings ranging from $0.25d$ to $4d$ (d is the rotor diameter), as well as a virtually unblocked case, which is included for comparison purposes. Next, the results of RANS-BEM simulations in which the rotor designs are tested in both design and off-design blockage conditions are presented.

5.2 Computational Parameters

The present study examines the performance of two-bladed rotors of diameter $d = 10$ m operating in infinitely long tidal fences with a range of local blockages. With the rotor disc

area constant, 4 computational domains of varying cross-sectional area are used to create the desired blockage conditions. The cross-sectional area of each domain is dependent on the specified lateral rotor tip-to-tip spacing, s, and domain height, h, as seen in Figure 5.1.

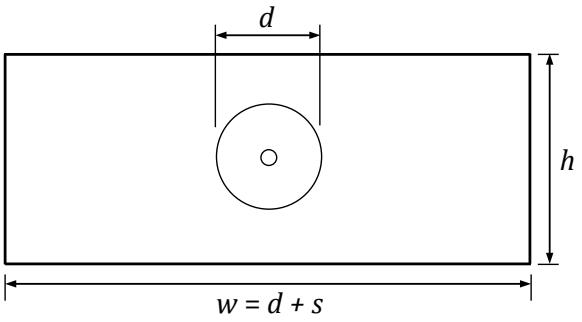

Figure 5.1: Cross-section of the computational domain at the rotor plane.

A nacelle of diameter $d_{nacelle} = 0.15d$ is explicitly included in each simulation. This was necessary as the nacelle blocks flow through the rotor centre and thus increases blockage. No other support structures were included in the simulations. The rotor disc area and nacelle geometry are fixed throughout the study. In the design process, the rotor discs are discretised into 80 concentric annuli of uniform radial width, δr. Symmetry boundary conditions are used at the side boundaries of each domain in order to simulate an infinite fence of turbines, each positioned at a tip-to-tip distance s from its neighbours. The lateral intra-rotor spacing, height, and blockage ratio, B, for each of the 4 domains considered are listed in Table 5.1. In the case of an infinitely long fence, there is no differentiation between the local and global blockage and the blockage $B = B_l = B_g$ is the ratio of the rotor disc area to the cross-sectional area of the computational domain at the rotor plane.

Following a grid convergence study similar to the spatial resolution study in Section 4.4.1, a mesh with element length $e = 0.25$ m was utilised in the rotor plane region, and a growth rate of 1.1 for the mesh elements was used in the wake region. The last column in Table 5.1 indicates the number of cells in each domain. The low cell count, enabled by the BEM

representation of the rotor, and the implementation of steady solution techniques result in low computational cost for the simulations.

Table 5.1: Computational domain parameters

Domain	s	h	B	Cell Count
1	$d/4$	$2d$	0.314	1.22 x 10^6
2	d	$2d$	0.196	1.38 x 10^6
3	$4d$	$2d$	0.079	1.56 x 10^6
4	$100d$	$100d$	0.0001	1.86 x 10^6

The height of the first 3 domains is held constant at $h = 2d$. The range of blockage ratios for these domains is achieved through variation in the lateral rotor spacing alone. Domain 4 approximates unblocked conditions, with the height increased to $h = 100d$. All domains extend $5d$ upstream and $10d$ downstream of the rotor. The surface of the channel is approximated with a rigid lid, the floor and lid of each domain are slip wall boundaries, and the domain side walls are symmetry boundaries. A simple uniform velocity profile with $U_\infty = 2$ m/s is used as the inlet boundary condition for each of the simulations in this study. This allows the effects of blockage on rotor design to be studied in isolation from the effects of shear, yaw, and gravity waves, which are not considered at present. The gauge pressure is prescribed to be constant at the outflow boundary.

The Risø-A1-24 blade section is used for all rotors from $0.15d/2 < r < d/2$, the entire span of the blades [126]. No cylindrical or transition blade sections are used for the rotor blades. The selected aerofoil has a realistic thickness for hydrokinetic applications (24%) as opposed to the much thinner aerofoils used in most wind turbines, which would face structural difficulties in the high-load conditions experienced by tidal turbines. In addition, experimental aerodynamic data for this blade is available for a wide range of attack angles, which allows for the blade forces to be calculated at the non-optimal attack angles that are expected to occur when the rotors are operated in off-design blockage conditions. A cross-section of the Risø-A1-24 blade is shown in Figure 5.2, while Figure 5.3 presents the aerodynamic data used for the Risø-A1-24 blade. The aerodynamic data used was ex-

perimentally determined for $Re = 1.6$ x 10^6 using an aerofoil with leading edge roughness [126].

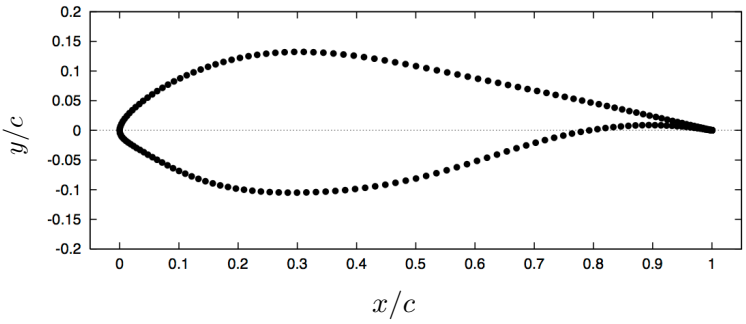

Figure 5.2: Cross-section of the Risø-A1-24 aerofoil (reproduced from Bertagnolio et al. [127]).

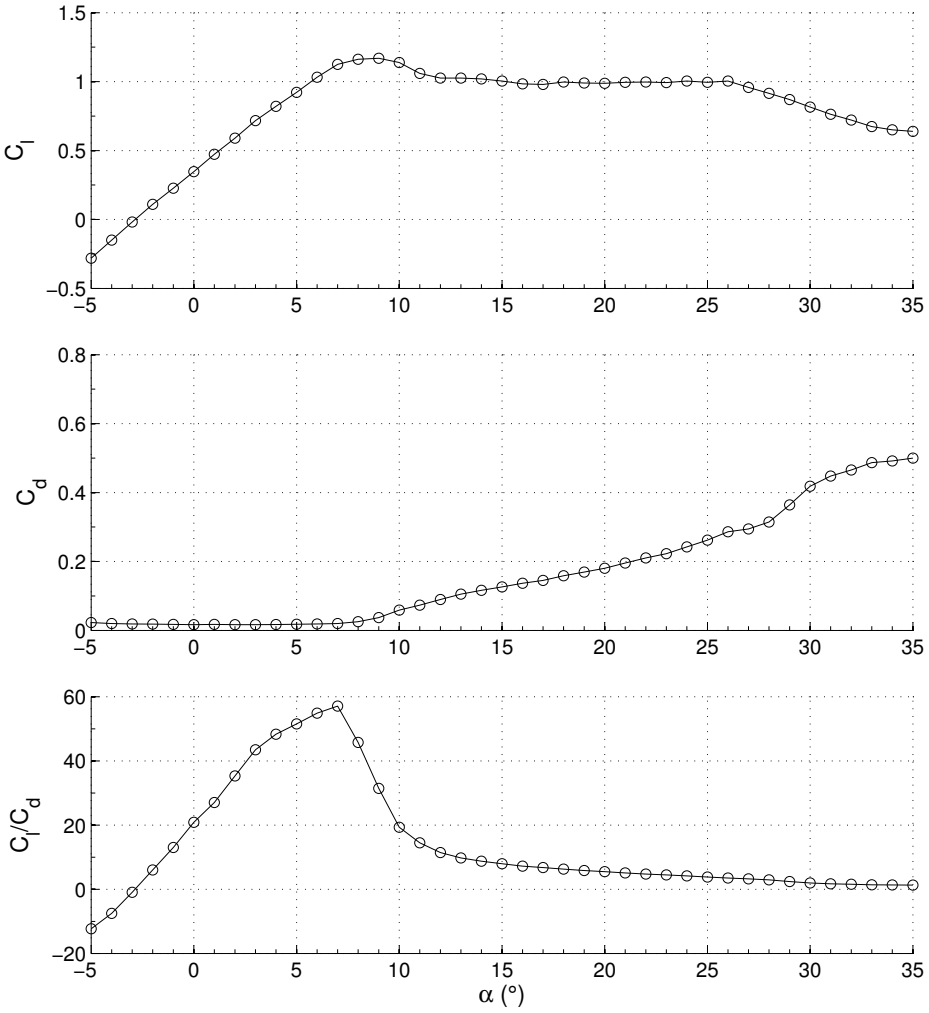

Figure 5.3: Risø-A1-24 lift and drag coefficients ($Re = 1.6$ x 10^6). Reproduced from reference [126].

The density of the water in the simulations is 1025 kg/m^3. The $k-\omega$ SST turbulence closure, discussed in Section 2.6.2, is used to close the steady-state, incompressible RANS equations for all simulations [92]. The SST model was chosen due to its use of the k - ω closure near the no-slip nacelle surface and the k - ϵ method in the remainder of the domain.

As discussed in Section 2.2.2 on page 32, the in-house RANS-BEM code and design tool used in this study requires the tip speed ratio, λ, and target constant local thrust coefficient, c_x, to be defined by the user. In the design optimisation process, the assigned values of these inputs are adjusted until a maximum value of the rotor power coefficient, C_p, is found. A maximum value of C_p indicates the optimal operating tip speed ratio and local thrust coefficient across the disc for the given blockage conditions, and the geometry returned by the design tool at this operating point is considered to be the hydrodynamically optimal blade design (the rotor design returned by the optimisation tool is different for every combination of c_x and λ).

A representative illustration of the design process is included in Figure 5.4. The figure includes maximum C_p values for a range of specified local thrust coefficients. All were computed using λ = 5 and the s/d = 4 domain (Domain 3). Due to the design optimisation which occurs in each simulation, each of the points plotted in Figure 5.4 corresponds to a different rotor design. It is seen from the results in Figure 5.4 that, for $\lambda = 5$, the optimal c_x is 2.4 for Domain 3. This process is repeated over a range of tip speed ratios until a global maximum C_p is found.

An upper limit of $\sigma = 0.95$ is set for the local solidity in Eqs. 2.24 and 2.28 in accordance with practical blade design constraints. A solidity greater than one would indicate that the rotor blades overlap, which would be physically possible but is undesirable from the perspective of pitch control. It is difficult to compare this solidity limit to those used in commercial tidal energy rotors because commercial rotor design information is not readily

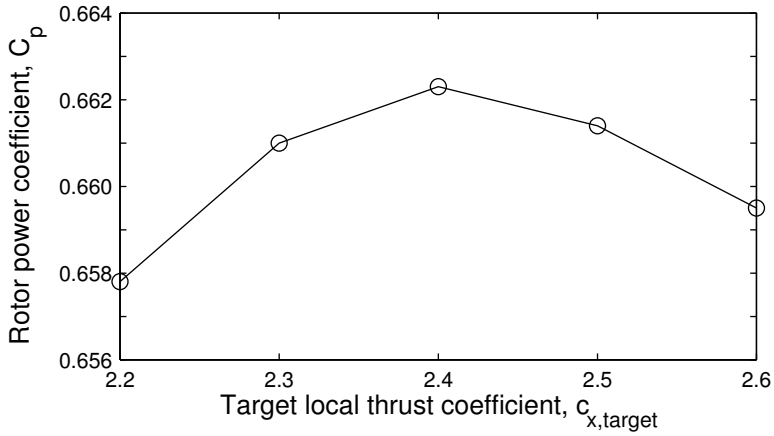

Figure 5.4: Representative case showing the dependence of C_p on target local thrust coefficient, $c_{x,target}$, during the rotor design process. Results shown are for $\lambda = 5$ with s/d = 4.

available. However, the imposed solidity limit is consistent with that used in a previous tidal turbine design study [53].

5.2.1 Tip Correction

The Prandtl tip correction factor, f, (defined in Eq. 2.33 in Section 2.2.2) is employed in the current RANS-BEM simulations. The tip correction, as discussed in Section 2.2.2, should be applied to the axial induction factor, a, when correctly implemented. However, previous works utilising the present RANS-BEM implementation have erroneously applied the tip-loss factor to the streamwise velocity component of the flow, u_x, [53, 54, 128]. Thus, the in-house RANS-BEM model has been adjusted to correct this error. In the current RANS-BEM model the axial flow velocity is passed directly from the CFD solver and, in contrast to analytical BEM models, an induction factor is not used. Thus, the Prandtl tip correction has been included in the simulations as follows.

Recall from Eq. 2.32 that the axial velocity, u_x, of the flow is defined as

$$u_x = U_\infty(1-a).$$

In the RANS-BEM simulations, u_x is a known value, as it is reported directly from the CFD solver. Inclusion of the Prandtl tip correction, f, gives the adjusted axial velocity, u'_x:

$$u'_x = U_\infty(1 - fa). \tag{5.1}$$

Combining Eqs. 2.32 and 5.1 yields

$$u'_x = U_\infty\left(1 - f\left(1 - \frac{u_x}{U_\infty}\right)\right). \tag{5.2}$$

Hence, the axial velocity adjusted for the influence of unsteady wake structures is determined using the Prandtl tip correction factor and the flow's axial velocity returned by the solver. The corrected tangential velocity, u'_θ is

$$u'_\theta = -\frac{U'^2_{rel}\sigma c'_\theta}{2u'_x}. \tag{5.3}$$

Similarly, the corrected relative velocity and angle of attack, assuming there is no yaw, are given by

$$U'_{rel} = \left(u'^2_x + \left(\Omega r - u'_\theta\right)^2\right)^{1/2}. \tag{5.4}$$

$$\alpha' = tan^{-1}\left(\frac{u'_x}{\Omega r - u'_\theta}\right) - \beta \tag{5.5}$$

The unknown variables in Eqs. 5.3 - 5.5 are u'_θ, U'_{rel}, c'_θ, and α'. Recall that c'_θ is a function of α'. In the RANS-BEM implementation, therefore, Eqs. 5.3 - 5.5 are solved iteratively within each CFD solution iteration until converged solutions for u'_θ, U'_{rel}, and α' are reached to a specified tolerance. At this point in the CFD solver iteration, the corrected change in pressure for each disc element may be computed using

$$\delta p' = \frac{1}{2}\rho U'^2_{rel}\sigma c'_x, \tag{5.6}$$

where c'_x is a function of the corrected angle of attack, α'. Finally, the corrected static

pressure jump and swirl velocity are applied to the flow, completing the CFD solver iteration.

In practice, the axial and tangential flow speeds are typically small compared to the rotational speed at the blade tips, and therefore the implementation of the Prandtl tip correction has little effect on the overall relative velocity magnitude, which is used to calculate the thrust and associated static pressure jump. However, the angle of attack is much more sensitive to small changes in u_x and u_θ. The lift and drag coefficients are therefore much more sensitive to change with the inclusion of the Prandtl tip correction than the relative velocity. Depending on the position on the C_l/C_d curve as a function of angle of attack, as well as whether α' is greater than or less than α, the performance of the rotor may increase or decrease when a Prandtl tip correction is applied.

5.3 Results and Discussion

The influence of lateral spacing on the optimal blade solidity and twist is discussed in Section 5.3.1. It is expected that for given blockage conditions, a rotor designed for operational blockage conditions will outperform rotors designed for different values of blockage. An array of RANS-BEM simulations in which each rotor design is operated in each of the 4 domains was completed to investigate this hypothesis. Results are presented and discussed in Section 5.3.2.

5.3.1 Rotor Designs

The blade optimisation tool is run for each of the 4 domains detailed in Table 5.1 using increments of $c_x = 0.1$ and $\lambda = 1$. Each rotor design computation (for a single combination of c_x and λ) required approximately 2 to 3 CPU hours to complete when run on a high-performance computing cluster. The optimum design for each domain is taken to be the design that results in the highest rotor power coefficient. The optimal tip speed ratio was

found to be $\lambda = 5$ for all of the cases. The maximum values of C_p obtained for each of the 4 domains during the blade optimisation process are listed in Table 5.2. Also included in Table 5.2 is the corresponding global thrust coefficient, C_t, required to achieve the maximum C_p for each domain.

Table 5.2: Maximum power coefficient and corresponding thrust coefficient for each domain

Domain	$C_{p,max}$	C_t at $C_{p,max}$
1	1.10	1.97
2	0.83	1.32
3	0.66	1.04
4	0.58	0.92

As expected, the power coefficient of the optimum rotors is highest for the domain with the lowest lateral spacing and highest blockage. Conversely, the unblocked rotor yields the lowest rotor efficiency. The thrust coefficient required to achieve $C_{p,max}$ increases as the rotor spacing decreases. The reasons for this are explained in Section 5.3.3, which includes a discussion of the mechanisms causing performance improvement in blocked flow.

It is notable that $C_{p,max}$ for the Domain 1 design is greater than 1. Garrett and Cummins showed that the maximum power coefficient for a single rotor operating in a bounded flow passage is $C_{p,max} = C_{p,Betz}(1 - B_l)^{-2}$, where $C_{p,Betz}$ = 16/27 is the Lanchester-Betz limit and $B = B_l = B_g$ is the ratio of the swept area of the rotor to the local channel cross-sectional area [36]. With this definition, the theoretical $C_{p,max}$ is greater than 1 if $B > 0.23$. The blockage for Domain 1 is $B = 0.314$, which leads to a theoretical maximum power coefficient of $C_{p,max} = 1.259$. Thus, the computed value of $C_{p,max} = 1.10$ is consistent with the theoretical results, falling below the theoretical limit due to viscous losses in the RANS-BEM simulations.

The power coefficient is calculated by normalising the power by the kinetic energy flux upstream of the rotor. However, in addition to extracting kinetic energy, the ability of a blocked flow to develop a pressure gradient from far upstream to far downstream enables pressure head to be extracted as well. This is most notable for highly blocked conditions,

and is the mechanism by which the power coefficient, as currently defined, is able to exceed unity. There is a change in fluid depth associated with the extraction of pressure head, but this is neglected in the present study.

The local solidity, $\sigma(r)$, and blade twist, $\beta(r)$, for the optimal rotor design for each lateral spacing are shown in Figures 5.5 and 5.6, respectively. In addition, sketches of the rotor blades corresponding to each design (for a 2-bladed rotor) are included in Figure 5.7.

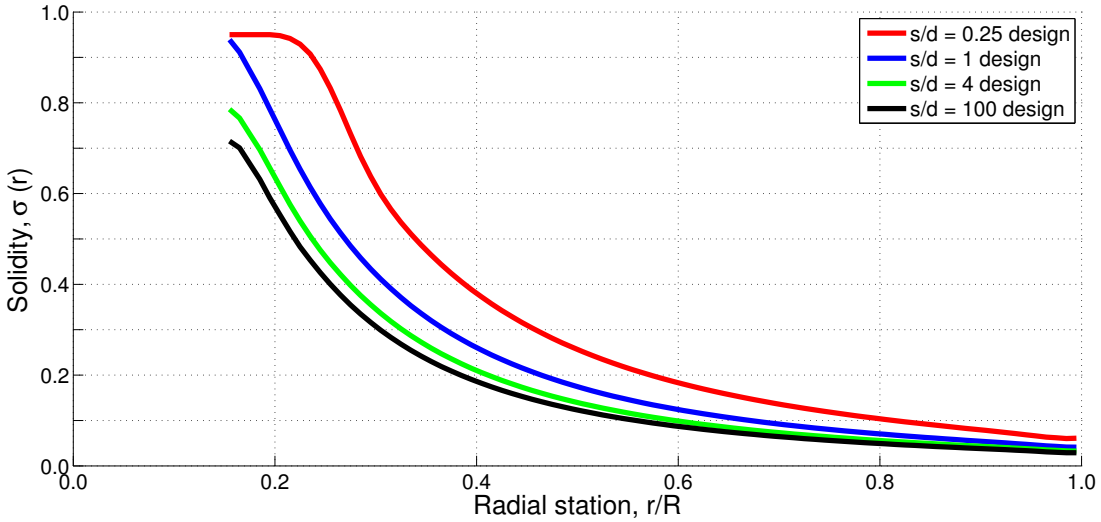

Figure 5.5: Comparison of the blade solidity, σ, for the 4 rotor designs.

It is seen in Figure 5.5 that the required local solidity increases as the spacing between rotors decreases. The upper limit for the local solidity ($\sigma = 0.95$) is reached for the design with the highest blockage conditions ($s/d = 0.25$). This limit was imposed to restrict blade overlap. If the blades were allowed slight overlap, it is expected that the maximum C_p for this case would be higher than the values computed with the solidity limit.

The optimal solidity for the closest rotor spacing is approximately double the solidity for the unblocked rotor design through most of the blade span. The results indicate that local blockage conditions have a large effect on optimal solidity and suggest that it is important to adapt rotor solidity for high blockage operating conditions in order to exert greater thrust

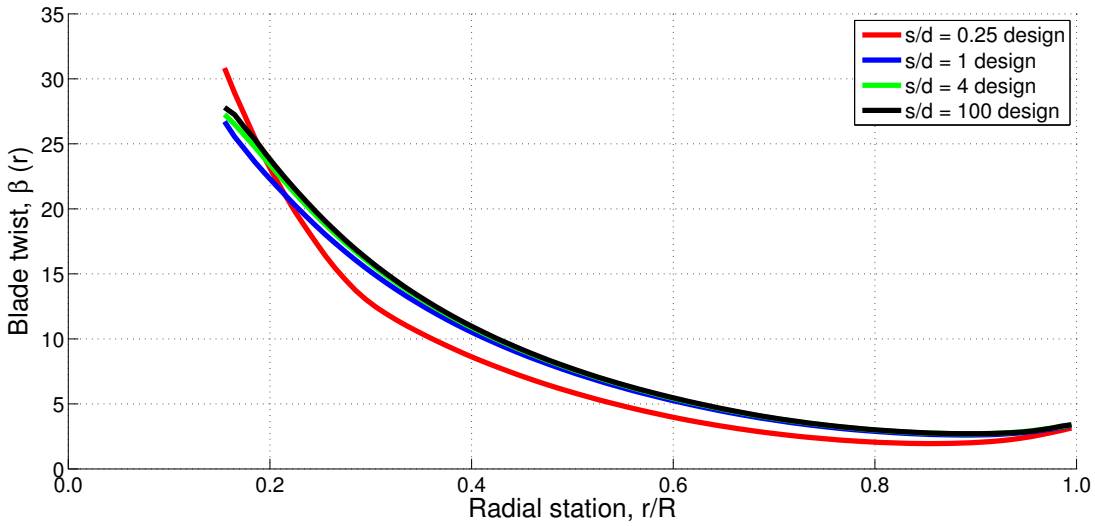

Figure 5.6: Comparison of the blade twist, β, for the 4 rotor designs.

and extract power with maximum rotor efficiency. This is further discussed in Section 5.3.3.

The effect of local blockage on the local blade twist is not as pronounced as its effect on the local solidity. Still, the results in Figure 5.6 show that β generally decreases as the rotor spacing is reduced. The optimal twist near the blade root for the closest intra-rotor spacing, $s/d = 0.25$, differs from the pattern seen for the other rotors. This is due to the imposed limit on solidity in the vicinity of the blade root for this rotor.

Contours of the streamwise velocity, u_x, on a horizontal centre plane for each of Domains 1-4 are shown in Figures 5.8a-5.8d, respectively. The contours depict the streamwise velocity when the optimised rotor is operated in its design blockage conditions at its design tip speed ratio ($\lambda = 5$ for all cases). The entire cross-stream width of Domains 1-3 is shown in Figures 5.8a-5.8c, whilst Figure 5.8d only shows part of Domain 4 due to its large width. The disc area in each of the figures is kept constant to allow for direct visual comparison of the varying levels of disc spacing.

The effects of the lateral rotor spacing on the streamwise velocity are quite evident. The speed of the flow bypassing the rotor becomes faster with each reduction in lateral rotor

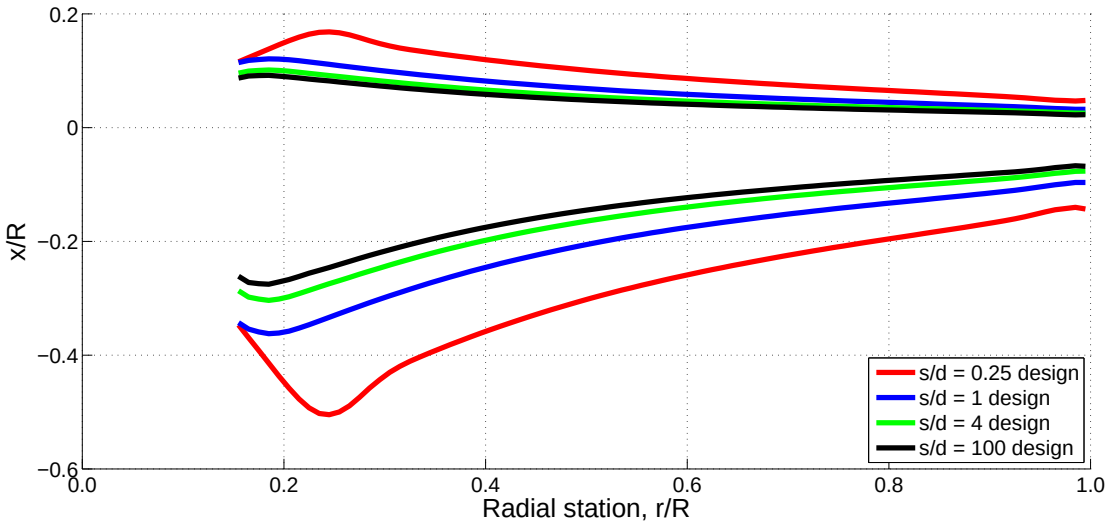

Figure 5.7: Sketch of the rotor designs. The leading edge (top) and trailing edge (bottom) of the rotor blade for a 2-bladed rotor are shown for each rotor design.

spacing. In addition, u_x downstream of the rotor is much lower for low lateral rotor spacing. The observed increase in momentum reduction across the rotor is consistent with the higher thrust applied by high blockage rotors to achieve maximum power.

The resolution upstream of the rotor as well as in the wake has been determined to have little effect on the optimised rotor design or the computed rotor loads. Thus a low upstream resolution and a low wake resolution are used in the simulations to maintain a low computational requirement. The effects of low resolution are visible in the contours in Figure 5.8, particularly for the domains with the highest blockage. Symmetric flow on either side of the nacelle is expected, but the streamwise velocity is not perfectly symmetric, particularly for the downstream flow in Figure 5.8a. However, increasing the upstream and wake resolution results in negligible change in computed thrust and power coefficients for each of the domains.

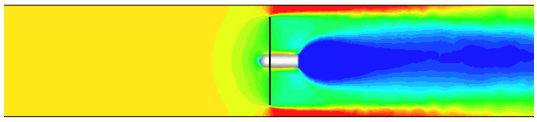

(a) Domain 1 ($s/d = 0.25$)

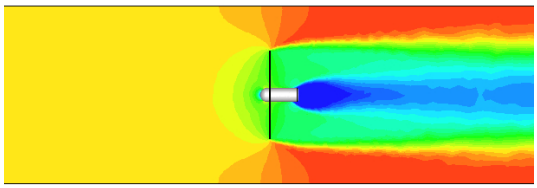

(b) Domain 2 ($s/d = 1$)

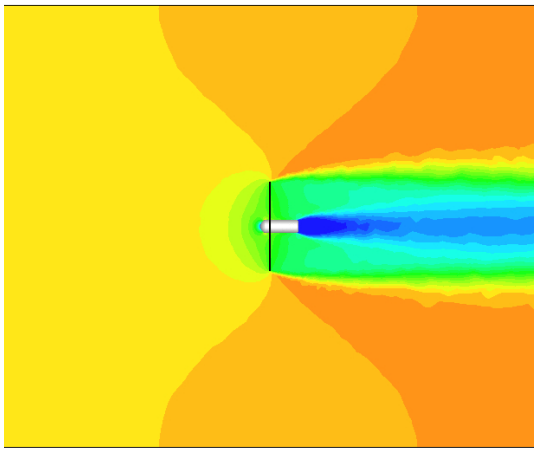

(c) Domain 3 ($s/d = 4$)

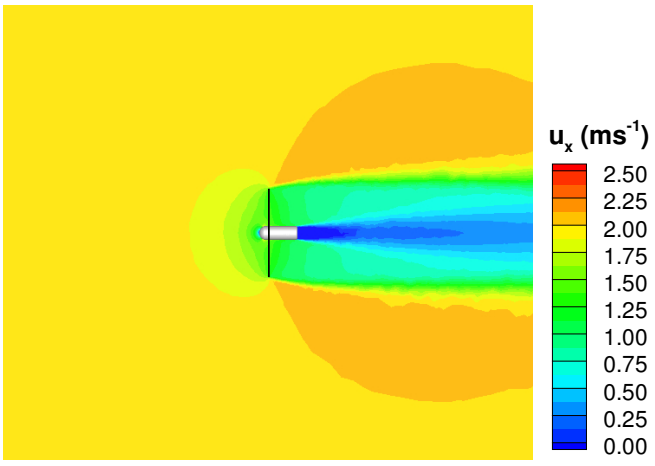

(d) Domain 4 ($s/d = 100$)

Figure 5.8: Contours of streamwise velocity, u_x, on the horizontal centre plane for the design rotor in each of the 4 domains. The flow is from left to right. The entire width of the domain is shown in Figures 5.8a - 5.8c. However, due to the size of Domain 4, only a fraction of the width of this domain is shown in Figure 5.8d. Note that the full range of velocity is not shown.

5.3.2 Rotor Performance in Off-Design Blockage Conditions

Next, a series of rotor simulations is completed in which each of the optimised rotors discussed in Section 5.3.1 is operated in the domain for which the rotor was designed as well as in each of the other domains used in the present study. For each combination of rotor design and domain, RANS-BEM simulations are performed over a range of tip speed ratios, allowing for a peak C_p to be determined. No further blade optimisation was conducted during this phase of the study.

The power coefficient curves resulting from the series of simulations are shown in Figure 5.9. Figure 5.9a shows the resultant C_p curve for each of the rotor designs when simulated in Domain 1, the domain with the lowest lateral spacing and the highest blockage ratio. Similarly, the results for each rotor design when simulated in Domains 2 - 4 are presented in Figures 5.9b - 5.9d, respectively.

All of the rotors exhibit improved performance with each reduction in lateral rotor spacing, regardless of whether the rotor is operating in design or off-design blockage conditions. Therefore, operating a rotor under highly blocked conditions improves performance irrespective of the rotor blade design. It is also seen in Figure 5.9 that for low blockage rotor designs, a higher tip speed ratio is required in order to achieve maximum C_p as the lateral spacing is reduced from the design spacing. Operating at increased tip speed ratio (i.e. spinning faster) in high blockage conditions allows rotors designed for lower blockage to achieve greater thrust and thus improved power at the new blockage condition.

The results in Figure 5.9a indicate that although the rotor efficiency for the virtually unblocked design improves more than 50%, from $C_p = 0.58$ to $C_p = 0.90$, when moved from unblocked to highly blocked flow (Domain 4 to 1), the power coefficient remains significantly lower than that of the rotor specifically designed for operation in high blockage flow, $C_p = 1.14$.

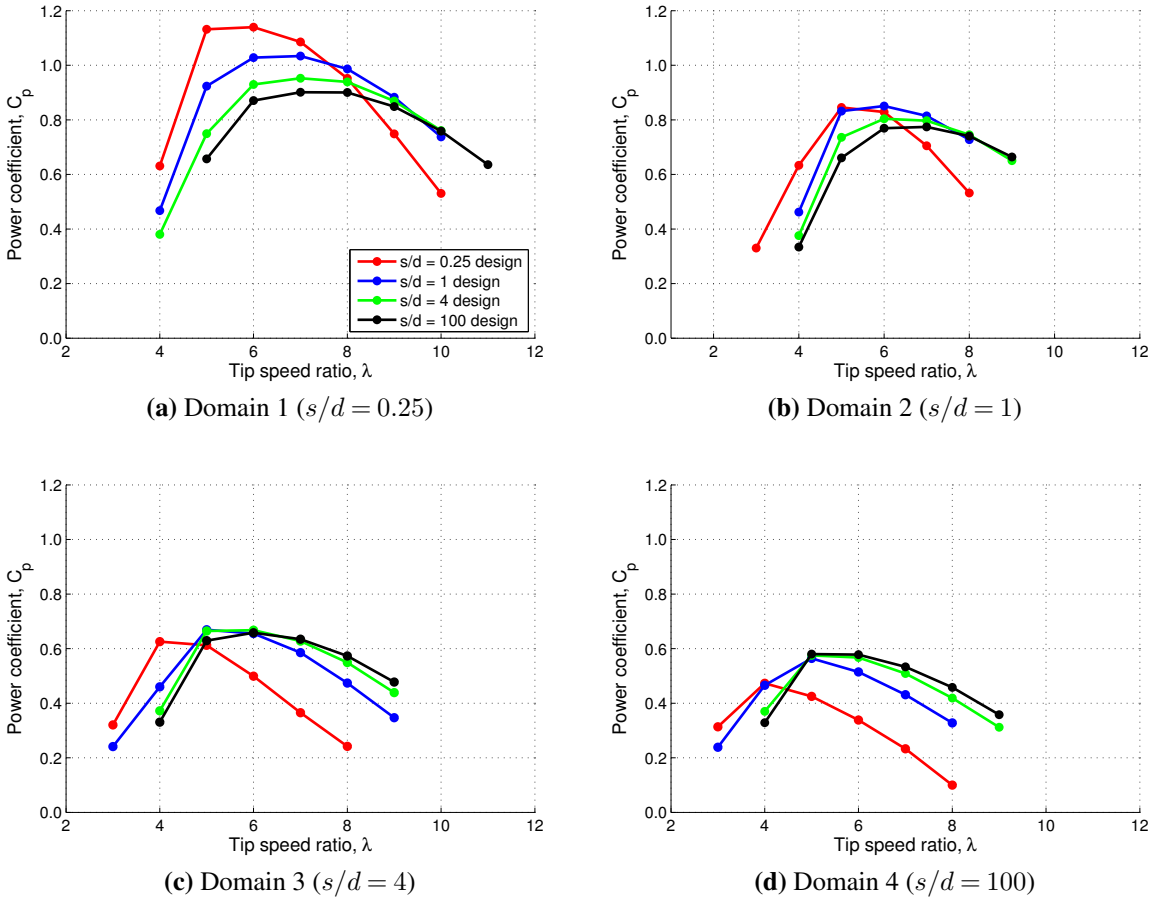

(a) Domain 1 ($s/d = 0.25$)

(b) Domain 2 ($s/d = 1$)

(c) Domain 3 ($s/d = 4$)

(d) Domain 4 ($s/d = 100$)

Figure 5.9: Power coefficient curves for each of the 4 rotor designs when operated in (a) Domain 1, (b) Domain 2, (c) Domain 3, and (d) Domain 4.

Conversely, the results presented in Figure 5.9d indicate that rotors designed for high blockage conditions are far inferior to the rotors designed for low blockage and unblocked flow when all are operated in minimal blockage conditions.

The relative performance for off-design rotor operation is shown in Figure 5.10. In this figure, the maximum power coefficients achieved for each of the 4 rotor designs operating at a given lateral spacing are normalised by the maximum power coefficient achieved by any rotor design at that spacing. For every spacing, the rotor with the highest power coefficient is found to be the rotor designed for the given spacing (as intended).

The rotors designed for low blockage see the greatest performance decrement when op-

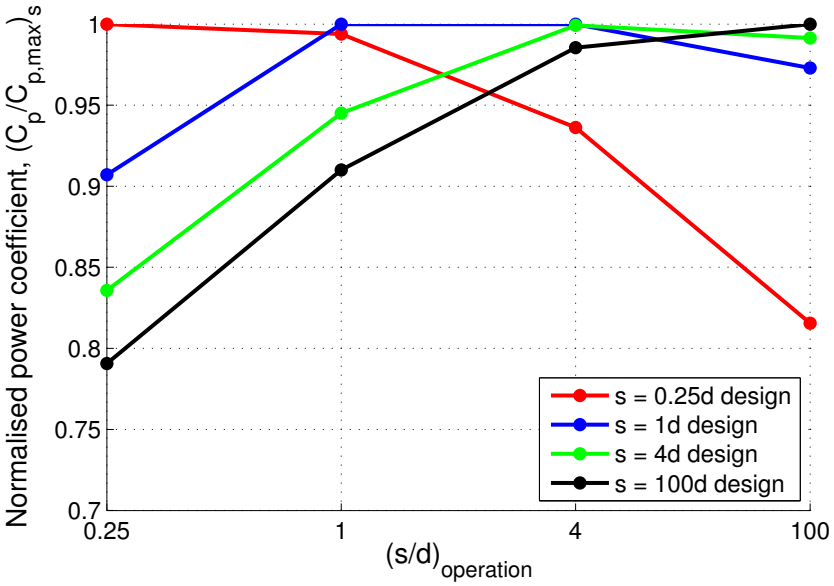

Figure 5.10: Maximum power coefficient for each rotor design for lateral rotor spacings $0.25 < s/d < 4$. Power coefficients are normalised with respect to the maximum power coefficient achieved by any rotor for that spacing.

erated in the domain with the highest blockage, Domain 1 ($s/d = 0.25$). The unblocked rotor design has the worst performance in this domain and has a decrement of 21% when compared to the rotor designed for Domain 1. Conversely, the rotor designed for high blockage conditions has the greatest power coefficient decrement when operated in Domain 4 ($s/d = 100$), which is the virtually unblocked domain. The maximum power coefficient for the rotor designed for Domain 1 is 19% lower than the maximum power coefficient for the Domain 4 rotor design when both are operated in Domain 4. The results indicate that all devices perform within 21% of the optimum achievable for a given spacing. Notably, the device designed for $s/d = 1$ does not perform more than 9% below the optimum achievable at any spacing.

Operating a rotor in off-design blockage conditions has significant effects on the bypass and wake flow velocities. These effects are seen in Figure 5.11. The maximum power coefficient and corresponding thrust coefficient for each of the cases shown in Figure 5.11 are tabulated in Table 5.3.

Table 5.3: Maximum power coefficient and corresponding thrust coefficient for each domain

s_{design}	$s_{operation}$	$C_{p,max}$	C_t at $C_{p,max}$
$0.25d$	$1d$	0.84	1.76
$1d$	$1d$	0.85	1.46
$4d$	$1d$	0.80	1.26
$100d$	$1d$	0.77	1.24

The rotor in Figure 5.11a is operating in lower blockage than it was designed for. The rotor has high solidity and has to apply greater than optimal thrust on the flow to produce maximum power. There is therefore greater resistance on the upstream flow than there is for the design rotor (Figure 5.11b), resulting in increased streamwise velocity in the bypass flow and decreased streamwise velocity in the wake. This, in turn, creates greater shear and an increase in mixing losses between the bypass and core flows in the wake.

The rotors in Figures 5.11c and 5.11d are operating in higher blockage than they were designed for. These rotors have lower than optimal solidity and are unable to apply a high enough thrust to achieve the optimum power generation possible for this domain. As these rotors impose less resistance on the flow than the rotor designed for the domain, the bypass flow speed is lower than that for the design rotor and the streamwise velocity of the flow in the wake is higher. Therefore, there is less shear between the bypass and core flows in the wake and hence reduced mixing losses.

5.3.3 Coupled Effects of Blockage and Design on Rotor Performance

Curves showing power coefficients as a function of coefficient of mass flow rate, $C_{\dot{m}}$, for rotors operating in Domains 1 ($B = 0.314$) and 4 ($B \approx 0$) are included in Figure 5.12. Here, $C_{\dot{m}}$ is defined as the ratio of mass flow rate through the rotor disc to the mass flow rate through the projected disc area at the domain inlet ($\dot{m}_{inlet} = \rho U_\infty A_{disc}$). Because ρ and the rotor disc area remain constant in all simulations, $C_{\dot{m}}$ is effectively the ratio of the mean velocity through each disc to the upstream flow speed. For steady uniform flow,

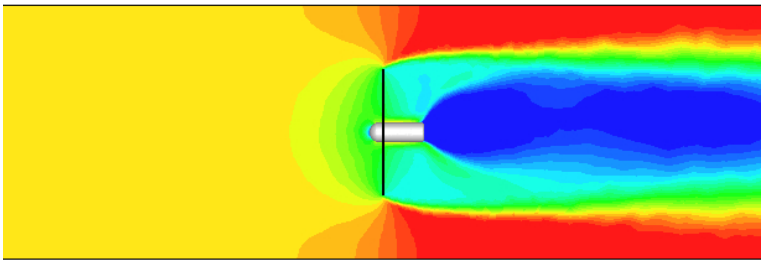

(a) $s/d = 0.25$ design operating in $s/d = 1$ domain

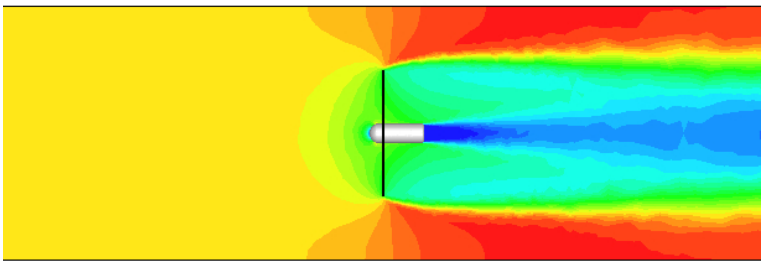

(b) $s/d = 1$ design operating in $s/d = 1$ domain

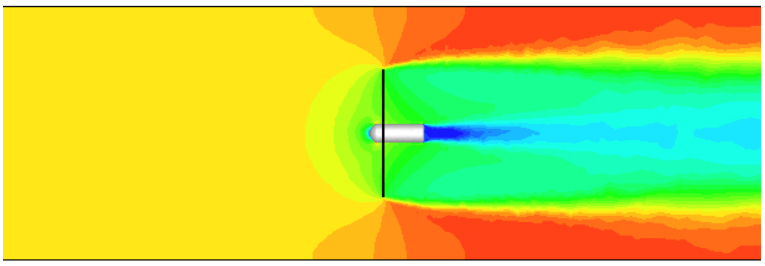

(c) $s/d = 4$ design operating in $s/d = 1$ domain

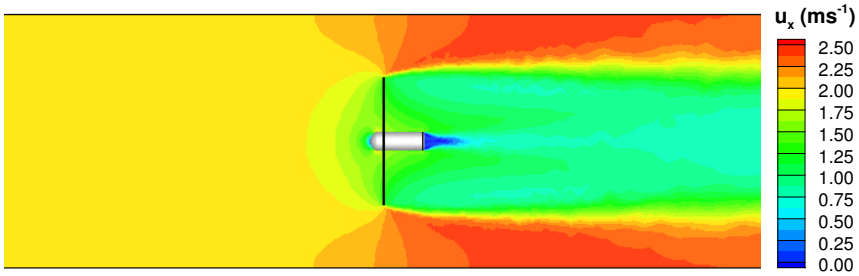

(d) $s/d = 100$ design operating in $s/d = 1$ domain

Figure 5.11: Contours of streamwise velocity, u_x, on the horizontal centre plane. Figures 5.11a - 5.11d show contours for the $s/d = 0.25$, $s/d = 1$, $s/d = 4$, and $s/d = 100$ rotor designs, respectively, operating in the $s/d = 1$ domain (Domain 2) at the optimal tip speed ratio for each rotor in Domain 2.

as considered in this section, $C_{\dot{m}}$ is related to the rotor-averaged axial induction factor as $1 - a$.

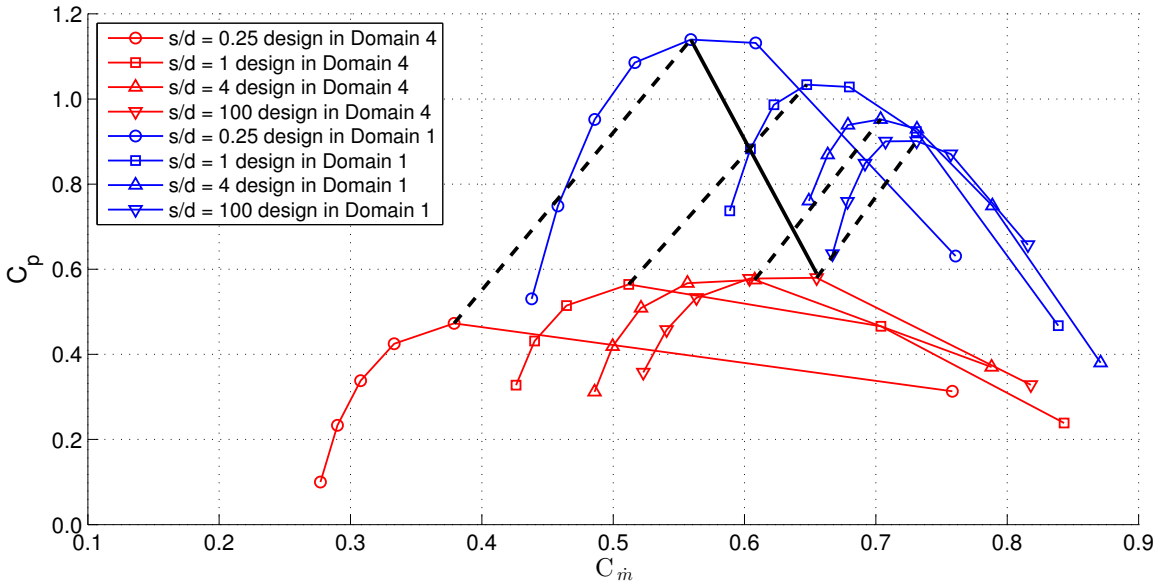

Figure 5.12: C_p variation with $C_{\dot{m}}$. The power curves for rotors operating in Domain 4 (virtually unblocked conditions) are shown in red and those operating in Domain 1 (high blockage conditions) are blue. The solid black line connects the peak operating points achieved by any rotor design for each blockage ratio.

As previously discussed, the peak operating point for each blockage ratio is achieved by the rotor designed for that configuration. It may be shown using the Garrett and Cummins result [36] that when blockage is increased, the velocity through the actuator disc at the peak power point for the new blockage will be lower than for the peak power point for a lower blockage configuration. The current results are in agreement with the Garrett and Cummins theory, as the solid black line shows.

The dashed lines in Figure 5.12 connect the peak operating points achieved by each individual rotor in the two blockage conditions shown. It is seen from these dashed lines that, for each specific rotor design, $C_{\dot{m}}$ (and therefore the mean velocity) through the rotor at the peak operating point increases as blockage increases. It is notable that peak performance for a specific rotor design occurs with higher $C_{\dot{m}}$ through the rotor at high blockage than at low blockage, whereas overall peak performance achieved by any rotor occurs with lower $C_{\dot{m}}$ at high blockage.

To understand these results, we must first understand the fundamental mechanism through which blockage can improve rotor performance. Nishino and Willden [129] provide the following explanation: increased blockage results in increased bypass flow acceleration and a corresponding increase in pressure head drop in the bypass flow passages. The pressure head in the bypass and core flow regions must be in equilibrium both far upstream and far downstream of the rotor plane. Hence, the increased pressure head drop in the bypass leads to an increased pressure head drop in the core flow and thus also across each disc, which in turn results in increased thrust and power coefficients. Thus, the principal drivers for rotor performance in blocked conditions are the magnitude of the flow acceleration and corresponding pressure head drop in the bypass flow region. For further explanation of this mechanism, see Nishino and Willden [129]. Note that this explanation provides a limit to what can be achieved for a perfect energy extractor, not what a specific rotor might experience.

For a given rotor design, an increase in blockage results not only in greater acceleration in the bypass regions, but also in greater resistance to the flow (due to the rotor wake expansion/bypass flow streamtube constriction) in the bypass regions. This resistance results in greater flow being pushed through the swept rotor area; hence the increase in $C_{\dot{m}}$ and therefore mean velocity through the rotor when blockage is increased and the rotor design is unchanged.

However, while operating a rotor designed for low blockage conditions in higher blockage conditions will improve $C_{p,max}$ for that rotor, a further adjustment must be made to achieve the overall $C_{p,max}$ for the higher blockage condition. The thrust the rotor applies to the flow must be increased in order to counter the increased resistance to the flow in the bypass region. This will reduce flow through the rotor and further increase the acceleration and pressure head drop in the bypass region, thereby improving C_p. A simple way to increase the thrust applied by a rotor is to increase its solidity. This helps explain why, in the rotor

design process discussed in Section 5.3.1, the solidity for the rotor designed for the highest blockage conditions was significantly larger than that for the rotor designed for unblocked conditions.

Figure 5.13 includes curves of mean thrust coefficient as a function of tip speed ratio for the cases shown in Figure 5.12. It is seen in Figure 5.13 that when the operational spacing between rotors is held constant, C_t for a given tip speed ratio increases as the design spacing for the rotor decreases (and hence as the rotor solidity increases). In Domain 1, the domain with the highest blockage ratio, this increased thrust for increased rotor solidity leads to improved $C_{p,max}$. However, in the virtually unblocked Domain 1, it results in decreased $C_{p,max}$ (see Figure 5.9).

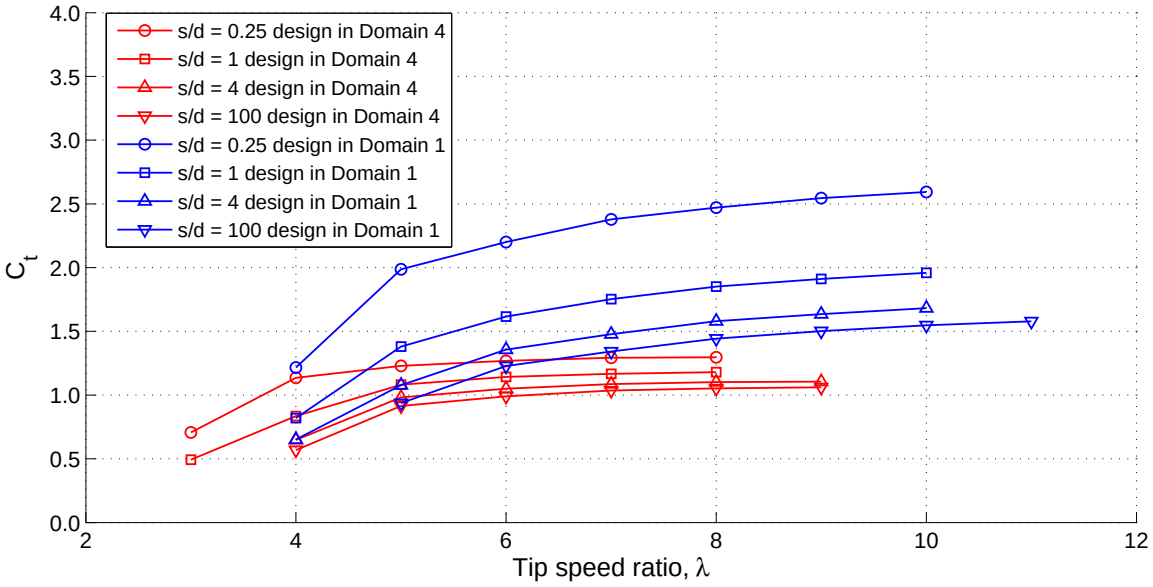

Figure 5.13: C_t variation with λ for rotors operating in Domains 1 (blue) and 4 (red).

5.3.4 Radial Variation of c_x

The discussion thus far has been limited to global rotor properties, including C_p and C_t. In this section, the radial variation of the local thrust coefficient will be discussed, for rotors operating in both design and off-design blockage conditions.

Rotors Operating in Design Blockage Conditions

Recall from Section 5.3.1 that, during the rotor design process, the optimal tip speed ratio was defined to be $\lambda = 5$ for each of the 4 cases. It is therefore notable that the peak operating point for the $s/d = 0.25$, 1, and 4 rotors when operating in design blockage conditions occurred not at $\lambda = 5$, but at $\lambda = 6$, as seen in Figures 5.9a-5.9c. Still, the performance at $\lambda = 5$ for these three cases is only slightly lower than the peak at $\lambda = 6$.

Inspection of the radial variation in local thrust coefficient, c_x, helps explain the apparent discrepancy in optimal tip speed ratio. The rotor design tool employed in the present work uses the assumption that optimal rotor performance is achieved when c_x is constant across the blade span. Belloni [55] showed that this assumption, while acceptable, is not strictly true. In this study, it was shown that both blade-element discs with constant c_x as well as discs with increased c_x in the blade tip region can achieve the maximum power output, creating a 'power plateau' rather than a discrete peak operating condition. Hence, it is possible to achieve similar, if not slightly greater, power when the local thrust coefficient is allowed to vary in the radial direction.

Radial variation in c_x is plotted for each the 4 rotors operating in design blockage conditions in Figure 5.14. Data for 5 different operating tip speed ratios are included in the plots, and the design c_x is denoted by the dashed lines. The region from $0 < r/R < 0.15$ does not contain data as this is the nacelle region.

For rotors designed for $s/d \geq 1$, c_x for the $\lambda = 5$ cases is nearly constant, as expected because the design process targeted constant c_x, with a slight aberration for the blade element closest to the blade tip. Also, c_x for this tip speed ratio is approximately equal to the design c_x for the rotors, which is expected, as this is the same tip speed ratio the rotors were designed for. The exception for $\lambda = 5$ is the rotor designed for and operating in Domain 1 ($s/d = 0.25$). For this rotor, there is non-constant c_x in the vicinity of the blade

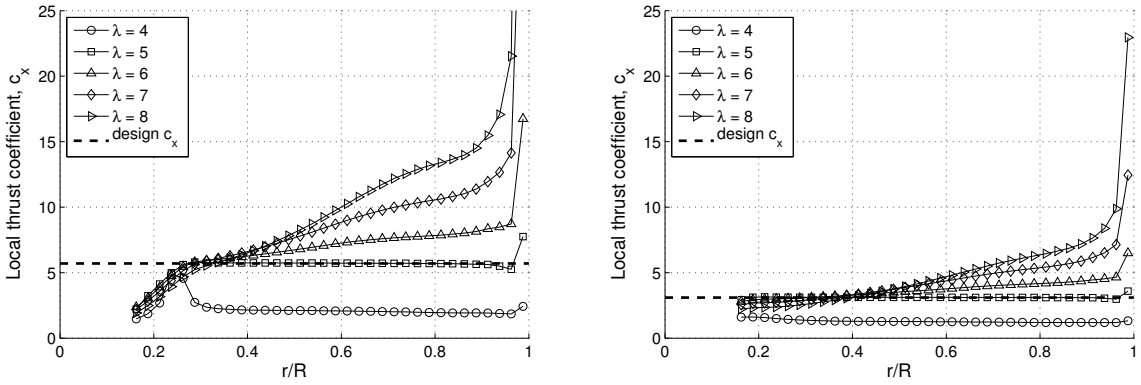

(a) Domain 1 ($s/d = 0.25$) **(b)** Domain 2 ($s/d = 1$)

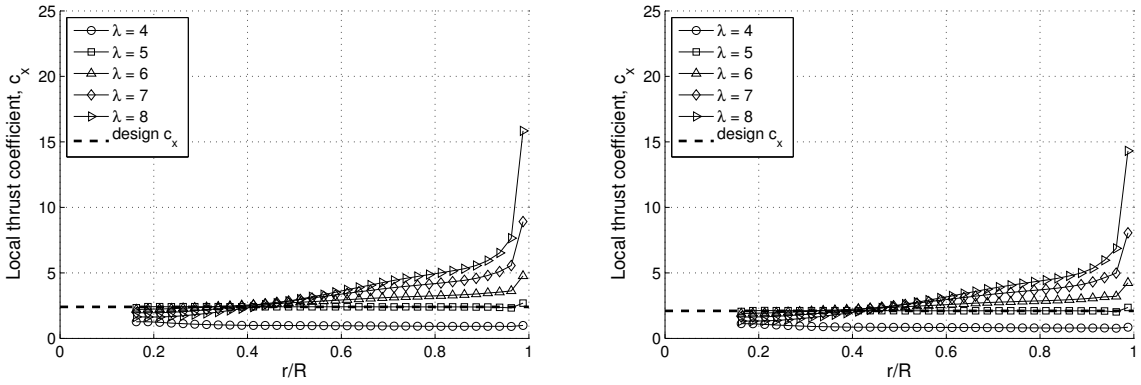

(c) Domain 3 ($s/d = 4$) **(d)** Domain 4 ($s/d = 100$)

Figure 5.14: Spanwise variation of c_x for rotors operating in their respective design domains.

root for $\lambda = 5$ (see Figure 5.14a). This, and deviation from the patterns seen in results for the other rotors near the blade root for all tip speed ratios, is a result of the solidity limit imposed in the root region of the $s/d = 0.25$ rotor design.

c_x for the $\lambda = 4$ simulations is also nearly constant for most of the rotors. However, the magnitude is much less than that of the design tip speed ratio for this lower than optimal rotational speed. This is because this rotor is unable to impart sufficient thrust on the flow, which results in a lower than optimal C_p.

Conversely, the rotors operating above the design tip speed ratio (the $\lambda = 6$, 7, and 8 cases) all experience increases in c_x as r/R increases, with the magnitude of c_x in the tip region increasing with λ for each of these cases. For the $\lambda = 6$ case, this non-constant variation in

local thrust coefficient enables the rotor to achieve a power coefficient slightly higher than the design power coefficient for the $s/d = 0.25$, 1, and 4 rotors, confirming the findings of Belloni [55]. For even higher tip speed ratios, however, the power coefficient drops, despite the extreme radial variations in c_x seen for $\lambda = 7$ and 8. For these high tip speed ratios, the rotor applies greater than optimal thrust to the flow (see Figures 5.9 and 5.13).

Although the $\lambda = 5$ and $\lambda = 6$ cases achieve similar power, the increased c_x as r/R increases for the $\lambda = 6$ case is not desirable from a structural standpoint, and it is thus preferable to operate at the lower of the two tip speed ratios.

Rotors Operating in Off-Design Blockage Conditions

It is seen in Figures 5.9a-5.9d and 5.10 that, for some blockage conditions, rotors operating in off-design conditions are capable of achieving maximum power coefficients that are very near the maximum power coefficient achieved by the rotor designed for the given domain. For example, the $s/d = 0.25$ rotor design, when operated in Domain 2 ($s/d = 1$) achieves a $C_{p,max}$ that is only 1% lower than the maximum achieved by the rotor designed for Domain 2.

Although the rotor power coefficients for these two cases are similar, the local thrust coefficients are quite different. The radial variation in local thrust coefficient is included in Figure 5.15.

c_x for the rotor designed for operation in Domain 1 is nearly twice that for the rotor designed for Domain 2 when each is operated at their respective $C_{p,max}$ in Domain 2. These results agree with the conclusions stemming from an analysis of Figures 5.11a and 5.11b; the higher solidity of the $s/d = 0.25$ design causes this rotor to apply greater than optimal thrust on the flow in order to achieve maximum power. This results in a larger than optimal reduction in momentum downstream of the rotor and, in turn, greater shear between the core and bypass flows in the wake, causing increased mixing losses. In addition, the

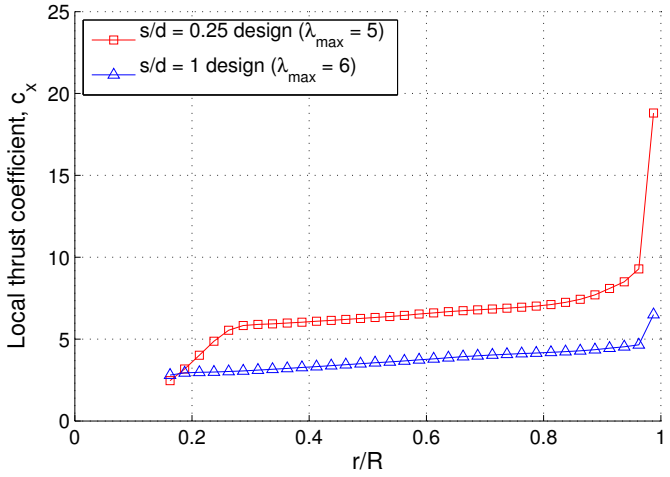

Figure 5.15: Radial variation of streamwise loading experienced at the peak operating tip speed ratio for the $s/d = 0.25$ and $s/d = 1$ rotor designs operating in Domain 2 ($s/d = 1$).

higher solidity rotor presents practical problems; more material is required to construct the blades and the increase in applied thrust necessitates the use of a material capable of withstanding higher blade loads.

5.4 Comparison of RANS-BEM and Actuator Line Results

Infinite-length fence simulations of the $s/d = 1$ rotor design operating in the $s/d = 1$ domain (Domain 2) were also completed for a range of tip speed ratios using the actuator line model. The boundary conditions for the actuator line simulations were the same as the boundary conditions for the RANS-BEM simulations. The mesh element length was $e = 0.25$ m in the rotor region and the growth rate of the mesh was 1.1 in the wake region. The rotor blades were simulated using actuator lines consisting of 40 collocation points in a cosine distribution along the blade span and 200 time steps were simulated for each rotor revolution.

No tip correction was used in the infinite-fence actuator line simulations. This is because,

although the Shen et al. tip correction ([121]) improved the results for the NREL Phase VI rotor simulations, this correction relies on experimental wind turbine results and its applicability to tidal turbines is unknown.

In addition, the Shen et al. tip correction attempts to account for the fact that discrepancies may exist between 2D stationary blade aerodynamic data, which are used for both BEM and actuator line models, and the aerodynamic properties of 3D rotating blades. This is a different objective than that of the Prandtl tip correction, which aims to add the influence of 3D helical vortices shed from the blade tips to the load predictions in steady state calculations, as these calculations are unable to directly account for the presence of these unsteady wake structures.

As the RANS-BEM and actuator line models both utilise blade-element theory, as well as 2D aerodynamic data, it is assumed that both modelling techniques encounter similar error due to the 2D blade approximation employed in blade-element theory. Therefore, a steady-state RANS-BEM result which employs the Prandtl tip correction to account for unsteady wake effects should be directly comparable to an actuator line model with no tip correction, as these unsteady wake effects will be present in the actuator line model solution.

5.4.1 Power Coefficient Curves

The power coefficient curve for the actuator line model with no tip correction is compared with the RANS-BEM results (computed using the Prandtl tip correction) in Figure 5.16 for the $s/d = 1$ rotor operating in its design domain.

The actuator line model results show good agreement with the RANS-BEM results. The power coefficients for $\lambda = 4$ and $\lambda = 5$ resulting from the actuator line simulations are within 3% of the power coefficients computed using RANS-BEM and predict slightly lower power output than the RANS-BEM results. At higher tip speed ratios, the actuator line model predicts slightly higher power than the RANS-BEM power.

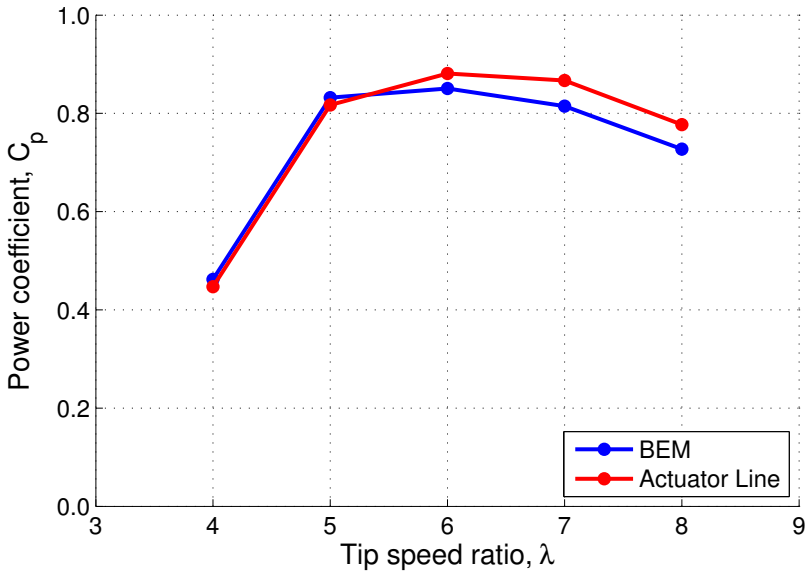

Figure 5.16: Power coefficient curves for BEM and actuator line simulations of the rotor designed for intra-rotor spacing $s/d = 1$ operating in its design blockage condition.

5.4.2 Radial Distribution of U_{rel} and α

Inspection of the radial distribution of the relative velocity, U_{rel} and angle of attack, α, help explain the differences in C_p for the actuator line and RANS-BEM simulations. In addition, these results demonstrate the effect that the Prandtl tip correction has on U_{rel} and α. Recall from Section 2.2.2 that the Prandtl tip correction is applied to the axial induction factor, thus increasing the magnitude of the axial velocity through the rotor plane. The Prandtl tip correction, however, has little effect on the relative velocity of the blade elements. This is because, although it's implementation results in adjusted values of u_x and u_θ, these velocities, for relatively small attack and pitch angles and typical tip speed ratios, are much smaller than the relative velocity component which arises due to the angular velocity of the blade element.

The small influence of the Prandtl tip correction on the computed relative velocity for RANS-BEM simulations is visible in Figure 5.17. This figure includes relative velocity as a function of radial location on the blade for $\lambda = 4$, 5, 6, 7, and 8 for the $s/d = 1$ rotor

operating in its design domain. RANS-BEM results, both with and without the Prandtl tip correction, and time-averaged actuator line model results are included.

There is negligible difference in the two sets of RANS-BEM results, confirming that the tip correction, as expected, has little effect on U_{rel}. The time-averaged actuator line results compare well with the RANS-BEM results, although these simulations predict slightly lower relative velocity in the root sections of the blade than the RANS-BEM simulations.

Figure 5.18 includes results for angle of attack as a function of r/R for the same operating cases. Again, RANS-BEM results with and without the Prandtl tip correction as well as time-averaged actuator line results are included in the figure.

It is evident from the results in Figure 5.18 that the Prandtl tip correction has a significant effect on the angle of attack in the tip regions of the blades for the RANS-BEM simulations. This is because at small attack angles, the change in U_{rel} that results from the application of Prandtl's correction results in a significant shift in the resulting relative flow direction. The lift and drag coefficients, used in Eqs. 2.17 and 2.18 to calculate the lift and drag on the blade elements, are sensitive to small perturbation in α, as seen for example in the aerodynamic data presented as a function of α in Figure 5.3. Therefore, although the Prandtl tip correction has little influence on the relative velocity at the blade, it nevertheless has a significant effect on the power output of the rotor. Further, the addition of the Prandtl tip correction to a BEM model does not always lead to reduced power output. Rather, the effect of the tip correction on the output is dependent in part on the aerodynamic properties and the geometry of the specific aerofoil employed. If the tip correction causes the angle of attack to shift to a value which corresponds with a reduced lift to drag coefficient ratio (C_l/C_d), the power output may indeed be reduced. However, it is entirely possible that for some cases, the shift in α resulting from application of the Prandtl tip correction will correspond to an increased value of C_l/C_d, thus increasing C_p for the rotor. Hence, it

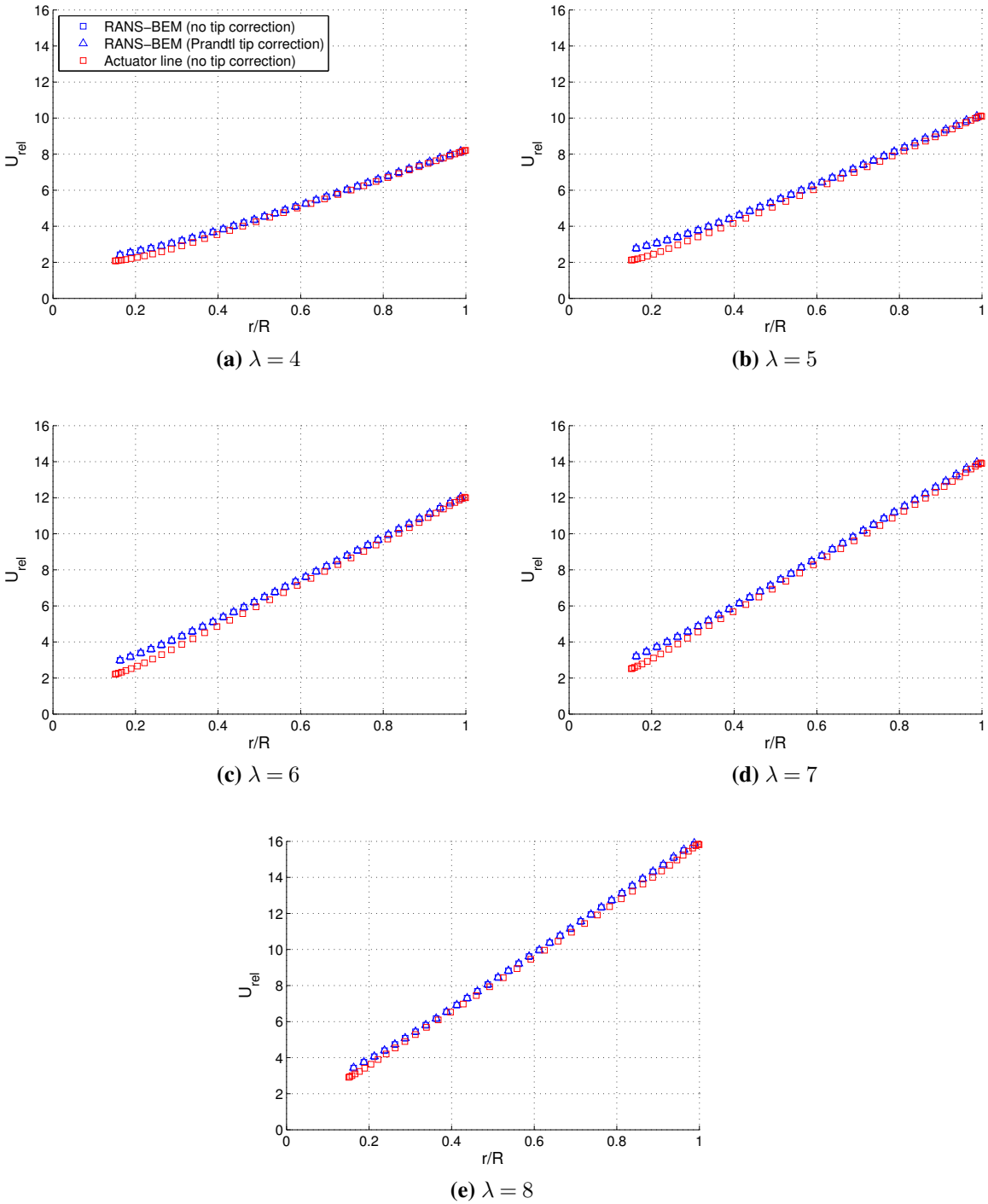

(a) $\lambda = 4$ **(b)** $\lambda = 5$

(c) $\lambda = 6$ **(d)** $\lambda = 7$

(e) $\lambda = 8$

Figure 5.17: Comparison of radial variation in relative velocity at the blade for RANS-BEM simulations (both with and without the Prandtl tip correction) and actuator line simulations of the $s/d = 1$ rotor design operating in its design domain, Domain 2.

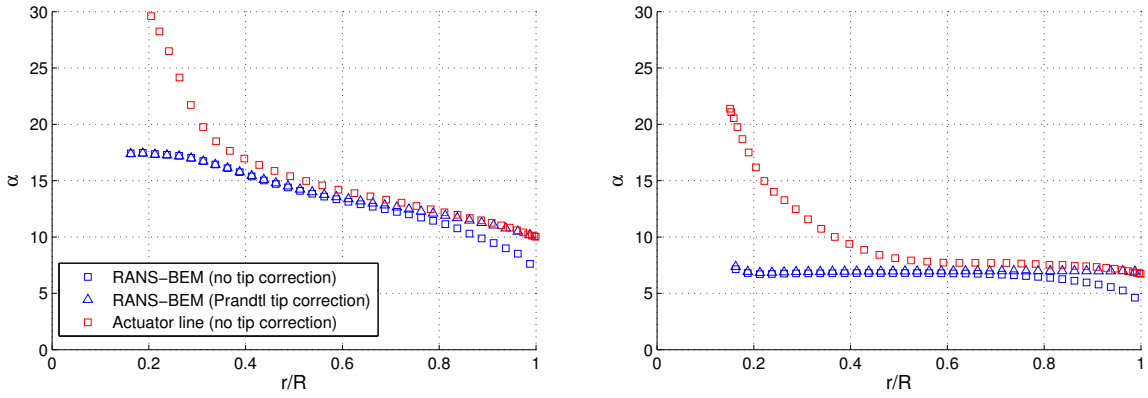

(a) $\lambda = 4$ **(b)** $\lambda = 5$

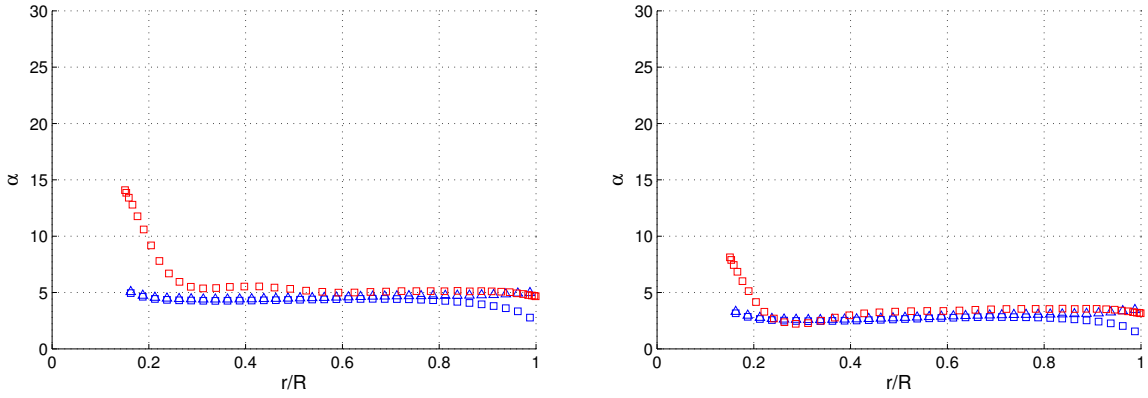

(c) $\lambda = 6$ **(d)** $\lambda = 7$

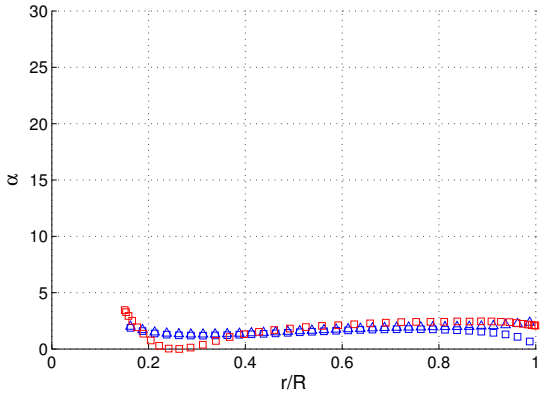

(e) $\lambda = 8$

Figure 5.18: Comparison of radial variation in angle of attack for RANS-BEM simulations (both with and without the Prandtl tip correction) and actuator line simulations of the $s/d = 1$ rotor design operating in its design domain, Domain 2.

is imperative that the Prandtl tip correction is understood to be a reduction in the axial induction factor but not necessarily a reduction in the relative velocity or power output (although both the relative velocity and power output *may* be reduced). For this reason, and to promote clarity in understanding, this work uses the terminology 'Prandtl tip correction' rather than the more commonly used term 'Prandtl tip loss'.

The actuator line results for angle of attack as a function of r/R in Figure 5.18 show good agreement with the RANS-BEM simulations utilising the Prandtl tip correction for $r/R > 0.5$ for all tip speed ratios, with values only slightly higher than those computed in the RANS-BEM simulations. However, the actuator line results deviate from the RANS-BEM results in the vicinity of the blade root. This deviation occurs at all tip speed ratios but is largest for $\lambda = 4$ and $\lambda = 5$.

Recall that, as seen in the plot of C_l/C_d as a function of α (Figure 5.3 on page 139), the angle of attack corresponding to maximum C_l/C_d, and thus optimal rotor efficiency, is $\alpha = 7^\circ$ for the aerofoil used in this study. At attack angles greater than 7°, the ratio C_l/C_d decreases as α increases. Conversely, for $\alpha < 7^\circ$, C_l/C_d increases as α increases.

For the $\lambda = 4$ and $\lambda = 5$ cases, the RANS-BEM attack angles are greater than or approximately equal to 7° and the actuator line simulations result in higher values of α than the RANS-BEM simulations. Thus, the ratio C_l/C_d is reduced, as is the rotor C_p. For $\lambda = 6$, 7, and 8, α for the RANS-BEM simulations is less than 7°. Therefore, the slightly higher values for α computed by the actuator line model simulations result in increased C_l/C_d values and increased C_p relative to the RANS-BEM simulations. For these higher tip speed ratios, the deviation in actuator line α from the RANS-BEM α in some of the blade root sections results in decreased C_l/C_d for the corresponding blade element. Still, this reduction does not offset the increase due to the higher values along the rest of the blade span, because properties at the blade root have lower influence on integrated moments, such as torque, than properties at the tip, where the moment arm is larger.

5.5 Conclusions

An investigation into the impact of local blockage conditions on turbine performance in tidal fences spanning infinitely wide channels has been carried out. The effects of local blockage are of particular concern for tidal power device design as tidal devices are far more likely to operate in blocked conditions than wind turbines due to the geometry of tidal channels.

A series of tidal rotors are designed for maximum efficiency in a range of local blockage conditions using an in-house RANS-BEM optimisation tool. The aerofoil section and rotor radius remain unchanged throughout the study. Results confirm that the highest power coefficient is achieved by the rotor designed for the highest blockage. Further, it is shown that in order to achieve maximum efficiency, rotors designed to operate in high local blockage require greater solidity and lower blade twist than rotors designed for operation in unblocked flow.

Additionally, RANS-BEM computations are completed in which each of the rotor designs are simulated in each of the 4 domains over a range of tip speed ratios. The maximum C_p achieved for each rotor design is improved with each reduction in rotor spacing. Though there is significant improvement in performance when a rotor designed for unblocked flow is operated in highly blocked conditions, C_p is further increased if the rotor is specifically designed for the operational blockage conditions. Similarly, the best performing rotor for every domain is found to be the rotor designed for the respective domain. Although this result is intuitive, current rotor design practices do not take blockage conditions into account. Therefore, it is suggested that the anticipated operational blockage conditions be considered during the rotor design process if true optimal rotor efficiency is to be achieved.

Examination of the radial variation in local thrust coefficient reveals that the power output

from a rotor with uniform thrust loading may be matched, or slightly exceeded, by a rotor for which there is increased loading at the blade tip as compared to the blade root. This confirms the assertion of Belloni [55] that, rather than a single optimal design for specified flow and blockage conditions, there exists a 'power plateau' for the rotor optimisation process, a maximum power output which is attainable both by rotors with uniform local thrust coefficient as well as by rotors with increased local thrust coefficient in the tip region. Still, a rotor with uniform c_x may be preferable due to structural implications.

Finally, the RANS-BEM results have been compared with actuator disc results for a selected case ($s/d = 1$ rotor operating in design blockage conditions). There is good agreement for the power coefficients, with the maximum difference being 6.8%. Investigation of the radial variation of U_{rel} and α for the RANS-BEM and actuator line models reveals that, although the models predict significantly different values for α in the root sections of the blade, this has little effect on the overall power because of the relatively small moment arm. Rather, the source of much of the difference in C_p between the two models is due to slight differences in computed α along the entirety of the blade span, as the overall power depends on the integrated moments.

Chapter 6

Rotor Performance in Finite-Length Tidal Fences

Chapter 5 included results for turbines operating in infinitely long tidal fences spanning the entire width of a channel. Although the infinite fence assumption proves useful for CFD modelling, a more realistic scenario is that tidal turbines will be deployed in finite arrays which do not span the entire width of a channel. In this chapter, the effects of local blockage on hydrodynamic rotor performance in tidal fences consisting of 2, 4, and 8 turbines in a wide channel are presented. In addition, the effects encountered at the ends of the finite-width arrays, both time-averaged and unsteady, are discussed.

6.1 Overview

An unstructured RANS-embedded actuator line method, with the velocity analysis routine introduced in Section 3.1.2, is utilised in this study. The actuator line method is well-suited for unsteady simulations of multiple rotors, as it is more computationally efficient than 3D blade-resolved methods. The $k-\omega$ SST turbulence closure, discussed in Section 2.6.2 is employed to close the 3D RANS equations.

Several tidal fences consisting of 2-bladed rotors placed in the middle of a wide channel are simulated. Fences with n = 2, 4, and 8 rotors are considered. It is vital that the computational domain is of sufficient size for array-scale flow effects to be captured in the computations. Nishino and Willden have previously utilised a domain extending $50d$ upstream and downstream of the tidal fence with width $w_{channel} = 10nd$ and height $h = 2d$, where d is the rotor diameter, for actuator disc simulations of finite tidal fences ranging from n = 2 to n = 16 turbines across [42]. The same domain dimensions are utilised in the current actuator line study (with rotor diameter $d = 10$ m), allowing for direct comparison of the unsteady actuator line results with the time-averaged actuator disc results. The height of the domain is also consistent with the height of the domain used in Chapter 5 for the BEM optimisation of rotor design for turbines operating in tidal turbine fences spanning an infinite channel and the corresponding study of relative rotor performance for varying blockage conditions.

The design of the rotors simulated in the finite-length tidal fences discussed in the current chapter is derived from the results of the RANS-BEM optimisation presented in Section 5.3.1. Specifically, the hydrodynamically optimal rotor design for Domain 2 (B_l = B_g = 0.196) is employed. This rotor was designed for operation at $\lambda = 5$ in an infinitely long fence with water of depth $h = 2d$, rotor spacing $s = 1d$, and no array bypass flow. The selected rotor performed well in all of the operating conditions considered in Chapter 5, with the difference between the power coefficient achieved by this rotor and that achieved by the respective optimal rotor for a range of intra-rotor spacings never greater than 9%.

Each rotor blade is represented by an actuator line consisting of 40 collocation points. The spacing of the collocation points is defined by a cosine distribution, which allows for finer resolution in the vicinity of the blade roots and tips, as discussed in Section 3.3.1.

A symmetry boundary is used at the vertical plane midway between the 2 centre rotors in the tidal fences. This allows for the simulation domains to include only half of each

tidal channel under consideration, which significantly reduces the computational load of the simulations. The width of the computational domains in the present study, w, is therefore defined as $w = 5nd$. This corresponds to domain widths of $10d$, $20d$, and $40d$ for simulations of fences consisting of 2, 4, and 8 rotors, respectively. A cross-section at the rotor plane of the domain used to simulate an 8-rotor fence, viewed from an upstream position, is included in Figure 6.1.

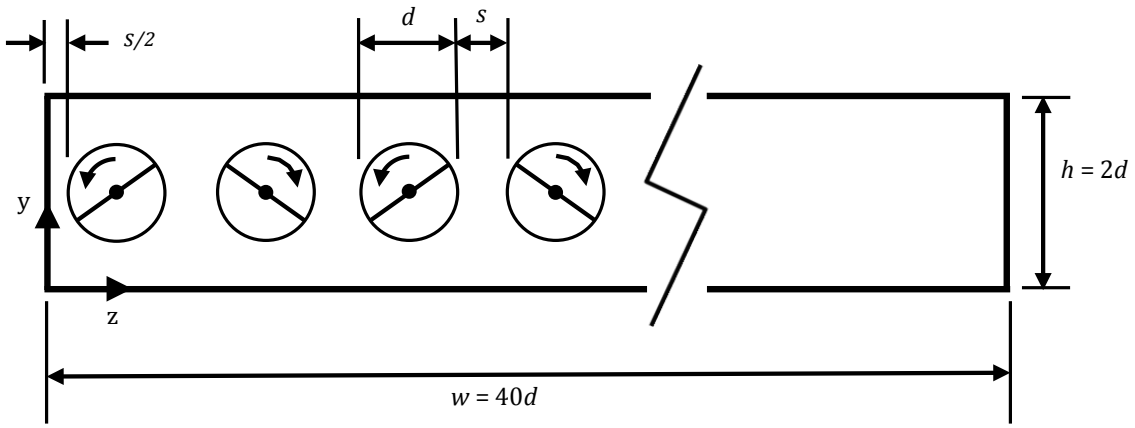

Figure 6.1: Rotor plane cross-section of the domain used to simulate an 8-rotor fence, viewed from an upstream position. The left wall is a symmetry boundary condition. d is the rotor diameter and s is the tip-to-tip rotor spacing. The direction of rotation for each rotor is indicated.

The rotation direction of each rotor for the $n = 8$ simulations is indicated in Figure 6.1. As indicated in the figure, the rotation direction alternates between anti-clockwise and clockwise. This alternating pattern was selected because it is maintained even with the use of the symmetry boundary at the vertical centre-plane of the tidal fence. Similarly, in the domain for the $n = 4$ simulations, the rotor nearest the symmetry boundary rotates in the anti-clockwise direction while the other rotates in the clockwise direction. In the domain for the $n = 2$ simulations, the simulated rotor rotates in the anti-clockwise direction.

In the present study, λ is normalised by the flow speed at the domain inlet far upstream of the tidal fence, which is $U_\infty = 2$ m/s for all cases. The tip speed ratio, λ, is uniform across all rotors in each simulation. Thus, all of the rotors in a tidal fence for a given simulation

have the same blade angular velocity. Although it is likely that the array power coefficient could be optimised through adjustment of angular velocity and thus λ for individual rotors, this is outside of the scope of the current work.

The starting position of the 2 rotor blades is consistent for each rotor in the array (although the direction of rotation alternates with each rotor). This starting position, coupled with uniform angular velocity for all rotors in the fence, results in a regular blade-passing pattern in which the counter-rotating blades of neighbouring rotors sweep past each other at same rotor position every revolution. In the majority of simulations, the blades sweep past each other at $\gamma = 90^\circ$ and 270°, where γ is the blade azimuthal angle and $\gamma = 0^\circ$ when the blade is in the vertical position and pointing towards the domain lid (top dead centre). In these simulations, the starting positions of the 2 rotor blades are $\gamma = 0^\circ$ and 180° for all rotors. Unless stated otherwise, the results presented below are from simulations employing this initial blade positioning. Section 6.2.4 includes a comparison between results from the configuration described above with results from simulations in which the initial blade positions for Rotors 1 and 3 are instead $\gamma = 90^\circ$ and 270° (Rotor 1 is the rotor closest to the symmetry boundary). In this alternative starting configuration, the rotation direction for each rotor remains as indicated in Figure 6.1.

6.1.1 Blockage Definitions

In the simulations discussed in Chapter 5, the tidal turbine fences span the entire width of the infinite channel and the local and global blockage are equal ($B_l = B_g$). However, in the finite-length tidal fence simulations, the row of turbines operates in the middle of a wide channel. Recall from Section 2.1.1 that the local blockage is defined as the ratio of the single device area to the local passage cross-sectional area, which is $h\,(d+s)$ in both the current finite-length tidal fence configuration and the infinite-length tidal fence configuration in Chapter 5. The relevant parameters are consistent for both configurations in the current work, and B_l for any given rotor spacing is therefore also the same for both

configurations. The global blockage is defined as the ratio of the total device area to the channel cross-sectional area. Because B_g has a dependancy on the width of the simulated channel and the number of rotors in the fence, the global blockage for the finite-length fence simulations is not equal to the local blockage, as it was in the infinite fence simulations in Chapter 5. Rather, B_g in the current chapter is always less than the local blockage.

Three intra-rotor lateral spacings are considered for the finite-length tidal fences: $s = 0.25d$, $1d$, and $4d$. Each of these spacings was also used in the study of a tidal fence spanning an infinitely wide channel discussed in Chapter 5. Adjustment of the intra-rotor spacing, s, results in varying values for B_l.

The selected definition of the channel width, $w_{channel} = 10nd$, is such that B_g remains fixed throughout the finite tidal fence study, regardless of the number of rotors simulated. Thus, a constant global blockage, $B_g = 0.039$, is maintained.

The fence configurations and associated parameters for the finite-length tidal fence study are listed in Table 6.1. The width listed in the table is the channel width rather than the width of the computational domain utilising the symmetry boundary. The table also includes the local and global blockage ratios corresponding to each rotor spacing. The same rotor is used in all simulations, regardless of local blockage. As mentioned previously, the rotor employed is the rotor designed for Domain 2 in Chapter 5.

Table 6.1: Finite-length tidal fence configurations.

Configuration	s	h	$w_{channel}$	n	B_l	B_g	Domain Cell Count
A2	$d/4$	$2d$	$20d$	2	0.314	0.039	0.99 x 10^6
A4	$d/4$	$2d$	$40d$	4	0.314	0.039	1.81 x 10^6
A8	$d/4$	$2d$	$80d$	8	0.314	0.039	3.65 x 10^6
B2	d	$2d$	$20d$	2	0.196	0.039	0.96 x 10^6
B4	d	$2d$	$40d$	4	0.196	0.039	1.92 x 10^6
B8	d	$2d$	$80d$	8	0.196	0.039	3.71 x 10^6
C2	$4d$	$2d$	$20d$	2	0.079	0.039	1.01 x 10^6
C4	$4d$	$2d$	$40d$	4	0.079	0.039	2.04 x 10^6
C8	$4d$	$2d$	$80d$	8	0.079	0.039	4.08 x 10^6

Schematics of the rotor plane cross-sections for selected cases from Table 6.1 are shown in Figure 6.2.

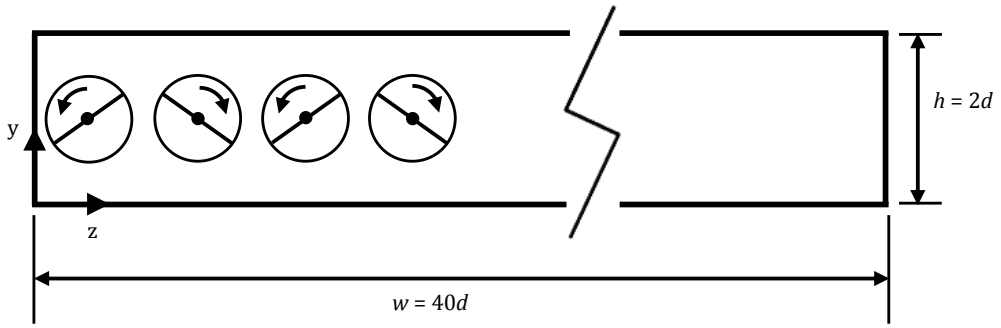

(a) Configuration A8

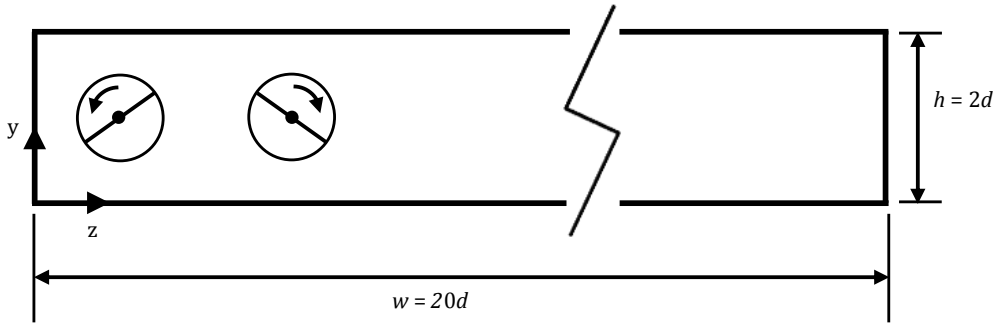

(b) Configuration B4

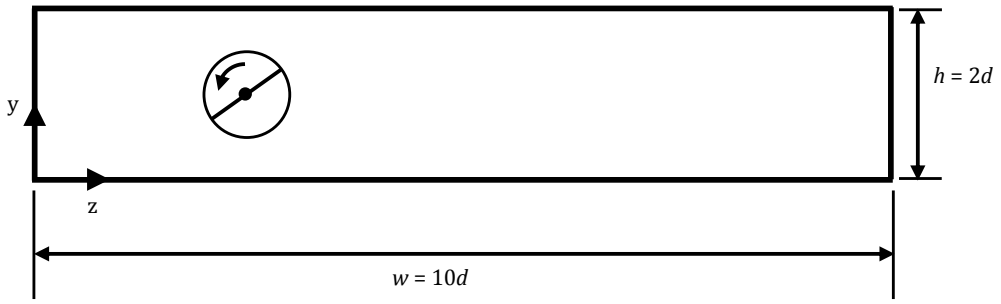

(c) Configuration C2

Figure 6.2: Schematics of the rotor plane cross-sections for Configurations (a) A8, (b) B4, and (c) C2. The symmetry plane is on the left for all configurations.

6.1.2 Boundary Conditions and Mesh Parameters

The lower and upper walls of the domain are defined as slip boundaries, as is the side wall far from the tidal fence. A uniform flow of water with velocity U_∞ =2 m/s, turbulence intensity $I = 5\%$, and turbulent length scale $l = 1$ m serves as the inlet boundary condition. Although the inlet turbulence dissipates far upstream of the rotor plane in the current simulations, the results are not insensitive to k and ω, as these affect wake expansion and recovery and hence effective blockage. The outlet boundary is a pressure outlet with constant gauge pressure set to 0 Pa. The nacelles of each turbine, of diameter $d_{nacelle} = 0.15d$ (matching the nacelle diameter for the BEM rotor optimisation in Section 5.3.1), are explicitly included in the domain via no-slip surfaces, but no other turbine components, aside from the blades modelled as actuator lines, are included in the simulations. In order to isolate the rotor effects, the turbine support towers are neglected in this study.

Unstructured meshes consisting of tetrahedral elements are employed in this study. The mesh element length in the near vicinity of the rotor plane is $e = 0.25$ m, which corresponds to $d/40$ for the rotors simulated. The elements increase in size from the rotor plane into the rotor wake at a growth rate of 1.1. This rotor plane resolution corresponds to that used in Meshes 2 and 4 in the NREL Phase VI validation study (page 112). The coarser rotor plane resolution of the validation study (discussed in Section 4.4.1) has been selected for the finite tidal fence actuator line study because the reduction in the number of mesh elements is attractive for the simulation of multiple rotors. In addition, it was shown in Section 4.4.1 that there was very little difference in the integrated blade loads when a finer mesh, with $e \approx c_{local}/4$ was employed. The total number of cells in each of the simulation domains is listed in the last column of Table 6.1.

The time step is selected such that 200 time steps are simulated per rotor revolution. This is in accordance with the findings of the time resolution study included in Section 4.4.1. In addition, a time resolution study was completed using Configuration A8. In this study, the

array was simulated using both 200 and 800 time steps per rotor revolution. The time-averaged blade torque was a maximum of 1.3% higher for the highest time resolution (smallest time step) and the solution was therefore judged to be sufficiently converged at 200 time steps per revolution.

6.2 Results and Discussion

Results of the study of finite-length tidal fences in wide channels are included in this section. First, effects of the number of rotors, n, and intra-rotor spacing, s, on the time-averaged global fence power coefficient curves will be presented. Next, the influences of these same parameters on the time-averaged power coefficients of individual rotors within a fence will be discussed. Finally, an analysis of the unsteady effects on single-blade torque for individual rotors within a tidal fence is included.

6.2.1 Global Fence Performance

In this section, time-averaged results from the finite-length tidal fence study will be discussed in terms of local and global coefficients. The local thrust coefficient, $C_{tl,i}$, for the i^{th} turbine in a fence is defined for the current study as

$$C_{tl,i} = \frac{T_{D,i}}{\frac{1}{2}\rho U_\infty^2 \frac{\pi d^2}{4}}, \tag{6.1}$$

where $T_{D,i}$ is the thrust applied by the i^{th} rotor, $\rho = 998$ kg/m^3 is the water density, and U_∞ is the flow speed at the channel inlet. Similarly, the local power coefficient, $C_{pl,i}$, is

$$C_{pl,i} = \frac{P_{D,i}}{\frac{1}{2}\rho U_\infty^3 \frac{\pi d^2}{4}}, \tag{6.2}$$

where $P_{D,i}$ is the power produced by the i^{th} rotor. The global power coefficient, C_{pg}, for a fence is defined as

$$C_{pg} = \frac{\sum_{i=1}^{n} P_{D,i}}{\frac{1}{2}\rho U_{\infty}^{3} n \frac{\pi d^2}{4}}. \tag{6.3}$$

With the current definition of C_{pl} (i.e. with U_{∞} used in the normalisation on $P_{D,i}$, as opposed to a local flow speed), the global power coefficient for a fence is simply the average of the local power coefficients for the n turbines in the fence:

$$C_{pg} = \frac{\sum_{i=1}^{n} C_{pl,i}}{n}. \tag{6.4}$$

Influence of n on Fence Performance

Power curves depicting the global power coefficient, C_{pg}, as a function of tip speed ratio, λ, are presented in Figures 6.3a-6.3c for each of the three intra-rotor spacings considered. Each plot includes results for the n = 2, 4, and 8-rotor fences. In addition, the theoretical maximum C_{pg} for a long fence ($n = \infty$) in a wide channel with the same local and global blockage as the respective simulated configurations is indicated in each plot. These theoretical values are calculated using the theory of Nishino and Willden [41].

For the cases with lateral intra-rotor spacing s/d = 4 ($B_l = 0.079$), very little improvement in rotor performance is seen as the number of rotors in the fence increases. This suggests that this low local blockage level is not sufficient to induce significant hydrodynamic rotor performance improvements, regardless of the length of the tidal fence.

Greater hydrodynamic performance improvement is seen as the number of rotors increase for the s/d = 1 ($B_l = 0.196$) spacing, with the the maximum global power coefficient, $C_{pg,max}$ increasing from 0.618 to 0.641 (3.7% increase) when the number of rotors in the fence is increased from 2 to 8.

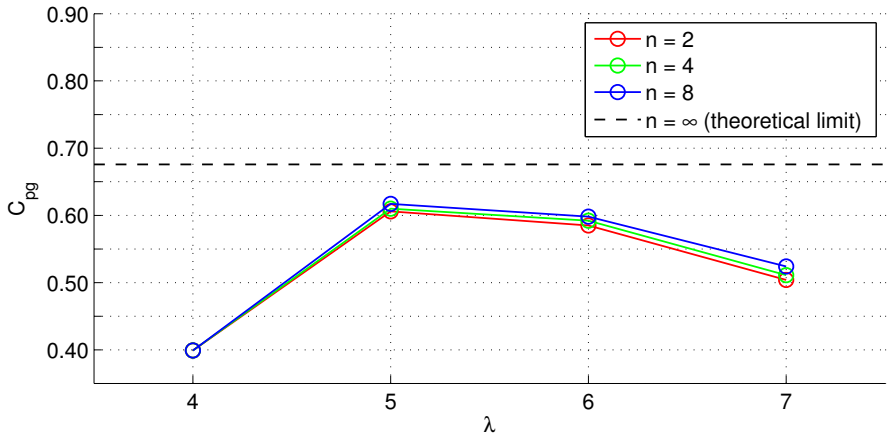

(a) $s/d = 4$ ($B_l = 0.079$)

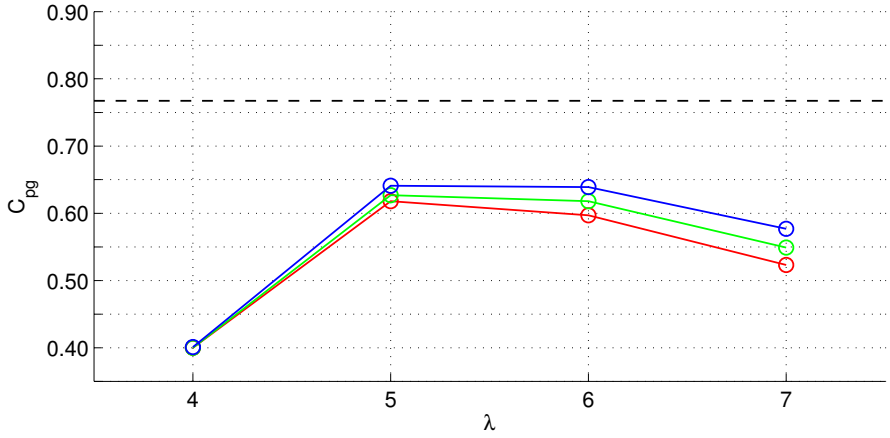

(b) $s/d = 1$ ($B_l = 0.196$)

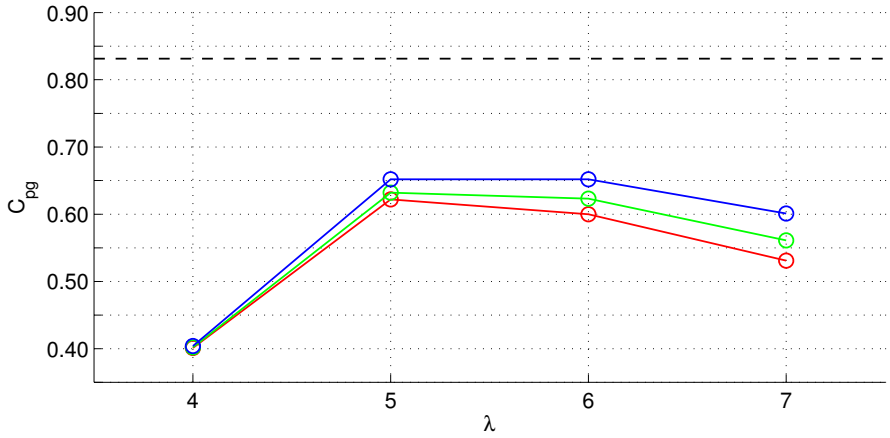

(c) $s/d = 0.25$ ($B_l = 0.314$)

Figure 6.3: Global power curve dependency on n for tidal fences in wide channels ($B_g = 0.039$).

The greatest improvement in performance due to the addition of rotors to the tidal fence is observed for the highest local blockage, $B_l = 0.314$ ($s/d = 0.25$). For this blockage ratio, $C_{pg,max}$ improved from 0.622 for a 2-rotor fence to 0.652 for an 8-rotor fence, an increase of 4.8%.

The global power coefficients increase as rotors are added to the fences because as $n \to \infty$, a lower fraction of the flow upstream of the fence is able to divert around the array. Hence, with all other conditions consistent, the local velocity at the rotors will be greater for longer fences, resulting in the improved global power coefficients for longer arrays. The physical causes of this performance improvement are further investigated in Section 6.2.2.

As expected, the maximum global power coefficient for each of the simulated tidal fences is below the theoretical C_{pg} limit for the respective configuration. This occurs because: 1) the theoretical limit is for an infinitely long tidal fence partially spanning the width of a wide channel whereas the current simulations are for finite-length fences, 2) the rotors were designed for an infinite homogenous fence with a specific intra-rotor spacing ($s/d = 1$) and not for operational conditions within a fence of finite length, and 3) the actuator line model simulates realistic rotors and allows for viscous losses that are dependent on the rotor geometry, such as those due to the formation of tip vortices. The formation of tip vortices causes induced drag, and simulations directly modelling this will have reduced computed hydrodynamic performance as compared to idealised models.

Notably, the maximum global power coefficients for the highest blockage configurations were furthest below the theoretical limit for the infinitely long fence. This is likely primarily due to the fact that the rotor design used in this study was optimised for intra-rotor spacing $s/d = 1$. As discussed in Chapter 5, this rotor design performed very well in both $s/d = 1$ and $s/d = 4$ configurations for fences spanning the width of infinite channels, however, its performance in the $s/d = 0.25$ configuration was further from the maximum achieved by the rotor designed for that spacing. Although the simulations in

Chapter 5 were of infinite fences with no array bypass and are thus quite different from the current simulations, it is expected that the optimal rotor design will tend towards the design from Chapter 5 as n becomes large. Thus, it is nevertheless relevant to discuss the rotor designs from the previous chapter. The performance of the finite-length fences with $s/d = 0.25$ could be further improved, as shown in Chapter 5, by employing a rotor specifically designed for the desired operational local and global blockage ratios. Also, it is possible that more rotors are needed to approach maximum C_p for the higher blockage cases, although more investigation is required if this is to be confirmed.

Table 6.2 includes results from actuator disc simulations completed by Nishino and Willden and results from the current actuator line simulations. The results in this table are for the $s/d = 1$ configurations (B2, B4, and B8). Recall that the domain dimensions in the current work are consistent with those in the work of Nishino and Willden [42]. Hence, the local and global blockage ratios for the simulations are identical. Nishino and Willden found a dependency on the RANS SST turbulence model parameter $C_{\epsilon 1}$ [42], but in this work only the actuator disc results for the standard value, $C_{\epsilon 1}$ = 1.44, are considered. Because this coefficient was used for both the actuator disc and actuator line simulations, the results can be directly compared without consideration of the additional effects caused by the turbulence closure employed (beyond the effects relating to the previously discussed differences between the actuator disc and actuator line models).

Table 6.2: Comparison of actuator disc and actuator line results for $C_{pg,max}$ for the s/d = 1 configurations.

Configuration	n	Actuator disc $C_{pg,max}$	Actuator line $C_{pg,max}$
B2	2	0.692	0.618
B4	4	0.708	0.627
B8	8	0.729	0.641

It is seen from the results included in Table 6.2 that $C_{pg,max}$ for each of the actuator disc configurations is roughly 12-14% greater than the $C_{pg,max}$ computed in the respective actuator line simulation. This is the result of several differences between the two sets

of simulations. First, the actuator disc models are idealised and do not include viscous losses related to blade drag and discrete blade effects while the actuator line simulations do. Second, the rotor design used in the actuator line simulations has not been optimised for each specific array configuration whilst by their nature, actuator discs simulate perfect energy extractors. While the current rotor design was optimised for the same intra-rotor spacing as that in the cases presented in Table 6.2, it was designed for operation in an infinitely long fence with no bypass flow around the array, rather than for short fences in wide channels. Because the rotor has not been designed for these operational conditions, there are even greater viscous losses due to the non-optimised rotor performance. Third, the actuator disc simulations did not include a nacelle, while the actuator line simulations did. The power coefficient in this work is normalised by the total frontal rotor area, rather than the swept blade area, for all cases. However, because the actuator line simulation rotor has lower swept area than the actuator disc rotor, its power output is slightly lower than that of the actuator disc. This effect, however, is likely of little importance due to the small moment arm in the relevant region.

It must be noted that the results in this chapter cannot be compared directly with the BEM results presented in Chapter 5. This is due to the fact that in Chapter 5, the simulated rotor fences spanned the entire channel, whereas in the current chapter, the fences span only a small part of a wide channel. Thus, in the current work there is an array bypass flow in each simulation, which results in reduced flow through the array and hence reduced power output compared with that of the fences in Chapter 5 which have similar local blockage but no array bypass flow.

Influence of s on Fence Performance

Figures 6.4a-6.4c include global power coefficient curves as a function of tip speed ratio for constant n. Each plot includes results for the intra-rotor spacings s/d = 0.25, 1, and 4. The data included in these plots is the same data as in Figures 6.3a-6.3c, but plotted such

that the effects of adjusting the intra-rotor spacing, isolated from the previously discussed performance improvement caused by an increase in n, may be seen.

The results for $n = 2$ (Figure 6.4a) indicate that the fences consisting of 2 rotors did not experience significant performance improvement as s was reduced, despite the resulting increase in local blockage from 0.079 to 0.314. $C_{pg,max}$ improved from 0.606 for the $s/d = 4$ configuration to 0.622 for the $s/d = 0.25$ fence configuration, an increase of 2.6%.

In addition, $C_{pg,max}$ increased 3.6% for $n = 4$ (Figure 6.4b) when the intra rotor spacing was decreased from $s/d = 4$ to $s/d = 0.25$ and 5.7% for $n = 8$ (Figure 6.4c). While the performance increase due to adding rotors to a fence is principally related to array-scale bypass flow, the increase in $C_{pg,max}$ caused by a reduction of the intra-rotor spacing is predominantly related to changes in the bypass flow at the device/rotor scale. As discussed in Section 5.3.3 and in Nishino and Willden [129], the primary driver affecting the performance of rotors in locally blocked flow is the acceleration (and associated drop in pressure head) in the device-scale bypass region. This acceleration is generally affected more by intra-rotor spacing than by the number of devices in a fence. A schematic of a tidal fence with array-scale and device-scale bypass flows indicated is given in Figure 6.5.

For each case represented in Figure 6.4, the majority of the improvement of $C_{pg,max}$ as the lateral intra-rotor spacing was decreased from s/d = 4 (B_l = 0.079) to $s/d = 0.25$ (B_l = 0.314) occurred in the intermediate step, when the spacing was s/d = 1 (B_l = 0.196). This adjustment accounted for 70-75% of the total improvement in $C_{pg,max}$. This may be a case-specific phenomena, however, because the rotor design used in this study was designed for $s/d = 1$ (albeit for fences spanning the width of a channel rather than for short fences in wide channels). In addition, this is likely dependent on the height, h, of the simulated channel.

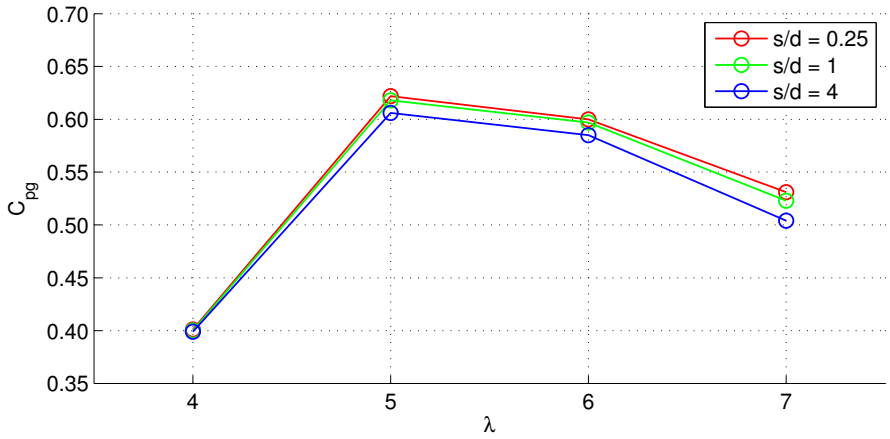

(a) $n = 2$

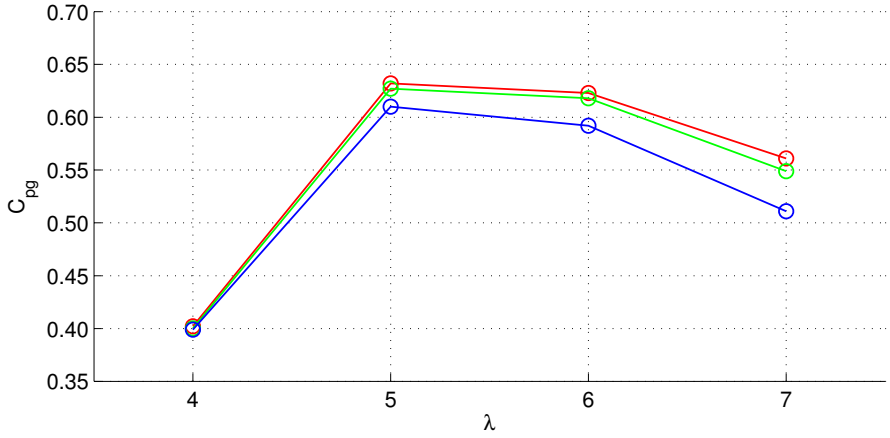

(b) $n = 4$

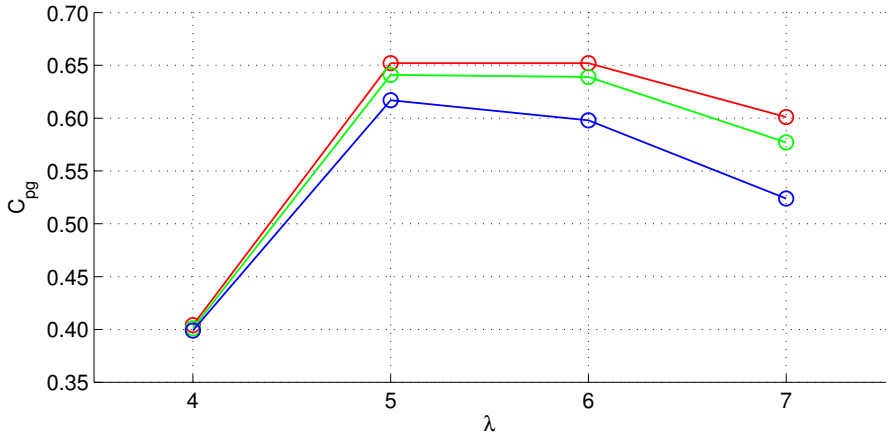

(c) $n = 8$

Figure 6.4: Global power curve dependency on intra-rotor spacing for tidal fences in wide channels ($B_g = 0.039$).

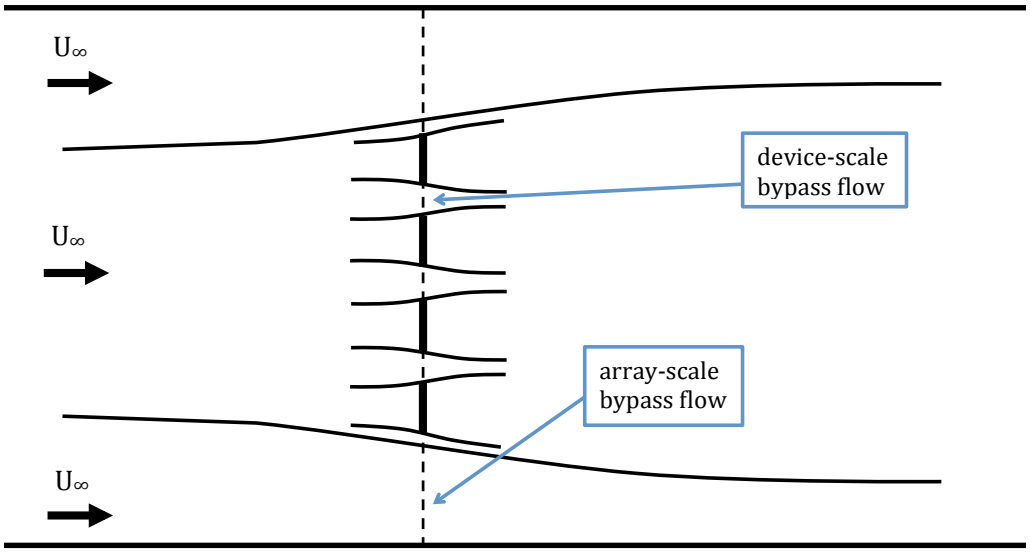

Figure 6.5: Schematic depicting array-scale and device-scale flows for a finite-length tidal fence in a channel.

Compiled $C_{pg,max}$ Results

Results for the maximum global power coefficient, $C_{pg,max}$, for each of the 9 fence configurations are compiled in Figure 6.6. The performance-enhancing effects of both increasing n and decreasing s are clearly visible in the figure. For the current rotor design, an improvement in hydrodynamic performance of 7.6% is seen when the rotor spacing is reduced from $s/d = 4$ to $s/d = 0.25$ and the number of rotors in the fence is concurrently increased from 2 to 8.

The performance could be further improved if the rotors were designed for operational conditions, with both the intended operational local blockage and the length of the fence considered in the design process. Still, it is significant that, for a representative rotor design, an improvement of 7.6% for $C_{pg,max}$ may be achieved simply by increasing the number of rotors in a fence and decreasing the lateral spacing. While it may not be feasible to design and manufacture rotors for specific anticipated operating conditions, these results suggest

that it is advantageous to deploy rotors in high blockage fences consisting of a minimum of 4 to 8 rotors.

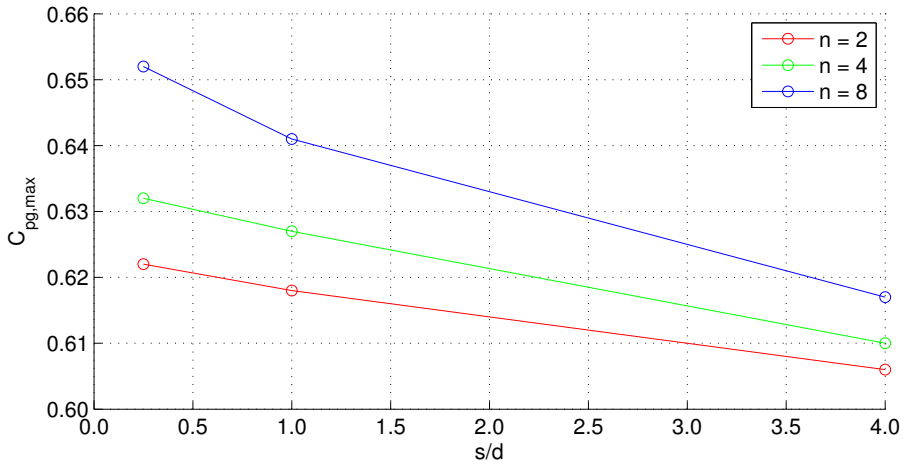

Figure 6.6: Maximum global power coefficient, $C_{pg,max}$, for each tidal fence configuration.

6.2.2 Rotor Performance within Tidal Fences

The results presented thus far have been limited to global power coefficients. More investigation into the local, rather than global, parameters and characteristics is required in order to better understand the effects that the local blockage ratio and the number of rotors have on tidal fence performance. In this section, time-averaged results relating to individual rotors within the tidal fence configurations are examined.

Local Power Coefficients

Figure 6.7 includes local power coefficients for all of the simulated rotors in each of the 9 configurations. The values plotted correspond with the peak operating point for the respective tidal fence, which in this work is always $\lambda = 5$. Rotor 1 is considered to be the rotor closest to the symmetry plane (the simulated rotor closest to the vertical centre-plane of the tidal fence).

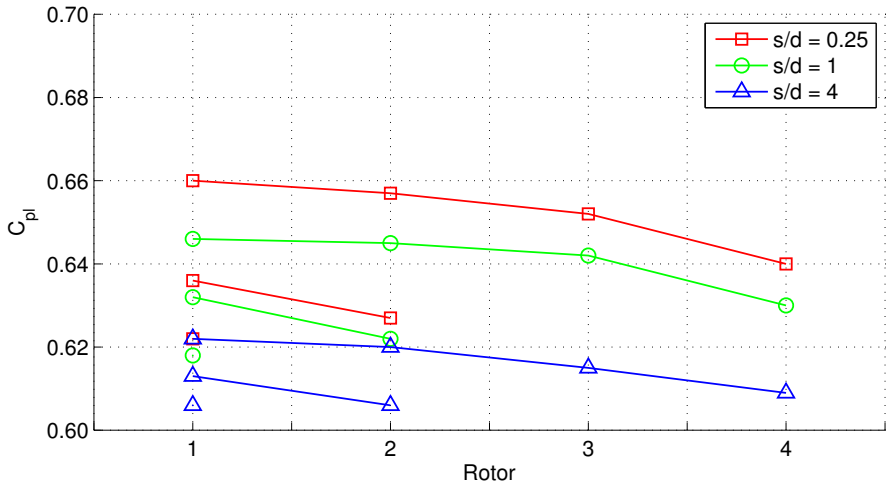

Figure 6.7: Local power coefficients for each of the nine configurations at the peak array operating point ($\lambda = 5$). Rotor 1 is the rotor closest to the symmetry plane (centre of full fence).

The $n = 2$, 4, and 8 cases for each lateral spacing are plotted in the same colour, and only results for the simulated half of the domain are included.

For each lateral spacing, the power achieved by Rotor 1 increases as the number of rotors in the fence increases. In addition, the highest local power coefficient is achieved by Rotor 1 for all nine configurations. Therefore, the beneficial effects of array blockage are greatest near the centre of the fence, regardless of the local blockage or fence length.

The effect of local blockage on the decrease in local power coefficient towards the ends of the fences was slight for $\lambda = 5$. The percentage reduction in C_{pl} between Rotors 1 and 4 for the $n = 8$ cases was 2.1% for s/d = 4, 2.4% for s/d = 1, and 2.9% for s/d = 0.25. It is possible that this drop-off in performance at the array ends could be reduced by tuning the tip speed ratio or altering the blade pitch of the end rotors. This is outside of the scope of the current work but should be investigated in future studies.

The tip speed ratio had a significant effect on the reduction of C_{pl} for the rotors on the end of the fences. The reduction in performance for the outer rotors due to increased tip speed ratio can be seen in Figure 6.8. In this figure, the local power coefficients for tip speed

ratios 4, 5, 6, and 7, normalised by the C_{pl} for Rotor 1, $C_{pl,1}$, for the respective tip speed ratio, are plotted for Configuration A8.

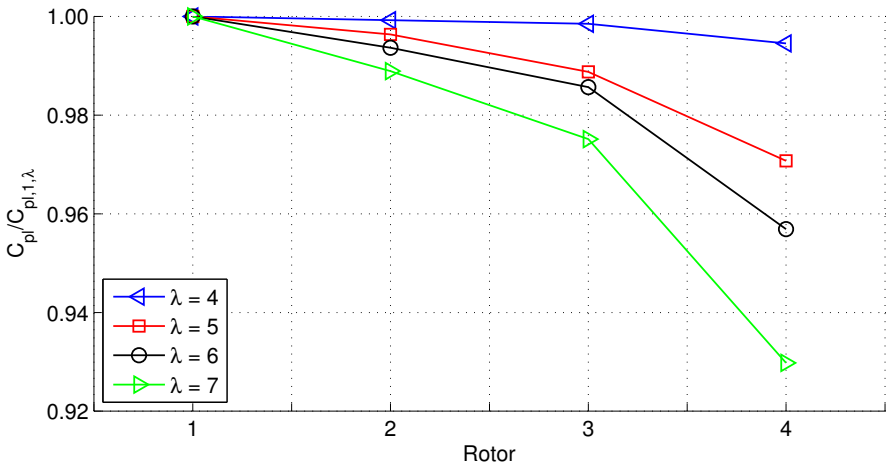

Figure 6.8: Local power coefficients for the $n = 8$, $s/d = 0.25$ case, normalised by $C_{pl,1}$ for the respective tip speed ratio.

It is clear from Figure 6.8 that as tip speed ratio is increased, the array-end rotors see increased drop-off in performance as compared to the rotors closer to the centre of the fence. As the tip speed ratio is increased, the rotors apply greater thrust to the flow. For Configuration A8, for example, the global thrust coefficients for the fence are $C_{tg,\lambda=4} = 0.72$, $C_{tg,\lambda=5} = 1.08$, $C_{tg,\lambda=6} = 1.20$, and $C_{tg,\lambda=7} = 1.26$. The increased thrust causes increased fence resistance, resulting in more flow being diverted around the fence in the form of array bypass flow. There is greater drop-off in performance at the array ends for high tip speed ratios because the increased array-scale flow diversion at high λ results in greater cross-stream flow at the array-end rotors. This causes misalignment of the flow with the array-end rotors and leads to reduced power for these rotors.

For $\lambda = 4$, there is less than 1% difference in C_{pl} for Rotors 1 and 4 for any of the intra-rotor spacings with $n = 8$, while for $\lambda = 7$ the power output of Rotor 4 is 3.5% lower than that of Rotor 1 for s/d = 4, 6.2% lower for s/d = 1, and 7.0% lower for s/d = 0.25. Thus, as the tip speed ratio is increased, the performance drop-off at array ends relative to array centre rotors increases, as discussed above. However, the performance drop-off

is affected not only by tip speed ratio, but also by local blockage. Decreased intra-rotor spacing and hence increased local blockage ratio results in a greater drop-off in the local power coefficient of Rotor 4.

This occurs because for high local blockage, as for high tip speed ratio, there is greater array thrust. This increased fence resistance results in more flow misalignment at the array-end rotors and hence reduced power for these rotors.

For Configuration A8 ($n = 8$, $s/d = 0.25$), $C_{pg,max}$ was achieved at both $\lambda = 5$ and $\lambda = 6$. The local power coefficients for these two cases are plotted in Figure 6.9.

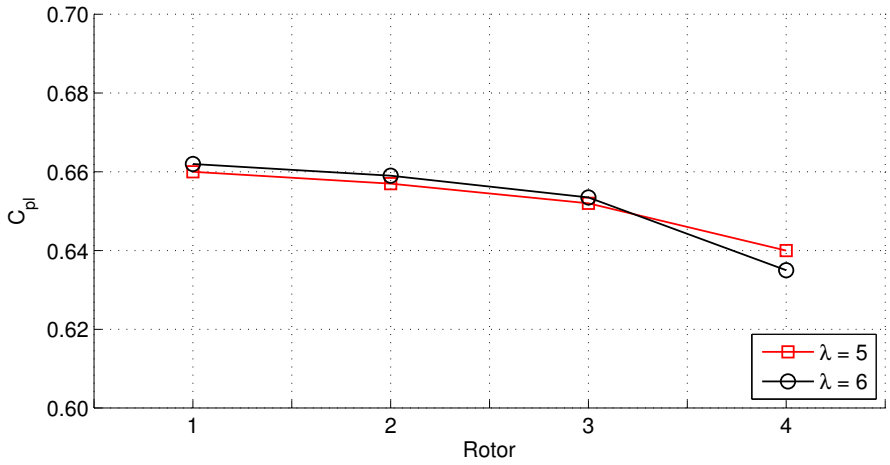

Figure 6.9: Local power coefficients for the $n = 8$, $s/d = 0.25$ case. Results for $\lambda = 5$ and $\lambda = 6$ are plotted.

As expected, the effect of the tip speed ratio on individual rotor performance can be seen in Figure 6.9. Although both cases plotted have the same global power coefficient, this is achieved in different ways. Specifically, Rotors 1, 2, and 3, when operating at $\lambda = 6$, have slightly greater power output than when operating at $\lambda = 5$. However, the power achieved by Rotor 4 at the higher tip speed ratio is lower than at $\lambda = 5$, and by a sufficient amount to completely negate the gains in power realised by the inner 3 rotors.

Local Thrust Coefficients

The local thrust coefficients for each of the 9 configurations at the respective peak array operating point ($\lambda = 5$ for all configurations) are plotted in Figure 6.10.

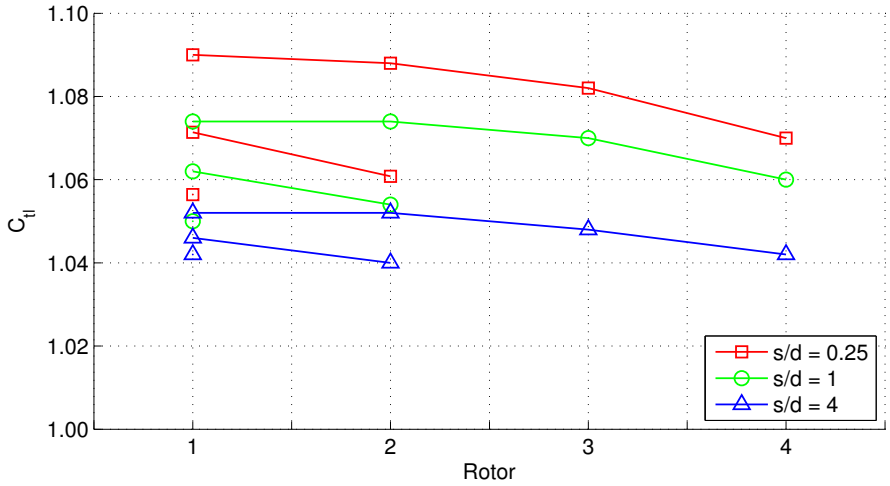

Figure 6.10: Local thrust coefficients for each of the nine configurations at the peak array operating point ($\lambda = 5$).

The local thrust coefficients follow a pattern similar to that of the local power coefficients. For each intra-rotor spacing, C_{tl} for Rotor 1 increases as rotors are added to the ends of the fence. The highest C_{tl} in each fence is achieved by the innermost rotor, Rotor 1, while the rotor on the end of each fence has the lowest C_{tl}.

The distribution of local thrust coefficients within the fences has a similar dependency on the tip speed ratio as the local power coefficient distribution. Figure 6.11 includes plots of the local thrust coefficients for Configuration A8, normalised by $C_{tl,1}$ for the respective tip speed ratio, at tip speed ratios 4, 5, 6, and 7.

The results are similar to those for the local power coefficient, in that for higher tip speed ratios there is greater reduction in the thrust coefficient for the rotors toward the ends of the fence as compared with the centre rotors.

As discussed previously, on the array scale, increased λ results in increased array thrust

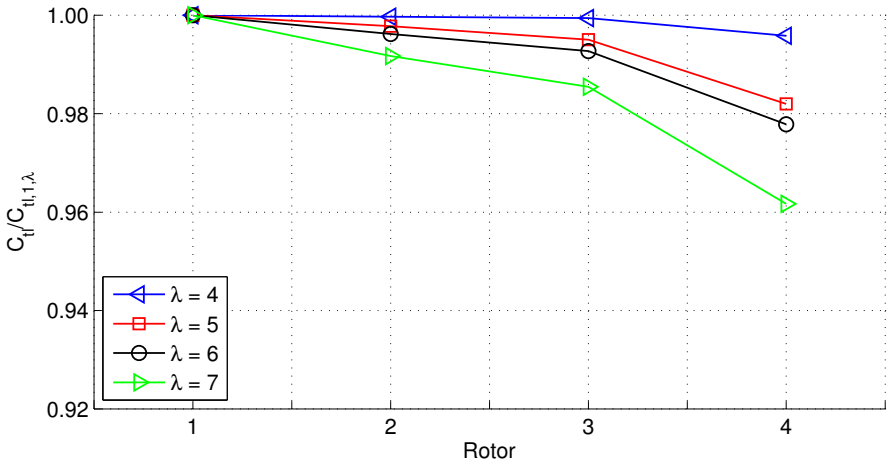

Figure 6.11: Local thrust coefficients for the $n = 8$, $s/d = 0.25$ case, normalised by $C_{tl,1}$ for the respective tip speed ratio.

and thus greater array-scale bypass flow speed and reduced speed through the tidal fence. As the fluid diversion increases, more of the fluid contributes to the array bypass flow and there is greater cross-stream flow at the array ends. This causes flow misalignment and hence reduced power at the array-end rotors. In addition, on the device scale, increased λ results in greater local thrust, which in turn increases the rotor-scale bypass acceleration. For the central rotors, this bypass is constrained on either side by the neighbouring rotors. This preserves the high acceleration in the bypass, allowing the centre rotors to maintain high thrust. Conversely, the rotor-scale bypass for the array-end rotors is constrained on only one side. Therefore, the device-scale bypass acceleration is lower at the array-ends, hence a larger drop-off in applied thrust.

Rotor Plane Pressure Coefficient and Streamwise Velocity Contour Plots

Analysis of rotor plane pressure coefficient and velocity contour plots for selected configurations provides further insight into the physical phenomena affecting rotor performance in high local blockage conditions. The pressure coefficient is defined as

$$C_{pressure} = \frac{p - p_\infty}{\frac{1}{2}\rho U_\infty^2}, \tag{6.5}$$

where p is the static pressure and p_∞ is the upstream static pressure (here, at the domain inlet).

Time-averaged rotor plane pressure coefficient contours at $\lambda = 5$ (the peak operating point) are shown in Figures 6.12 (Configurations B2, B4, and B8) and 6.14 (Configurations A8, B8, and C8). The corresponding time-averaged rotor plane streamwise velocity contours are shown in Figures 6.13 and 6.15, respectively. All figures show only the simulated half of the tidal fence.

There is no flow through the centre of each rotor due to the presence of the nacelle geometry in the computational domain. Because of the non-physical flow-field perturbations that occur in the near vicinity of the blades when point sources are applied to simulate the presence of the rotor blades in the actuator line model (as discussed in Section 3.1.1), the pressure coefficients and velocities within the swept blade area are not meaningful in Figures 6.12 - 6.15. These perturbations occur within a radius of $c/2$ around each collocation point; hence, the velocity field upstream and downstream of the swept blade area is non-physical in the range of +/- $c/2$ from the rotor plane.

Although the flow through the rotors cannot be examined using these contour plots, it is nonetheless useful to scrutinise the flow around the rotors and arrays, as these rotor-scale and array-scale bypass flows have a marked effect on the local and array performance.

The effects of adding rotors to a tidal fence with fixed local blockage can be seen from Figures 6.12 and 6.13. For all of the tidal fences, the flow in the array bypass near the end of the fence has higher velocity than the far-field flow closer to the channel side walls. This results in a low pressure region on the free-stream side of the array-end rotor of each fence.

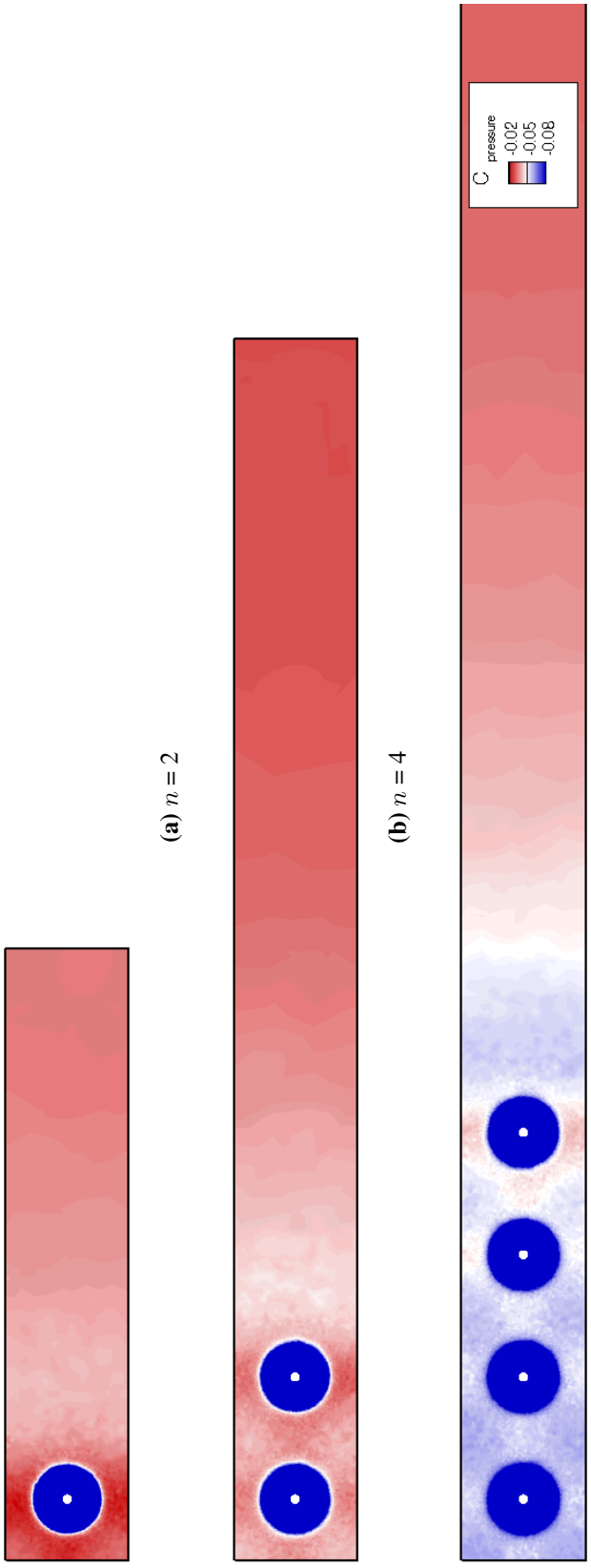

Figure 6.12: Time-averaged rotor plane pressure coefficient contours for (a) n = 2, (b) $n = 4$, and (c) $n = 8$, all with intra-rotor spacing $s/d = 1$ (Configurations B2, B4, and B8) and $\lambda = 5$. Figure (c) does not include the entire width of the domain.

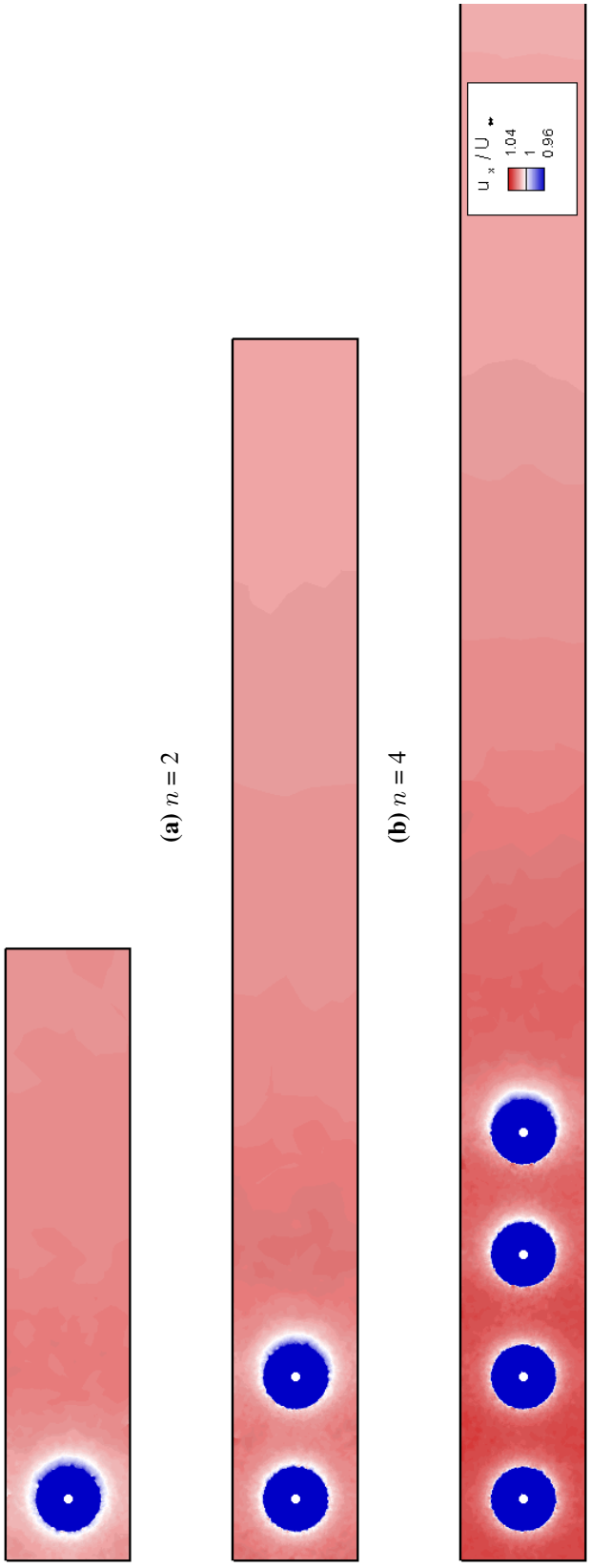

Figure 6.13: Time-averaged rotor plane normalised streamwise velocity contours for (a) n = 2, (b) $n = 4$, and (c) $n = 8$, all with intra-rotor spacing $s/d = 1$ (Configurations B2, B4, and B8) and $\lambda = 5$. Figure (c) does not include the entire width of the domain.

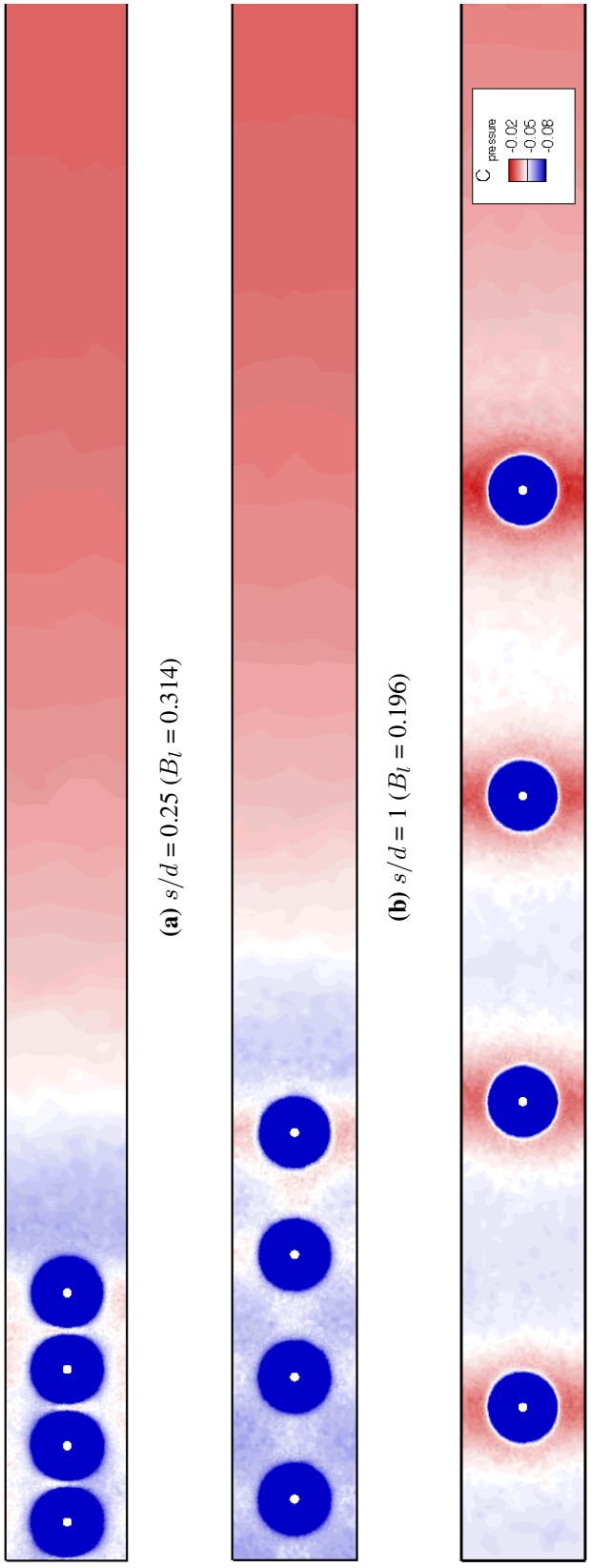

(a) $s/d = 0.25$ ($B_l = 0.314$)

(b) $s/d = 1$ ($B_l = 0.196$)

(c) $s/d = 4$ ($B_l = 0.039$)

Figure 6.14: Time-averaged rotor plane pressure coefficient contours for intra-rotor spacings (a) $s/d = 0.25$, (b) $s/d = 1$, and (c) $s/d = 4$, all with n = 8 (Configurations A8, B8, and C8) and $\lambda = 5$. Only part of the plane is shown.

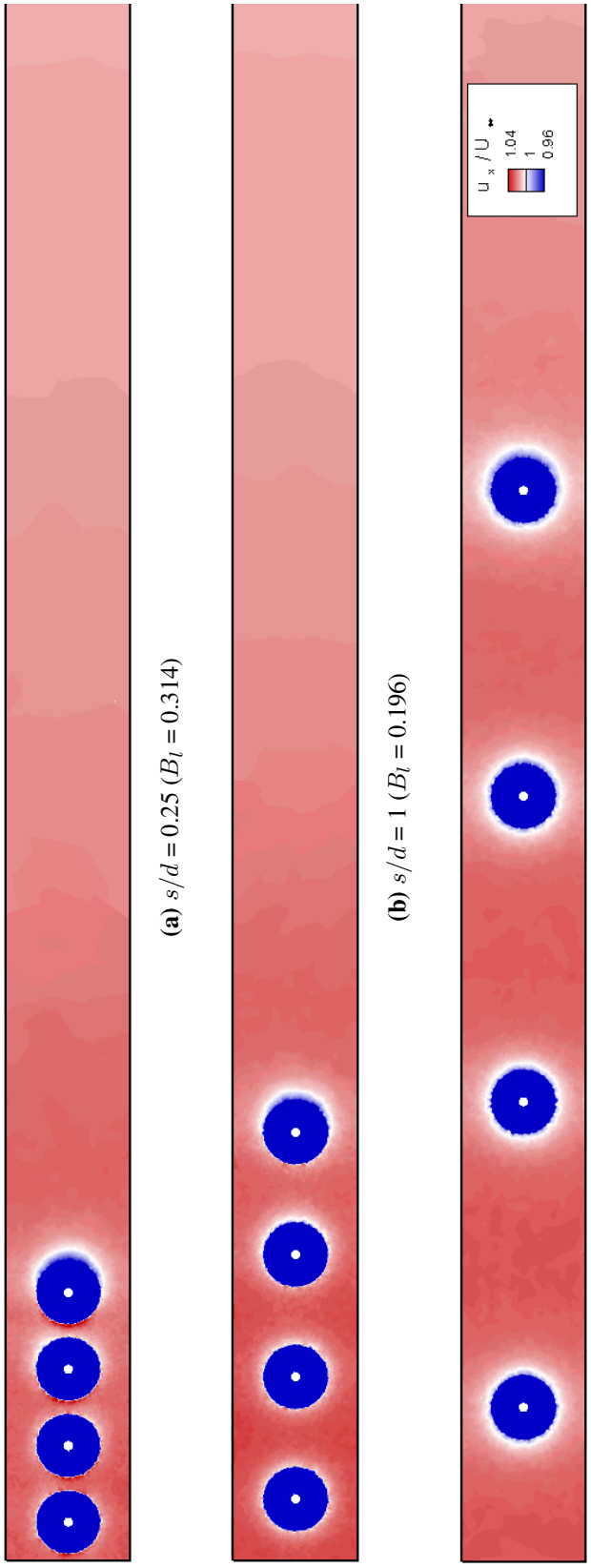

(a) $s/d = 0.25$ ($B_l = 0.314$)

(b) $s/d = 1$ ($B_l = 0.196$)

(c) $s/d = 4$ ($B_l = 0.039$)

Figure 6.15: Time-averaged rotor plane normalised streamwise velocity contours for intra-rotor spacings (a) $s/d = 0.25$, (b) $s/d = 1$, and (c) $s/d = 4$, all with n = 8 (Configurations A8, B8, and C8) and $\lambda = 5$. Only part of the plane is shown.

The pressure coefficient in this region decreases as more rotors are added to the fence. This occurs because as the fence lengthens and is able to apply greater thrust, more flow is diverted around the fence and the flow speeds in the array-scale bypass increase. The increase of streamwise velocity in this region as additional rotors are added to the fence may be seen in Figure 6.13.

Similarly, the streamwise velocity in the rotor-scale bypass flow is increased as the number of rotors grows, and there is a corresponding decrease in pressure coefficient in the rotor bypass flow field. However, there is not as much pressure coefficient reduction in the flow field around the array-end rotor for the $n = 4$ and $n = 8$ cases. Thus, the array-end rotors operate in a high-pressure region as compared with the centre rotors, resulting in lower performance of the array-end rotors relative to the centre rotors.

Notably, the streamwise velocity close to the swept rotor area in Figure 6.13 is not always symmetric around the rotor axis. This is clearest in the contours near Rotors 3 and 4 in Figure 6.13c, in which the streamwise velocity on the side of the rotors closest to the array centre is greater than that on the side closest to the free stream flow. This asymmetry suggests that unsteady variation in the blade loading is likely for rotors operating in this region (this will be further discussed in Section 6.2.4).

The cross-stream velocity, u_z, is defined to be positive in the direction from the vertical centre-plane to the free stream region. On the device scale, it is expected that the local bypass flow around each rotor will induce a positive u_z on the $+z$ side of each rotor and a negative u_z on the $-z$ side. However, on the array scale, all of the flow diverted due to array-scale bypass flow will be in the $+z$ direction in the simulated half of the domain. This is super-imposed on the device-scale flow, negating some or all of the negative u_z caused by the device-scale bypass flow. The bypass flow on the $-z$ side of the rotors is therefore constrained in its horizontal expansion, resulting in higher velocities close to the $-z$ edge of each rotor.

Figures 6.14 and 6.15 present pressure coefficient and streamwise velocity contours at the rotor plane for an array of 8 rotors with varying local blockage. Hence, the effects of local blockage variations on the flow are isolated from the effects of varying n in these plots. The array-scale bypass flow pressure coefficient is seen to increase in the region directly adjacent to the end of the fence as the intra-rotor spacing grows from $s/d = 0.25$ to $s/d = 1$ to $s/d = 4$. The streamwise velocity in the array bypass flow likewise decreases as s is increased.

Although the swept rotor disc areas in Figure 6.14a seem to be distorted and enlarged compared to the true rotor area, this is simply due to the limits used in the contour plots, which have been selected such that other more subtle flow features could be visualised.

The intra-rotor spacing has a marked effect on the device-scale pressure coefficient and streamwise velocity in the rotor plane. High-pressure regions are seen above and below each turbine for $s/d = 4$ in Figure 6.14c which are not present for the higher local blockage configurations. For this configuration (Configuration C8), the intra-rotor spacing is sufficiently large for the flow to easily bypass the rotors on the device-scale. Thus, increasing the number of rotors in the fence will have little effect on the global performance because the flow is dominated by local rather than array-scale blockage effects (or the lack thereof). As s decreases and B_l increases, performance-enhancing device-scale blockage effects become more influential.

The asymmetry of the streamwise velocity contours around Rotors 3 and 4 for Configuration B8 in Figure 6.13c is also notable in the streamwise velocity contours for Configuration A8 in Figure 6.15a. Streamwise velocity contour asymmetry about each individual rotor increases as local blockage is increased.

6.2.3 Wake Recovery

This section includes a brief discussion of the factors affecting wake recovery for a tidal fence. There are two primary mixing mechanisms by which the local blockage of a tidal turbine fence affects the wake recovery. First, rotors operating in a fence with high local blockage are able to apply a greater thrust to the flow, as discussed in Section 6.2.2. While this results in a greater wake momentum deficit downstream of the turbines than for low blockage fences, it also influences wake recovery rates. Compared with a low local blockage fence, a fence with high local blockage generally has 1) reduced velocity in the near wake of the rotors and 2) increased velocity in the device and array-scale bypass flow (initially; prior to mixing). There is therefore increased shear between the core wake flows and the bypass flows, which increases the mixing rates and hence velocity recovery rates in the wake for high local blockage fences.

Second, rapid mixing between device-scale bypass flow and device wake for fences with low intra-rotor spacing and high local blockage results in a wake in which the individual rotor wakes become indistinguishable and develop into a single array wake shortly downstream of the rotor plane. This leads to a reduced array mixing surface area and thus slower overall array wake mixing and recovery.

Contours of streamwise velocity, u_x, on the horizontal plane through the mid-height of the rotors are shown in Figure 6.16. Contours for Configurations A8, B8, and C8 at the respective peak operating point ($\lambda = 5$ for all configurations) are included. The upper edge of each figure is the symmetry plane (only the simulated half of each fence is shown) and the flow is from left to right.

It is seen in Figure 6.16 that, in the current simulations, the effects of faster device-scale mixing due to greater shear for high local blockage conditions are offset against the slower array-scale mixing and higher momentum deficit that occurs for high local blockage.

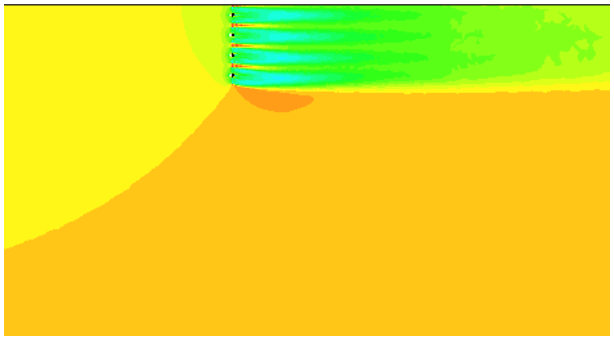

(a) $s/d = 0.25$

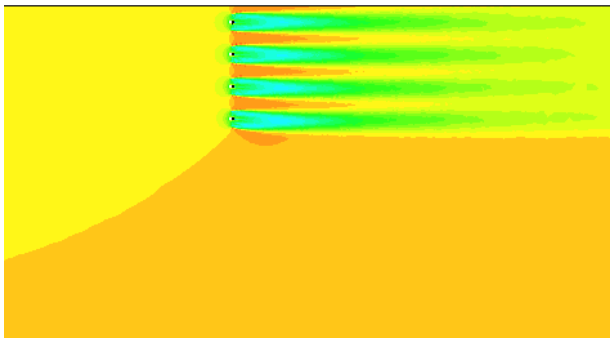

(b) $s/d = 1$

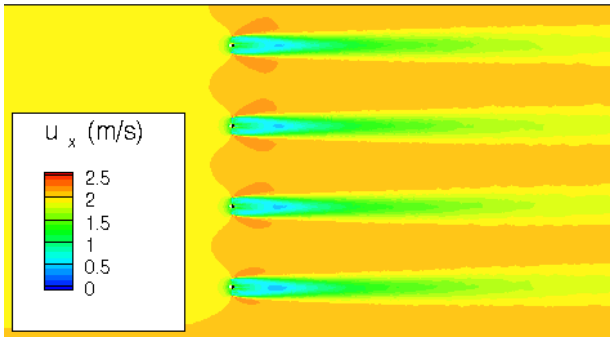

(c) $s/d = 4$

Figure 6.16: Streamwise velocity contours for intra-rotor spacings (a) $s/d = 0.25$, (b) $s/d = 1$, and (c) $s/d = 4$, all for $\lambda = 5$ and n = 8. The flow is from left to right.

For Configuration A8 (Figure 6.16a), for example, it is clear that the device-scale wake rapidly mixes into an array-scale wake, thereby reducing the mixing surface area in the far wake.

Conversely, the low-blockage case, Configuration C8 (Figure 6.16c), experiences more rapid wake recovery to the upstream flow condition than the other two configurations shown. The momentum deficit directly behind the rotors is less for this configuration than

for the others because the applied thrust is lowest for this case. Also, the device-scale bypass flow extends far into the wake, thus increasing mixing surface area.

The magnitude of the shear between the core wake and bypass flows depends on the turbulence model used (see, for example, Figure 4.17). Further investigation into the effect of various turbulence models on tidal fence wake recovery is recommended. Also, turbulence intensity (and turbulence dissipation) plays a significant role in the wake velocity recovery rate [28]. Although this was not a focus of the current study, future work should investigate the effect that varying ambient turbulence levels and turbulence dissipation rate have on wake recovery in high local blockage tidal turbine fences. A much higher mesh resolution in the wake than in the current simulations would be required for such a study.

6.2.4 Unsteady Rotor Hydrodynamics

The discussion for the finite-length fence study has to this point been focused on time-averaged results. However, as discussed in Section 6.2.2, the rotor plane streamwise velocity contours are asymmetric about the rotors near the ends of the highly blocked 8-rotor fences, suggesting that unsteady variation in blade loading is likely to occur for these rotors. In this section, unsteady single-blade torque results will be discussed. The discussion will focus on results for Configuration A8, the configuration with the greatest asymmetry about the rotors in the rotor plane streamwise velocity contours. The $\lambda = 5$ case (the design point of a turbine operating at this local blockage within an infinite fence spanning the full channel width) will be considered.

Unsteady Single-Blade Torque

Figure 6.18a includes normalised instantaneous single-blade torque as a function of blade azimuthal angle, γ, for the rotors in Configuration A8 over one rotor revolution. The instantaneous torque for the i^{th} rotor is normalised by the mean single-blade torque for

the respective rotor, $Q_{i,mean}$. $\gamma = 0$ occurs at blade top dead centre and we consider the azimuthal angle to be positive in the direction of rotation of the rotor, recalling that the rotation direction of the rotors alternates between clockwise and anti-clockwise. A schematic showing the blade starting positions and the rotor rotation directions (and thus the orientation of γ for each rotor) is given in Figure 6.17.

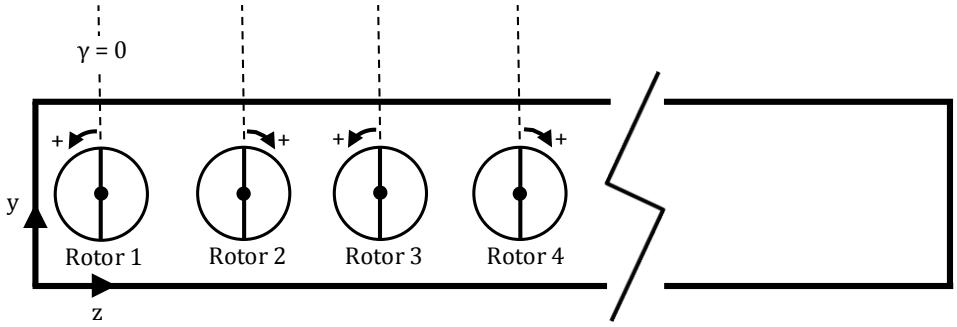

Figure 6.17: Rotor plane cross-section of the domain, viewed from an upstream position. For each rotor, the blade starting positions, rotation direction, and orientation of γ are indicated. The left wall is a symmetry boundary condition.

It is seen in Figure 6.18a that there is some high-frequency variation in the single-blade torque which is likely due to numerical effects, such as those arising from the use of a first order interpolation method to determine the velocities at the velocity sampling points (rather than a more computationally expensive higher order method). In order to highlight the most pertinent physical effects, a first order low pass filter is used to filter the data at two frequencies: once and four times per revolution. Specifically, cutoff frequency values of $f_{\text{cutoff}} = 1.01$ and 1.05 were used for the once per revolution frequency and values of $f_{\text{cutoff}} = 4.01$ and 4.05 were used for the four times per revolution frequency. The value of the cutoff frequency used for each desired frequency did not affect the results.

The once and four times per revolution frequencies have inherent physical importance in the current simulations; the once per revolution frequency is associated with the blades sweeping toward the unblocked bypass flow region and the four times per revolution frequency is associated with the blades passing the neighbouring two rotors and the floor and

lid of the domain during each revolution. A Cooley-Tukey fast Fourier transform (FFT) algorithm [130] is used to transform the data from the physical domain to the frequency domain prior to the application of the low pass filter. The normalised instantaneous torque data, filtered such that only the lowest frequency (once per rotor revolution) component remains, is shown in Figure 6.18b.

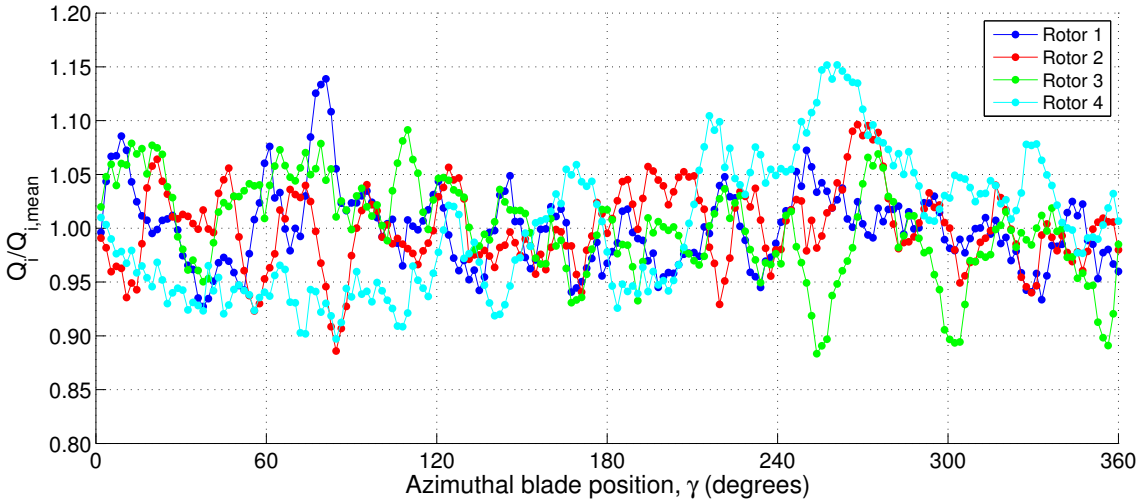

(a) Computed $Q_i/Q_{i,mean}$

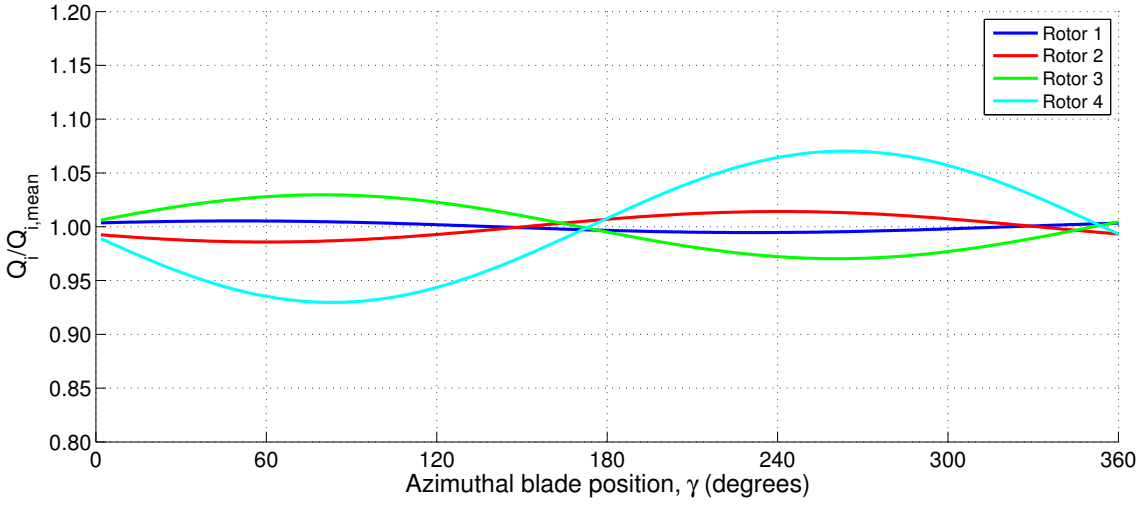

(b) Filtered $Q_i/Q_{i,mean}$

Figure 6.18: (a) Normalised instantaneous torque as a function of γ for Configuration A8 at $\lambda = 5$. (b) Corresponding filtered normalised instantaneous torque (filtered at the once per revolution frequency).

The once per revolution frequency is related to the rotor blades sweeping towards and

away from the centre of the fence during each rotor revolution. Blockage effects (which in this context are the positive effects of blockage on rotor performance) are greatest near the centre of the fence and decrease with lateral distance from the fence centre. This occurs due to transverse variation of streamwise velocity and affects the instantaneous blade torque as a blade sweeps through a revolution. It is seen in Figure 6.18b that at this cutoff frequency, all of the blades experience the highest torque when sweeping in towards the centre of the fence ($\gamma = 90°$ for Rotors 1 and 3 and $\gamma = 270°$ for Rotors 2 and 4) and the lowest when sweeping away from the fence centre toward the array bypass region ($\gamma = 270°$ for Rotors 1 and 3 and $\gamma = 90°$ for Rotors 2 and 4). The magnitudes of the filtered torque variation indicate that this effect is smallest on the centre-most rotor, Rotor 1, and largest on the array-end rotor, Rotor 4.

The maximum and minimum instantaneous torque, filtered with cutoff frequencies of once per revolution and four times per revolution, are plotted in Figure 6.19. The unfiltered time-averaged mean torque for each rotor is also included.

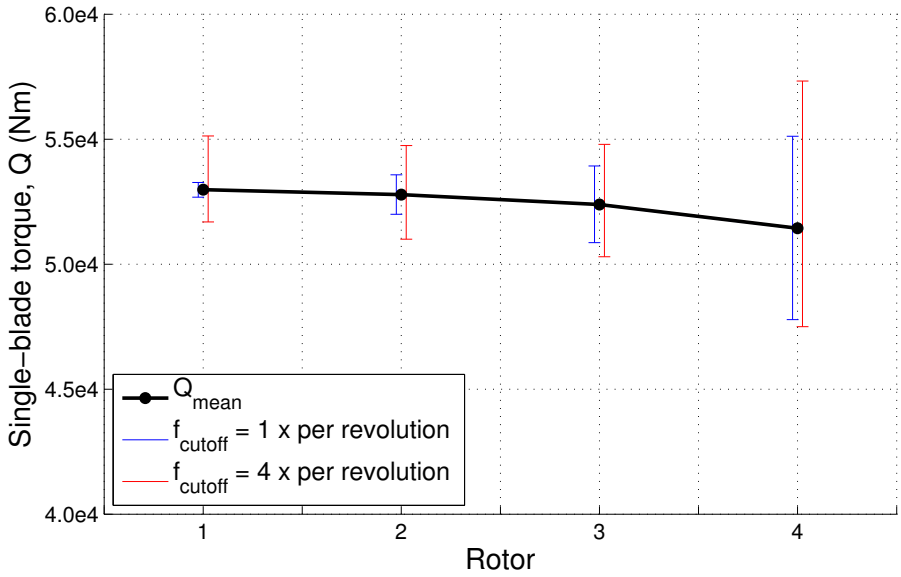

Figure 6.19: Mean single-blade torque (black) for each rotor in Configuration A8 at $\lambda = 5$ and corresponding maximum and minimum instantaneous torque for $f_{\text{cutoff}} =$ once (blue) and four times (red) per revolution.

For the centre-most rotor, the unsteady torque variation occurring at or below the four times per revolution cutoff frequency is considerably larger than that at the once per revolution frequency. This suggests that for this configuration, the near presence of the domain boundaries and neighbouring rotors account for more of the Rotor 1 unsteady torque variation than array-scale blockage effects. Conversely, for Rotor 4, the torque variation at the once per revolution frequency is a significant portion of the torque variation at or below the four times per revolution cutoff frequency. For both the once and four times per revolution cutoff frequencies, the unsteady blade torque variation increases as the rotor's distance from the centre-most position in the fence increases.

Effect of Azimuthal Position of Neighbouring Rotor Blades

In all of the simulations discussed thus far, the starting position of the 2 rotor blades is consistent for each rotor in the array; the starting positions of the 2 blades for each rotor are $\gamma = 0^\circ$ and 180°. Because the rotors have uniform angular velocity, this leads to a regular blade-passing pattern, in which the blades pass blades from neighbouring rotors at $\gamma = 90^\circ$ and 270°.

It is of interest to determine whether the azimuthal position of neighbouring rotors' blades has a significant effect on the unsteady variation in a blade's instantaneous torque. Simulations in which the Rotor 1 and Rotor 3 blades start at $\gamma = 90^\circ$ and 270°, rather than at 0° and 180°, were completed for Configuration A8. The direction of rotation remains the same as in the previous simulations for all rotors. The adjusted blade starting positions, along with the direction of rotation/orientation of γ, are indicated in Figure 6.20.

The time-averaged mean torque and maximum and minimum instantaneous torque, filtered with cutoff frequencies of once per revolution and four times per revolution, are plotted for the original blade starting positions (grey) as well as for the alternative initial blade

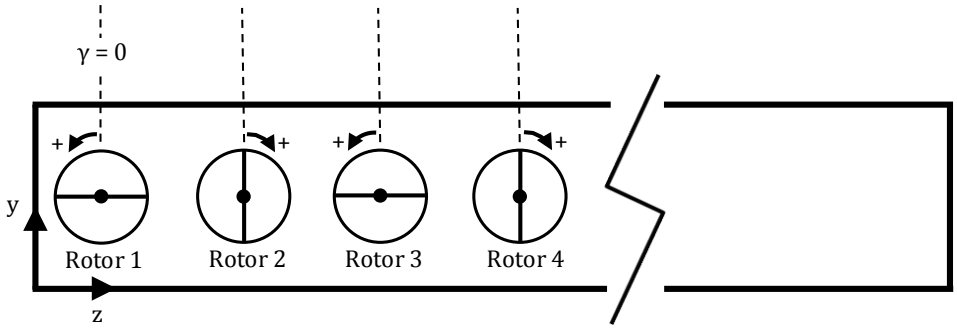

Figure 6.20: Rotor plane cross-section of the domain with the alternative initial blade position, viewed from an upstream position. For each rotor, the blade starting positions, rotation direction, and orientation of γ are indicated. The left wall is a symmetry boundary condition.

positions in Figure 6.21. The original blade starting position results are the same as those presented in Figure 6.19.

It is seen in Figure 6.21 that the azimuthal position of neighbouring rotor blades has little effect on the mean single-blade torque for the rotors in the fence. In addition, it is evident from the results in Figure 6.21 that the azimuthal position of neighbouring blades does not have a large influence on the range of variation in instantaneous torque through a blade cycle.

6.3 Conclusions

Finite-length tidal fences consisting of $n = 2$, 4, and 8 rotors have been simulated for a range of local blockage ratios. The maximum global power coefficient for each fence improves with increasing n and also improves with reduced intra-rotor spacing (and hence increased B_l). The improvement with greater n occurs because increasing n reduces the proportion of upstream flow that is able to divert around the tidal fence by way of the array-scale bypass flow, even whilst constant global blockage is maintained.

The performance of individual rotors operating within the tidal fences was also considered. Both the local power and local thrust coefficients (C_{pl} and C_{tl}, respectively) were greatest

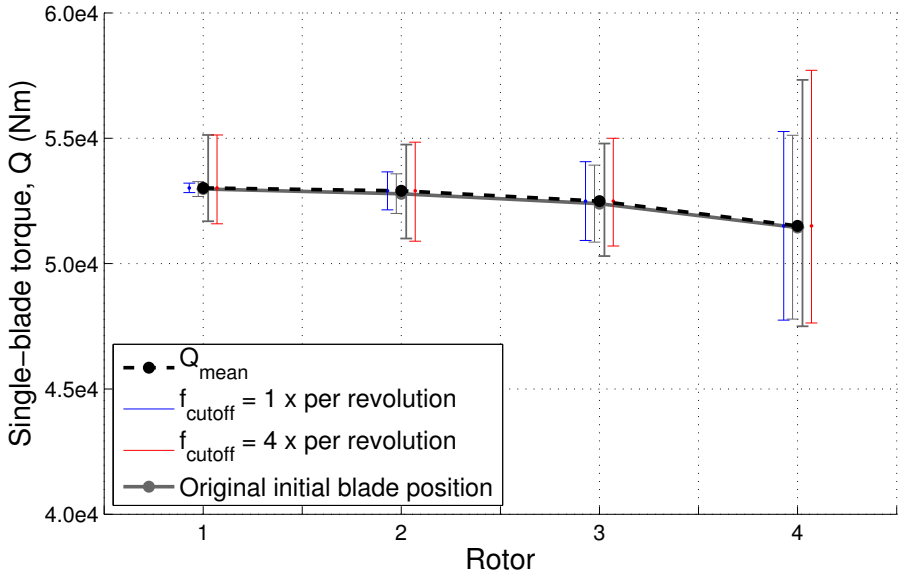

Figure 6.21: Mean single-blade torque (black) for each rotor in Configuration A8 at $\lambda = 5$ and corresponding maximum and minimum instantaneous torque for $f_{\text{cutoff}} =$ once (blue) and four times (red) per revolution for the alternate initial blade positions. Results for the original initial blade positions (plotted in Figure 6.19) are included for comparison (grey).

for Rotor 1, the rotor operating closest to the centre of the tidal fence, and were lowest for the rotor operating closest to the free-stream flow. The drop-off in hydrodynamic performance at the array-ends (compared with the performance of Rotor 1) was amplified with increased thrust, for example in fence configurations with higher local blockage and for higher tip speed ratios.

A number of physical effects caused by alteration of the number of rotors in a tidal fence as well as intra-rotor spacing (and hence local blockage) are visible in rotor plane pressure coefficient and streamwise velocity contour plots. The addition of rotors to a tidal fence results in higher streamwise velocity and lower pressure coefficient in the array-scale bypass region directly adjacent to the fence as well as in the device-scale bypass region. An increase in local blockage also leads to lower pressure coefficient and increased streamwise velocity in the array bypass region. Increasing the local blockage also results in reduced

pressure coefficient around the individual rotors and asymmetric streamwise velocity fields around the rotors, particularly at the extremity of the fence.

For the 8-rotor fences, far-field wake recovery is seen to be fastest for the configuration with the lowest local blockage (Configuration A8). However, this is dependent on the rotor design/geometry used, the thrust applied by each fence (which varies for the three cases shown), the ambient turbulence conditions, and turbulence dissipation rates, and it cannot be expected that this will always be the case.

Investigation of unsteady single-blade torque results for Configuration A8 has indicated that instantaneous torque variation due to low frequency effects is smallest for the array-centre rotor and greatest for the array end rotor. This is because transverse shear is smallest at the fence centre and largest at the ends of the fences. The effects of shear on blade loading have been investigated in previous studies. It has been shown, for instance, that increased shear in the vertical direction results in greater variation in unsteady blade loads [105].

Further, it has been shown that the starting position of the rotor blades (and hence the azimuthal position of neighbouring rotor blades) has little effect on the magnitude of unsteady single-blade torque variation through a rotor revolution. It should be noted that although only effects due to relative blade positioning are considered here, additional unsteady loads would occur at a frequency of once per revolution with the inclusion of a supporting tower in the simulations.

Tidal fence power coefficients could be further maximised by designing rotors for *in-situ* conditions. For instance, consideration of both the local blockage and the number of rotors in a tidal fence during the rotor design process will improve the hydrodynamic efficiency of the array. In addition, further work on the subject should include an investigation into the effectiveness of tuning the tip-speed ratios of individual rotors within tidal turbine fences.

Such tuning of the tip speed ratio may reduce the drop-off in performance at the array-ends.

Chapter 7

Conclusions and Future Work

Conclusions regarding the completed work and plans for future work are presented in this chapter. The work discussed in Chapters 3 and 4 is summarised in Section 7.1. Summaries of the findings of Chapters 5 and 6 are included in Sections 7.2 and 7.3, respectively. Section 7.4 includes suggestions for future work and Section 7.5 provides a summary of the contributions made by this thesis.

7.1 Actuator Line Model Modifications and Validation

CFD simulations of tidal turbines provide insight into the physical phenomena of flow through and around the turbines and arrays of turbines. These simulations often provide more detail than experimental tests as well. Models that employ blade element theory, such as blade element-momentum models and their unsteady counterparts, actuator line models, are particularly useful for array-scale simulations. Both classes of models allow rotor geometry characteristics to be considered in the simulations, while avoiding the need to discretise blade boundary layers or employ sliding meshes.

A difficulty of actuator line models is that the application of point sources in the simulation can lead to local flow field distortion in the near vicinity of the actuator lines. This can

result in incorrect velocities being returned by the solver and inaccurate computations of the forces on the blade segments. Previous actuator line models have employed a Gaussian distribution for each point source to reduce the distortion in the flow field, thereby improving the computational results. This method, however, is dependent on a parameter, ϵ, which influences the weighting of the distribution. The value selected for ϵ can affect the velocity returned by the solver, and therefore the results for the computation.

An alternative method of obtaining the magnitude and angle of attack of the relative velocity at the collocation points without the use of a Gaussian distribution is proposed, verified, implemented, and validated in Chapters 3 and 4. In this method, flow velocity is sampled at three points relative to the collocation point for each blade segment at the start of each solution iteration. A potential flow equivalence method is then used to calculate the relative velocity at each blade segment from the respective sampled velocities.

It is imperative that the velocity sampling points do not lie in the region near the actuator line in which the flow field is distorted. To determine the appropriate distance between the collocation point and the sampling points, an in-depth study of the influence of selected parameters on the velocity field of a 2D symmetric thin aerofoil was completed. The results of this study indicated that a mesh element length of $c/4$ or less, where c is the chord of the blade element, is appropriate for the actuator line model. The results also suggested that the points at which the velocity is sampled for use in the flow analysis routine should be at least one chord length away from the corresponding collocation point and should be upstream of the aerofoil, in the range $\pi/2 < \gamma < 3\pi/2$, where γ is the azimuthal angle and $\gamma = 0$ is on the blade chord line downstream of the aerofoil.

Prior to its implementation in a 3D unsteady simulation, the flow analysis routine was verified for 2D stationary aerofoils, 2D aerofoils moving with constant velocity, and 3D stationary elliptic wings. A stationary 3D elliptic wing was also used to verify the concept of using an actuator line to simulate a lifting surface and the unstructured grid adaptation

that was presented in Chapter 3. Unstructured mesh simulations of the elliptic wing at attack angle $\alpha = 12^{\circ}$ provided results for circulation at the blade root that were within 3.3% of the circulation determined using analytic methods. The compatibility of the current actuator line model implementation with unstructured grids allows for the straightforward inclusion of turbine components including the nacelle and tower, and any additional solid bodies of interest, in the computational mesh.

The 3D unsteady actuator line method, including the new flow analysis routine and unstructured grid adaptation, has been validated using the NREL Phase VI wind tunnel experimental results. Results from the validation simulations indicate that although the overall performance of the model is acceptable, improvements in accuracy can be made in the vicinity of the blade tips, where rotational effects are significant and the assumption that it is acceptable to use 2D steady flow aerofoil data may be less valid.

7.2 Fences Spanning an Infinitely Long Channel

In order to produce significant power using tidal turbines, it will be necessary for the turbines to be deployed in arrays. Nishino and Willden have investigated tidal fences, a type of array in which all rotors are in a single row, using both analytical and RANS-embedded actuator disc methods [41, 42]. These studies indicated that reducing the spacing between turbines in a fence (and thereby increasing the local blockage) can result in significant improvement in the maximum attainable power coefficient for a tidal fence. The theoretical model and actuator disc simulations used by Nishino and Willden allowed for idealised rotors to be examined, but were not capable of taking rotor design and blade geometry into consideration.

In this thesis, both BEM and actuator line simulations of tidal fences have been completed. Because both of these simulation methods employ blade element theory, blade geometry

affects the simulation results. Thus, results for specific rotor geometries, rather than results for rotors idealised as discs, were obtained.

A BEM tool for the design and simulation of horizontal-axis axial rotors has been employed to design rotors for hydrodynamically optimal operation in tidal fences spanning an infinitely long channel. Four intra-rotor spacings were considered, and therefore four rotor designs were generated. The resulting designs indicate that in order to take full advantage of moderate to highly-blocked conditions, the rotor solidity must increase to allow greater thrust to be applied to the flow. The optimal solidity for the domain with the highest blockage was approximately double the solidity for the unblocked rotor design through most of the blade span.

Next, each of the rotor designs was simulated for a range of tip speed ratios in each of the four fence configurations. The resulting power curves indicate that the rotor designed for the highest blockage has the best hydrodynamic performance of all cases considered when operating in design conditions, but has poor performance relative to other rotor designs in lower blockage operational conditions. Although peak performance declines for all rotors in off-design blockage conditions, rotors designed for moderately high local blockage (i.e. the rotor designed for s/d = 1) perform well for a range of intra-rotor spacings relative to the optimal rotor for each spacing (i.e. within 9% of the optimum $C_{p,max}$ achievable at each spacing).

Also, the peak power coefficient achieved by each rotor design increases when intra-rotor spacing is reduced from the design spacing for the rotor. For instance, the peak power coefficient for the unblocked rotor operating in the $s/d = 0.25$ domain is 55% greater than its peak power coefficient in the virtually unblocked domain. A 44% increase in the rotor thrust coefficient accompanies this improvement in $C_{p,max}$. In order to achieve this increased power coefficient without altering the rotor design, the tip speed ratio cor-

responding to peak performance must be increased. This increased tip speed ratio enables the rotor to apply greater thrust to the flow.

Actuator line simulations of an infinite-length tidal fence spanning a channel were compared with the BEM results for a selected intra-rotor spacing ($s/d = 1$). Time-averaged actuator line power coefficient results for tip speed ratios below the peak operating point were in very good agreement with the BEM results (within 3%). Results for C_p at higher tip speed ratios had greater discrepancies, but still showed generally good agreement. Plots of the radial distribution of time-averaged angle of attack for the actuator line and BEM simulations indicated that much of the difference in rotor power coefficients at high tip speed ratios was due to slight disagreement in angle of attack along the the blade span. Greater disagreement is seen near the blade root, but due to the low moment arm in this region of the blade, this has little effect on the power coefficients.

7.3 Fences Partially Spanning Wide Channels

Although the infinite channel assumption discussed above is useful for CFD modelling, a more realistic assumption is that tidal turbines will be deployed in fences of finite length that span only part of a wide channel. For this reason, actuator line simulations of finite-length tidal fences consisting of 2, 4, and 8 rotors were carried out. Each of the fences was simulated over a range of tip speed ratios for three different intra-rotor spacings. Thus the effects of altering both the number of rotors in the fence and the intra-rotor spacing on the performance of the fence and individual rotors within the fence could be assessed.

The results of the finite-length tidal fence study indicate that both the addition of rotors to a tidal fence and reduction of the intra-rotor spacing result in an improvement in the fence's peak global power coefficient. Reducing the intra-rotor spacing from $s/d = 4$ to $s/d = 0.25$, combined with increasing the number of rotors in the fence from 2 to 8, resulted in an improvement of 7.6% for $C_{pg,max}$. This general trend is in agreement with the analytical

findings of Nishino and Willden [42]. However, a comparison of the current actuator line results for the $s/d = 1$ configurations with actuator disc results from Nishino and Willden indicates that the actuator disc values for C_{pg} are 12-14% greater than for the actuator line results. Several factors contribute to this discrepancy; chief among them is the inclusion of viscous losses due to the presence of discrete blades in actuator line simulations. These discrete blade effects are not modelled in the actuator disc simulations.

It was also seen that the rotors in the centre of the tidal fence have higher local power and thrust coefficients than those at the end of the fence. The magnitude of the relative drop-off in thrust and power coefficients from the centre rotor to the array-end rotor is affected by both the number of rotors in a fence and the tip speed ratio of the rotors. For the $n = 8$, $s/d = 0.25$ case, there was less than 1% difference in C_{pl} for the centre and end rotors of the fence at $\lambda = 4$, but this increases to 7% difference for $\lambda = 7$.

Rotor-plane contours of the pressure coefficient and streamwise velocity give insight into the effects that varying the local blockage and/or number of rotors in an array have on the flow around the rotors and hence rotor performance. Alteration of the fence length and local blockage affect the interactions between the device-scale bypass flow and the array-scale bypass flow. The coupled effects of the modified device and array-scale bypass flows influence the magnitude of transverse shear at each of the individual rotors in the tidal fence. Specifically, rotors at the ends of fences with high blockage and a large number of rotors experience greater transverse shear than rotors at the centre of fences or rotors in shorter, lower blockage fences. The high transverse shear at the array-end rotors results in increased unsteady load variations for these rotors.

7.4 Model Limitations and Future Work

This section includes a summary of the main limitations of the current work and suggestions for future work relating to actuator line modelling and tidal turbine fence studies.

7.4.1 Limitations

One of the most important limitations of actuator line and RANS-BEM models is their dependence on high-quality aerodynamic data for the relevant blade section(s). In the NREL Phase VI validation study presented in Chapter 4, experimental aerodynamic data was not available for the full range of Reynolds numbers required. It was therefore necessary to use interpolated/approximated data, which resulted in lower accuracy simulations. Also, the requirement for accurate aerodynamic data over a large range of attack angles resulted in limited choices for the aerofoil section used in the rotor design process in Chapter 5.

In addition, although the tidal fence studies provide useful insight into the physical effects of operating rotors in blocked flows, the resolution in the wakes of the simulations was limited by the available computational resource. The resolution of the wake affects the wake expansion and hence the effective blockage. This, in turn, will affect the power output of the rotors. Similarly, the magnitude of ambient turbulence and turbulence dissipation will affect wake expansion and rotor power, but this project did not explore these effects.

Further, it was assumed in the tidal fence studies that the Prandtl tip correction could be employed in RANS-BEM simulations of rotors in highly blocked flows. However, it has not been shown that the Prandtl tip correction is applicable for highly blocked flows. This correction relies on the assumption that the flow bypassing the rotor and mixing with the core wake flow has speed U_∞, which is not the case for blocked flows, in which the bypass flow is accelerated through the bypass region.

7.4.2 Future Work

Actuator Line Model

The results from this thesis and other actuator line validation simulations of the NREL Phase VI rotor [74] have shown that the models disagree with the experimental results in the vicinity of the blade tips. Although the use of the Shen et al. tip correction [121] improved agreement between the results in the current work and experiments, discrepancies with the experimental results remain. Further investigation into the physical phenomena causing the inaccuracies at the blade tips, including developing a better understanding of any dependency that aerodynamic coefficients may have on rotational speed and blade geometry, is recommended. In addition, it is possible that improvements could be made to the unstructured grid adaptation used in the current work. For example, the use of higher order interpolation of sampling point velocities (rather than the inverse distance weighting method currently used) in the flow analysis routine may improve results.

Design of Rotors

In the current work, rotor designs were optimised for operation in infinitely long fences spanning a channel. One of these designs was then selected for use in a study of finite-length fences operating in a wide channel. Thus, although the effects of local blockage and fence length could be examined in the finite-length fence study, maximum power coefficients for *in-situ* local and global blockage have not been determined. Future work should include adaptation of the BEM design tool to accommodate multiple rotors. With this adaptation, rotors may be optimised for specific tidal fence configurations with known local and global blockage conditions. In addition, future work should investigate whether different aerofoils can provide greater power output than the one currently used. This ability to complete this work, however, relies on the availability of accurate aerodynamic data for a range of aerofoil sections.

Tidal Turbine Fence Studies

As discussed above, the RANS-BEM tidal fence simulations in Chapter 5 employed the Prandtl tip correction, even though it is not known whether this correction is applicable for rotors operating in highly blocked flows. Future work should investigate the suitability of the Prandtl tip correction in blocked flows prior to its implementation. Also, the current work employed a number of approximations to simplify the simulations and isolate the effects of local blockage and fence length on tidal fence performance. These included the use of uniform flow at the inlet boundary condition, the use of a rigid lid, and low ambient turbulence. It is of interest to include a sheared inlet velocity profile, tidal cycles, a free surface, waves, and varied ambient turbulence and turbulence dissipation levels in future tidal fence studies. These will affect the wake development and recovery, which in turn will affect the device and array-scale bypass flows and hence fence power coefficients. Further, because free surface deformation would affect the blockage and hence performance of tidal turbines (particularly in closely packed fences), volume of fluid (VOF) method simulations confirming the viability of the rigid lid assumption used in this work should be completed. In addition, the tip speed ratio in the current work was constant for all rotors in each fence simulation. The possibility of employing non-uniform tip speed ratios across the fences to further improve power coefficients or reduce the unsteady loading variation of array-end rotors should be investigated. Alternatively, it is possible that reorienting the rotors at the array ends at an angle to the centre rotors of the fence (rather than all rotors facing directly upstream) could reduce the transverse shear across these rotors and thus improve their performance.

7.5 Contributions

The primary contributions of this thesis to the fields of wind and tidal energy are discussed in this section.

Actuator Line Modelling

A new method of obtaining the relative velocity at each blade segment in actuator line models has been introduced, verified, and validated. The method relies on potential flow equivalence and eliminates the need for a Gaussian distribution of the sources applied to the flow field. The method for obtaining relative flow velocities has also been coupled with a new method for adapting actuator line models for use with unstructured tetrahedral meshes.

Tidal Turbine Design for Blocked Conditions

This is the first work in which tidal rotors are designed for *in-situ* blockage conditions. The results of this study indicate that while the power coefficient for an unaltered rotor design will increase with an increase in blockage, hydrodynamic performance can be further improved if the rotor is redesigned for the new operational blockage conditions. In the current work, rotors designed for high-blockage operational conditions have higher solidity than those designed for low-blockage and unblocked conditions. This increased solidity allows the rotors to impart greater thrust on the flow, which in turn amplifies the performance-enhancing mechanism for blocked flows.

Individual Rotor Performance in Finite-Length Tidal Fences

Previous finite-length tidal fence studies have focused on global fence performance and/or wake recovery. This thesis includes a study of local effects for rotors operating in a finite-length fence. It was found that when fence thrust is increased, i.e. by increasing the local blockage or the tip speed ratio, the performance of array-end rotors relative to that of the rotors at the centre of the fence declines. The physical causes for this and other local effects are discussed in this thesis.

Appendix A

Publications

Schluntz, J., Vogel, C.R., and Willden, R.H.J., 2014. "Blockage-enhanced performance of tidal turbine arrays." In Proc. 2^{nd} Asian Wave and Tidal Energy Conference, Tokyo, Japan.

Schluntz, J. and Willden, R.H.J, 2014. "An actuator line method with novel blade flow field coupling based on potential flow equivalence." *Wind Energy*. (Accepted 15 May 2014)

Willden, R.H.J., Nishino, T., and Schluntz, J., 2014. "Tidal stream energy: designing for blockage." In Proc. 3^{rd} Oxford Tidal Energy Workshop, Oxford, UK.

Schluntz, J. and Willden, R.H.J., 2013. "The effect of rotor design on the power output of closely packed tidal turbines." In Proc. 10^{th} European Wave and Tidal Energy Conf., Aalborg, Denmark.

Schluntz, J. and Willden, R.H.J., 2013. "Validation of an actuator line model for tidal turbine simulations." In Proc. 2^{nd} Oxford Tidal Energy Workshop, Oxford, UK.

Schluntz, J. and Willden, R.H.J., 2012. "Development of an actuator line model for tidal turbine simulations." In Proc. Oxford Tidal Energy Workshop, Oxford, UK.

Bibliography

[1] D.J.C. MacKay. *Sustainable Energy - Without the Hot Air*. UIT Cambridge Ltd, Cambridge, England, 2009.

[2] HM Government. The UK renewable energy strategy. The Stationary Office, UK, 2009.

[3] Renewable Energy Advisory Board. 2020 VISION - how the UK can meet its target of 15% renewable energy, 2008.

[4] T. McErlean and N. Crothers. *Harnessing the Tides: The Early Medieval Tide Mills at Nendrum Monastery*. Stationary Office Books, UK, 2007.

[5] The Guardian. *Severn barrage ditched as new nuclear power plants get green light*. Online: `http://www.theguardian.com/environment/2010/oct/18/severn-barrage-nuclear`, October 18, 2010.

[6] B.V. Davis, D.H. Swan, and A. Kenneth. Ultra low-head hydroelectric power generation using ducted vertical axis water turbines. Technical Report NEL-022, National Research Council, Canada, 1981.

[7] P. Greenacre, R. Gross, and P. Heptonstall. Great expectations: The cost of offshore wind in UK waters. Technical report, UK Energy Research Centre, 2010.

[8] Black and Veatch. Tidal stream resource and technology summary report. Report to Carbon Trust, UK, 2005.

[9] Carbon Trust. UK tidal current resource & economics. Technical Report CTC799, June 2011.

[10] Carbon Trust. Accelerating marine energy. Technical Report CTC797, July 2011.

[11] OpenHydro. *Technology: Open-Centre Turbine*. `http://www.openhydro.com/techOCT.html`, 2014.

[12] Marine Current Turbines. *SeaGen Technology*. `http://www.marineturbines.com/seagen-technology`, 2014.

[13] Blue Energy. *VAHT - Vertical Axis Hydro Turbine*. `http://www.bluenergy.com/vertical-axis-turbine/vaht/`, 2011.

[14] R.A. McAdam, G.T. Houlsby, M.L.G. Oldfield, and M.D. McCulloch. Experimental testing of the Transverse Horizontal Axis Water Turbine. In *Proc. engordnumber8 European Wave and Tidal Energy Conf.*, pages 360–365, 2009.

[15] Ocean Renewable Power Company. *Turbine Generator Unit*. `http://www.orpc.co/orpcpowersystem_turbinegeneratorunit.aspx`, 2014.

[16] BioPower Systems. *bioSTREAM*. `http://www.biopowersystems.com/biostream.html`, 2013.

[17] Pulse Tidal. *Our Technology - Overview*. `http://www.pulsetidal.com/our-technology.html`, 2014.

[18] Verdant Power Inc. *The Rite Project*. `http://www.verdantpower.com/rite-project.html`, 2014.

[19] Marine Current Turbines. *Testing*. `http://www.marineturbines.com/SeaGen-Technology/Testing`, 2014.

[20] OpenHydro Group Limited. *news: press releases*. `www.openhydro.com/news/archive.html`, 2014.

[21] OpenHydro. *EDF and OpenHydro Prepare to Install First Tidal Turbine in Brittany, France*. `http://www.openhydro.com/news/OpenHydroPR-010911.pdf`, september 1, 2011.

[22] UK Government. *20 million boost for UK marine power*. `https://www.gov.uk/government/news/20-million-boost-for-uk-marine-power`, February 27, 2013.

[23] MeyGen Ltd. *The Project*. `http://www.meygen.com/the-project/`, 2014.

[24] SeaGeneration Wales Ltd. *Project Description*. `http://seagenwales.co.uk/description.php`, 2014.

[25] Scottish Power Ltd. *Islay Tidal Array*. `http://www.scottishpower.com/pages/islay_tidal_array.asp`, 2014.

[26] T. Daly, L.E. Myers, and A.S. Bahaj. Experimental analysis of the local flow effects around single row tidal turbine arrays. In *3rd International Conference on Ocean Energy*, 2010.

[27] L.E. Myers, B. Keogh, and A.S. Bahaj. Experimental investigation of inter-array wake properties in early tidal turbine arrays. In IEEE, editor, *OCEANS 2011*, 2011.

[28] T. Stallard, R. Collings, T. Feng, and J. I. Whelan. Interactions between tidal turbine wakes: Experimental study of a group of three-bladed rotors. *Philosophical Transactions of the Royal Society A*, 371, 2013.

[29] E.J.M. Rankine. On the mechanical principles of the action of propellers. *Trans. Inst. Naval Architects*, 6:13–39, 1865.

[30] R.E. Froude. On the part played in propulsion by difference in pressure. *Trans. Inst. Naval Architects*, 30:390–423, 1889.

[31] X. Sun, J.P. Chick, and I.G. Bryden. Laboratory-scale simulation of energy extraction from tidal currents. *Renewable Energy*, 33:1267–1274, 2008.

[32] D.L.F. Gaden and E.L. Bibeau. A numerical investigation into the effect of diffusers on the performance of hydro kinetic turbines using a validated momentum source turbine model. *Renewable Energy*, 35:1152–1158, 2010.

[33] M.E. Harrison, W.M.J. Batten, L.E. Myers, and A.S. Bahaj. Comparison between CFD simulations and experiments for predicting the far wake of horizontal axis tidal turbines. In *Proc. 8th European Wave and Tidal Energy Conf.*, pages 566–575, 2009.

[34] S. Gant and T. Stallard. Modelling a tidal turbine in unsteady flow. In *ISOPE*, 2008.

[35] C. Belloni and R. H. J. Willden. A computational study of a bi-directional ducted tidal turbine. In *Proc. 3rd International Conf. on Ocean Energy*, 2010.

[36] C. Garrett and P. Cummins. The efficiency of a turbine in a tidal channel. *J. Fluid Mech.*, 588:243–251, 2007.

[37] J. I. Whelan, J. M. R. Graham, and J. Peiró. A free-surface and blockage correction for tidal turbines. *J. Fluid Mech.*, 624:281–291, 2009.

[38] R. Vennell. Tuning turbines in a tidal channel. *J. Fluid Mech.*, 663:253–267, 2010.

[39] C. Garrett and P. Cummins. The power potential of tidal currents in channels. *Proc. Royal Society A*, 461:2563–2572, 2005.

[40] R. Vennell. Tuning tidal turbines in-concert to maximise farm efficiency. *J. Fluid Mech.*, 671:587–604, 2011.

[41] T. Nishino and R. H. J. Willden. The efficiency of an array of tidal turbines partially blocking a wide channel. *J. Fluid Mech.*, 708:596–606, 2012.

[42] T. Nishino and R. H. J. Willden. Two-scale dynamics of flow past a partial cross-stream array of tidal turbines. *J. Fluid Mech.*, 730:220–244, 2013.

[43] H. Glauert. The analysis of experimental results in the windmill brake and vortex ring states of an airscrew. *Reports and Memoranda, No. 1026, Her Majesty's Stationery Office*, 1926.

[44] C.N.H Lock, H. Bateman, and H.C.H. Tiwsend. An extension of the vortex theory of airscrews with applications to airscrews of small pitch, including experimental results. *Reports and Memoranda, No. 1014, Her Majesty's Stationery Office*, 1925.

[45] H. Glauert. Airplane Propellers. In *Aerodynamic Theory*, pages 169–360. Julius Springer, Berlin, fourth edition, 1935.

[46] J.G. Leishman. *Principles of Helicopter Aerodynamics*. Cambridge University Press, New York, second edition, 2006.

[47] DNV GL. *Bladed: Wind Turbine Design Software*. `http://www.gl-garradhassan.com/en/software/GHBladed.php`, 2013.

[48] DNV GL. *Bladed: A design tool for tidal current turbines*. `http://www.gl-garradhassan.com/en/software/GHTidalBladed.php`, 2013.

[49] P.J. Moriarty and A.C. Hansen. AeroDyn theory manual. Technical Report NREL/EL-500-36881, National Renewable Energy Laboratory, 2005.

[50] A. Hallanger and I.Ø. Sand. CFD wake modelling with a BEM wind turbine submodel. *Modeling, Identification, and Control*, 34(1):19–33, 2013.

[51] M.E. Harrison, W.M.J. Batten, and A.S. Bahaj. A blade element actuator disc approach applied to tidal stream turbines. *Oceans*, pages 1–8, 2010.

[52] R. Malki, Williams A.J., T.N. Croft, M. Togneri, and I. Masters. A coupled blade element momentum - computational fluid dynamics model for evaluating tidal stream turbine performance. *Applied Mathematical Modelling*, 37:3006–3020, 2013.

[53] S. C. McIntosh, C. F. Fleming, and R. H. J. Willden. Embedded RANS-BEM tidal turbine design. In *Proc. 9^{th} European Wave and Tidal Energy Conf.*, 2011.

[54] C. F. Fleming, S. C. McIntosh, and R. H. J. Willden. Design and analysis of a bi-directional ducted tidal turbine. In *Proc. 9^{th} European Wave and Tidal Energy Conf.*, 2011.

[55] C. Belloni. *Hydrodynamics of Ducted and Open-Centre Tidal Turbines*. PhD thesis, University of Oxford, 2013.

[56] L. Prandtl and A. Betz. Vier abhandlungen zur hydrodynamik und aerodynamic. Technical report, Göttingen, 1927.

[57] M.L. Buhl. A new empirical relationship between thrust coefficient and induction factor for the turbulent windmill state. Technical Report NREL/TP-500-36834, National Renewable Energy Laboratory, 2005.

[58] H. Snel and J.G. Schepers. Joint investigation of dynamic inflow effects and implementation of an engineering method. Technical Report ECN-C–94-107, Energy research Centre of the Netherlands, 1995.

[59] H. Snel, R. Houwink, G. van Bussel, and A. Bruining. Sectional prediction of 3D effects for stalled flow on rotating blades and comparison with measurements. In *1993 European Community Wind Energy Conference Proceedings*, 1993.

[60] G.J.W. van Bussel. The application of advanced rotor (performance) methods for design calculations. In *Proc. 10^{th} Windturbine Aerodynamics Specialists Symposium*, pages 141–157, 1993.

[61] T. Burton, N. Jenkins, D. Sharpe, and E. Bossanyi. *Wind Energy Handbook*. John Wiley & Sons Ltd., West Sussex, UK, 2011.

[62] S.G. Voutsinas, M.A. Beleiss, and K.G. Rados. Investigation of the yawed operation of wind turbines by means of a vortex particle method. In *AGARD Conf. Proc.*, volume 552, pages 11.1–11.11, 1994.

[63] R.H. Miller. The aerodynamic and dynamic analysis of horizontal axis wind turbines. *J. Wind Eng. Ind. Aerodyn.*, 15:329–340, 1983.

[64] A. Van Garrel. Development of a wind turbine aerodynamics simulation module. Technical Report ECN-C-03-079, ECN, 2003.

[65] J. Katz and A. Plotkin. *Low-Speed Aerodynamics*. Cambridge University Press, New York, second edition, 2001.

[66] Y. Li and S.M. Çalişal. Discrete vortex method for simulating a stand-alone tidal-current turbine: Modeling and validation. *J. Offshore Mech. Arct.*, 132, 2010.

[67] J.N. Sørensen and W.Z. Shen. Numerical modeling of wind turbine wakes. *J. Fluid Mech.*, 124:393–399, 2002.

[68] R.E. Brown. Rotor wake modeling for flight dynamic simulation of helicopters. *AIAA Journal*, 38:57–63, 2000.

[69] R.E. Brown and A.J. Line. Efficient high-resolution wake modeling using the vorticity transport equation. *AIAA Journal*, 43:1434–1443, 2005.

[70] R. Mikkelsen. *Actuator Disc Methods Applied to Wind Turbines*. PhD thesis, Technical University of Denmark, Lyngby, Denmark, 2003.

[71] W. Haans and R. Mikkelsen. Airfoil models in the actuator line code assessed with near-wake measurements on a yawed rotor. In *45th AIAA Aerospace Sciences Meeting and Exhibit, Reno, Nevada*, 2007.

[72] S. Ivanell, J.N. Sørensen, R. Mikkelsen, and D. Henningson. Analysis of numerically generated wake structures. *Wind Energy*, 12:63–80, 2009.

[73] W.Z. Shen, W.J. Zhu, and J.N. Sørensen. Actuator line/Navier-Stokes computations for the MEXICO rotor: Comparison with detailed measurements. *Wind Energy*, 15:811–825, 2012.

[74] P.K. Jha, M.J. Churchfield, P.J. Moriarty, and S. Schmitz. Accuracy of state-of-the-art actuator-line modeling for wind turbine wakes. In *51st AIAA Aerospace Sciences Meeting*, 2013.

[75] N. Troldborg, J.N. Sørensen, and R. Mikkelsen. Numerical simulations of wake characteristics of a wind turbine in uniform inflow. *Wind Energy*, 13:86–99, 2010.

[76] N. Troldborg, J.N. Sørensen, and R. Mikkelsen. Actuator line simulation of wakes of wind turbines operating in turbulent inflow. In *2nd EWEA Conf. on the Science of Making Torque from Wind*, 2007.

[77] R. Mikkelsen, J.N. Sørensen, S. Øye, and N. Troldborg. Analysis of power enhancement for a row of wind turbines using the actuator line technique. *Journal of Physics: Conference Series*, 75, 2007.

[78] M.J. Churchfield, S. Lee, P.J. Moriarty, L.A. Martinez, S. Leonardi, G. Vijayakumar, and J.G. Brasseur. A large-eddy simulation of wind-plant aerodynamics. In *50^{th} AIAA Aerospace Sciences Meeting, Nashville, Tennessee*, 2012.

[79] M.J. Churchfield, Y. Li, and P.J. Moriarty. A large-eddy simulation study of wake propagation and power production in an array of tidal-current turbines. In *9^{th} European Wave and Tidal Energy Conf*, 2011.

[80] M.J. Churchfield, Y. Li, and P.J. Moriarty. A large-eddy simulation study of wake propagation and power production in an array of tidal-current turbines. *Philosophical Transactions of the Royal Society A*, 371, 2013.

[81] M. Shives and C. Crawford. Mesh and load distribution requirements for actuator line CFD simulations. *Wind Energy*, 2012.

[82] G.K. Batchelor. *An Introduction to Fluid Dynamics*. Cambridge University Press, 1967.

[83] J.D. Anderson. *Computational Fluid Dynamics: The basics with applications*. McGraw-Hill, Inc., 1995.

[84] R.L. Panton. *Incompressible Flow*. Wiley, 2nd edition, 1996.

[85] S.B. Pope. *Turbulent Flows*. Cambridge University Press, 2000.

[86] D.C. Wilcox. *Turbulence Modeling for CFD*. DCW Industries, Inc., La Canada, California, 1993.

[87] B.E. Launder, G.J. Reece, and W. Rodi. Progress in the development of a Reynolds-stress turbulence closure. *J. Fluid Mech.*, 68(3):537–566, 1975.

[88] M.M. Gibson and B.E. Launder. Ground effects on pressure fluctuations in the atmospheric boundary layer. *J. Fluid Mech.*, 86:491–511, 1978.

[89] P. Spalart and S. Allmaras. A one-equation turbulence model for aerodynamic flows. Technical Report AIAA-92-439, American Institute of Aeronautics and Astronautics, 1992.

[90] B.E. Launder and D.B. Spalding. *Lectures in Mathematical Models of Turbulence*. Academic Press, London, England, 1972.

[91] R. Lanzafame, S. Mauro, and M. Messina. Wind turbine CFD modeling using a correlation-based transitional model. *Renewable Energy*, 52:31–39, 2013.

[92] F.R. Menter. Two-equation eddy-viscosity turbulence models for engineering applications. *AIAA Journal*, 32:1598–1605, 1994.

[93] N.N. Sørensen, J.A. Michelsen, and S. Schreck. Navier-Stokes predictions of the NREL Phase VI rotor in the NASA Ames 80 ft x 120 ft wind tunnel. *Wind Energy*, 5:151–169, 2002.

[94] R. Mahu and F. Popescu. NREL Phase VI rotor modeling and simulation using ANSYS FLUENT® 12.1. *Mathematical Modeling in Civil Engineering*, 1/2:185, 2011.

[95] J. McNaughton, I. Afgan, D.D. Apsley, S. Rolfo, T. Stallard, and P. Stansby. A simple sliding-mesh interface procedure and its application to the CFD simulation of a tidal-stream turbine. *International Journal for Numerical Methods*, 74(4):250–269, 2014.

[96] ANSYS Inc. ANSYS FLUENT 14.5 Theory Guide, 2012.

[97] J.O. Hinze. *Turbulence*. McGraw-Hill Publishing Co., New York, 1975.

[98] J. Smagorinsky. General circulation experiments with the primitive equations. I. The basic experiment. *Month. Wea. Rev.*, 91:99–164, 1963.

[99] I. Afgan, J. McNaughton, S. Rolfo, D. Apsley, T. Stallard, and P.K. Stansby. Large eddy simulation of a 3-bladed horizontal axis tidal stream turbine: Comparisons to RANS and experiments. *International Journal of Heat and Fluid Flow*, 43:96–108, 2013.

[100] F. Porté-Agel, Y. Wu, H. Lu, and R.J. Conzemius. Large-eddy simulation of atmospheric boundary layer flow through wind turbines and wind farms. *J. Wind Eng. Ind. Aerodyn.*, 99:154–168, 2011.

[101] ANSYS Inc. ANSYS FLUENT 14.5 User's Guide, 2012.

[102] H.K. Versteeg and W. Malalasekera. *An Introduction to Computational Fluid Dynamics: The Finite Volume Method*. Pearson Prentice Hall, 1995.

[103] ANSYS Inc. ANSYS ICEM CFD 14.5 User Manual, 2012.

[104] R. Courant, K. Friedrichs, and H. Lewy. Über die partiellen Differenzengleichungen der mathmatischen Physik. *Mathematische Annalen*, 100(1):32–74, 1928.

[105] C. Fleming. *Tidal Turbine Performance in the Offshore Environment*. PhD thesis, University of Oxford, 2014.

[106] N. Troldborg. *Actuator Line Modeling of Wind Turbine Wakes*. PhD thesis, Technical University of Denmark, Lyngby, Denmark, 2008.

[107] S.J. Miley. A catalog of low Reynolds Number airfoil data for wind turbine applications. Technical Report RFP-3387 UC-60, US Dept. of Energy, Wind Energy Technology Division, Federal Wind Energy Program, 1982.

[108] R.E. Sheldahl and P.C. Klimas. Aerodynamic characteristics of seven airfoil sections through 180 degrees angle of attack for use in aerodynamic analysis of vertical

axis wind turbines. Technical Report SAND80-2114, Sandia National Laboratories, Albuquerque, New Mexico, 1981.

[109] P. Fleming, P. Gebraad, M.J. Churchfield, S. Lee, K. Johnson, J. Michalakes, J. van Wingerden, and P.J. Moriarty. SOWFA + Super Controller User's Manual. Technical Report NREL/TP-5000-59197, National Renewable Energy Laboratory, 2013.

[110] C.B. Barber, D.P. Dobkin, and H.T. Huhdanpaa. The Quickhull algorithm for convex hulls. Online: `http://www.qhull.org`. *ACM Trans. on Mathematical Software*, 22(4):469–483, 1996.

[111] E. Mucke, I. Saias, and B. Zhu. Fast randomized point location without preprocessing in two- and three-dimensional Delaunay triangulations. In *Proc. 12th ACM Symposium on Computational Geometry*, pages 274–283, 1996.

[112] D. Shepard. A two-dimensional interpolation function for irregularly-spaced data. In *Proceedings - 1968 ACM National Conference*, 1968.

[113] D.A. Simms, S. Schreck, M.M. Hand, and L.J. Fingersh. NREL unsteady aerodynamics experiment in the NASA-Ames wind tunnel: A comparison of predictions to measurements. Technical Report NREL/TP-500-29494, National Renewable Energy Laboratory, Colorado, USA, June 2001.

[114] M.M. Hand, D.A. Simms, L.J. Fingersh, D.W. Jager, J.R. Cotrell, S. Schreck, and S.M. Larwood. Unsteady aerodynamics experiment Phase VI: Wind tunnel test configurations and available data campaigns. Technical Report NREL/TP-500-29955, National Renewable Energy Laboratory, Colorado, USA, December 2001.

[115] National Renewable Energy Laboratory. http://www.nrel.gov/.

[116] S. Gómez-Iradi, R. Steijl, and G.N. Barakos. Development and validation of a CFD technique for the aerodynamic analysis of HAWT. *Journal of Solar Energy Engineering*, 131, August 2009.

[117] S. Gómez-Iradi and G.N. Barakos. Computational fluid dynamics investigation of some wind turbine rotor design parameters. *Proc. Inst. Mech. Eng., Part A: Journal of Power and Energy*, 222(5):455–470, 2008.

[118] J.L. Tangler. The nebulous art of using wind-tunnel airfoil data for predicting rotor performance: Preprint. Technical Report NREL/CP-500-31243, National Renewable Energy Laboratory, Colorado, USA, 2002.

[119] P.T. Zell and K. Flack. Performance and test section flow characteristics of the national full-scale aerodynamics complex 40- by 80-foot wind tunnel. Technical Report NASA Technical Memorandum 101065, National Aeronautics and Space Administration, February 1989.

[120] C. Ostowari and D. Naik. Post-stall wind tunnel data for NACA 44xx series airfoil sections. Technical Report STR-2559, Solar Energy Research Institute, January 1985.

[121] W.Z. Shen, R. Mikkelsen, and J.N. Sørensen. Tip loss corrections for wind turbine computations. *Wind Energy*, 8:457–475, 2005.

[122] C. Bak, J. Johansen, and P. Andersen. Three-dimensional corrections of airfoil characteristics based on pressure distributions. In *European Wind Energy Conference Proceedings*, 2006.

[123] S-P. Breton, F.N. Coton, and Geir Moe. A study on rotational effects and different stall delay models using a prescribed wake vortex scheme and NREL Phase VI experiment data. *Wind Energy*, 11:459–482, 2008.

[124] A. Betz. Das maximum der theoretisch möglichen ausnützung des windes durch windmotoren. *Zeitschrift für das gesamte Turbinenwesen*, 26:307–309, 1920.

[125] F.W. Lanchester. A contribution to the theory of propulsion and the screw propeller. *Transactions of the Institution of Naval Architects*, 57:98–116, 1915.

[126] P. Fuglsang, K. S. Dahl, and I. Antoniou. Wind tunnel tests of the Risø-A1-18, Risø-A1-21 and Risø-A1-24 airfoils. Technical Report Risø-R-1112(EN), Risø National Laboratory, Roskilde, Denmark, 1999.

[127] F. Bertagnolio, N.N. Sørensen, J. Johansen, and P. Fuglsang. Wind turbine airfoil catalogue. Technical Report Risø-R-1280(EN), Risø National Laboratory, 2001.

[128] J. Schluntz and R. H. J. Willden. The effect of rotor design on the power output of closely packed tidal turbines. In *Proc. 10^{th} European Wave and Tidal Energy Conf.*, 2013.

[129] T. Nishino and R. H. J. Willden. Effects of 3-D channel blockage and turbulent wake mixing on the limit of power extraction by tidal turbines. *International Journal of Heat and Fluid Flow*, 37:123–135, 2012.

[130] J.W. Cooley and J.W. Tukey. An alborithm for the machine computation of the complex Fourier series. *Mathematics of Computation*, 19:297–301, 1965.